INFORMATION TO USERS

This manuscript has been reproduced from the microfilm master. UMI films the text directly from the original or copy submitted. Thus, some thesis and dissertation copies are in typewriter face, while others may be from any type of computer printer.

The quality of this reproduction is dependent upon the quality of the copy submitted. Broken or indistinct print, colored or poor quality illustrations and photographs, print bleedthrough, substandard margins, and improper alignment can adversely affect reproduction.

In the unlikely event that the author did not send UMI a complete manuscript and there are missing pages, these will be noted. Also, if unauthorized copyright material had to be removed, a note will indicate the deletion.

Oversize materials (e.g., maps, drawings, charts) are reproduced by sectioning the original, beginning at the upper left-hand corner and continuing from left to right in equal sections with small overlaps. Each original is also photographed in one exposure and is included in reduced form at the back of the book.

Photographs included in the original manuscript have been reproduced xerographically in this copy. Higher quality 6" x 9" black and white photographic prints are available for any photographs or illustrations appearing in this copy for an additional charge. Contact UMI directly to order.

UMI

A Bell & Howell Information Company
300 North Zeeb Road, Ann Arbor MI 48106-1346 USA
313/761-4700 800/521-0600

ENTROPIC FORCES AND PHASE SEPARATION IN BINARY NEARLY HARD-SPHERE COLLOIDS

Anthony D. Dinsmore

A DISSERTATION

in

PHYSICS AND ASTRONOMY

Presented to the Faculties of the University of Pennsylvania in Partial Fulfillment of the Requirements for the Degree of Doctor of Philosophy

1997

Arjun G. Yodh

Supervisor of Dissertation

Nigel Lockyer

Graduate Group Chairperson

UMI Number: 9800858

UMI Microform 9800858
Copyright 1997, by UMI Company. All rights reserved.

This microform edition is protected against unauthorized copying under Title 17, United States Code.

UMI
300 North Zeeb Road
Ann Arbor, MI 48103

COPYRIGHT

Anthony D. Dinsmore

1997

ACKNOWLEDGEMENTS

In the course of my research, I have benefited tremendously from collaborations with many people. First and foremost, I would like to thank my thesis advisor, Arjun Yodh, for providing a very active and stimulating research environment. His encouragement to undertake a variety of projects (about which I initially knew nothing) has certainly made me a more productive and flexible researcher. I believe I have also benefited from his very high standards of scientific work, oral presentation, and writing. Most of all, I have enjoyed sharing his enthusiasm for the subject.

Bill Angerer and I have shared a lot of lab time together; I am grateful for the many things he has taught me and for making the lab a more fun and interesting place. I thank Peter Kaplan for helping me get started when I joined the group and for his continued advice. I also thank John Crocker for the past eight months of continuous conversations about colloid physics and optics. I have learned a great deal from them. I am grateful to Cecil Cheung, Keng-Hui Lin, David Boas, Maureen O'Leary, Jining Qi, Kristen Jester, Joe Culver, Xingde Li, Ming-Hsu Kao, Amani Gandour, Ningping Yang, and Mohsen Yeganeh for their help with optics, electronics and computer problems. I also thank Maria Zuckerman, Anthony Smith, and A. Jared Ledbetter for their summer work in the lab.

David J. Pine (UCSB) has contributed valuable research guidance and many insightful ideas over the years. I also thank Prof. Larry Campbell for time spent with

us during his year on leave from Hobart and William Smith Colleges. Larry contributed a lot to my understanding of colloid chemistry and thermodynamics and of light scattering by asking questions – and then answering most of them. I thank Sarah L. Keller (then a postdoc at U. of California, Santa Barbara) for her work on freeze-fracture transmission-electron microscopy and Philippe Poulin for sharing his expertise in surfactant chemistry.

Zhiming Yu and Prof. Charlie Johnson devoted a great deal of time, expertise and equipment to the electron-beam lithography work. Their contributions enabled a great variety of experiments on surface effects and photonic structures which would otherwise have been impossible. I also thank Prof. George H. Watson, on leave from Univ. of Delaware, for his recent progress on this project, and Jonah Paransky and Manoj Aggarwal for their work on the e-beam lithography and the wet chemistry, respectively. I thank Derek Rethwisch and Joe Matteo for work on the lithography and on the convective assembly. Radoslav Antonov and Thomas Heinzel also provided a lot of useful technical advice about the use of the SEM and other microfabrication equipment.

It has been a pleasure to work with Derek T. Wong on the vesicle experiments. I thank Prof. Dennis E. Discher for his time and expertise in making unilamellar vesicles and manipulating them with microcapillary tubes. Prof. Phil Nelson made valuable contributions to the theoretical prediction of spontaneous envelopment of

particles by membranes. I thank him for his interest and for his clear thinking which improved my own understanding of the problem, and for his short course in Biological Physics.

I thank Prof. Tom Lubensky for many conversations about statistical mechanics and for proofreading manuscripts. I am grateful to him, Arjun, and to my other thesis committee members – Professors Paul Heiney, Charlie Johnson, and Mirjam Cvetic – for their critical evaluations of this dissertation.

Not all of my time was spent on research. I thank Vivian Hasiuk for arranging part-time teaching positions and Yongming Cai, for whom I was T.A. for several semesters, for his successful efforts at stimulating the students' interest, improving the organization of the lab class, and enriching my teaching experience.

Finally, I am very happy to thank my parents, Jenn's parents, and my brothers for their interest in my research. Their visits to the lab were among the most enjoyable moments of my time at Penn. Most of all, I thank my wife Jenn, without whom my graduate-student career would have been exceedingly one-dimensional. Sharing my excitement at new-found discoveries has been as much fun as participating in her enthusiasm for her own research. I thank her for reading manuscripts, asking questions, and contributing her ideas. Her companionship, even from a distance, has been a tremendous source of strength for me.

ABSTRACT

ENTROPIC FORCES AND PHASE SEPARATION IN BINARY NEARLY HARD-SPHERE COLLOIDS

Anthony D. Dinsmore

Arjun G. Yodh

We present the results of experimental and theoretical studies of the statistical mechanics of suspensions of hard spheres of two different sizes. We have focused on the effects of entropic depletion (or excluded-volume) effects, which play an important role in many real mixtures. In the first set of experiments, we studied the phase behavior of binary hard-sphere mixtures with diameter ratios between 2 and 12. We found that even when the volume fraction of spheres was only 0.20, separation into coexisting fluid and solid phases occurred despite the absence of attractive pair interactions. We measured the structures and compositions of the equilibrium phases both in the bulk of the sample and at the wall of the container. We also propose an original, physically-transparent model that predicts fluid-solid phase separation in hard-sphere mixtures without fit parameters, in close agreement with our measurements and with previously-published results for monodisperse hard-sphere mixtures.

Investigating the effects of hard (inert) surfaces, we demonstrated for the first time that inert walls of complex shape can induce entropic force fields that can trap, repel, or induce drift of the larger particles in a binary suspension. We measured

the entropic force on a large sphere as a function of its position near the edge of a terrace and found that it is repelled by a 40-femto-Newton force. A similar mechanism confined large spheres in a corner and, inside rigid phospholipid vesicles, pushed the larger spheres along the wall in the direction of increasing curvature. We predict that, under some circumstances, a unilamellar vesicle will spontaneously envelop a large sphere. Aside from their fundamental interest, these results are likely to improve our understanding of the behavior of complex fluids inside porous media and of proteins inside cells.

We have also developed new techniques for making arrays of submicron particles for photonic applications. Two-dimensional patterns made with electron-beam lithography and three-dimensional crystallites made using an extension of the "convective assembly" technique will be presented.

Contents

1 Introduction to Depletion Forces **1**

1.1 Introduction and Outline 1

1.2 Some Forces on Colloidal Particles: Water, Gravity, and DLVO Theory 4

1.3 Depletion Forces among Hard Spheres 6

1.3.1 Ideal-Gas Approximation for the Small Spheres 7

1.3.2 A Functional Form for the Depletion Force 10

1.3.3 Depletion Forces at Walls 12

1.3.4 Accounting for the Hard-Sphere Structure of the Small Particles 13

2 Measurements of the Phase Behavior of Binary Nearly-Hard Sphere Colloids **16**

2.1 Background 19

2.2 Experimental Techniques 22

2.2.1 Sample Preparation 22

2.2.2 Measurement and Probe Techniques 23

2.3 Results: Bulk of the Sample 30

2.3.1 Detailed Observations of the Phase Separation 30

2.3.2 Crossover from Ordered to Disordered Dense Phase 37

2.3.3 The Effect of Gravity on the Equilibrium State 40

2.3.4 Measured Phase Diagrams 43

2.3.5 Crystallization in Samples with Low Diameter Ratios 51

2.4 Results: Surface of the Sample Container 54

2.4.1 Dense Fluid at the Surface of the Sample Container 57

2.4.2 Structure and Morphology of Surface Crystals 61

2.4.3 Kinetics of Crystallization at the Surface 62

2.5 Conclusions 65

3 Calculation of Phase Diagrams of Binary Hard-Sphere Mixtures 68

3.1 Background 71

3.2 Theoretical Model 75

3.2.1 Large-Sphere Crystal 80

3.2.2 Fluid Structures 83

3.2.3 Equilibrium Conditions 92

3.3 Results 98

3.4 Conclusions 102

4 Entropic Force Fields within Surface Microstructures **103**

4.1 Repulsion from the Edge of a Terrace 106

4.1.1 Measurement of a Free Energy Barrier 106

4.1.2 Comparison to Theory 115

4.1.3 Conclusions 119

4.2 Confinement to a Corner 119

4.2.1 Measurements of Lifetimes 122

4.2.2 Theory 126

4.2.3 Conclusions 131

4.3 Other Microstructures and Applications 133

5 Hard Spheres inside Vesicles: Curvature and Excluded-Volume Effects **136**

5.1 Rigid Walls 139

5.1.1 Calculation of Depletion Force along a Curved, Rigid Wall . . 139

5.1.2 Measurement of Depletion Force along a Curved, Rigid Wall . 141

5.1.3 Conclusions 149

5.2 Flexible Vesicle Walls 149

5.3 Conclusions 154

6 Colloidal Assembly **157**

6.1 Background 159

6.1.1 Photonic Band Gap Materials 159

6.1.2 Other Assembly Techniques 165

6.2 Making Colloidal Templates with Electron-Beam Lithography 166

6.2.1 Experimental Procedure 166

6.2.2 Results 171

6.3 Convective Assembly of Three-Dimensional Colloidal Crystals 173

6.3.1 Theory 174

6.3.2 Experimental Procedure 180

6.3.3 Experimental Results 183

6.4 Conclusion 188

6.4.1 Combining Lithography and Convective Assembly 188

6.4.2 Light Scattering Experiments 191

7 Experimental Methods **193**

7.1 Introduction 193

7.2 Sample Preparation 194

7.2.1 Colloids 194

7.2.2 Vesicles 196

7.2.3 Treatment of Glass: Hydrophilic and Hydrophobic Surfaces . . 197

7.2.4 Making Glass Sample Cells 200

7.3 Using the Microscope 201

7.3.1 Cleaning Optics 201

7.3.2 Care of the Optical Microscope 201

7.3.3 Imaging: the Zeiss Axiovert 135 202

7.3.4 Laser Tweezers 206

7.3.5 Light Scattering in the Optical Microscope 209

7.4 Computer Control, Acquisition, and Image Analysis 210

7.4.1 Image Processing and Analysis 212

7.5 Electron-Beam Lithography and Microassembly 213

7.5.1 Coverslip Preparation 214

7.5.2 Electron-Beam Lithography 216

7.5.3 Glue Processing 217

7.5.4 Adding the Colloidal Particles 218

7.5.5 Etching Microscopic Holes in Silicon 219

A NIH Image Macros **223**

B Determining Free Energy from Particle Dynamics **226**

C Glossary of Symbols and Acronyms **228**

List of Tables

2.1 Table of (ϕ_L,ϕ_S) values which separate the region of ordered, crystalline solid from the region of non-equilibrium (glassy) behavior. 40

2.2 Table of measured and extrapolated volume fractions of the phases in equilibrium in samples with $\alpha = 6.7$, 8.8, and 12.0. 48

2.3 Previous table continued. 49

2.4 Table of results for $\alpha \leq 4.6$. 52

2.5 Previous table continued 53

List of Figures

1.1 Illustration of the DLVO potential between a pair of nearly hard spheres. 6

1.2 Illustration of depletion "attraction through repulsion". 8

1.3 Illustration of the depletion force from the entropic point of view. . . 9

1.4 Plot of the depletion potential between two large spheres. 11

1.5 Illustration of the excluded-volume overlap between a large sphere and a flat wall. 13

1.6 Cartoon of depletion repulsion in binary hard-sphere mixtures. 14

2.1 Optical micrograph of size-segregation and spontaneous ordering at the surface of a ternary mixture of hard spheres 17

2.2 Schematic of apparatus used by S. L. Keller and J. Zasadzinski for freeze-fracture of colloidal crystals. 26

2.3 Schematic illustration of the apparatus for diffusing wave spectroscopy (DWS) in reflection geometry. 28

2.4 Plot of light-intensity temporal correlation function for a fluid sample and for a solid (or glass) sample. 29

2.5 Stability diagram, showing the final phases of binary hard-sphere mixtures. 31

2.6 Cartoon of the sediment that appears at the bottom of samples that undergo fluid-solid phase separation in the bulk. 34

2.7 Freeze-fracture transmission electron micrographs of the solid phase in a binary suspension of polystyrene spheres. 36

2.8 Optical micrographs of a binary mixture of polystyrene spheres, showing the "glassy" behavior. 38

2.9 Plot comparing settling rate to solidification rate for two samples with the same colloid content but different water mass densities. 42

2.10 Experimentally-determined phase diagrams. 44

2.11 Optical micrographs of 0.825-μm polystyrene spheres (ϕ_L=0.02) next to a glass wall. 56

2.12 Plot of the area fraction of 0.605-μm spheres (η_L^{wall}) at a flat glass wall. 58

2.13 Scanning-electron micrographs of the crystallites that grow on the glass wall of the sample container. 63

3.1 Drawing of large and small spheres showing the excluded-volume regions described in the text. 69

3.2 Cartoon of a colloid in equilibrium with the room. 78

3.3 Diagram of the large-sphere crystal. 81

3.4 Left – Plot of the osmotic pressure of a monodisperse hard-sphere FCC or HCP crystal as a function of volume fraction of spheres. Right — The fractional volume accessible to the small particles as a function of large-sphere volume fraction. 84

3.5 Plot of the dimensionless pressure as a function of volume fraction, comparing the ideal-gas and hard-sphere (Carnahan-Starling) results. 86

3.6 Cartoon showing how the effective volume fractions, $\tilde{\phi}_{L,S}$, are defined. 87

3.7 Cartoon showing the fundamental difference between inserting a large sphere into a small-sphere fluid and inserting a small sphere into a large-sphere fluid. 90

3.8 Comparison of the pressure of a binary fluid ($\alpha = 10$) calculated in the present theory to the result of scaled particle theory. 93

3.9 Same as the previous Figure, but with size ratio $\alpha = 20$. 94

3.10 Comparison of the chemical potentials ($\alpha = 10$) calculated in the present thoery to the result of SPT. 95

3.11 Same as the previous Figure, but with size ratio, $\alpha = 20$. 96

3.12 (a) A phase diagram calculated from the present theory is compared to that of Poon and Warren. (b) A phase diagram calculated from the present theory (for binary hard-sphere mixtures) is compared to that of Lekkerkerker *et al.* (for mixtures of hard spheres and polymer). . . 100

4.1 Illustration of how the shape of a sample container can affect the behavior of particles within it. 104

4.2 Schematic diagram of the step edge and experimental apparatus. . . . 108

4.3 The measured free energy of the mixture F/k_BT, as a function of the distance of a large sphere from the step edge. 110

4.4 Measured probability distributions of a single large sphere parallel and perpendicular to the step edge. 111

4.5 Exact calculation of the probability distributions of a particle diffusing near an infinitely-repulsive wall. 114

4.6 Illustration of the origin of the step-edge repulsion. 116

4.7 Surface plot of predicted free energy *vs.* position of the large sphere. . 118

4.8 Optical micrograph of large spheres that are diffusing along the line of a corner, pinned there by the smaller spheres. 120

4.9 Optical micrograph of nucleation of the larger spheres starting at a corner. 121

4.10 Schematic diagram of sample cell and imaging geometry used to study the diffusion of polystyrene spheres near corners. 123

4.11 Measured diffusion coefficient (D) *vs.* salt concentration on glass and on silicon. 125

4.12 Plot of $ln(\tau)$ *vs.* the ideal-gas pressure (top) and *vs.* the hard-sphere pressure (bottom) 129

4.13 Cartoon showing the change in excluded-volume overlap when a large sphere "escapes" from a corner. 130

4.14 Schematic plot of the depletion free energy as a function of the distance, r, between the large sphere and the wall. 132

4.15 Cartoons of surface microstructures that could order the large spheres while increasing the total entropy. 135

5.1 Cartoon illustrating the depletion force along a wall with varying curvature 140

5.2 Plot of the free energy F of a binary mixture when the large sphere is against a concave wall with curvature radius R_C. 141

5.3 Cartoon of the 600-nm thick optical slice through an SOPC vesicle. . 143

5.4 The measured probability distributions of a large sphere in a vesicle by itself (a) and in the presence of small spheres (b). 145

5.5 The measured total free energy of the binary mixture, F, when the large (0.237-μm-radius) sphere was at the vesicle wall 148

5.6 Cartoon demonstrating how hard spheres can induce a change in shape of a vesicle. 150

5.7 Illustration of the entropic repulsion between a hard object and a fluctuating membrane. 151

5.8 Illustration of the free energy barrier against complete envelopment of a large sphere. 154

5.9 Cartoon showing how the distribution of particles in a vesicle can correlate with the composition of a two-component membrane. 156

5.10 Illustration of membrane-induced interactions that could arise among large spheres that are stuck to the membrane by the depletion force. . 156

6.1 Illustration of the use of defects in photonc band-gap materials as waveguides and cavities. 162

6.2 Schematic of the lithographic procedure for making two-dimensional particle arrays. 167

6.3 Optical micrograph of patterns of holes in PMMA. 168

6.4 Cartoon of (a) a good exposure and developing of PMMA layer and of (b) an overexposure. 169

6.5 Optical micrograph of 0.460-μm-diameter spheres stuck to glass by poly-L-lysine. 171

6.6 Optical micrographs of 0.46-μm polystyrene spheres stuck to two- dimensional patterns made by electron-beam lithography. 172

6.7 Schematic diagram of the forces at work in convective assembly . . . 175

6.8 Cartoon of the thin film formed by water at a hydrophilic surface. . . 176

6.9 Illustration of the capillary force that pulls immersed particles toward one another. 177

6.10 Illustration of the ordering of particles in a second layer atop the first layer. 178

6.11 Photograph of marbles in the AB_2 binary crystal structure. 180

6.12 Apparatus used for convective assembly. 181

6.13 Optical micrograph of a sample after one round of convective assembly. 184

6.14 Optical micrograph of three layers of a binary AB_2 crystal made by convective assembly. 186

6.15 Optical micrographs of two different planes in the same area of an AB_2 crystal made by convective assembly. 187

6.16 Illustration of the stacking faults that arise when stacking spheres randomly atop a layer with triangular order. 189

7.1 Schematic diagram of procedure for making vesicles. 198

7.2 Schematic diagram of the optical microscope. 203

7.3 Schematic diagram of the optics for control of the laser tweezers. . . . 207

7.4 Marking and scratching coverslips. 215

7.5 Scanning electron micrograph of the piano-shaped structure etched in silicon. 220

7.6 Scanning electron micrograph of the profile of the $SF_6 + CCl_2F_2$ plasma etch of silicon. 221

7.7 Scanning electron micrograph of the profile of the $CF_4 + H_2$ plasma etch of silicon. 222

Chapter 1

Introduction to Depletion Forces

1.1 Introduction and Outline

The goal of this thesis was to learn about the statistical mechanics of colloidal particles. We studied hard spheres because they provide a unique opportunity to isolate and understand the implications of the fact that particles *take up space*. Rearranging hard spheres – stacking them in different ways, putting them near walls, in corners, etc. – changes the amount of volume accessible to the other particles, hence the entropy of the system. These experiments answered some fundamental questions about phase transitions and demonstrated some new ideas concerning the effects of walls. All of the thermodynamic effects considered here arise from excluded-volume (depletion) effects, which will be reviewed later in this chapter.

In Chapter 2, we address the question of whether purely repulsive forces among particles can lead to phase separation. We present a comprehensive study of the phase behavior of binary nearly hard-sphere mixtures with size ratios between 2 and

12. In particular, we observed fluid-solid coexistence in the bulk at total volume fractions as low as 0.2, as well as formation of a loose gel. In Chapter 3, we present a complete and physically-transparent theoretical model with which we calculated phase diagrams for these systems *without* fit parameters. We obtained good agreement with experimental results of Chapter 2 and with published studies of the freezing of monodisperse hard-sphere mixtures. In Chapter 2, we also investigate how the behavior of hard spheres changes when a flat surface is nearby. We have observed a dense fluid of large spheres that appears at a flat wall in binary mixtures, and we have observed nucleation of crystallites within this dense, quasi-two-dimensional fluid. In Chapters 4 and 5, we show that inert surfaces of various shapes can create repulsive or attractive "entropic force fields" that act on the larger spheres in binary mixtures. We show how these effects manifest themselves inside rigid (multilamellar) vesicles and present theoretical evidence that depletion forces provide a new mechanism for shape changes of unilamellar vesicles containing particles. Finally, in Chapter 6, we describe two techniques that we have developed for assembling microscopic particles into arrays. Two-dimensional arrays of submicron particles made using electron-beam lithography and three dimensional crystallites made with "convective assembly" will be presented. These techniques (and those demonstrated in the previous chapters) will allow basic studies of the optical properties of colloidal crystals, a subject rich with technological implications.

In addition to providing fundamental insight into the role of entropy in thermodynamics, the hard-sphere model is a useful first step toward understanding mixtures with more complex interactions. There exist theoretical techniques for extrapolating from the hard-sphere case to include other interactions [1]. For these reasons, the question of whether (and in what way) particles can phase separate in a purely repulsive system has been of long-standing interest and debate. Furthermore, the novel surface effects that are presented in Chapters 2, 4 and 5 are expected to be present in systems with non-hard-core interactions as well.

Rather than overwhelming the depletion attraction, adding repulsion between particles can *enhance* it! Experiments have investigated the effects of increasing the range of electrostatic repulsion and found that the strength [2] and range [3] of the depletion attraction are greatly increased. Even when the repulsion among the smaller particles is reduced (for example, by replacing hard spheres with interpenetrable polymers), there is still a depletion attraction, although its strength may be reduced [4]. Furthermore, theories based on the binary hard-sphere model compare well with experimental measurements of the activities of proteins in water [5, 6]. The hard-sphere model is qualitatively applicable to a wide range of real mixtures (in addition to the nearly hard-sphere mixtures described in this thesis), including industrial colloids (paint, ink, paper size), foods, blood, and the interior of biological cells.

1.2 Some Forces on Colloidal Particles: Water, Gravity, and DLVO Theory

This section provides a very brief introduction to some of the forces acting on colloidal particles. The intent is to show the reader how the strength and range of depletion forces compare to those of other forces.

When looking at submicron particles in the microscope, the most striking fact is that they are constantly in motion. With a diffusion constant on the order of one $\mu m^2/s$, particles seldom stay within the focus depth for longer than a second or two [7, 8, 9]. The reason for this diffusive, or Brownian, motion is random collisions of the particle with the water molecules. Non-random, collective collisions with water molecules are known as convective forces and will not be discussed here. The diffusion of particles, however, is an essential cornerstone of the present work. We rely on Brownian motion to enable the particles to explore all the available stacking arrangements in order to find the one with the lowest free energy. Because the particles are able freely to explore phase space, the laws of thermodynamics and statistical mechanics are relevant (as noted, for example, by Einstein in [10] and by Vrij [11]).

Gravity does apply a downward force on the particles. Fortunately, this force is small in our experiments because of the small density mismatch compared to the solvent (water), because of the small particle size, and because the tendency to settle is resisted by the water molecules [7, 12]. In all of the present experiments, sedimen-

tation of *individual* particles could be safely ignored (except in the phase diagram measurements, in which steps were taken to show that gravity was not relevant). Since the sedimentation rate of an object increases with the square of its size, *clusters* of particles sediment relatively quickly. This fact was useful in observing phase separation in the bulk of samples, since the clusters could be seen as a sediment at the bottom of the sample cell.

Interactions among pairs of colloidal particles include attractive van der Waals and repulsive electrostatic forces. Van der Waals forces are comparatively strong, but their range is generally restricted to a few nm (the length scale of large molecules) [13]. In the absence of any barrier against the van der Waals attraction, however, the particles do flocculate. Fortunately, electrostatic forces among the charges on the particles' surfaces and the ions in solution provide a stabilizing barrier[1]. The sum of van der Waals and electrostatic forces among colloidal particles is known as the Derjaguin-Landau-Verwey-Overbeek (DLVO) theory [13, 9, 15, 16]. For the present purposes, the important results are that the electrostatic repulsion prevents flocculation, yet can be screened out to very short range – approximately 5 nm in the experiments performed here (at 0.01 M salt). The range of these non-hard-sphere interactions is determined by the Debye screening length, $l_D \propto 1/\sqrt{\text{ion concentration}}$. Since the screening length is so short compared to the particle size ($\sim$ 100 nm), the

[1]Steric forces among polymers grafted to the particles' surfaces can also stabilize the particles [13, 14]

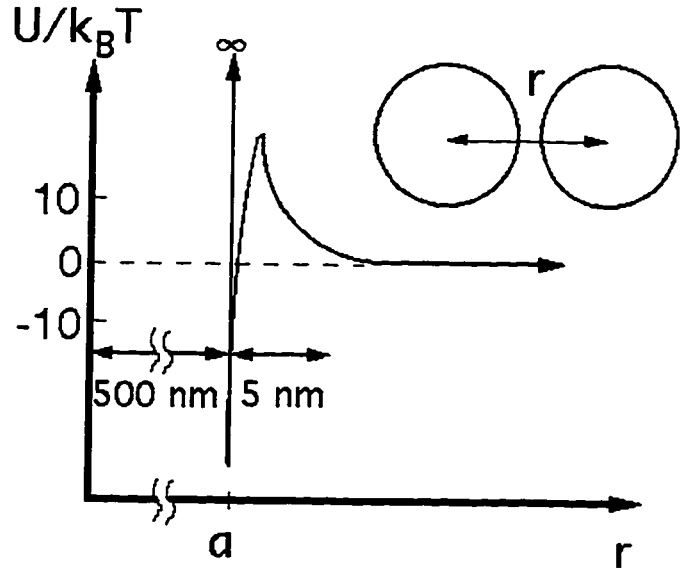

Figure 1.1: Illustration of the DLVO potential between a pair of nearly hard spheres. The very steep, short-ranged repulsion of the potential resembles a hard-sphere potential.

particles closely resembled hard spheres (see Fig. 1.1).

1.3 Depletion Forces among Hard Spheres

We now come to forces due to collisions among colloidal particles. All particles occupy some finite volume (unlike an ideal gas) and therefore occasionally bump into one another. In a mixture of hard spheres of two different sizes, the collisions give rise to depletion forces. As is so often the case in physics, there are two ways to think about the depletion force. The two models described below both rely on an ideal-gas approximation and obtain identical results. We will look beyond the ideal-gas

approximation in section 1.3.4.

1.3.1 Ideal-Gas Approximation for the Small Spheres

In 1976, A. Vrij used the term "attraction through repulsion" to describe the depletion force [11]. The idea is illustrated in Fig. 1.2. In (a), the small spheres collide with the large sphere, thus exerting small forces on it. The collisions occur with equal probability everywhere on the large sphere's surface, so the average net force is zero. When the large spheres approach one another, as in (b), the small spheres can no longer exert a backward force on the spheres. They therefore exert a *net* force that pushes the large spheres together. An estimate of the magnitude of the force is the small-sphere pressure, P_S, times the area of the sheltered region. The question of what model to use to calculate P_S will be discussed below. The ideal-gas model allows a single mean-field pressure to be used; using the hard-sphere model requires careful consideration of how the small particles quasi-statically rearrange themselves as the larger spheres move together.

One can also consider the entropy gained when the two large spheres move together (the view proposed by Asakura and Oosawa, in 1954 [17, 18]). This point of view is particularly relevant for thermodynamics, since entropy is a universally important quantity. Since we are considering a mixture containing only two large spheres and many (hundreds or thousands) of small ones, we can ignore the entropy of the large

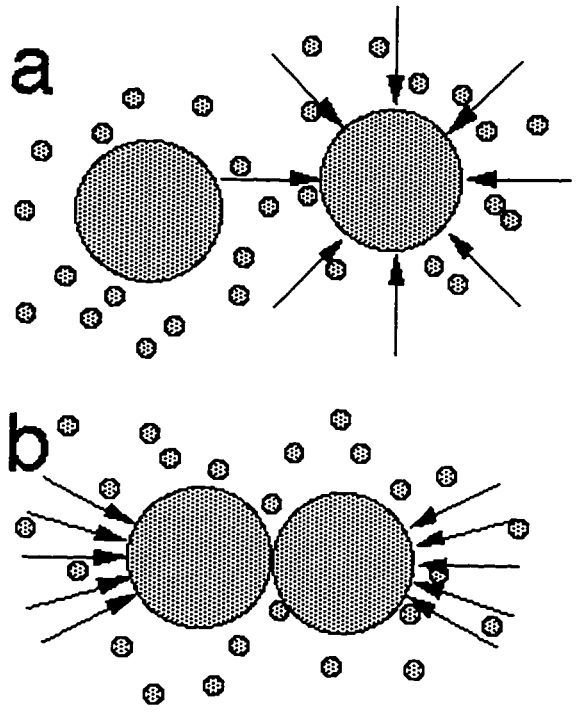

Figure 1.2: Illustration of depletion "attraction through repulsion". The arrows illustrate the forces on the larger sphere due to the smaller spheres when (a) the large spheres are separated and when (b) their surface are within a small-sphere diameter.

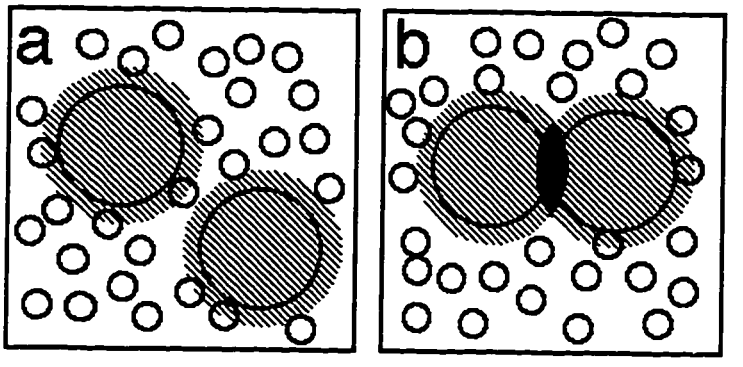

Figure 1.3: Illustration of the depletion force from the entropic point of view. The small spheres are excluded from the hatched regions. In (a), the volume accessible to the small spheres is the total volume of the box minus the black region. In (b), the accessible volume increases by the volume of the black overlap region.

spheres. (We drop this assumption in Chapter 3.) Here, we only consider the entropy of the small particles. We assume (for the moment) that the entropy of the small spheres is given by the ideal-gas approximation [19]: $S = S_0 + k_B \ln(V_{\text{acc}})$, where S is the entropy, S_0 is a term that does not depend on any degrees of freedom of the particles, k_B is Boltzmann's constant, and V_{acc} is the volume accessible to the centers of mass of the small spheres.

Due to the hard-core repulsion, the center of mass of each small sphere is excluded from within its radius of each large-sphere surface (shaded regions in Fig. 1.3). When the large spheres are well separated (as in (a)), the accessible volume, $V_{\text{acc}}^{(a)}$, is the volume of the box minus the two exclusion zones. When the two large spheres come within a small-sphere diameter of one another, the exclusion zones overlap (black region in Fig. 1.3(b)). Now, the accessible volume, $V_{\text{acc}}^{(b)}$, is the total volume minus

the two spherical exclusion zones *plus* the volume of the overlap region. The entropy change is $k_B N_S[(\ln(V_{\text{acc}}^{(b)}) - \ln(V_{\text{acc}}^{(a)})] \approx k_B N_S V_{\text{overlap}}$. The (Helmholtz) free energy change, ΔF, is simply $-T\Delta S$ (since the internal energy does not change). Thus, ΔF decreases by $(N_S k_B T)V_{\text{overlap}}$. We note that, within the ideal gas approximation that we have used, $N_S k_B T = P_S$. Thus, $\Delta F = -P_S V_{\text{overlap}}$. Equivalently, one could have written the free energy change as

$$\Delta F = \frac{\partial F}{\partial V}\Delta V = -P_S V_{\text{overlap}}, \tag{1.1}$$

since $P = -(\partial F)(\partial V)$. The *internal energy* does not change, but the *free energy* decreases when the large spheres approach. The gradient of the energy is a real force (as in Vrij's picture).

1.3.2 A Functional Form for the Depletion Force

The size of the overlap volume, V_{overlap} can be calculated from geometry. For two large spheres of diameter a_L surrounded by small spheres of diameter a_S, V_{overlap} is

$$V_{\text{overlap}}(r) = \frac{\pi}{6}(a_L + a_S - r)^2(a_L + a_S + \frac{r}{2}), \tag{1.2}$$

where r is the distance between the large-sphere centers. The above is true only when $a_L < r < a_L + a_S$. To obtain the free energy, we multiply by

$$P_S = \phi_S k_B T \frac{6}{\pi a_S^3}, \tag{1.3}$$

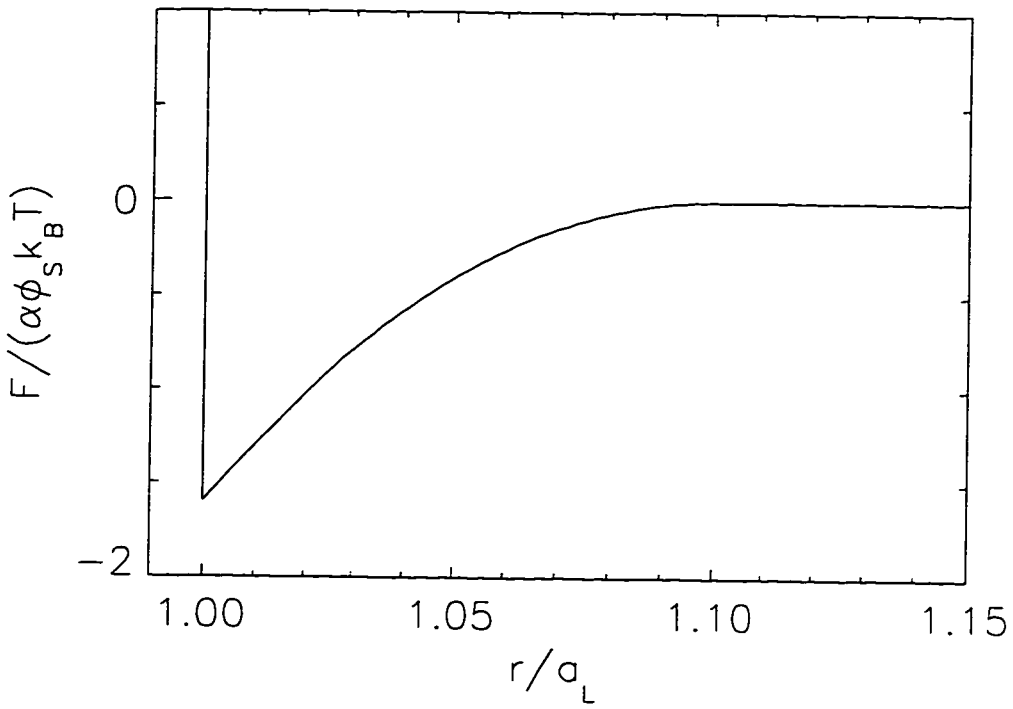

Figure 1.4: Plot of the depletion potential between two large spheres. The sphere diameter ratio, α, is 10. The free energy of the mixture, F, is plotted in units of $\alpha\phi_S k_B T$ and the minimum occurs at approximately -1.5. The small spheres are treated as an ideal gas.

where ϕ_S is the small-sphere volume fraction, defined as the number of small spheres per unit volume times the volume of a single small sphere. The resulting potential is plotted in Fig. 1.4 as a function of separation between two large spheres.

The depletion potential should significantly affect the distribution of the large spheres when its magnitude becomes comparable to the mean particle kinetic energy per particle, (3/2 $k_B T$). The greatest depletion potential occurs at contact ($r = a_L$).

From the above, we find that

$$F(r = a_L) = -(3/2)\alpha\phi_S k_B T, \tag{1.4}$$

where α is the ratio of sphere diameters ($\alpha = a_L/a_S$). For sphere diameter ratios of order 10 and $\phi_S \sim 0.30$, the depletion force is expected (and observed) to influence the equilibrium state.

1.3.3 Depletion Forces at Walls

Kaplan, Rouke, Yodh and Pine noted that precisely the same arguments can be applied for the case of a large sphere approaching a wall [20]. As shown in Fig. 1.5, the exclusion zones overlap when the large sphere is near a wall, thus increasing the volume accessible to the small spheres. At the wall, the overlap volume is given by

$$V_{\text{overlap}} = \frac{\pi}{3}(r - \frac{a_L}{2} - a_S)^2(r + a_L + \frac{a_S}{2}). \tag{1.5}$$

The excluded volume overlap is approximately *twice as large* as the two-sphere overlap. Therefore, in the ideal-gas approximation discussed above, the attraction between a large sphere and a wall is twice as strong as that between two large spheres. The depletion attraction to a flat wall has been directly measured in binary hard-sphere mixtures [21, 22], in mixtures of colloidal spheres and micelles [23, 3], and in mixtures of colloidal spheres and nonadsorbing polymers [4]. Chapters 2, 4 and 5 explore in detail the consequences of the depletion forces at flat walls, walls with grooves, and at curved walls.

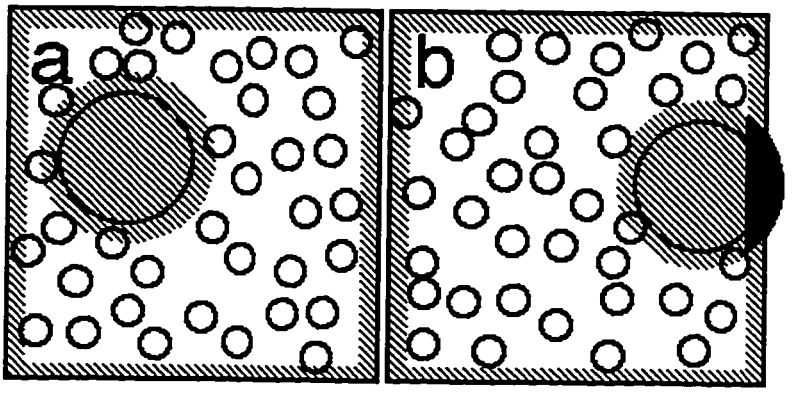

Figure 1.5: Illustration of the excluded-volume overlap between a large sphere and a flat wall. The volume accessible to the small spheres increases by the volume of the overlpa region shown in black.

1.3.4 Accounting for the Hard-Sphere Structure of the Small Particles

In the above discussion, we have neglected the fact that the small spheres also bump into one another – that they are hard spheres too! We have used the ideal-gas approximation to describe them, ignoring the effects they have on each other. One might guess that the solution is to let P_S be the pressure of a hard-sphere fluid. This approach is wrong because it fails to account for the rearrangement of small spheres as the large ones move together. From our simple arguments, it is clear that the density of small spheres will be slightly larger right next to the wall than, say, one radius inward. A sphere located a small distance from the wall has effectively blocked off the space between itself and the wall – unnecessarily reducing the entropy. This sphere will (on average) simply move closer to the wall. More detailed calculations have confirmed this result [24, 25]. Now, if we imagine bringing two large spheres together

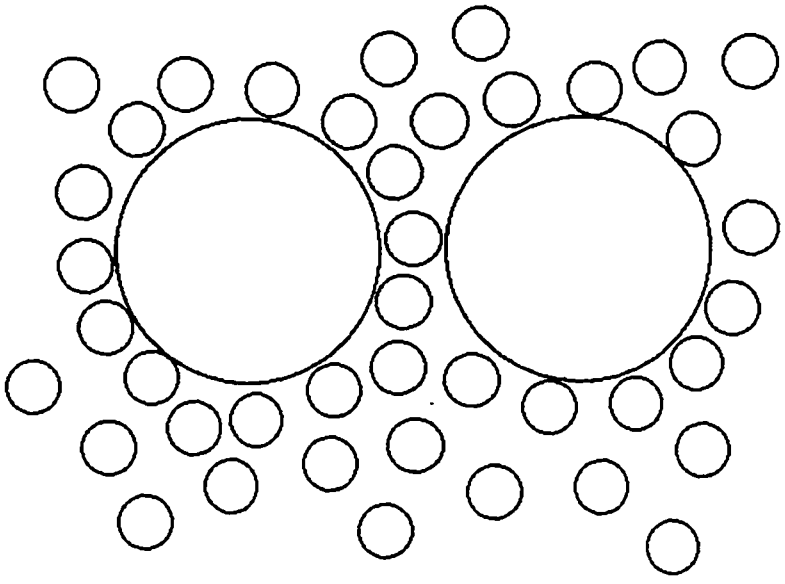

Figure 1.6: Cartoon of depletion repulsion in binary hard-sphere mixtures. In order for the large spheres to get closer to one another, the small spheres must first be expelled.

using this more accurate picture, we see that the small spheres must first be *expelled* from some of the space around the large spheres (Fig. 1.6). The result is a relatively weak depletion *repulsion* when the large-sphere surfaces are approximately one small-sphere diameter apart [26, 27, 28]. In Vrij's model, the structural rearrangement of the small spheres results in a larger density of them between the large spheres, enhancing the backward pressure and reducing the net attractive force. Thus, the correct P_S is less than the hard-sphere pressure.

Accounting for the real structure of the small-sphere fluid requires very considerable efforts (and approximations) on the part of theorists. Results from liquid

structure theory and computer simulations indicate that the depletion potential in fact looks like a damped oscillatory function (see Fig. 4.14, page 132). One study indicates that the ideal-gas model (coincidentally) estimates the contact-value of the depletion force correctly [26]. Other results suggest that the ideal-gas model overestimates it [27]. The results of the surface-depletion-force measurements described in Chapters 4 and 5 suggest that the ideal-gas law gives a reasonably accurate estimate of the strength of the depletion attraction. Yet the corner-confinement experiment (section 4.2) and the good agreement between the measured phase diagrams and the hard-sphere theory suggest that the hard-sphere equation of state is more reliable. Experiments are currently underway in our laboratory to measure directly the depletion force in a binary hard-sphere mixture [29].

Chapter 2

Measurements of the Phase Behavior of Binary Nearly-Hard Sphere Colloids

Given the purely repulsive interaction between pairs of hard spheres, one might expect a binary mixture of them to remain in a disordered, homogeneous fluid state for all but very high concentrations. Yet, as will be shown below, hard spheres in a dilute mixture can spontaneously separate by size and form dense, ordered phases! An outstanding example of this "demixing" in a three-component mixture is shown in Fig. 2. In this chapter, I describe systematic measurements of this phase separation in the bulk, with special attention devoted to the behavior at flat surfaces (also published in [30]). Section 2.1 will present a brief survey of other published experiments. In section 2.3, measurements of the equilibrium volume fractions (ϕ_L and ϕ_S) of phases appearing in the bulk will be presented in the form of phase diagrams. We observed coexisting fluid and (crystalline) solid phases in samples with sphere diameter ratios between 2 and 12. Two-fluid coexistence was not observed. Typically, 90% of the large

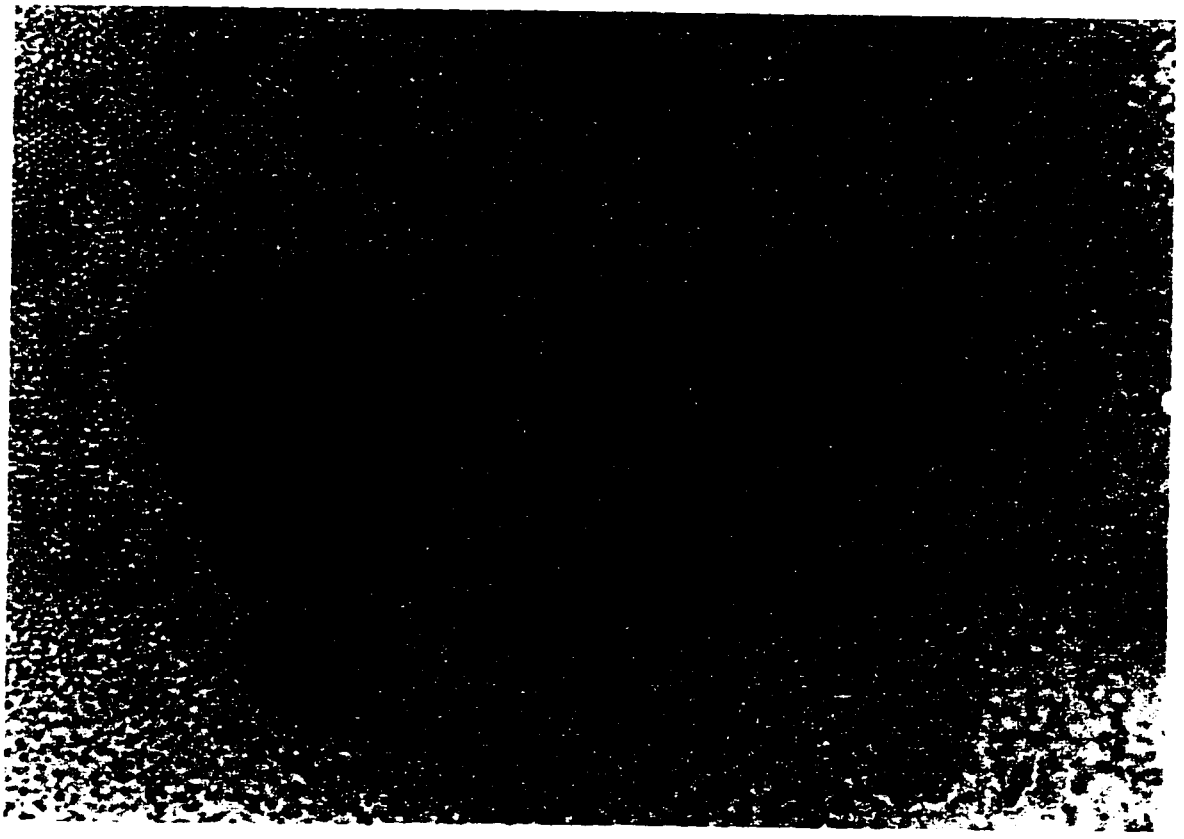

Figure 2.1: Optical micrograph of size-segregation and spontaneous ordering (or "freezing") at the surface of a *ternary* mixture of polystyrene spheres. The sphere diameters are 0.825, 0.460 and 0.069 μm and the volume fractions are 0.03, 0.03, and 0.12. The smallest spheres (invisible) remained in a disordered "fluid" state. The larger particles have sorted themselves by size. The largest, roughly hexagonal object is a highly-ordered crystallite of 0.46-μm spheres, dozens of layers thick. (Individual 0.46-μm spheres cannot be seen). The 0.825-μm spheres are visible as dots in the smaller, thinner crystallites. The larger spheres can also be seen in the surrounding fluid phase. Note the contiguous domains of 0.46- and 0.825-μm spheres – the two do not mix in the solid phase.

spheres and about 5% of the small spheres are found in the solid phase, comprised of a random stacking of close-packed planes of large spheres, permeated by a dilute fluid of small spheres. Section 2.4 will describe our studies of the phase behavior at a flat wall. We found that the density of large spheres is dramatically enhanced at the wall even at volume fractions well below the point of crystallization. We provide quantitative studies of this surface fluid. We also report nucleation of a (previously reported [20]) surface solid phase, which had the same structure as the bulk solid. Finally, in section 2.5, I summarize our observations and discuss some areas for future research.

A thorough understanding of the hard-sphere system is important because calculations for non-ideal systems often begin with the hard-sphere model. Further fundamental interest arises because the thermodynamics of hard spheres depends exclusively on entropy. These studies provide a unique opportunity to focus exclusively on entropy, which plays an important role in all thermodynamic systems.

Even though the pair interaction seems to be of the simplest possible sort (except for the ideal gas model), the thermodynamics of binary hard-sphere mixtures has not been well understood. Previously-published theories have predicted a variety of results, depending on the approximations used (see section 3.1). Only recently has it become clear from experiments and theory that phase separation and demixing can occur. The goal of the present work was to determine the nature of the second phase,

which had not been known, and to determine the phase diagram in a quantitative way.

2.1 Background

The first experimental work on hard spheres was done on monodisperse mixtures of PMMA [31, 32, 33, 34]. A combination of experiments and theory have found that when the volume fraction, ϕ, reaches 0.494, a crystalline solid phase with $\phi = 0.545$ coexists with the disordered fluid phase ($\phi = 0.494$) [35, 36]. Formation of a disordered glass in place of the crystal occurs (on Earth, at least) when $\phi > 0.58$ [37, 38, 39][1]. Freezing occurs at *lower* volume fractions next to a flat wall (when $\phi = 0.486$), according to molecular dynamics (MD) simulations [41, 42]). All of these effects are also found in the binary mixtures considered here, but at much lower total concentrations and with the added feature of size-segregation of the spheres.

In concentrated mixtures of similar-sized hard spheres (α approximately 1.7, total ϕ approximately 0.5), a variety of spectacular crystal structures, such as AB_{13} and AB_2, have been observed in binary mixtures of (polymethylmethacrylate (PMMA) spheres or silica spheres) [43, 44, 45, 46, 47]. As in monodisperse mixtures, phase separation in mixtures with such low α occurs only when the total volume fraction exceeds approximately 0.5, at which point the structure is largely determined by

[1] This behavior is different in space [40].

packing geometry and is thus strongly α-dependent. The phases observed in this size-ratio regime (AB_2 and AB_{13}) are quite different from those observed in mixtures with $\alpha \geq 6$.

Experiments with highly asymmetric sphere sizes have been been done using silica spheres [48] and polystyrene spheres [20, 49] in the hard-sphere limit. These early experiments, however, left undetermined the structures and compositions of the bulk phases at equilibrium. The experiments described below (and in [30]) are certainly the most extensive and, along with those of Imhof and Dhont [50], were the first to address the question of the structure of the dense phase in equilibrium. Some results of Imhof and Dhont will be compared to those of the present work.

Phase separation induced by the depletion force has also been observed in several non-hard-sphere binary mixtures: monodisperse colloids with added polymer [51, 52, 46, 53, 54], monodisperse emulsions with added polymer [55, 56], binary emulsions [57], and binary colloids with non-hard-sphere interactions [58]. The results from polymer solutions are, in general, different from the binary hard-sphere results since the polymers are more like an ideal gas because they can overlap one another. Another feature of the sphere-polymer mixture is that the potential is "non-additive" (they can overlap one another but not the large spheres). The repulsion length, σ between the centers of two large spheres is $\sigma_{LL} = a_L$, the large-sphere diameter. On the other hand, the repulsion length between *non-interacting* polymer molecules is $\sigma_{PP}=0$. The

repulsion length between one large sphere and one polymer molecule, $\sigma_{LP} = (a_L + a_P)/2$, where a_P is twice the polymer's radius of gyration. Thus, $\sigma_{LP} > (\sigma_{LL}+\sigma_{PP})/2$, and the mixture is said to be non-additive. In such a mixture, if the polymers are all bunched together, the entropic price they pay is less than the entropic gain of the large spheres simply because of the different interaction lengths. One expects phase separation in non-additive mixtures even without the depletion effect [59]. The result of these differences is that phase separation requires approximately twice as much small polymers as is does small hard spheres (for size ratio = 10; see the following chapter). When the size ratio is less than approximately 5, fluid-fluid, as well as fluid-solid, coexistence have been observed in the polymer-particle systems. In contrast, no fluid-fluid coexistence has been observed in binary hard-sphere mixtures, suggesting that there is a fundamental difference between the hard-sphere + polymer and binary hard sphere mixtures.

Emulsion droplets, on the other hand, can deform, as shown by their ability to attain volume fractions well above 0.74. Deformation is likely to change the free energy of the solid phase, as will be discussed below. Although the quantitative details of the phase diagrams for these materials depends on the details of the particle interactions, their behavior in a large region of the phase diagram is qualitatively similar to that of binary hard-sphere mixtures.

2.2 Experimental Techniques

2.2.1 Sample Preparation

As a model hard-sphere system, we have chosen charge-stabilized polystyrene spheres dispersed in water (Seradyn Inc., Indianapolis, IN, (317)266-2991). The small-sphere diameter (a_S) is 0.069 μm, and the large-sphere diameter (a_L) ranges from 0.137 to 0.825 μm, small enough that the particles diffuse, exploring all possible structural arrangements and (in most cases) selecting the one that is most stable. Because the inter-particle repulsion is screened to a very short range (less than 1% of a_L), these particles closely resemble hard spheres. Polystyrene spheres have the advantages of a mass density very near to that of water (only 5% greater), so they sediment very slowly (over days). They also have a high refractive index (near 1.59 in the visible range; see page 155 of [60]), allowing some very useful light-scattering techniques to be used. Most important, perhaps, is the fact that the particles are also large enough to see directly in a microscope, and move slowly enough to allow us to track them using easily accessible video technology. The same cannot be said of molecules.

The polystyrene microspheres are not perfect hard spheres. Their interaction is described by the Derjaguin-Landau-Vermeer-Overbeek (DLVO) theory [13, 16]. At very close range, there is a strong attraction due to the Van der Waals force. A slightly longer-range Coulombic repulsion, due to charged sulfate groups on the sphere surfaces, acts as a barrier to the Van der Waals attraction, thus preventing irreversible

aggregation of the particles. Seradyn manufactures solutions with enough salt dissolved in the water (approximately 0.01 Molar) to screen the coulombic repulsion to short distances. As reported in reference [20], measurements of the lowest volume fraction at which 0.205 μm spheres crystallize indicate that the effective particle radius exceeds the physical radius by less than 4 nm. Thus, we used the stock solutions as delivered. We found that purifying the particle solutions and adding more salt did not affect the results. Bulk and surface [20] crystals could be melted by shaking or by addition of enough filtered water to reduce the volume fractions below the liquidus curve. Thus, the spheres in the solid phase were not held together by the irreversible Van der Waals attraction.

2.2.2 Measurement and Probe Techniques

Using optical microscopy, diffusing-wave spectroscopy [60, 61, 62, 63, 64, 65], and Kossel scattering [66, 67], I have probed the structures and compositions of the samples *in situ*. I have also used scanning electron microscopy to study dried samples. Sarah Keller and her postdoctoral advisor, J. Zasadzinski, have also done freeze-fracture transmission electron microscopy (TEM) on some of our samples, looking at the particles in their "native state" with very high resolution. This section provides a brief summary of techniques used, along with references. More detailed descriptions can also be found in Chapter 7.

The mass density of the polystyrene particles is 5.0% greater than that of the surrounding water. While Brownian motion maintains single particles with diameters as large as 0.8 μm in suspension for several days, particle *clusters* settle to the bottom within a few hours. Therefore, in our samples, the bulk solid phase fell to the bottom of the sample and the fluid phase rose to the top, making it possible to identify phase separation by eye. All behaviors reported in this paper were observed within 2 days, often within 12 hours. Several samples were prepared with enough heavy water to make the polystyrene neutrally buoyant. As discussed below, we found that gravitational sedimentation had a negligible effect on the equilibrium structure.

We determined the volume fractions of the stock solutions by weighing samples before and after drying in an oven at 50° for 48 hours. Solutions of spheres of two different sizes were mixed in glass, quartz (NSG Company, Farmingdale, NY, (516)249-7474) or polystyrene cuvettes 1-10 mm in thickness, 10 mm in width, and approximately 0.3-1.0 ml in volume. The initial volume fractions, ϕ_S and ϕ_L, were measured to a precision of approximately 1% by weighing the ingredients as they were added. Immediately after mixing, we thoroughly shook the samples by hand and in an ultrasonic bath. They were then stored at room temperature in a vertical position. For most ϕ_S and ϕ_L investigated, multiple samples were mixed, giving consistent results.

We directly observed the structure of the binary colloids in equilibrium using an

optical microscope. After mixing, some samples were injected into cells approximately 100 μm thick, made of glass slides, standard cover slips, and 5-minute epoxy. Using the optical microscope (Zeiss Axiovert 135, 100x Plan-Neo or Plan-Apo objective), we could observe individual large spheres as they formed clusters. After approximately two days, when no further phase separation was observed, we determined the structure of the crystalline phase by direct observation. To verify that crystallization was not affected by the small volume of the cell, we let samples phase separate in 1 mm-thick cuvettes, extracted the sediment with a syringe and injected it into a thin cell for viewing under the optical microscope. No differences between thin-cell and thick-cell samples were observed.

A few samples were prepared for observation under scanning electron microscope (SEM). For these images, cells were made with glass coverslips that could be carefully cracked apart so as to avoid fluid flow which could destroy the sample. Once dry, the resulting glass shards were sputtered with a few angstroms of carbon, attached to an aluminum disk with conducting carbon tape, and put into the SEM. The resulting micrographs will be shown in section 2.4.2. Although multiple preparations of the same samples gave similar results, the possibility remains that the small particles (if not the large ones) reorganized somewhat during the drying process. For more faithful reproductions, freeze-fracture transmission electron microscope (TEM) images were obtained by Sarah Keller. Small samples, approximately 20μL, were

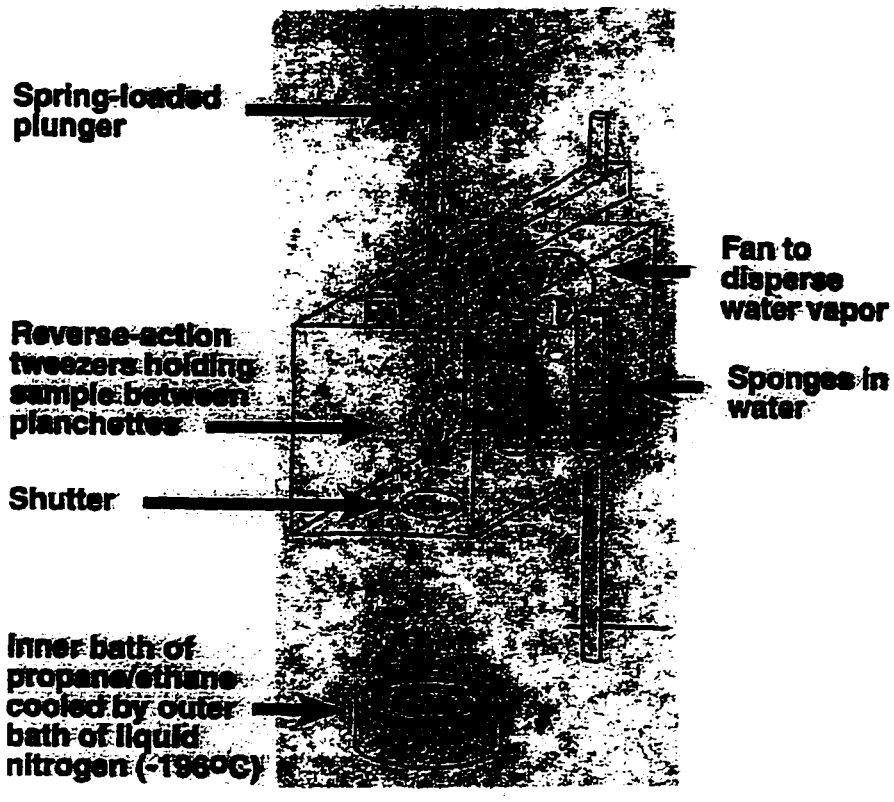

Figure 2.2: Schematic of apparatus used by S. L. Keller and J. Zasadzinski for freeze-fracture of colloidal crystals. The sample sits in the chamber (which is humidified to slow evaporation) while phase separation occurs, and is then mechanically plunged into the cold bath. (Figure by Sarah L. Keller, UCSB)

injected into a gold or copper planchette, left for a few hours, then plunged into a bath of propane/ethane, which was cooled by liquid nitrogen to -196° (Fig. 2.2). The cooling rate was fast enough (10^4-10^6 Kelvins/s) so that the water vitrified without expanding. The samples were then coated with a thick layer of carbon on one side and a thin film of platinum on the other. Platinum was applied at an angle to provide contrast ("shading") in the image. Unfortunately, this technique could not be used

to look at surface crystals because the metal planchette plates interact electrostatically with the particles. As a result, only images of bulk crystallites are available (presented in section 2.3.1).

To measure ϕ_L and ϕ_S in the equilibrium bulk fluid phase, we carefully extracted the fluid from the top of two-day old samples using a syringe. Some of this supernatant was weighed, dried in an oven for 2 days, and weighed again to measure to within 1% the total volume fraction in the fluid phase, $\phi_L^{fl} + \phi_S^{fl}$, where the superscript fl denotes the fluid phase at equilibrium. The rest of the supernatant was diluted with a measured amount of filtered water so that the average distance between large spheres was much greater than the particle diameter (for imaging clarity). The small spheres, 0.069 μm in diameter, were too small to be resolved. We measured ϕ_L^{fl} by scanning the microscope's focal plane through a well-defined depth of approximately 100 μm and counting all of the large spheres with the aid of a CCD camera, video recorder, frame grabber, computer, and NIH Image software. We used reference samples of known volume fractions to calibrate the relation between number of particles and volume fraction. In all cases, at least several hundred particles were imaged. These measurements gave ϕ_L^{fl} to within approximately 10%. We determined ϕ_S^{fl} by subtracting ϕ_L^{fl} from the total fluid-phase volume fraction. To determine the exact compositions of the solid phase, we had to assume a volume fraction of large spheres in the solid, ϕ_L^{sol}, as discussed in the following section.

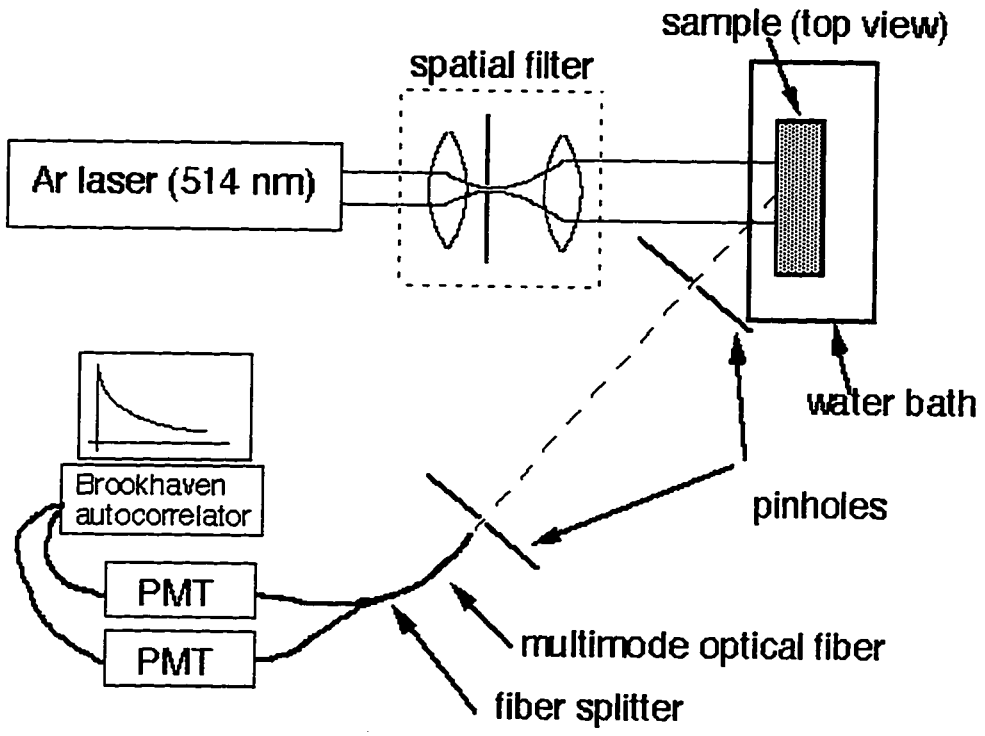

Figure 2.3: Schematic illustration of the apparatus for diffusing wave spectroscopy (DWS) in reflection geometry. Two photomultiplier tubes (PMTs) were used to obtain a cross-correlation function and reduce noise from random PMT signals. The correlation function of the light intensity, $g(\tau)$, was measured at intervals while samples underwent phase separation. Results will be shown below.

To probe the structure of thick samples as phase separation occurred, we used diffusing-wave spectroscopy (DWS) [61, 62, 60] in the reflection geometry to measure the translational diffusivity of the particles (Fig. 2.3). Typically, in DWS, when the motion of the scatterers is constrained (indicating a glass or solid structure), the intensity temporal autocorrelation function does not decay to zero. We mixed samples and measured the light-intensity autocorrelation function at various times.

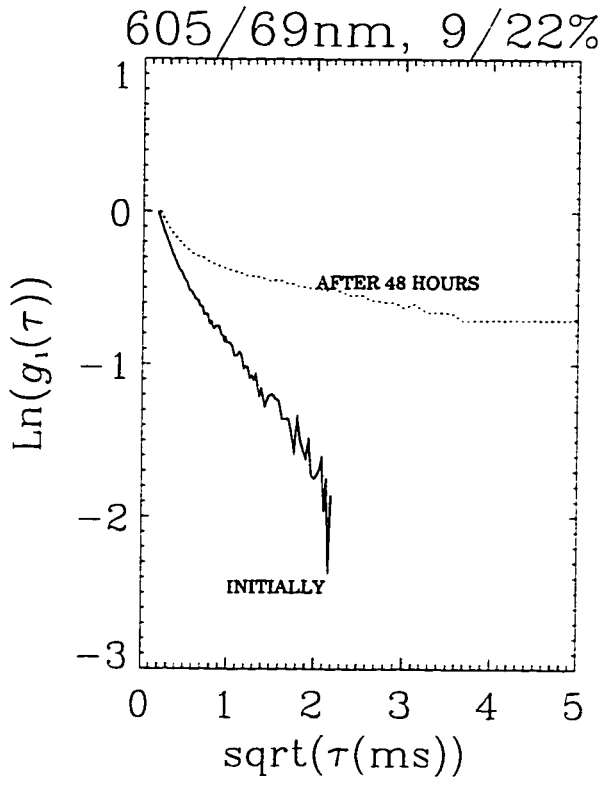

Figure 2.4: Plot of light-intensity correlation function *vs.* time, τ. When the sample is in the fluid state, the particles diffues freely so that the light completely decorrelates after some time ($g_1(\tau)$ decays to zero). When the large spheres solidify, their diffusion is constratined and the light no longer completely decorrelates, so that $g_1(\tau)$ reaches a plateau.

Immediately after mixing, DWS confirmed the fluid structure of the particles. When the intensity autocorrelation function of the dense region (sediment) no longer decayed to zero, we concluded that it had become solid or glass-like (see Fig. 2.4). We used this technique to investigate the role of gravity in phase separation, as discussed in section 2.3.3.

2.3 Results: Bulk of the Sample

In this section, I describe the results of our experiments. The nature of the sediment and the structures of the phases (section 2.3.1), formation of a gel (2.3.2), and the effect of gravity (2.3.3) are discussed. In section 2.3.4, the measured phase diagrams are presented for sphere-diameter ratios equal to 6.7, 8.8, and 12.0. For these samples, the small spheres could freely diffuse through close-packed lattice of the larger spheres. Section 2.3.5, concerns phase separation in mixtures with diameter ratio, α, as low as 2.0. The size ratios of these samples may lead to different structures in the solid phase.

2.3.1 Detailed Observations of the Phase Separation

Figure 2.5 presents the final phases of several binary samples which we observed over a period of one to four days after mixing (see also [20]). Initially, all samples were opaque white because the larger polystyrene spheres strongly scatter visible light. Some samples remained uniformly white for several days or weeks, until gravity induced settling of individual particles, and the sample was discarded. These samples were considered stable in the binary fluid phase (represented in figure 2.5 by a "+"). In some samples, concentration fluctuations could be seen by eye minutes or hours after mixing. Subsequently, a well-defined interface could clearly be seen between a dilute fluid on the top and a more optically dense sediment on the bottom. Over a

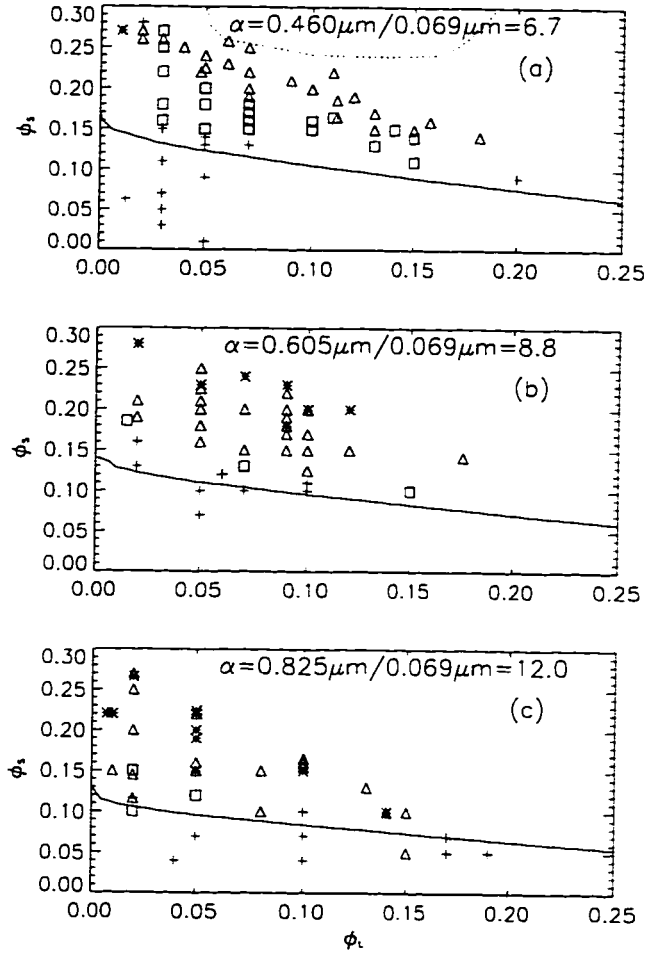

Figure 2.5: Final phases of binary hard-sphere mixtures. The horizontal and vertical axes indicate the initial volume fractions of large and small spheres, respectively. Each symbol indicates a sample which we investigated and represents the phase behavior observed: "+"— no phase separation; "□"— growth of solid phase at surface; "△"— phase separation at surface and in bulk; "*"— fluid/solid phase separation in bulk only. The solid lines are liquidus curves derived in the following chapter. The dashed curve in (a) represents the liquidus curve measured by van Duijneveldt *et al.* in suspensions of silica spheres with $\alpha = 6$.

period of 12 to 48 hours, this interface fell to the bottom of the sample (as described in more detail below). These were samples with bulk phase separation (represented by a "$*$" in figure 2.5). In other samples, small spots on the surface of the cuvette became visible within approximately 12 hours and no bulk interface was observed. These were samples with surface solidification only ("□"). As α was increased, this surface-only region became narrower, nearly disappearing when $\alpha = 12.0$. The surface-phase measurements are discussed in section 2.4. Other samples exhibited surface spots *and* bulk interfaces ("△"). The lack of phase separation at the highest total volume fractions may have been caused by the slowing of the dynamics due to high viscosity.

The liquidus curve separates the region of the phase space in which samples are homogeneous fluid in the bulk from the region in which samples have coexisting fluid and solid phases in the bulk. In figure 2.5, the measured liquidus curve (not drawn) separates the "△" from the "+" or "□". In the figure, we have plotted the liquidus curves calculated from the theory described in the next chapter (solid curves).

For comparison, the dashed curve in Fig. 2.5(a) represents the experimental results of van Duijneveldt *et al.* [48] who investigated mixtures of silica spheres with $\alpha = 6$, suspended in cyclohexane. They observed two-phase coexistence in samples above the dashed curve and a single bulk fluid phase in those below it. No surface phase was reported and the nature of the resulting phases was not determined. The dashed curve should be compared to a curve separating the "□" from the "△" in the same

figure. We observed phase separation at slightly lower ϕ_S, which is consistent with our slightly higher value of α, since the depletion energy is approximately proportional to $\alpha\phi_S$. Van Duijneveldt *et al.*, however, find that the two-phase region has a high-ϕ_L boundary which we did not observe ($\phi_L \leq 0.20$). As pointed out in [48], the apparent high-ϕ_L boundary may be due to slow phase-separation dynamics in samples with relatively high particle concentrations. The relatively rapid gravitational settling (over a few fours) in those experiments prevented a definite characterization of the equilibrium structure of the second phase.

Optical microscopy of our samples revealed that the sediment was a concentrated suspension of either crystalline or glass clusters dispersed in the dilute fluid phase. The clusters contained from 20 (when $\phi_S \approx 0.30$) to 100 (ϕ_S near the liquidus curve) large spheres. In the higher-ϕ_S samples, these clusters rapidly formed a loose gel, as discussed in the following subsection. For several samples with a range of ϕ_S, we measured the total volume fractions (of large and small spheres) in the sediment to be 0.50-0.58. This volume fraction is consistent with a mixture of dense ($\phi_L + \phi_S \approx .74$) solid aggregates or crystallites comprising approximately 65% of the total sediment volume, with the surrounding fluid phase ($\phi_L + \phi_S \approx 0.2$) comprising the rest of the sediment volume (Fig. 2.6). Measuring the volume fractions in the sediment, therefore, does not accurately determine the volume fractions in the solid phase (although it does place a lower bound on them). In samples with ϕ_S within approximately 0.05

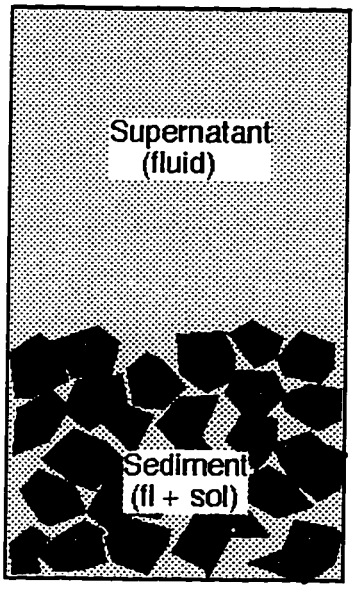

Figure 2.6: Cartoon of the sediment that appears at the bottom of samples that undergo fluid-solid phase separation in the bulk. The solid phase (crystallites) comprise only approximately 65% of the total volume, so that the volume fractions in the sediment are not the same as those of the solid phase.

of the liquidus curve, the surface spots were strongly iridescent and the bulk sediment developed iridescent spots after a day or more. For the first day, the sediment in these samples would flow very slowly when the sample was tilted, after which time it would not flow to any visible extent. Possibly, neighboring crystallites in the sediment had begun to join, making the sediment more rigid. The early-time fluid nature of the sediment caused an earlier incorrect conclusion that the dense phase is a fluid instead of a solid [20].

In samples with ϕ_S within approximately 0.05 of the liquidus curve, optical microscopy of the solid phase showed that the large spheres were arranged in close-packed planes. The spheres in one plane always fit over the gaps in the neighboring planes. We concluded, however, that there were no long-range correlations among planes, so that the structure was a random hexagonal close-packed structure (RHCP). Correlations among next-nearest planes could create either face-centered cubic (FCC) or hexagonal close-packed (HCP) structure (see Fig. 6.16, page 189). We obtained a similar result for the surface crystals, as discussed in section 2.4. From the TEM images (Fig. 2.7), we found that the small spheres were not ordered within the solid phase, as expected since they comprise only approximately 20-30% of the available (interstitial) space, as described below.

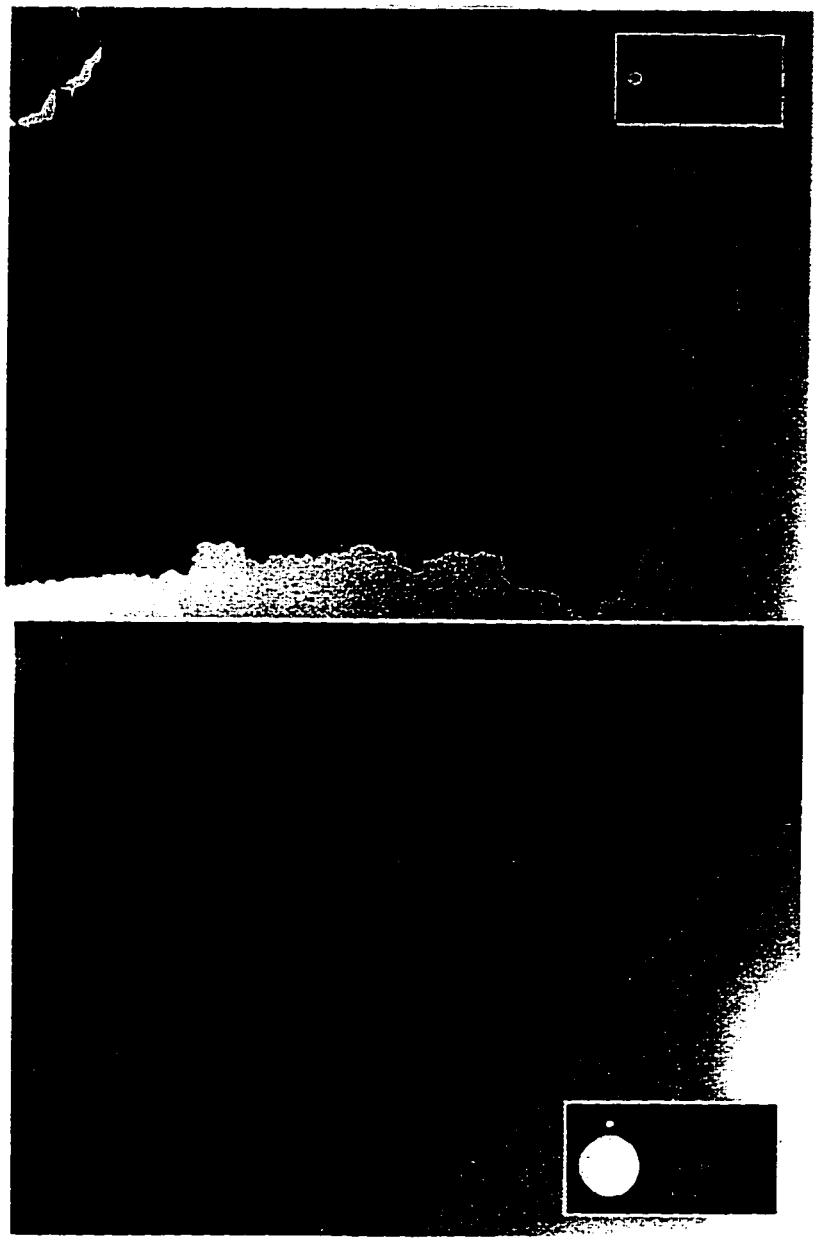

Figure 2.7: Freeze-fracture transmission electron micrographs of the solid phase in a binary suspension of polystyrene spheres. The sphere sizes are 0.605 μm and 0.083 μm. The volume fractions are ϕ_L=0.05 and ϕ_S = 0.20. The large spheres are ordered and the small spheres are not. Photograph taken by Sarah L. Keller with J. Zasadzinski.

2.3.2 Crossover from Ordered to Disordered Dense Phase

When ϕ_S was more than approximately 0.05 above the liquidus curve, the sediment exhibited no Bragg scattering and retained the ability to flow for several days. Large-sphere clusters were observed in these samples, but had structure significantly less well-ordered than in samples with lower ϕ_S. With optical microscopy, it was not possible to recognize a regular crystal lattice in the solid phase of these samples (Fig. 2.8(a)). In samples with the highest α and ϕ_S, (*e.g.* a_L/a_S=0.825μm/0.069 μm = 12.0, $\phi_L = 0.02$, and $\phi_S \geq 0.24$), the large spheres formed randomly-packed clusters of approximately 20 particles within 10 minutes. Over the next 60 minutes, we observed these clusters fall to the bottom of the 100 μm-thick sample cell and form a loose gel of apparently fractal aggregates (Fig. 2.8(b)). With $\phi_S = 0.24$, these aggregates were as large as 75 μm across. Increasing ϕ_S by 0.02 increased the aggregate size to as large as 100 μm across.

We have observed a dramatic change in sedimentation behavior which further suggests a change in phase-separation dynamics as ϕ_S is changed. We videotaped five samples containing 0.605 μm and 0.069 μm spheres ($\alpha = 8.8$) with $\phi_L = 0.09$. In the sample with $\phi_S = 0.15$, an opaque sediment appeared at the bottom of the container and grew upward at approximately 1 cm/hr, with no subsequent observable change in opacity. When ϕ_S was increased by just 0.02, another interface appeared at the top of the container and moved downward rapidly (approximately 2 cm/hr). This interface

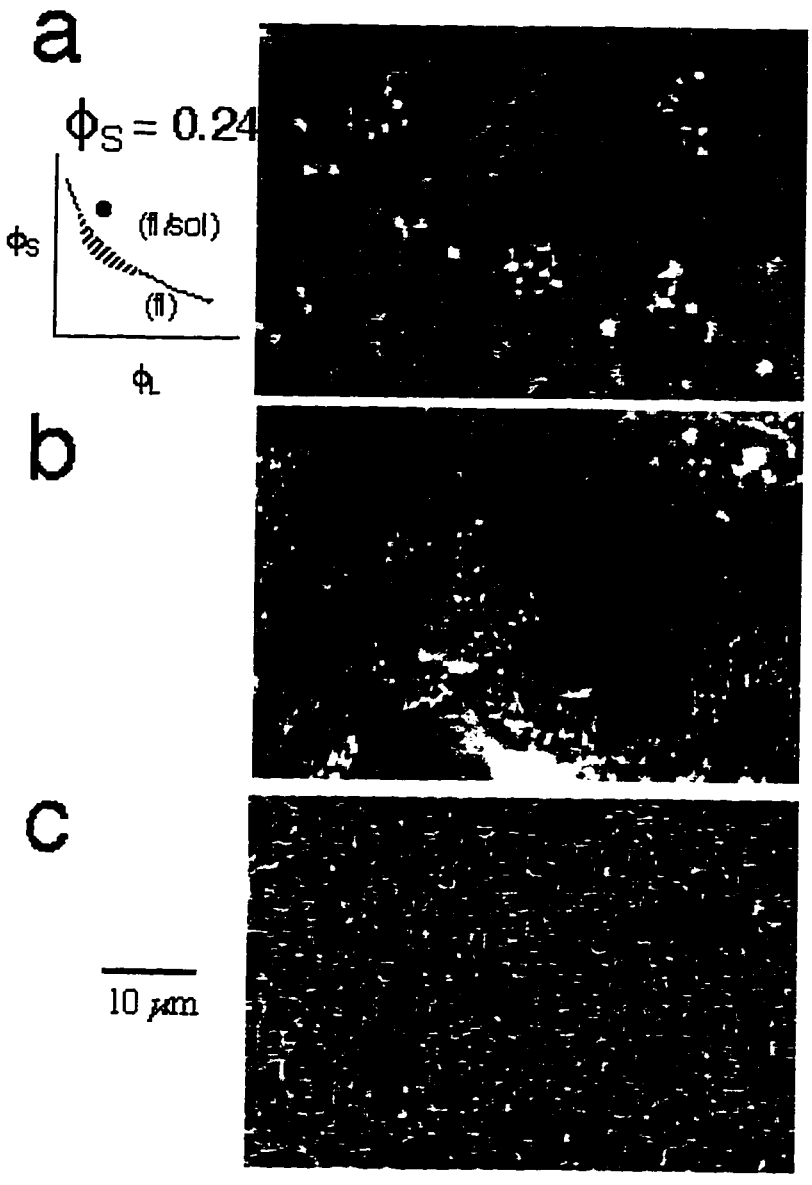

Figure 2.8: Optical micrographs of a binary mixture of polystyrene spheres, showing the "glassy" behavior. The sphere diameters are 0.825 and 0.069 μm($\alpha = 12$) and ϕ_L,$\phi_S = 0.02, 0.24$. As shown by the cartoon, the sample lies well above the fluid-solid coexistence curve. The small spheres are invisible. (a) This 100x-image of the bulk of the samples was made 5 minutes after mixing. Dense clusters of the large spheres are clearly visible. (b) After one hour, the dense clusters form apparently fractal clusters. (c) At low magnification, a macroscopic loose gel is visible.

separated the dilute fluid phase (on top) from a sediment which became more opaque as the interface fell. When $\phi_S \geq 0.19$, only the top interface appeared. Increasing ϕ_S caused this interface to fall more slowly. We obtained similar results using samples with $\phi_L = 0.05$, with the second interface appearing when $\phi_S \geq 0.20$.

The above observations support the explanation proposed by Pusey *et al.* [68] of a similar crossover in the sedimentation behavior of mixtures of hard spheres with polymer. At low ϕ_S, the binary fluid is metastable, so that phase separation occurs by nucleation of ordered, dense crystallites which rapidly pile up at the bottom. In samples with higher ϕ_S, the depletion attraction between large spheres is sufficiently strong so that once they touch one another, they are unlikely to rearrange themselves to the lowest-free-energy structure and instead form a metastable disordered (glass-like) structure. Glass formation has also been observed in monodisperse hard-sphere colloids [31, 33, 39]. Our microscopic observations of the growth of fractal-like aggregates of large-spheres indicate that the sediment is a gel. Pusey *et al.* [68] suggest that a slow rearrangement of the particles weakens the structure so that it collapses due to gravity, thus causing the interface to fall. According to our experiments, increasing ϕ_S causes the interface to fall more slowly, perhaps due to a slowing of the large-sphere rearrangement in the presence of a stronger depletion force and in the presence of a higher effective viscosity.

Using a combination of the settling behavior and the Bragg scattering and flow

Table 2.1: List of (ϕ_L,ϕ_S) values which separate the region of ordered, crystalline solid (at low ϕ) from the region of non-equilibrium (glassy) behavior (at high ϕ).

Sample	a_L / $a_S(\mu m)$	ϕ_L	$\phi_S(\pm 0.01)$
1	0.460 / 0.069	0.07	> 0.22
2	0.460 / 0.069	0.12	0.18
3	0.605 / 0.069	0.05	0.20
4	0.605 / 0.069	0.09	0.17
5	0.825 / 0.069	0.05	0.15
6	0.825 / 0.069	0.15	0.11

properties of the sediment, we have determined the several points in the (α, ϕ_L,ϕ_S) space that separate samples that were crystal-like from those that were glass-like. The results are listed in Table 2.1. It has been predicted that the onset of the glass-like behavior might be related to a metastable gas-liquid transition [69]. These results may be of use for comparison to theoretical predictions

2.3.3 The Effect of Gravity on the Equilibrium State

Although previous investigations of binary hard-sphere mixtures [48] have observed formation of crystals after several days, they could not rule out the possibility that a dense fluid of large spheres had formed, settled to the bottom, and become compressed by gravity to the point of solidification. To determine the effect of sedimentation on

solidification, we prepared two samples (A and B) with the same volume fractions of large and small spheres. In sample A we replaced enough water with heavy water to make the polystyrene particles nearly neutrally-buoyant (in fact, their density is less than that of the water by $< 1\%$). In sample B the mass densities differed by 5.0%. We then measured the sedimentation rate of the bulk interface using time-lapse video (Fig. 2.9). Note that if there were no small spheres, almost no evidence of sedimentation would have been found in the same time period. Simultaneously, we used DWS at regular intervals to determine when the sediment solidified (as described in section 2.2.2). This typically occurred a few hours after the first visible signs of phase separation, but before the bulk interface had completely settled. We found that sample B settled approximately 10 times faster than A, consistent with the mass densities. Sample B, however, solidified only 2-4 times faster than sample A, as determined by DWS. If solidification were *entirely* due to gravity, then the rate of solidification would scale with the rate of sedimentation. We found, however, that the solidification rate only *loosely* depended on sedimentation — gravity speeds up solidification, but is not required for the process. From the above evidence, we conclude that the same phase separation would occur even in the absence of gravity.

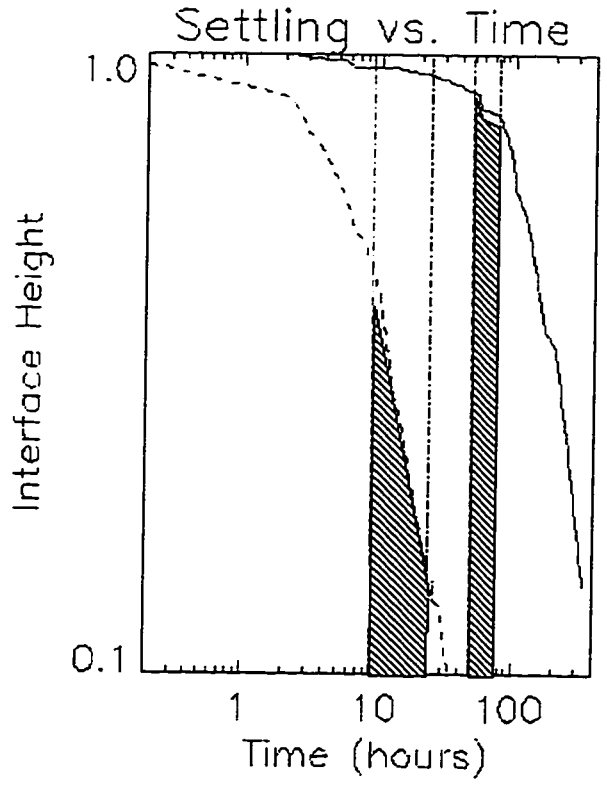

Figure 2.9: Plot comparing settling rate to solidification rate for two samples with the same colloid content but different water mass densities. The particle diameters are a_L,a_S = 0.605, 0.069 μm and the volume fractions are ϕ_L,ϕ_S = 0.09, 0.23. According to light scattering (DWS), the samples became solid-like sometime during the hatched interval. The maximum interface height for both samples was $\approx$ 6 cm.

2.3.4 Measured Phase Diagrams

In figure 2.10, we present experimental phase diagrams for three sphere-diameter ratios (α = 6.7, 8.8, and 12.0). In each diagram, the solid line represents the bulk liquidus, determined by observing which samples had coexisting fluid and solid phases in the bulk and which did not (*i.e.* by drawing a curve between the "△" and the "+" or "□" of figure 2.5). As α is increased, the liquidus curves move to lower ϕ_S. Thus, increasing α makes the fluid phase thermodynamically unstable at lower ϕ_S, as expected from the simple model in which the energy of the depletion attraction is proportional to $\alpha\phi_S k_B T$ [11]. For comparison, we also plot the bulk phase diagram calculated from the theory described in the following chapter. The measured liquidus agrees closely with the calculated liquidus at the higher values of α.

For several samples, we measured the volume fractions in the fluid phase at equilibrium, ϕ_L^{fl} and ϕ_S^{fl}, using the method described in section 2.2.2. The results of these measurements are listed in table 2.2 and plotted in figure 2.10. The "×" represent the volume fractions immediately after mixing, while the "◇" represent the volume fractions in the fluid phase, ϕ_L^{fl} and ϕ_S^{fl}, measured two days after the samples were mixed (after which no further changes in the sediment were observable). In the absence of phase separation at the surface, the equilibrium-fluid-phase volume fractions ("◇") must lie on the bulk liquidus curve. In samples with $\alpha = 6.7$, however, the "◇" lie *below* the bulk liquidus curve. In these samples, the growth of crystallites on the

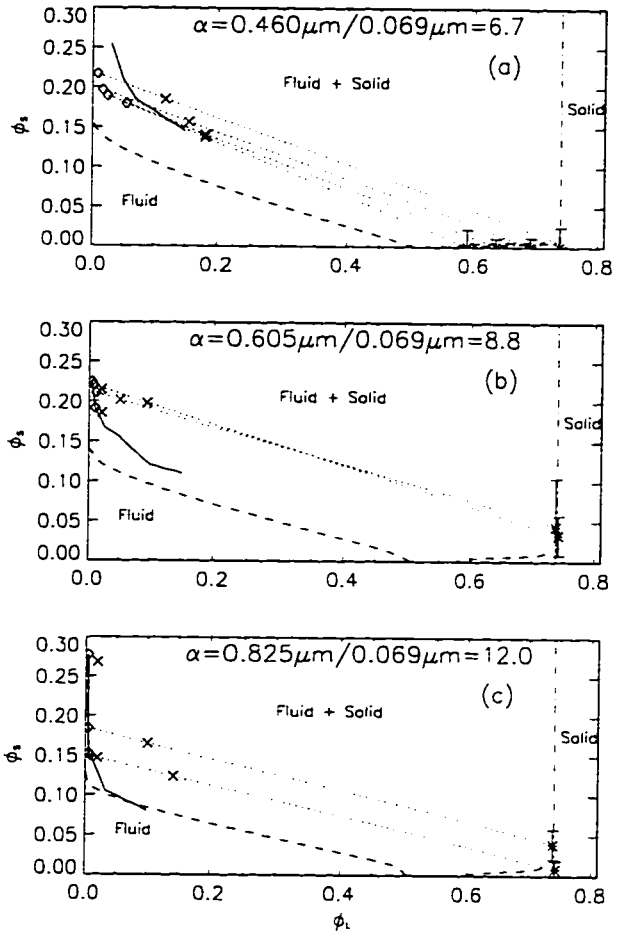

Figure 2.10: Experimentally-determined phase diagrams. The "×" represent the initial volume fractions (before phase separation) and the "◇" represent the measured volume fractions in the fluid phase at equilibrium. The dotted lines represent measured tie lines, determined by the "◇" and "×". The end points of the tie lines must lie on the liquidus and solidus curves (the disagreement in (a) is discussed in the text). The measured bulk liquidus curves, determined from the data in figure 2, are represented by the solid lines. The estimated solidus curves (corresponding to the upper bound for ϕ_L^{sol}) are represented by the dot-dashed lines. The error bars represent the uncertainties in the extrapolated ϕ_S^{sol}. Errors for the "◇" and "×" are smaller than the plot symbols. All of these results are listed in table I. The dashed and dot-dashed curves represent the liquidus and solidus curves derived from the theory of the following chapter

surface of the container reduces the equilibrium values of ϕ_L^{fl}. Due to these surface crystals, the equilibrium ϕ_L^{fl} and ϕ_S^{fl} ("$\diamond$") should lie along the boundary *between* the homogeneous-fluid region and surface-solid-only region, *i.e.* between the "+" and the "$\square$" of figure 2.5. The "$\diamond$" lie in the middle of the surface-solid-only region, however, indicating that these samples had not yet reached equilibrium with respect to the surface-phase separation when we made the measurements. We decanted the samples after two days to avoid the effects of gravitational settling of individual particles. According to our observations of similar samples, however, the surface crystals continue to grow for at least two weeks and sometimes for several months. In these samples, therefore, the large spheres may still have been in the process of crystallizing on the surface. Repeating the measurements with two-week-old samples would likely give slightly lower ϕ_L^{fl} (even if gravitational settling could be eliminated). In samples with $\alpha = 8.8$ and 12.0, the surface-phase-only region is very narrow, so that the measured ϕ_L^{fl} and ϕ_S^{fl} are very close to the bulk liquidus curve. We always found large spheres in the fluid phase, indicating that only a fraction of the large spheres solidified. For given initial volume fractions, however, increasing the size asymmetry caused more large spheres to separate out of the fluid. For example, with initial $\phi_L/\phi_S = 0.10/0.19$, increasing α from 6.7 to 8.8 increased the relative number of large spheres in the solid from 85% to 90%.

We next considered the composition of the solid phase, ϕ_S^{sol} and ϕ_L^{sol}. The sediment

which falls to the bottom of the sample container during phase separation is a *mixture* of the solid and fluid phases. Therefore measurements of its composition do not determine the volume fractions in the solid, although they do provide a lower bound of between 0.50 and 0.58 for $\phi_L^{sol} + \phi_S^{sol}$. To determine the composition of the solid phase, we plot a straight line between $(\phi_L^{fl}, \phi_S^{fl})$ and (initial ϕ_L, initial ϕ_S). This "tie line" [70] indicates the equilibrium state of any mixture with initial volume fractions given by a point along the tie line. Such a sample will separate into two phases whose compositions are given by the tie line's end points, which lie on the liquidus and solidus curves. The relative volume of each phase is inversely proportional to the distance from the initial point to the corresponding end of the tie line. To determine uniquely the composition of the solid phase from the tie line, we must assume a value for either ϕ_L^{sol} or ϕ_S^{sol}. The *upper* bound for ϕ_L^{sol} is determined by the geometry of packing the spheres: $\phi_L^{sol} \leq 0.7405$. For the three samples numbered 1, 2, and 3 in table I, however, assuming $\phi_L^{sol} = 0.74$ leads to negative ϕ_S^{sol}. Therefore, these three samples, which have the lowest values of α and ϕ_S, must have $\phi_L^{sol} < 0.74$, *i.e.* the large spheres in the lattice do not touch one another. For these samples, the upper bound for ϕ_L^{sol} is determined by the intersection of the tie line with the ϕ_L-axis. The dashed line in Fig. 2.10 represents the solidus curve obtained using these upper limits for ϕ_L^{sol}. The corresponding values for ϕ_S^{sol}, listed in table 2.2, range from 0 to 0.04±0.06. Only in sample number 11 does ϕ_S^{sol} not equal zero within

the experimental uncertainty. These results agree, within experimental uncertainties, with calculations using the theory described in section IV. We determine the *lower* bound for ϕ_L^{sol} of all of the samples in the following way. Because sample number 1 has the lowest α and initial ϕ_S (therefore the weakest depletion force pulling the large spheres together), it is likely to have the lowest ϕ_L^{sol}. For this sample, the lower bound for $\phi_L^{sol} + \phi_S^{sol}$ is 0.57±0.02, obtained by analyzing the sediment as mentioned above. Applying this condition to the measured tie line, we find that $\phi_L^{sol} \geq 0.55$. A similar analysis applied to sample number 2 (for which the total volume fraction of polystyrene in the sediment is 0.58±0.02) gives the condition $\phi_L^{sol} \geq 0.56$. All of the other samples which we studied had larger α or ϕ_S, and are therefore assumed to have $\phi_L^{sol} > 0.56$. The upper bounds for ϕ_S^{sol} are obtained by setting ϕ_L^{sol} to its minimum value, 0.56. The largest value of ϕ_S^{sol} thus obtained is 0.09±0.05, evident from the tie lines. Finally, the minimum value of ϕ_L^{sol}, 0.56, obtained for the $\alpha = 6.7$ system corresponds to a distance between large spheres of less than $a_L + a_S$, as expected from the theory of the depletion force and corroborated by the TEM micrographs (Fig. 2.7).

Imhof and Dhont [50] also recently reported fluid-solid coexistence in a binary mixture of silica spheres in inorganic dimethylformadide (DMF), in the high-screening limit. A single size ratio of $\alpha = 9.3$ was used in the experiment. As reported here, measurements of the large-sphere lattice parameter (solid phase) showed that it was

Table 2.2: Table of measured and extrapolated volume fractions of the phases in equilibrium in samples with $\alpha = 6.7$, 8.8, and 12.0. The initial and equilibrium-fluid-phase volume fractions were measured directly. The last column lists the upper limits for ϕ_L^{sol} and the corresponding values of ϕ_S^{sol} in each sample, calculated from the data in the third and fourth columns. For some samples, the extrapolated solid-phase compositions are not listed because the error bars for the extrapolated ϕ_S^{sol} are very large, approximately ±0.20. The same data are plotted in the experimental phase diagram.

	a_L / $a_S(\mu m)$	$\phi_L^{init}/\phi_S^{init}(\pm 1\%)$	ϕ_L^{fl} / ϕ_S^{fl}	ϕ_L^{sol} / ϕ_S^{sol}
1	0.460 / 0.069	0.1810 / 0.1374	0.0556 / 0.1796	0.589 / 0.00
	=6.7		±0.0054 / ±0.0059	/ ±0.022
2		0.1818 / 0.1408	0.0251 / 0.1893	0.637 / 0.00
			±0.0019 / ±0.0029	/ ± 0.011
3		0.1558 / 0.1566	0.01719 / 0.1970	0.693 / 0.00
			±0.00066 / ±0.0022	/ ±0.012
4		0.1179 / 0.1853	0.0087 / 0.2168	0.7405 / 0.0055
			±0.0013 / ±0.0026	/ ±0.0196
5	0.605 / 0.069	0.0944 / 0.1981	0.00709 / 0.2204	0.7405 / 0.033
	=8.8		±0.00086 / ±0.0024	/ ±0.025
6		0.0215 / 0.1857	0.0102 / 0.1912	- / -
			±0.0011 / ±0.0023	

Table 2.3: Previous table continued.

	a_L / $a_S(\mu m)$	$\phi_L^{init}/\phi_S^{init}(\pm 1\%)$	ϕ_L^{fl} / ϕ_S^{fl}	ϕ_L^{sol} / ϕ_S^{sol}
7	0.605 / 0.069	0.0506 / 0.2018	0.0120 / 0.2106	0.7405 / 0.0441
	=8.8		±0.0013 / ±0.0026	/ ±0.0606
8		0.0210 / 0.2151	0.0050 / 0.2243	- / -
			±0.0006 / ±0.0024	
9	0.825 / 0.069	0.0196 / 0.1468	0.00538 / 0.1526	- / -
	=12.0		±0.00063 / ±0.0017	
10		0.1417 / 0.1236	0.00856 / 0.1492	0.7405 / 0.0084
			±0.00072 / ±0.0017	/ ±0.0105
11		0.1003 / 0.1653	0.00452 / 0.1842	0.7405 / 0.039
			±0.00055 / ±0.0020	/ ±0.018
12		0.0191 / 0.2682	0.0039 / 0.2775	- / -
			±0.0005 / ±0.0029	

compressed by addition of small spheres. They also point out the existence of two glassy phases. In one, the small spheres are fluid-like; in the other both large and small are glass-like. The principal difference from the present experiments, however, is that their measured liquidus lay at considerably higher ϕ_S. For example, with $\phi_L = 0.10$, the binary fluid was stable when $\phi_S < 0.45$, compared to $\phi_S < 0.12$ from our results ($\alpha = 8.8$). Furthermore, they did not observe crystallites on the surface of the sample container (see below), nor did they observe any Bragg scattering in the unstable samples with $\phi_L < 0.4$. Such large disagreements are difficult to explain, but may be due to the large difference in mass densities of silica (>2 g/cc) and DMF (as in the van Duijneveldt experiment [48]). At low volume fractions, they reported a sedimentation rate of 1 mm/h. Whereas monodisperse mixtures (with $\phi > 0.5$) showed Bragg scattering after 15 minutes, the binary samples required "several hours to almost two days". Although sedimentation is slower at higher volume fractions, it is quite possible that in samples well below the reported liquidus, the binary fluid was metastable but that there was insufficient time for the second phase to appear. The authors suggest that the small deviations in the short-range (non-hard-sphere) potential might explain the differences among polystyrene in water and silica in cyclohexane or in DMF. In monodisperse mixtures, however, experiments using PMMA, silica and polystyrene spheres have given very similar results, suggesting that the details of the very short-ranged interactions are not sufficient to account for such large deviations.

Steiner *et al.* [57] have obtained stability diagrams of binary emulsions (silicon oil droplets in water) with size ratios, $\alpha = 3.3$, 7.1, and 11.1. Although the nature of the second phase was not reported, the location of their reported liquidus curve for $\alpha = 7.1$ is similar to that reported here [30] for $\alpha = 6.7$. Compared to our results, howver, they found that the liquidus curve fell more dramatically toward smaller ϕ_S as a_L was increased. Possibly, the increasing flexibility of the emulsion droplets (due to the reduced LaPlace pressure inside) allowed the largest solid-phase droplets to deform the most. Deformations would increase the excluded-volume overlap, thus decreasing the free energy of the solid and extending its stability to lower ϕ_S.

2.3.5 Crystallization in Samples with Low Diameter Ratios

We have observed surface crystallization and bulk separation into a fluid plus a crystalline or glass phase in samples with α as low as 2.0 and $\phi_L + \phi_S$ as low as 0.35. The results are summarized in table 2.5. All of the surface crystallites have a 3-fold symmetry normal to the wall, similar to the higher-α samples. Using DWS, we determined that the sediment had a solid or glass structure similar to the higher-α samples described above.

There are intriguing geometric constraints on these low-α crystals. If the large spheres are touching and if $\alpha > 6.4$, then the small particles can flow freely (like a gas) through the interstices. If $2.4 < \alpha < 6.4$, the small particles would be trapped

Table 2.4: Table of results for $\alpha \leq 4.6$. Results for samples with α= 6.7, 8.8, and 12.0 are plotted in figure 2. The Phase Behavior column describes our observations: "-"indicates no observed phase separation of any type, and "surface" and "bulk" indicate phase separation into fluid and solid phases at the container wall and in the bulk of the sample, respectively. No fluid/fluid separation was observed.

a_L / $a_S(\mu m)$	$\alpha \equiv a_L/a_S$	ϕ_L / ϕ_S	Observed Phase Behavior
0.299 / 0.065	4.6	0.05 / 0.17	-
		0.05 / 0.25	-
		0.05 / 0.30	-
		0.05 / 0.40	-
		0.07 / 0.29	surface
		0.07 / 0.35	-
		0.10 / 0.19	-
0.460 / 0.137	3.4	0.05 / 0.16	-
		0.05 / 0.26	-
0.204 / 0.069	3.0	0.03 / 0.10	-
		0.05 / 0.05	-
		0.05 / 0.25	-
		0.15 / 0.15	-
		0.18 / 0.19	bulk, surface

Table 2.5: Previous table continued

a_L / $a_S(\mu m)$	$\alpha \equiv a_L/a_S$	ϕ_L / ϕ_S	Observed Phase Behavior
0.204 / 0.069	3.0	0.23 / 0.22	bulk, surface
0.605 / 0.296	2.0	0.25 / 0.18	-
0.137 / 0.069	2.0	0.18 / 0.18	-
		0.15 / 0.27	surface
		0.22 / 0.20	bulk, surface
		0.28 / 0.07	bulk, surface

in the large-sphere interstices. If α <2.4, the small spheres would not fit anywhere inside the large-sphere crystal (if it were face-centered cubic, hexagonal close-packed or random hexagonal close-packed). To my knowledge, detailed measurements of the structures of these crystals have not been reported. The question of how (or if) the large spheres accomodate the small spheres will provide further insight into the role of entropy in stacking of spheres in a crystal lattice.

We did not observe two-fluid coexistence, in contrast to some theoretical models which predict a fluid-fluid phase separation in mixtures of hard spheres and polymer with $\alpha < 3$ [71, 1, 72]. Two-fluid coexistence has been observed in hard sphere + polymer mixtures [51, 46, 53, 54] with α (using the polymer radius of gyration or hydrodynamic radius) = 3.0, 4.0, and 4.75. For $\alpha = 2.0$ and 3.0, we observed single-

fluid and fluid-solid regions, with no fluid-fluid region in between. It is possible, however, that fluid-fluid separation in binary hard-sphere mixtures appears in the narrow range of volume fractions which we happened to miss.

2.4 Results: Surface of the Sample Container

The glass wall of the sample container is negatively charged with $(OH)^-$ groups and acts like a hard wall [73], allowing us to observe how an ideal surface affects the particle behavior. The flat wall therefore provides our first insight into more complex confining geometries (with more to come in later chapters). The experiments described here, as well as the ones suggested in section 2.5 aim to understand how the density distribution, the freezing point and the kinetics of phase separation depend on finite-volume effects. All containers have surfaces, so these phenomena are likely to be very common, even dominant in samples with small volumes. Complex fluids inside porous media or inside cells, for example, are likely to be strongly affected by these surface effects, since a large fraction of the suspended particles are near a surface.

Recent experiments have uncovered some unexpected behavior at flat surfaces. Kaplan, Rouke, Yodh, and Pine [20] found that the depletion effects observed in the bulk of a sample can have an even stronger effect at a flat surface (see the introductory chapter). The large spheres were found to form a crystalline phase on the surface of

the container, even when the total particle concentration was well below the level at which phase separation occurs in the bulk. In section 2.4.1, I report that, at still lower concentrations, a fluid monolayer (enriched in the larger spheres) forms at the wall [74]. Observations of nucleation of the surface solid phase will also be reported, along with measurements of its structure (section 2.4.2).

The micrographs shown in Fig. 2.11 summarize the wall effects that we have seen. The photographs were taken in the optical microscope using a 100x (Plan-Neofluar, 1.3 numerical aperture) objective, focussed on the layer of particles next to the glass coverslip. In all cases, there are "large" spheres with a_L=0.825 μm and $\phi_L = 0.02$, and the particles are neutrally-buoyant to within much less than 1%. The series shows what we typically see when small spheres are added to the mixture ($a_S = 0.069$ μm). The small spheres are invisible, but their effect on the large spheres is obvious.

Fig. 2.11(a) and (b) show the accumulation of a dense fluid of large spheres at the surface with increasing ϕ_S. In section 2.4.1, measurements of the large-sphere area fraction *vs.* small-sphere bulk concentration will be presented. Fig. 2.11(c) and (d) show the nucleation of a crystallite on the surface and its subsequent growth into the bulk. Measurements of the structure and composition of this surface solid phase will be described in section 2.4.

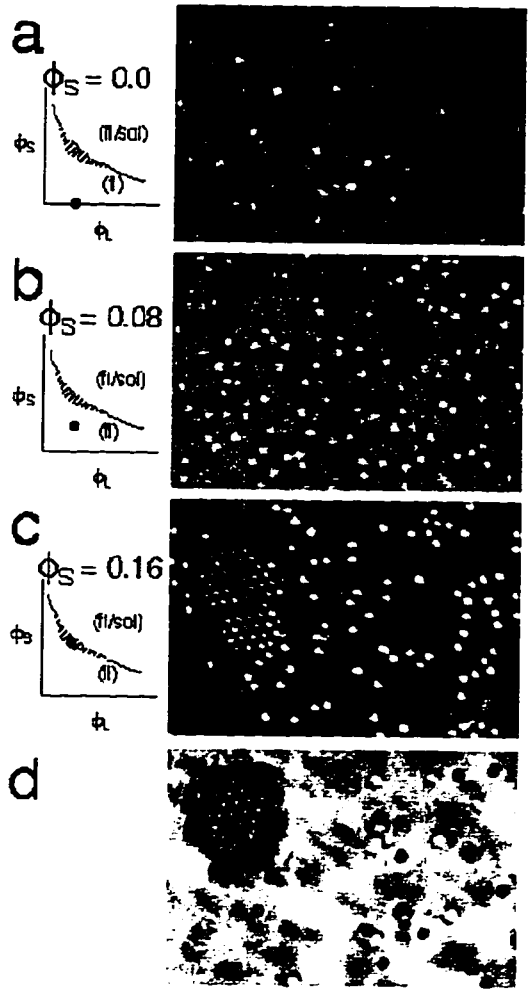

Figure 2.11: Optical micrographs of 0.825-μm polystyrene spheres (ϕ_L=0.02) next to a glass wall. The cartoon represents the location of the sample with respect to the fluid-solid coexistence curve and the surface-solid-only region (hatched area). In (a), there were relatively few spheres next to the surface, and each sphere remained in view for a small fraction of a second. In (b), small spheres (a_S=0.069 μm) have been added (ϕ_S=0.08) and the area density of large spheres has increased noticeably. In (c) (taken after 40 h), ϕ_S = 0.16, and surface crystals have nucleated. In (d), the microscope was focussed a distance a_L into the bulk to look at the second layer of the crystallite shown in (c). In (b)-(d), the large spheres stayed at the surface for an average of minutes.

2.4.1 Dense Fluid at the Surface of the Sample Container

We measured the enhancement of large spheres at the surface as small spheres were added to the bulk and found qualitative agreement with a theoretical prediction. We also observed fluid-solid *coexistence* on the wall, which contradicts theoretical predictions, probably due to kinetic effects.

We measured the large-sphere density at the wall layer using video microscopy [74]. To reduce sedimentation, heavy water was added to make the particles (approximately) neutrally buoyant. Results were repeateable from sample to sample and were independent of sample orientation. All samples studied remained a single fluid phase in the bulk. The wall area fraction, η_L^{wall}, of large spheres with centers lying within a distance of $a_L/2$ and $a_L/2 + t$ of the wall was measured by counting: $\eta_L^{\text{wall}} = N_L \pi a_L^2/(4A)$, where N_L is the number of large spheres observed in an area A ($N_L \approx 10,000 - 20,000$). The thickness of the wall layer, t, depended only on the depth of field of the microscope objective and on the image-processing algorithm. An estimate of t can be obtained by assuming that when $\phi_S = 0$, there was no enhancement of large-sphere concentration at the wall, so that N_L is the number of large spheres in the volume $A \times t$: $N_L = 3At\phi_L/(\pi a_L^3)$. Thus, $\eta_L^{\text{wall}}(\phi_S = 0) = 3\phi_L(t/a_L)$. In this way, we estimate that $t = 130\text{nm}$[2]. Results for a system with $a_L = 0.605$ μm, $a_S = 0.083$ μm at $\phi_L = 0.03$ are shown in Fig. 2.12 as a function of ϕ_S. All samples

[2]The fact that $t > a_S$ does not matter, since we are looking at the *increase* of the wall coverage as ϕ_S is increased.

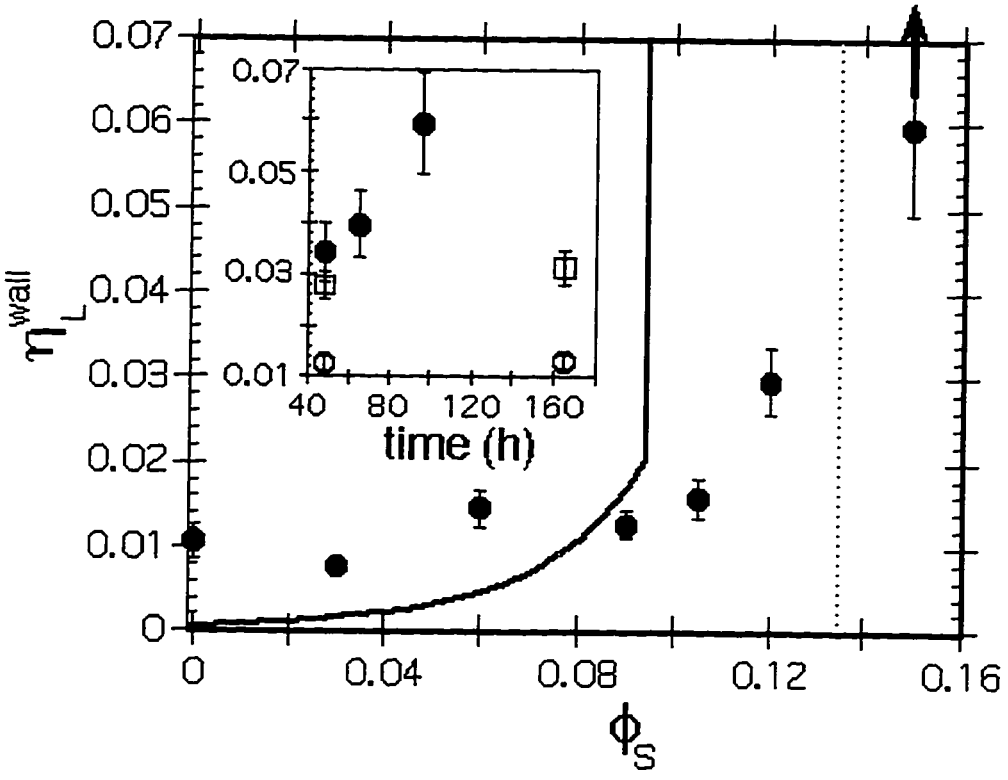

Figure 2.12: Plot of the area fraction of 0.605-μm spheres (η_L^{wall}) at a flat glass wall. In each case, ϕ_L is held at 0.03. η_L^{wall} *vs.* ϕ_S. The solid line represents the theory of Poon and Warren. Inset: η_L^{wall} *vs.* elapsed time for various ϕ_S; $\circ$ ($\phi_S = 0.09$), $\square$ ($\phi_S = 0.12$) and filled circle ($\phi_S = 0.15$). In the last sample, η_L^{wall} continued to increase over time.

with $\phi_S \leq 0.12$ remained in the wall-fluid phase, with no crystallites even after 3 weeks (similar to Fig. 2.11(b)). In the samples with $\phi_S = 0.15$, wall-crystallites became visible after one week and continued to increase in size for several weeks, until the samples were discarded. These samples were similar to that shown in Fig. 2.11(c). For several samples, we measured η_L^{wall} as a function of time, *before* the wall crystallites appeared (inset of Fig. 2.12). In samples which remained fluid at the wall ($\phi_S \leq 0.12$), η_L^{wall} did not change between 50 and 170 hours after mixing, indicating full equilibration. At $\phi_S = 0.15$ (above the wall-freezing point), however, we found that the area fraction was still rapidly increasing with time even before crystallites had appeared. The crystallites, which appeared after one week, continued to grow (in area and in thickness) for up to several weeks, indicating that these mixtures had not reached equilibrium. The last data point on Fig. 2.12 therefore represents a *lower bound* for η_L^{wall}. Possibly, if one could wait long enough before doing the experiment, there would be closer agreement with the *equilibrium* statistical mechanical prediction of η_L^{wall}.

The experimental measurements of η_L^{wall} confirm the presence of an equilibrium wall-fluid phase, enriched in large spheres. With $\phi_S > 0.1$, η_1^{wall} was noticeably larger than in the monodisperse mixture ($\phi_S = 0.$). With $\phi_S \geq 0.15$, the wall-solid phase appears.

For comparison to the measurements, Fig. 2.12 also shows the results of a calculation by Poon and Warren [74]. For the bulk free energies, they follow the approach

that is outlined in their previous paper [75] (also briefly described in the next chapter). There are two adjustable parameters needed to describe the surface phases. The first, λ, is the length of decay of correlations in the pair distribution function of a two-dimensional hard-disk fluid; the other is the thickness of the wall layer, b (the distance perpendicular to the wall over which centres of adsorbed large spheres may move). The predictions of the theory are only weakly sensitive to the values of these two parameters (see [74]). Here $b = 0.014a_L$, chosen so that the wall crystallization transition at $\phi_S = 0$ occurs at $\phi_L = 0.486$, the value obtained in computer simulations [41, 42]. The theory is insensitive to large variations in b. The small spheres are assumed to be a disordered fluid throughout. The free energy density of the wall layer of large spheres is made up of three parts:

$$f = f_{\text{ideal}}(b) + f_{\text{2D}} + f_{\text{depletion}}(\lambda) \,. \tag{2.1}$$

The first term denotes the free energy density of an ideal gas confined to a layer of thickness b; the middle term is the non-ideal contribution from a two-dimensional system of hard *discs* (fluid or crystal), parametrised from simulations; the last term accounts for the depletion attraction between big spheres induced by small spheres, calculated using a two-body approximation (which depends on the probability of finding two big spheres next to each other within the wall layer, and hence the parameter λ). Below the wall crystallization boundary, the adsorbed layer of large spheres is predicted to be a fluid state. Across the boundary, the large spheres at the wall freeze

into a (single-layer) two-dimensional triangular arrangement with an abrupt change in density. The results are shown by the solid curve in Fig. 2.12.

Whereas fluid and solid phases can coexist in the bulk, we expect from the theory a *sharp transition* between wall-fluid and wall-solid phases. The bulk in a colloidal experiment is effectively a constant-particle-number system, where it is possible to observe *coexisting* fluid and solid phases. The wall layer, however, freely exchanges spheres with the bulk, so that the chemical potentials of the two species are held constant. The bulk acts like a particle reservoir; as soon as the wall-solid chemical potentials fall below the wall-fluid chemical potentials, the entire surface should be covered with the solid phase. This prediction is contrary to our observations, probably due to the fact that the samples in which crystallites appeared never reached equilibrium.

2.4.2 Structure and Morphology of Surface Crystals

As previously reported [20], we often observed (by eye) iridescent spots growing on the walls of the container, even in samples that were stable in the bulk. Such samples are marked with "□" in figure 2. Optical microscopy of these spots revealed crystallites thought to have formed due to the depletion attraction (Fig. 2.11 (c) and (d)). The crystals had domains of triangular-ordered large-sphere planes aligned parallel to the wall. Each crystallite had many such domains, which ranged in size from 5 to 500 large

spheres per plane, with the larger domains and larger crystallites always appearing in samples with lower ϕ_S. The crystallites' thickness consistently varied from 1 or 2 layers, at high α and/or high ϕ_S, to approximately 100 layers, at lower α and ϕ_S. We measured the thickness by optical microscopy, by inspection of the crystallites from both sides of a 1 mm-thick sample, and by addition of enough salt to the system to cause rapid, irreversible flocculation which allowed the surface crystallites to be removed from the surrounding fluid and inspected. Due to the strong scattering of visible light, we were unable to see far enough into the sample to determine directly the sequence of plane stacking normal to the cell wall. The symmetry of Kossel-scattering patterns [66] and measurements of spacings in various crystallographic directions (using scanning electron microscopy, Fig. 2.13), however, ruled out body-centered cubic (bcc) structure and suggested random stacking of close-packed planes (RHCP) [76]. Our results indicate that the surface crystalline phase has the same structure as the bulk crystalline phase, with similar concentrations of small spheres and a similar decrease in large-sphere order with increasing ϕ_S.

2.4.3 Kinetics of Crystallization at the Surface

From our experiments, it appears that the arrangement of particles within bulk and surface crystallites is the same. The wall only affects those particles that are in the very first layer (or, at least, very close to it). In a thick crystal, then, there is no

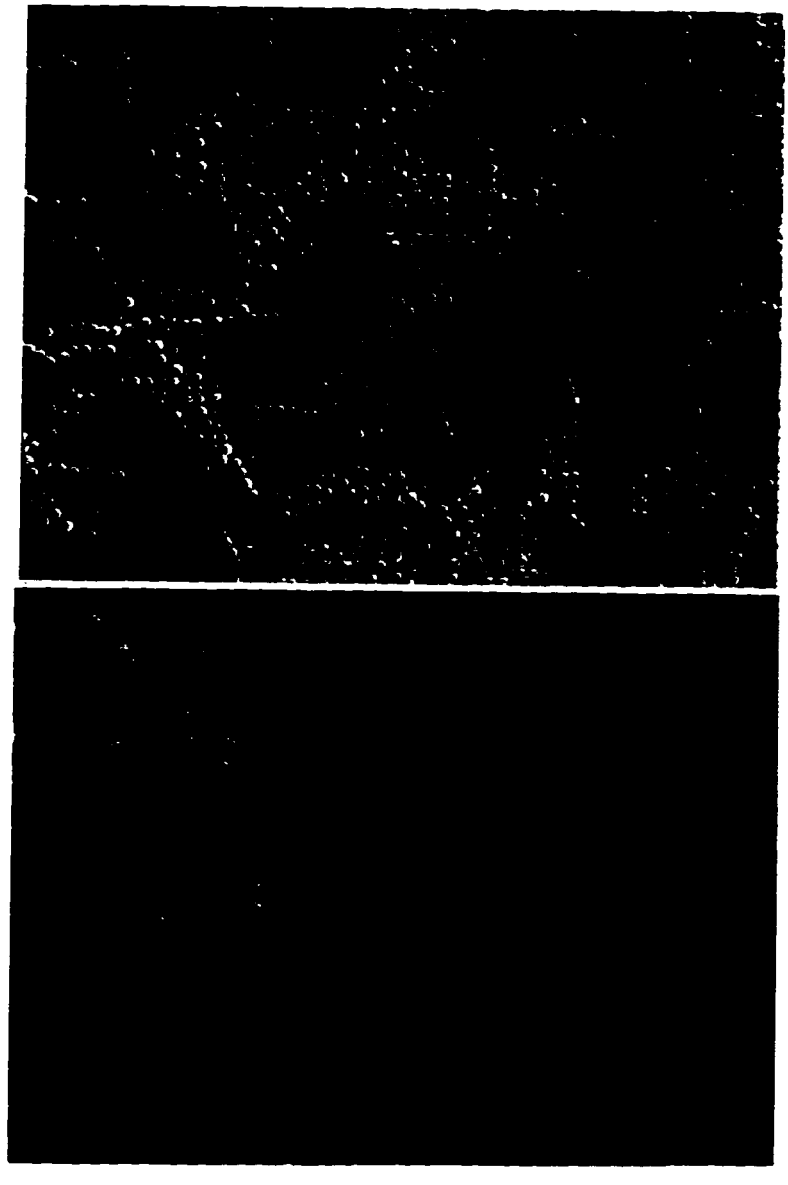

Figure 2.13: Scanning-electron micrographs of the crystallites that grow on the glass wall of the sample container. Several samples were prepared as described in the experimental section and gave consistent results. Here, the large spheres are 0.460 μm in diameter and the small spheres 0.065 μm. Volume fractions are ϕ_L/ϕ_S= 0.07/0.15 (top) and 0.05/0.16 (bottom). The small spheres are visible in an apparently disordered state.

thermodynamic distinction between "surface" and "bulk: in principal, the crystallite will eventually get large enough so that the relative number of spheres along the wall becomes negligible. This observation suggests that the squares (□) shown in the stability diagram (Fig. 2.5(a)) in fact represent regions of formation of the "bulk" solid phase, since these crystallites were always many layers thick.

Further insight into the freezing process comes from Fig. 2.11 (c), which shows nucleation in action. By watching clusters appear and disappear along the wall of this sample, I observed a critical size, N_C, of 10-12 large spheres. Any clusters with fewer large spheres typically broke up; larger ones were stable and slowly grew. The presence of a critical size implies that there is some entropic cost associated with freezing that is only overwhelmed by the depletion effect when the cluster is large. The traditional approach, in molecular fluids, is to assume an energy cost per unit area (surface tension), which becomes overwhelmed by the energy loss per unit volume when the cluster is large. For hard-sphere mixtures, there is no obvious source of surface tension. Furthermore, accounting for the translation entropy lost by each large sphere when it become tied to a cluster implies a very small critical size of ≈ 2, which is found to be incorrect. Detailed measurements of, for example, critical size as a function of ϕ_L, ϕ_S and α might shed some light on this fundamentally important question.

The nucleation model does help to explain why large surface crystals appear in

some samples. If the critical size is large, then nucleation is much more likely to occur at the wall, where the density of large spheres is larger. The number of nucleation sites should scale with ${\phi_L}^{N_C}$, which can be a large factor if, for example, the wall density is twice as large as the bulk ($2^{12} = 4096$). Thus, even if the bulk solid is thermodynamically stable, it will not appear as a sediment in the experimentally accessible time of a few weeks. As α, ϕ_S or ϕ_L increases, N_C decreases and bulk freezing become rapid enough to observe. When the crystallization rate in the bulk becomes comparable to that of the surface, the surface crystallites disappear, since there are many more large spheres in the bulk than there are near the surface. This conclusion is consistent with the observations reported above.

Possibly the appearance of a single ordered layer (accompanied by a large density jump) can also be seen as the first step in a sequence of layering transitions [77], of which only the initial stage is treated by the theory described above. Consideration of such layering (or similar, roughening) effects may explain why large, thick and faceted crystallites formed at lower ϕ_S and small, thin and rough crystallites (1-2 layers) formed at higher ϕ_S, well above the wall phase transition point.

2.5 Conclusions

We have determined the structures and compositions of the phases of binary mixtures of polystyrene particles which closely resemble hard spheres. We found fluid-solid

coexistence and have measured phase diagrams for mixtures with $12.0 > (a_L/a_S) > 6.7$. We have discussed the effects of gravity and kinetics of phase separation on the structure and sedimentation of the phases, with special emphasis on some novel behavior at flat walls. Perhaps the most remarkable finding is that this seemingly simple and purely entropic system exhibits so many phenomena seen in systems with very complicated interactions.

The work presented in this chapter has decided some issues while uncovering others. One question that arises from Fig. 2 is the miscibility of spheres of different sizes within the solid phase. How large can the secoind size be and still appear within the lattice? What are the effects of many defects on the freezing point? How do the defects arrange themsevles in the lattice? Another question that arises is how deviations from hard-sphere interactions affect the phase behavior. A motivation for the present work is that the hard-sphere system is often used as a reference state for understanding mixtures with other interactions. Systematic determinations of, for example, the position of the liquidus as the strngth electrostatic repulsion is increased would provide an important experimental test of our ability to extrapolate theoretically from hard-sphere to more realistic cases. As a counterpart to these phase-diagram measurements, the interactions among particles could be measured using techniques described in [15, 78, 29].

Further insight into finite-volume effects could be gained by creating samples of

various shapes (aside from the flat wall considered here). For example, the concentration of large spheres in small pores or thin slabs can be measured by optical microscopy. If the pore is in equilibrium with a reservoir of small and large particles (with known chemical potentials), the chemical potential of large spheres in the pore is also known (it is the same as the reservoir value). By repeating the experiments with various volume fractions in the reservoir, the chemical potential of large spheres can be directly measured as a function of ϕ_L and pore shape. Similarly, measuring the *bulk* volume fractions at which freezing occurs *in the pore* will demonstrate how the freezing point depends on pore shape.

Chapter 3

Calculation of Phase Diagrams of Binary Hard-Sphere Mixtures

Usually, one thinks of freezing as a competition between attractive two-body forces and entropy, with the latter typically favoring "disorder". Hard spheres lack these attractive interactions, yet, as we have seen, they can spontaneously crystallize and separate themselves by size. In this chapter, I discuss in detail an original theory [30] to account for the entropy of the mixture and show how entropy can, in fact, favor freezing – spontaneous ordering – in the bulk. The Asakura/Oosawa depletion picture (section 1.3, page 6 and Fig. 3.1) provides a glimpse of the essential point: the entropy of the particles depends on the accessible volume. We therefore take a strictly geometric approach to calculate accessible volumes and determine the free energy.

Specifically, I will describe a simple model for the bulk fluid phase which avoids the ideal-gas approximation. For the solid phase, we use geometric arguments to calculate the free energy of the large-sphere crystal (following the approach of [79])

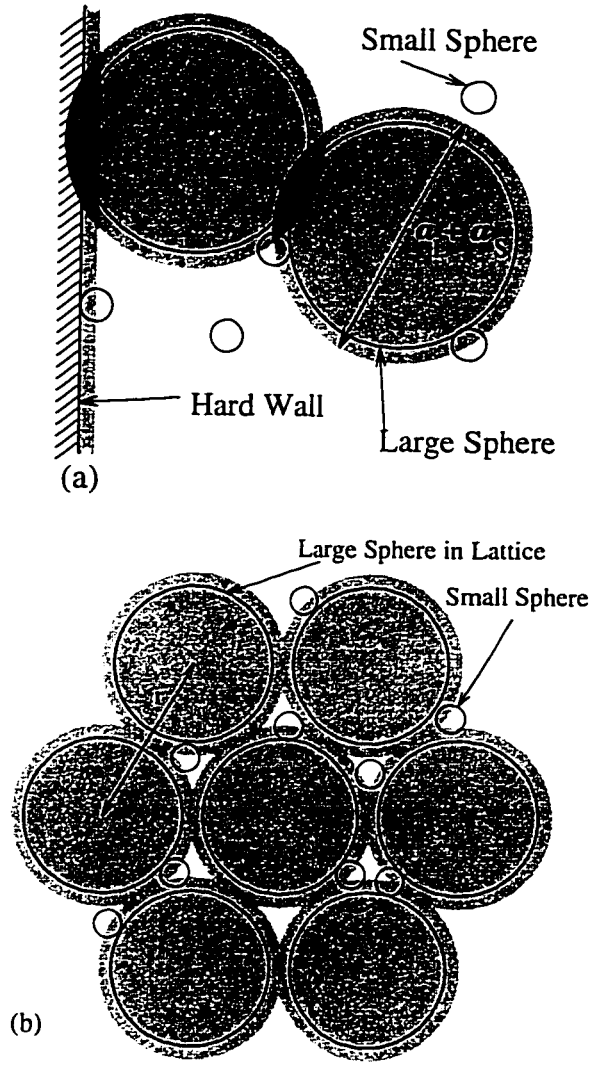

Figure 3.1: Drawing of large and small spheres showing the excluded-volume regions described in the text. (a) The small-sphere centers of mass cannot penetrate within the shaded regions. When the large spheres approach one another or the wall, these excluded-volume regions overlap, increasing the volume accessible to the small spheres by the volume of the heavily-shaded regions. (b) Diagram of the solid phase. The white regions represent the volume accessible to the small spheres, defined in the text as $(\xi + \gamma)V$.

and the free energy of the small-sphere fluid that permeates the large-sphere crystal. The model is independent of fit parameters. It is the first calculation of the coexisting fluid- and solid-phase volume fractions in *monodisperse* hard-sphere colloids (0.50 and 0.57) that is in reasonable agreement with the results of computer simulations (0.49 and 0.55, respectively) [36] and experiments [31, 33, 39]. For the *binary*-colloid case, the model predicts fluid-solid phase separation at much lower total volume fractions than in monodisperse colloids, in agreement with our measurements. The results and assumptions are discussed and compared to those of Lekkerkerker *et al.* [80, 71] and of Poon *et al.* [75], who consider binary hard-sphere colloids and colloid-polymer mixtures.

The thermodynamics of (infinitely large) binary hard-sphere mixtures depends on just three dimensionless parameters: the volume fractions ϕ_L and ϕ_S of the large and small spheres, respectively, and the ratio, α ($\equiv a_L/a_S$), of the large- and small-sphere diameters, a_L and a_S. Temperature (T) does not influence the equilibrium state. How can this be? Raising the temperature increases each large sphere's kinetic energy $(3/2)k_BT$) and would seem to increase the ability of the large spheres to "boil" out of the depletion well. Simultaneously, however, the osmotic pressure of the small spheres increases just enough to strengthen the depletion force and counteract the boiling out. The ratio of kinetic energy to depletion energy does not depend on temperature. From another point of view, the Boltzmann factor, e^{-U/k_BT} is always

either 0 or 1 for hard spheres, and is thus independent of T. Finally, it will be clear from the equations derived in this chapter that the temperature appears in the free energy only as an overall prefactor which cancels out.

3.1 Background

In 1964, in the first attempt to calculate a phase diagram for binary hard-sphere mixtures, Lebowitz and Rowlinson [81] solved the Ornstein-Zernike equation using the Percus-Yevick (PY) closure relation and predicted *no* instability in the fluid phase for any α, ϕ_L, or ϕ_S. Their approach was to look for a divergence of the compressibility, which would indicate a spinodal instability. Liquid structure theory relates the compressibility to the structure factor ($S(k=0)$), which is related to the Fourier transform of the pair distribution function $g(r)$. (The function $g(r)$ is the probability of finding a particle located a distance r from another particle located at the origin.) The Ornstein-Zernike integral equation relates $g(r)$ to the "direct correlation function", $c(r)$, which in turn is defined by a "closure" relation. A closure relation is thermodynamically self-consistent if the pressure caculated using the compressibility relation (mentioned above) is identical to the pressure calculated from the virial expansion. The PY closure allows $g(r)$ to be calculated exactly, but is not thermodynamically self-consistent. For a detailed description of liquid structure theory, see ch. 5 of [82].

More recent attempts in this decade, however, have demonstrated a spinodal instability in the binary fluid phase when the size ratio, α, and particle concentration are sufficiently large. Biben and Hansen have solved the integral equations for the pair structure within the Rogers-Young (RY) closure and found a spinodal instability when $\alpha > 5$ [83]. The RY approximation interpolates between the hyper-netted chain (HNC) and PY closures to enforce thermodynamic self-consistency. Using density functional theory (DFT), Rosenfeld has predicted a spinodal instability in systems with $\alpha \geq 4$ [84]. In DFT, one must first write down the free energy functional, which describes the free energy in terms of density functions. Rosenfeld has derived a functional from geometric arguments [85]. Minimizing this free energy functional yields results that are similar to those of Biben and Hansen. This approach is more readily applied to cases involving an external potential such as gravity or walls [85, 86]. Finally, further evidence for a spinodal instability has come from a combination of molecular dynamics and Monte Carlo simulations [28]. The spinodal curves predicted by Biben and Hansen and by Rosenfeld are consistent with most of the experimental results in that they lie well above the measured liquidus curves (see [84] for an explicit comparison). An exception is the work of [50] (silica spheres, $\alpha = 9.3$), who found the fluid-solid coexistence curve to lie well above the spinodal lines calculated by [84, 83, 80]. The location of the spinodal curve has not been measured directly.

While finding evidence of thermodynamic instability, the RY and DFT approaches

have not determined the structures or compositions of the coexisting phases, nor could they predict the coexistence curves. Although the authors hazard guesses (resp. fluid-solid and fluid-fluid), the calculations do not provide any hard evidence. This problem, therefore, remains inaccessible to the most reliable first-principles theories available.

A more phenomenological approach has also been used, in which one first assumes the structures of the coexisting phases, then computes the free energy and minimizes it to determine the phase diagram. Recently, Poon *et al.* [75] (discussed in further detail below) calculated a phase diagram for mixtures with α =7.1. In this approach, the melting and freezing volume fractions of a monodisperse mixture must be assumed. Furthermore, the free energy of the large-sphere crystal is obtained from computer simulations, so that the underlying physics is somewhat obscured. The model described here *predicts* the freezing and melting points of monodisperse mixtures. It also provides a first-principles estimate of the Helmholtz free energy of the large-sphere crystal, based on simple geometric considerations [79].

Phase diagrams have been derived for hard-sphere mixtures with similar-sized spheres (α = 1.2 and 1.5) [87]. These calculations rely on a fluid-phase equation of state derived from the PY closure and on computer simulations for the solid phases. Phase separation in these low-α mixtures has been observed only when the total volume fraction exceeded approximately 0.5, at which concentration the structure

was largely determined by packing geometry and was therefore strongly α-dependent. The AB_2 and AB_{13} phases observed in this size-ratio regime are quite different from those observed in mixtures with $\alpha \geq 6$. Denton and Ashcroft have calculated the relative thermodynamic stabilities of various solid-phase structures (at high total ϕ) as a function of α, using density functional theory (DFT) [88]. For $1 < \alpha < 1.3$, the stable solid phase was found to be a sustitutionally-disordered face-centered cubic (FCC); for $\alpha > 1.3$ the stable phase was predicted to be a pure large-sphere FCC lattice. Similar results were found by Barrat *et al.* [89]. In another DFT approach, the stable structures were found to be NaCl and CsCl structures [90]. These calculations were done at much higher densities than the experiments reported in the previous chapter, and none of the phases that were predicted to be stable have been found experimentally thus far.

In other theoretical models, Gast *et al.* [1], Vincent *et al.* [91], and Lekkerkerker *et al.* [80, 71] assume that the small (polymer) particles are an ideal gas. While valid for polymer solutions, this approximation is not very accurate for the mixtures of hard spheres we consider here. While there are similar features, polymers and emulsions are in general neither hard nor spherical, and the potentials are non-additive [1], so the thermodynamics are somewhat different from the hard-sphere systems considered here. A quantitative comparison of the theories of binary hard-sphere and hard-

[1] For a discusssion of non-additivity, see [59] and the Background section of the previous chapter.

sphere+polymer mixtures will be given in section 3.3.

Lattice-model calculations and simulations of binary hard-sphere mixtures have contributed to the evidence for fluid-solid and fluid-fluid transitions. A lattice model with large and small cubes has been solved by Monte Carlo simulation in three dimensions [92]. The results indicated fluid-fluid coexistence when the size ratio $\alpha = 3$. but no instability when $\alpha = 2$. A two-dimensional lattice model with hexagons and points in a triangular lattice has predicted fluid-solid, fluid-fluid, and three-phase coexistence [93]. These results contribute to the evidence that pure hard-core repulsions can lead to phase separation, but do not provide quantitative results for phase diagrams of real mixtures.

3.2 Theoretical Model

In this section we will calculate the phase diagram for the binary hard-sphere system with $\alpha > 6.4$. For the solid phase, I employ a simple model [79] to calculate the Helmholtz free energy with no arbitrary parameters. To calculate the free energy of the binary fluid phase, I use the well-known equation of state due to Carnahan and Starling [94] with modifications. The model predicts fluid/solid phase transitions in monodisperse hard-sphere colloids, in close agreement with the results of computer simulations. We also predict fluid-solid phase separation in binary mixtures, in agreement with our measurements.

It is constructive to compare our approach to that of Poon *et al.* [75] (who follow the approach of references [80] and [71]). Both approaches predict coexistence of a binary fluid and a close-packed lattice of large spheres permeated by a dilute fluid of small spheres. To determine the free energy of the large spheres in the fluid phase, both rely on the equation of state due to Carnahan and Starling [94]. Also, both assume that the small particles reside in a reduced volume which depends on the volume fraction of the large spheres. There are, however, significant differences. First, in references [75, 71], the reduced volume in which the small particles reside, in both the fluid and solid phases, is determined by comparison of the chemical potential of an ideal gas of small particles in the reduced volume to the chemical potential of the small particles in a binary hard-sphere fluid, calculated within the Percus-Yevick approximation (which, as discussed above, by itself predicts no instability in the binary fluid phase). In the present approach, this reduced volume is calculated using simple geometric arguments. Second, for the large-sphere crystal, references [75, 71] use the results of a computer simulation, whereas the present approach derives the free energy analytically, following Buehler *et al.* [79]. Our method has the advantage of calculating the chemical potential without unknown additive constants. Finally, the present approach does not *a priori* assume phase separation in a monodisperse mixture with ϕ approximately 0.5. Instead, this behavior is predicted. The phase diagrams calculated within these two approaches agree reasonably well, as shown in

Fig. 3.12(a).

We would like to understand the equilibrium state of colloidal particles that are confined to the water in their container. Thus, the particles are held to a constant total volume, V. Because the sample container (glass) can conduct heat, the sample is also held at constant temperature (T, in Kelvins) by the room, which acts as a thermal reservoir.

Clausius' theorem [95, 96] states that the heat of a system will either stay the same or decrease for any cyclic (round-trip) process:

$$\oint \frac{dQ}{T} \leq 0. \tag{3.1}$$

The equality is true for a reversible process. In thermodynamics, entropy (S) is defined as

$$S_B - S_A \equiv \int_A^B \frac{dQ}{T}, \tag{3.2}$$

where the path $\overline{AB}$ represents a *reversible* process. Combining these two, we have

$$S_B - S_A = dS \geq \frac{dQ}{T}. \tag{3.3}$$

For a closed system ($dQ = 0$), $dS \geq 0$, so entropy always increases. In colloid experiments, heat can flow to the sample from the room, so $dQ \neq 0$. The first law of thermodynamics allows us to write the amount of heat flow in any process in terms of the change in internal energy (U) and the mechanical work done:

$$dU = dQ - PdV, \tag{3.4}$$

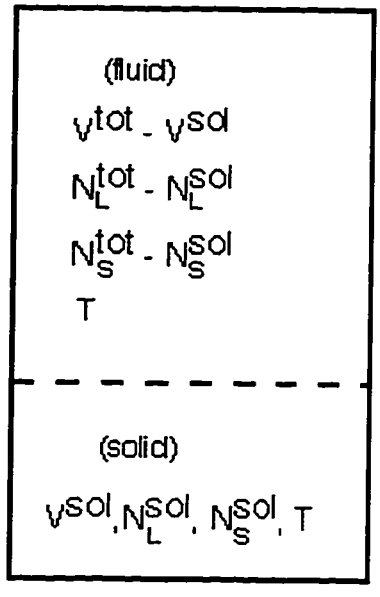

Figure 3.2: Cartoon of a colloid in equilibrium with the room. The colloidal particles are confined to the volume of the water in the (sealed) sample cell, V^{tot}. Thus, the system is characterized by constant temperature and volume (T, V^{tot}).

where P is the pressure. We now combine these last two equations:

$$dU + PdV - TdS \leq 0. \tag{3.5}$$

For a system held at constant volume ($dV = 0$) and temperature, we find the end result:

$$dF \equiv dU - TdS \leq 0. \tag{3.6}$$

Thus, the Helmholtz free energy, F, moves toward its minimum for any process. The equilibrium conditions for colloids are therefore obtained by minimizing the total Helmholtz free energy of the colloidal particles, F, with respect to all free parameters (Fig. 3.2). If T and P were constant, then the Gibbs free energy would be minimized.

Here we investigate the possibility of coexistence of two phases and write the total

Helmholtz Free energy as the sum of two terms: $F^{\text{tot}} = F^{fl} + F^{sol}$. The superscripts fl and sol denote fluid and solid phase, respectively. In considering possible coexistence of two phases, there are three free parameters (Fig. 3.2): volume of the solid phase (V^{sol}), number of large spheres in the solid phase (N_L^{sol}), and number of small spheres in the solid phase (N_S^{sol}). Our procedure was to choose an initial ϕ_L, $\phi_S$and V^{tot} (which scales out of the problem) and minimize F^{tot}. Minimizing with respect to V^{sol} is equivalent to equating the osmotic pressure, P, of the two phases (recall that $P \equiv -dF/dV$). Minimizing with respect to $N_L^{sol}(N_S^{sol})$ is equivalent to equating the large- (small-) sphere chemical potentials of each phase ($\mu_{L,S} = dF/dN_{L,S}$). The resulting three equations were solved to determine the volume fractions of the fluid and solid phases which coexist at equilibrium. The set of points $(\phi_L^{fl}, \phi_S^{fl})$ at which $V^{sol}/V^{tot} = 0$ determines the liquidus curve, while the corresponding $(\phi_L^{sol}, \phi_S^{sol})$ determine the solidus. (Note that there is no guarantee of real, physical solutions of the equilibrium conditions. Their absence would indicate that the fluid phase is always stable with respect to the solid phase that is considered.)

We omit the water from considerations of the particle thermodynamics. Water plays an important role in the particle dynamics, and it keeps the particles suspended, but its free energy does not depend on the arrangement of the colloidal spheres[2].

[2]We are assuming that each sphere has a thin layer of water molecules around it – a hydration layer – that is not influenced by the sphere positions. If, for example, the spheres were hydrophobic, the water would push the spheres into clumps (as our small spheres do!) to minimize the area of contact with the hydrophobic surface.

Therefore it has no effect on the equilibrium colloidal structure.

For the fluid and solid phases, we divide the Helmholtz free energy into two pieces: one due to the large spheres (denoted by the subscript L) and one due to the small spheres (denoted by the subscript S). Thus $F^{fl}_{total} = F^{fl}_L + F^{fl}_S$ and $F^{sol}_{total} = F^{sol}_L + F^{sol}_S$.

3.2.1 Large-Sphere Crystal

We explicitly calculate the free energy of the crystal of large spheres. Since there is no interaction between the spheres when they are not touching, we do not rely on harmonic-solid approximations. Instead, we use the method of Buehler *et al.* [79], who consider each sphere to move freely in a hard "cage" formed by its nearest neighbors which are assumed to lie on a lattice (see figure 3.3). In this mean-field approach, the effect of lattice fluctuations on the cage volumes is neglected. The volume of the cage, v^*, is equal to the volume accessible to the center of mass of each sphere in the lattice. We do not subtract from v^* the volume of the small particles, since they are excluded from most of the volume that is available to the large spheres (see figure 3.1(b)). Therefore the free energy of the large-sphere crystal is independent of the small-sphere volume fraction. The energy of the crystal is just the kinetic energy, $p^2/2m$, where p and m are the momentum and mass of each sphere. The partition function, Z, and Helmholtz free energy, F^{sol}_L can therefore be calculated.

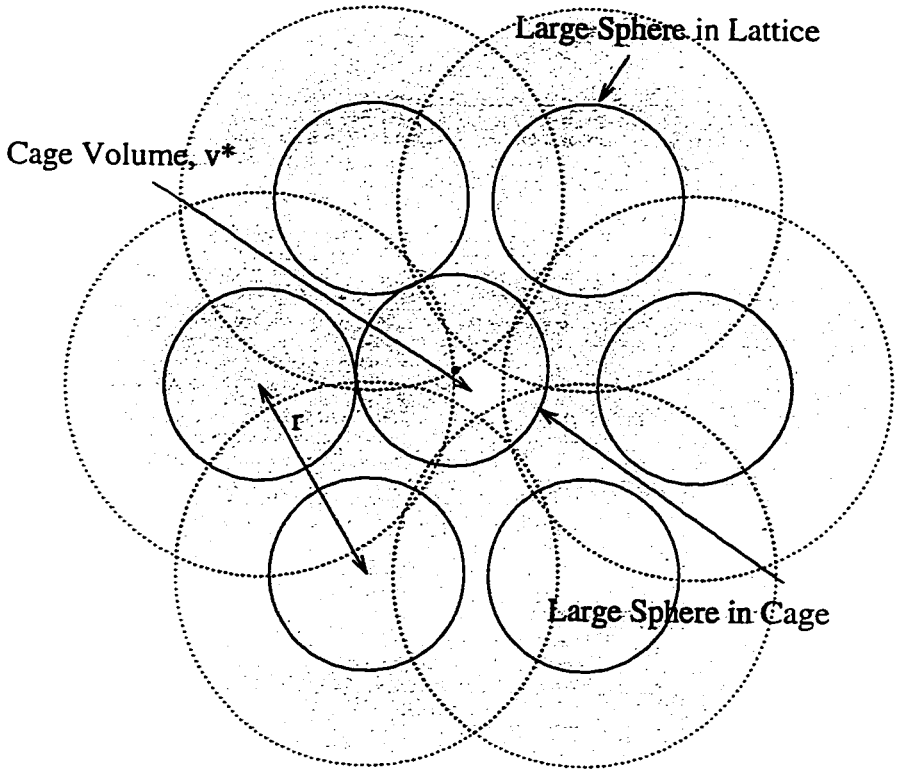

Figure 3.3: Diagram of the large-sphere crystal. Due to the hard-core repulsion, the middle sphere's center of mass can fit only in the small central white region which is a two-dimensional slice of the cage volume, v^*.

$$Z = \left\{ \frac{1}{(2\pi\hbar)^{\frac{3}{2}}} \int_{v^*} d^3r \int d^3p \, \exp(-\frac{p^2}{2mk_BT}) \right\}^{N_L}, \tag{3.7}$$

$$\frac{F_L^{sol}}{k_BT} = -\ln Z = -N_L \ln v^* + 3N_L \ln \Lambda, \tag{3.8}$$

where k_B, T, and N_L are Boltzmann's constant, temperature, and number of large spheres (in the solid), respectively. The thermal wavelength, Λ, is defined as $\Lambda \equiv \sqrt{2\pi\hbar^2/(mk_BT)}$, where $\hbar$ is Planck's constant. This equation for the partition function, Z, differs from the ideal-gas result in two ways: the spatial integral is limited to the cage volume v^*, and the factor $1/N_L!$ is omitted in order to make F_L^{sol} extensive[3].

To calculate v^* as a function of lattice spacing, we divide space into small voxels and use a computer to count the number of voxels in which the center of a large sphere can reside without that sphere's overlapping any neighbors. The values of v^* for FCC, HCP, and RHCP structures are identical. We fit a polynomial to the results of our calculation:

$$\frac{v^*}{a^3} = 6.733 \times 10^{-7}(\frac{r}{a} - 1) - 4.313 \times 10^{-4}(\frac{r}{a} - 1)^2 + 4.809(\frac{r}{a} - 1)^3, \tag{3.9}$$

where r is the distance between the centers of neighboring spheres in the lattice and a is the sphere diameter. This form of the expansion shows that v^* can also be approximated by a sphere of radius $(r - a)$. We used this polynomial form, which

[3]Since each large sphere is uniquely associated with a particular cage, the spheres are distinguishable.

deviates from the computer results by less than 3% when $\phi > 0.56$. In the calculated phase diagram, ϕ is always greater than 0.56. We find that varying v^* by 10% has a less than 1% effect on the calculated coexisting volume fractions in the monodisperse case.

In figure 3.4 (left), we compare the osmotic pressure ($-\partial F/\partial V$) of the monodisperse hard-sphere crystal calculated here (and in [79]) to the results of a fit by Hall to computer simulation results (equation (13) of reference [97]). The agreement indicates that the cage model provides a reasonably accurate understanding of the hard-sphere crystal, although it appears to underestimate the solid-phase pressure by as much as 7% when $\phi = 0.57$. This disagreement might arise from neglecting long-wavelength fluctuations (phonons), which would distort the shape of the cages. Agreement improves substantially with increasing ϕ, except very near closest packing, at which point the pressure diverges. In the calculations shown here, the solid-phase large-sphere volume fraction never exceeded 0.73; in the region of interest, this model agrees closely with computer simulations.

3.2.2 Fluid Structures

We model the small and large spheres in the fluid phase and the small spheres in the solid phase as hard-sphere fluids existing in *effective* volumes, as defined below. The hard-sphere-fluid free energy is obtained by integration of the Carnahan-Starling

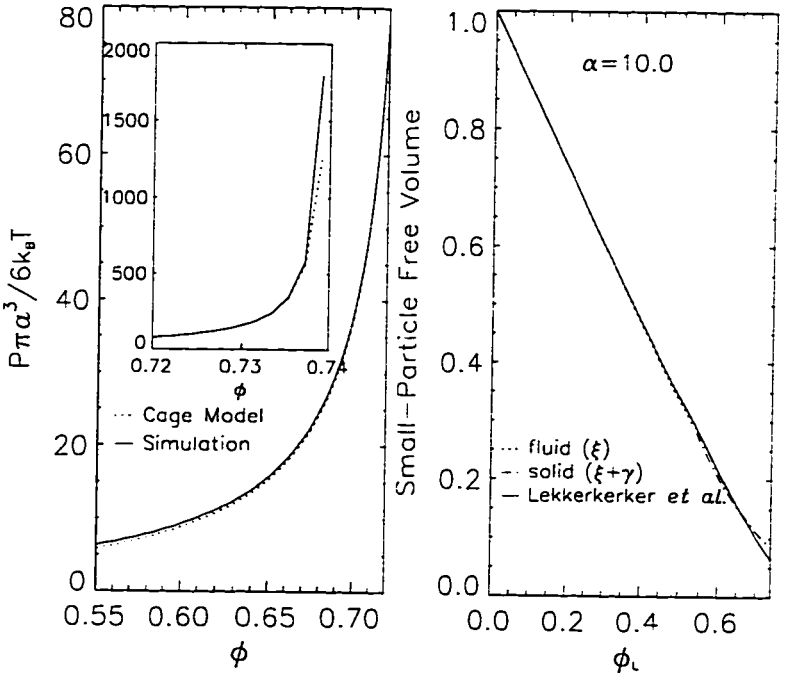

Figure 3.4: Left — Plot of the osmotic pressure of a monodisperse hard-sphere FCC or HCP crystal as a function of volume fraction of spheres. The dotted line represents the results of the calculation described in the text, while the solid line represents the results of Hall, from a fit to computer-simulation results. There are no free parameters. Right — The fractional volume accessible to the small particles as a function of large-sphere volume fraction. The dotted and dashed lines show the results of the present approach, equations (8) (for fluid phase, with $\phi_L < 0.55$) and (9) (for solid phase, with $\phi_L \geq 0.55$). The solid line shows the result of Poon *et al.*, equation (9).

(C-S) equation of state for a monodisperse hard-sphere fluid [94],

$$\frac{P^{C-S}V}{Nk_BT} = \frac{1+\phi+\phi^2-\phi^3}{(1-\phi)^3}. \tag{3.10}$$

$$\frac{F}{k_BT} = -\int_0^V \frac{P(N,T,V')}{k_BT}dV' = \frac{V}{\pi a^3/6}\left(\frac{3\phi-2\phi^2}{(1-\phi)^2}+\phi\ln\phi\right)+\frac{F_0(N,T)}{k_BT}, \tag{3.11}$$

where P is the fluid osmotic pressure, V is the total volume of the fluid phase, a is the sphere diameter, N is the number of spheres, ϕ is the volume fraction of spheres ($\phi \equiv N\pi a^3/6V$), and F_0 is the integration constant, independent of V. The Carnahan-Starling equation of state was derived from a fit to the first seven terms of a viral expansion, and deviates from results of molecular dynamics simulations by less than 0.5% when ϕ is less than 0.49. A comparison of the hard-sphere pressure and the ideal-gas pressure is provided in Fig. 3.5.

To account for the mixture of two different sizes, we note that the centers of the small spheres are excluded from the interior of shells of diameter $a_L + a_S$ centered at each large sphere (Fig. 3.6). Therefore the *effective* small-sphere volume fractions in the fluid and solid phases ($\tilde{\phi}_S^{fl}$ and $\tilde{\phi}_S^{sol}$) are greater than the real volume fractions:

$$\tilde{\phi}_S^{fl} \equiv \frac{N_S\pi a_S^3/6}{\xi V} = \frac{\phi_S^{fl}}{\xi}, \tag{3.12}$$

$$\tilde{\phi}_S^{sol} \equiv \frac{N_S\pi a_S^3/6}{(\xi+\gamma)V} = \frac{\phi_S^{sol}}{(\xi+\gamma)}, \tag{3.13}$$

where ξV and $(\xi+\gamma)V$, (defined below) are the volumes accessible to the centers of mass of the small spheres in the fluid and solid phases, respectively. Although these quantities depend on the number and positions of the large spheres, in a mean-field

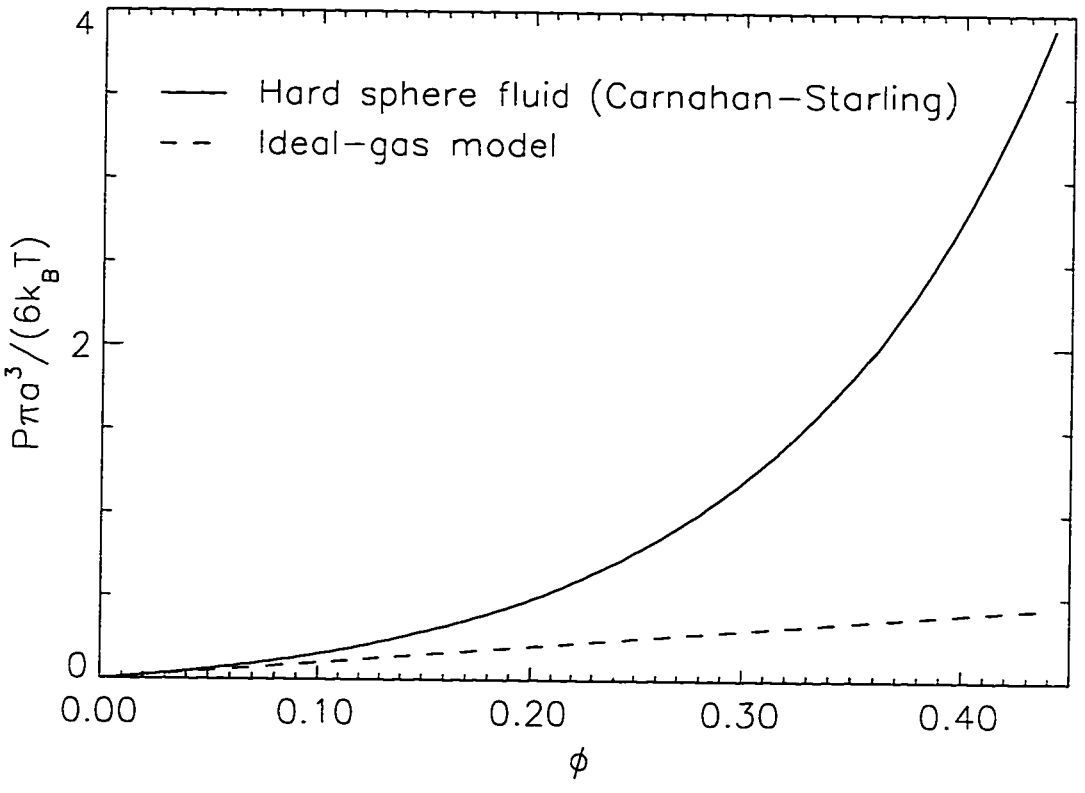

Figure 3.5: Plot of the dimensionless pressure as a function of volume fraction, comparing the ideal-gas and hard-sphere (Carnahan-Starling) results. The ideal-gas reduced pressure is ϕ, and the hard-sphere pressure is defined in the text. The finite size of the particles becomes important when $\phi > 0.05$.

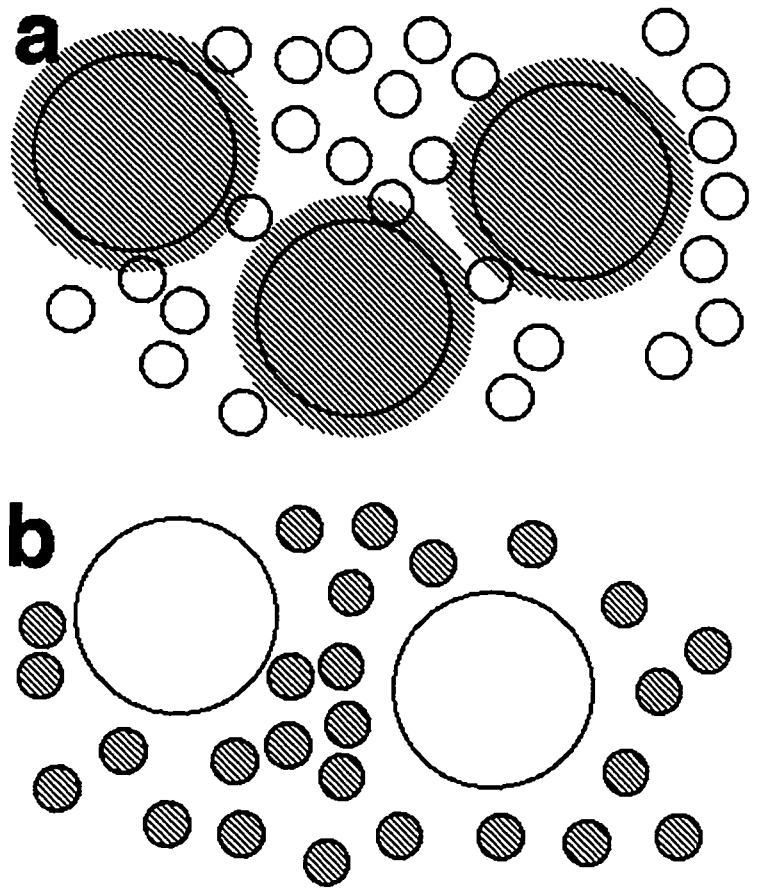

Figure 3.6: Cartoon showing how the effective volume fractions, $\tilde{\phi}_{L,S}$, are defined. (a) For the small spheres, the accessible volume is the total volume minus the hatched regions around each large sphere. (b) For the large spheres, the accessible volume is obtained by subtracting only the volume taken up by the small spheres.

approach they are assumed to depend only on ϕ_L. In the fluid phase, the large spheres are well separated, on average, so that the exclusion regions do not overlap and the accessible volume is the total volume minus the excluded-volume spheres of diameter $a_L + a_S$:

$$\xi = \frac{1}{V}(V - N_L \frac{\pi}{6}(a_L + a_S)^3) = 1 - \phi_L^{fl}(1 + \frac{1}{\alpha})^3. \tag{3.14}$$

In the solid (*i.e.* for $\phi_L >\approx 0.5$), the large spheres are close enough together so that the excluded-volume regions overlap (see figure 3.1(b)), thus *increasing* the volume accessible to the small-sphere centers of mass by the amount γV, and increasing the small spheres' entropy. Thus the term γ may be thought of as representing the driving (depletion) force of the phase separation.

$$\gamma = (N^{\text{bonds}})\frac{N_L}{V}V^{\text{overlap}} = 6\phi_L\left(1 + \frac{1}{\alpha} - \frac{r}{a_L}\right)^2\left(1 + \frac{1}{\alpha} + \frac{r}{2a_L}\right), \tag{3.15}$$

where V^{overlap} is the volume of the region of overlap of the two excluded-volume spheres (heavily shaded region in figure 3.1) and r is the separation between large-sphere centers in the lattice, $r/a_L = (0.7405/\phi_L)^{1/3}$. N^{bonds} is the number of "bonds" for each large sphere in the lattice, equal to half the number of nearest neighbors. For the close-packed lattice considered here, $N^{bonds} = 6$. In figure 3.4, we compare the volume accessible to the small spheres in the present theory to the free volume accessible to the small particles in the theory of Lekkerkerker *et al.* [71] (derived using the PY theory; see section 3.1). The two results agree closely except near closest packing, where the present theory predicts a 40% larger free volume, corresponding

to lower crystal free energy. This deviation is consistent with the fact that the PY approximation predicts no instability in the binary fluid phase.

Similarly, we define an effective volume fraction, $\tilde{\phi}_L^{fl}$, for the large spheres in the fluid phase. The volume accessible to the centers of the large spheres is λV, where λ accounts for the presence of the small spheres (Fig. 3.6):

$$\tilde{\phi}_L^{fl} \equiv \frac{N_L \pi a_L^3/6}{\lambda V} = \frac{\phi_L^{fl}}{\lambda}, \tag{3.16}$$

$$\lambda = \frac{1}{V}(V - N_S \pi a_S^3/6) = 1 - \phi_S^{fl}. \tag{3.17}$$

The small and large spheres are not treated equally in the above formulae for accessible volumes. The small spheres are excluded from the depletion zones around the large spheres, while the large spheres are excluded only from the volume taken up by the small spheres themselves. One argument in favor of this asymmetry is that, if we subtract spheres of diameter $a_L + a_S$ centered at each small sphere, the volume accessible to the large spheres is negative. The exclusion zones around the large spheres overlap one another extensively. Furthermore, the inherent asymmetry between small and large is illustrated by Fig. 3.7. A small sphere can be added to a large-sphere mixture without deformation. Inserting a large sphere into a small-sphere fluid, however, requires moving some small spheres *in order maintain the shape* of the large sphere. The scaled particle theory discussed below calculates the work that is done in rearranging the small spheres to make space for a large one [98].

Finally, to obtain F_L^{fl}, F_S^{fl}, and F_S^{sol}, we write the fluid free energy of equation

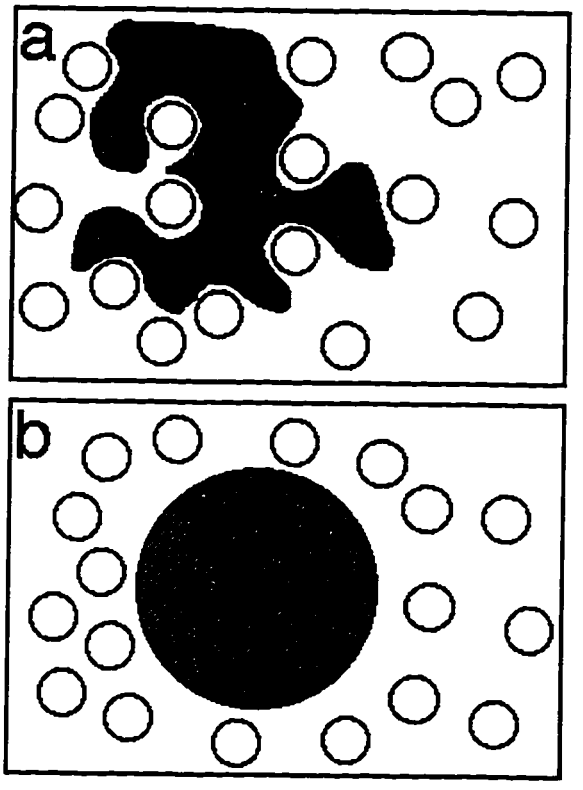

Figure 3.7: Cartoon showing the fundamental difference between inserting a large sphere into a small-sphere fluid and inserting a small sphere into a large-sphere fluid. When inserting a small sphere into a large-sphere fluid, no redistribution of the large spheres is needed. When inserting a large sphere, however, the large sphere must be deformed (a) or the small spheres must be rearranged (b).

(3.11) in terms of the effective volume fractions $\tilde{\phi}_L^{fl}$, $\tilde{\phi}_S^{fl}$, and $\tilde{\phi}_S^{sol}$. The osmotic pressure for each phase is given by the negative of the derivative of the total free energy with respect to volume. The chemical potentials are calculated by taking the derivative of the total free energy with respect to particle number, keeping in mind that $\tilde{\phi}_S$ depends on N_S *and* on N_L. Differentiation of the integration constant, $F_0(N,T)$ of equation (3.11), results in an additive constant, μ_0, in the chemical potential. Since the small spheres are a fluid in both phases, $\mu_{0,S}$ is the same in both solid and fluid phases and cancels out when the chemical potentials are set equal. For the large spheres, however, $\mu_{0,L}$ is different in the two phases. While μ_L^{sol} is completely determined by equation (3.8), we determine $\mu_{0,L}^{fl}$ by requiring that the chemical potential of the large spheres ($\phi_S = 0$) equal that of an ideal gas of large spheres as $\phi_L \to 0$. This extrapolation to the ideal-gas result gives $\mu_{0,L}^{fl} = \ln(6\Lambda^3/\pi a^3)$-4.

As a useful check of the above approach, we compare to the results of the scaled particle theory (SPT) of Lebowitz, Helfand and Praestgaard [98]. In SPT, one imagines adding a sphere of radius R_j to a mixture of spheres of radius R_i (see Fig. 3.7). The work necessary to create a spherical cavity of radius R_j can be calculated exactly in the limits of negative R_j and very large, positive R_j[4]. SPT interpolates between these two results, providing expressions for the chemical potentials, pressure, and contact-values of the radial distribution functions. The last two agree well

[4]SPT therefore also shows an asymmetry between small and large spheres. The functions μ_L and μ_S are not related by permutation of ϕ_S and $\phi_L$or any other simple quantities.

(or exactly) with, respectively, the PY theory and computer simulations.

The pressures and chemical potentials computed from scaled particle theory and the present theory (DYP) are compared in Figures 3.8 - 3.11. When $\alpha = 10$, the pressure is accurately described by the present theory when $\phi_L + \phi_S < 0.4$; agreement improves when $\alpha = 20$. The small-sphere chemical potential μ_S is also accurately described. The present theory slightly overestimates μ_L when $\phi_S$and $\phi_L$exceed $\approx$ 0.20. The present theory does not account for the redistribution of small spheres around the surfaces of each large sphere, which would tend to reduce the free energy (hence μ_L).

3.2.3 Equilibrium Conditions

For convenience, we define a dimension-less pressure, Π, which is the Carnahan-Starling pressure times the volume of a particle divided by k_BT:

$$\Pi(\phi) \equiv \frac{P^{C-S}\pi a^3/6}{k_B T} = \left(\frac{\phi + \phi^2 + \phi^3 - \phi^4}{(1-\phi)^3}\right). \tag{3.18}$$

The total osmotic pressures, $\mathrm{P}(\pi \mathrm{a}_L^3/6)/(\mathrm{k}_B\mathrm{T})$, in the fluid and solid phases must be equal:

$$\alpha^3\Pi(\tilde{\phi}_S^{fl}) + \Pi(\tilde{\phi}_L^{fl}) = -(\phi_L^{sol})^2\frac{\partial \ln v^*}{\partial \phi_L^{sol}} + \alpha^3\Pi(\tilde{\phi}_S^{sol})\left(\xi + \gamma - \phi_L^{sol}\frac{\partial(\xi+\gamma)}{\partial \phi_L^{sol}}\right). \tag{3.19}$$

The fluid pressure (LHS of equation (3.19)) is simply the sum of the pressures of the large and small particles in their effective volumes. In the solid-phase pressure (RHS),

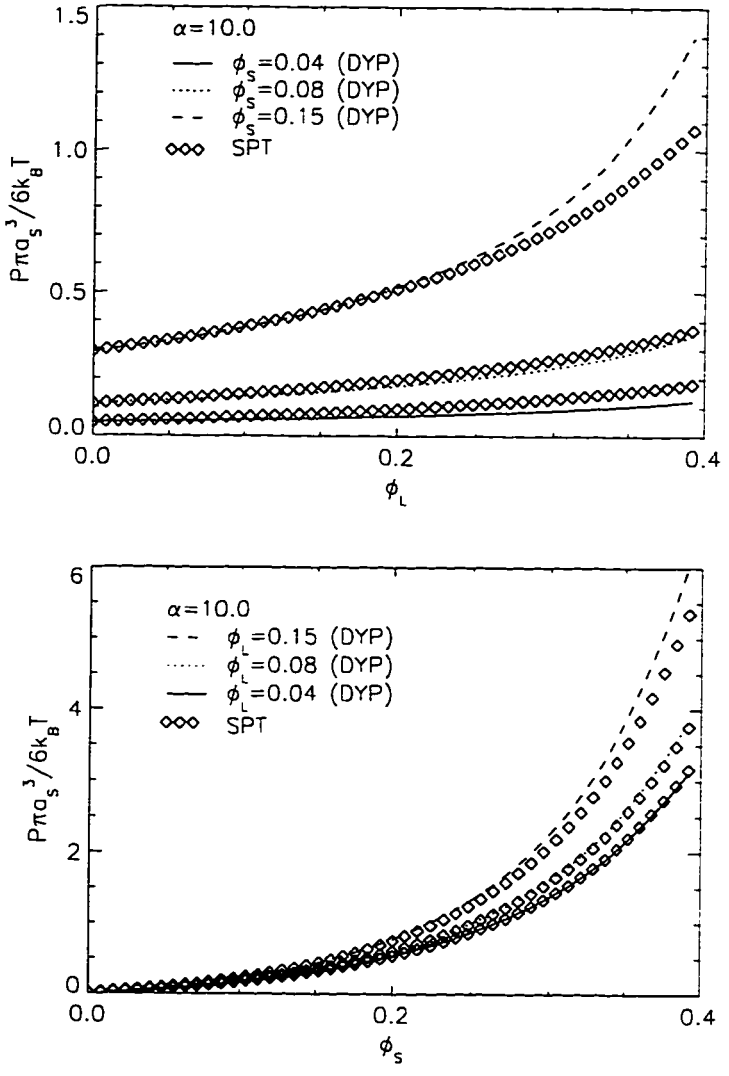

Figure 3.8: The (dimensionless) pressure of a binary hard-sphere fluid is plotted *vs.* $\phi_L$and ϕ_S, for a diameter ratio, $\alpha = 10.0$. The solid lines represent the present theory ("DYP") and the diamonds represent scaled-particle theory (SPT).

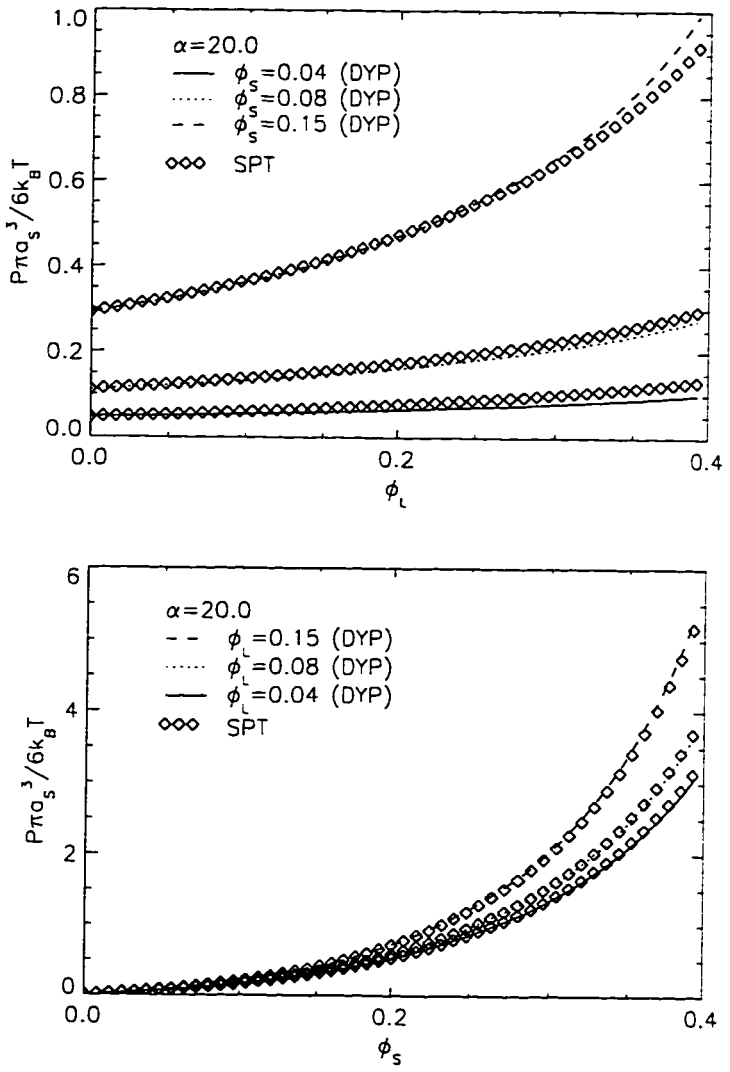

Figure 3.9: Same as the previous Figure, but with size ratio $\alpha = 20$.

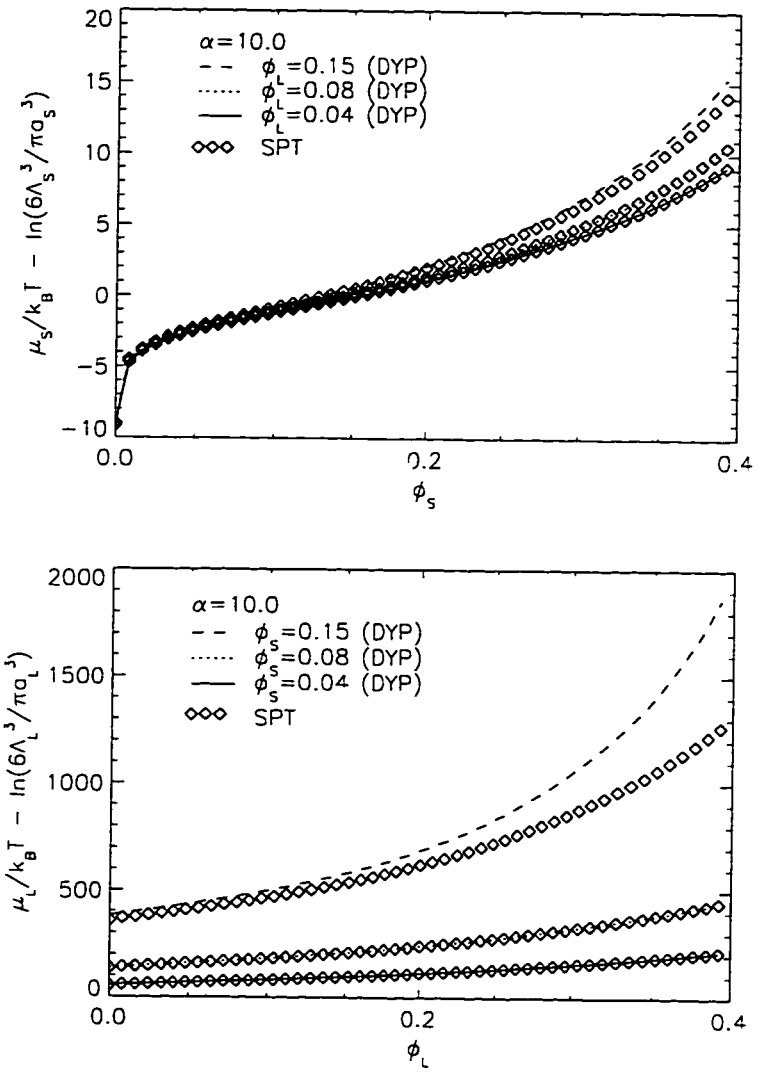

Figure 3.10: The chemical potentials of a binary hard-sphere fluid is plotted *vs.* $\phi_L$and ϕ_S, for a diameter ratio, $\alpha = 10.0$. The solid line represents the present theory ("DYP") and the diamonds represent the scaled-particle theory (SPT).

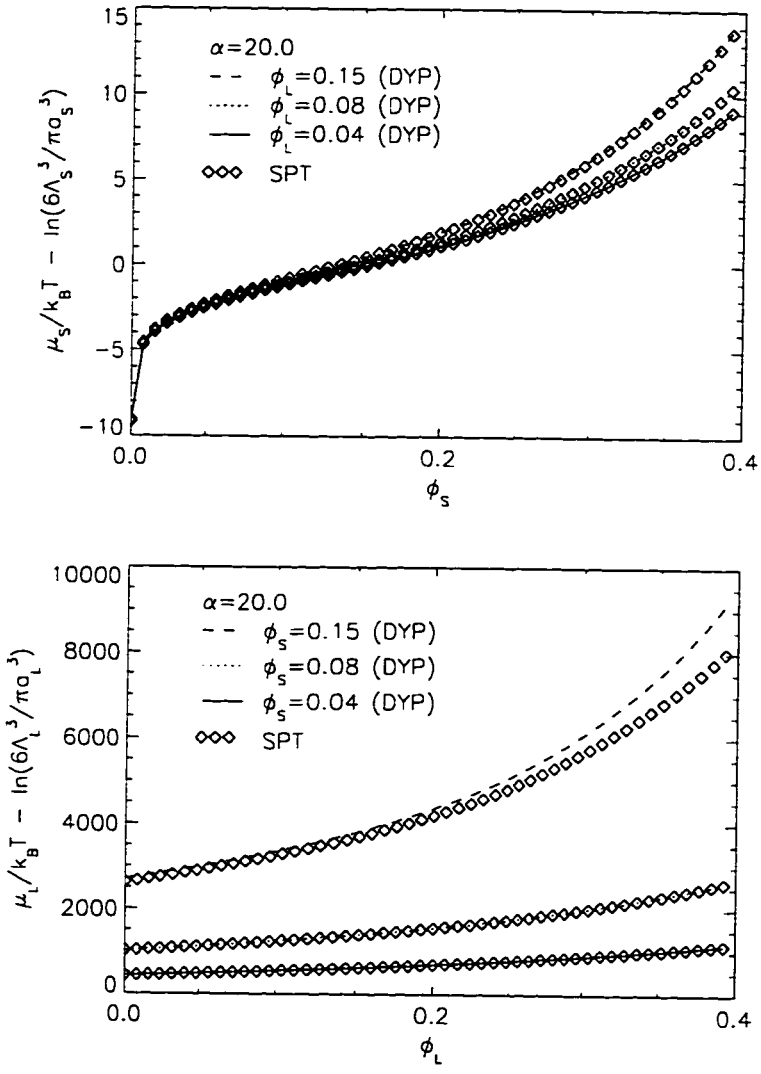

Figure 3.11: Same as the previous Figure, but with size ratio, $\alpha = 20$.

the first term represents the change of large-sphere free energy with volume, while the second term represents the effect that changes in ϕ_L have on the volume accessible to the small spheres, weighted by the pressure exerted by the small spheres.

The small-sphere chemical potentials, $\mu_S/k_B\mathrm{T}$, must be equal:

$$\frac{4-4\tilde{\phi}_S^{fl}+3(\tilde{\phi}_S^{fl})^2-(\tilde{\phi}_S^{fl})^3}{(1-\tilde{\phi}_S^{fl})^3}+\ln\tilde{\phi}_S^{fl}+\frac{1}{\alpha^3}\Pi(\tilde{\phi}_L^{fl})=\frac{4-4\tilde{\phi}_S^{sol}+3(\tilde{\phi}_S^{sol})^2-(\tilde{\phi}_S^{sol})^3}{(1-\tilde{\phi}_S^{sol})^3}+\ln\tilde{\phi}_S^{sol}. \tag{3.20}$$

The chemical potential in the fluid phase (LHS of equation (3.20)) has two terms due purely to the small spheres. The third term on the LHS accounts for the resistance of the large spheres against the addition of small spheres, which take up volume. The solid phase lacks the latter term because F_L^{sol} does not depend on the small-sphere concentration. Because the chemical potential does not have the same functional form in both phases, the reduced small-sphere volume fractions are not quite equal at equilibrium.

Finally, the large-sphere chemical potentials, $\mu_L/k_B\mathrm{T}$, must be equal[5]:

$$\begin{aligned}&\frac{4-4\tilde{\phi}_L^{fl}+3(\tilde{\phi}_L^{fl})^2-(\tilde{\phi}_L^{fl})^3}{(1-\tilde{\phi}_L^{fl})^3}+\ln\tilde{\phi}_L^{fl}-4-\alpha^3\frac{\partial\xi}{\partial\phi_L^{fl}}\Pi(\tilde{\phi}_S^{fl})\\&=-\ln\frac{v^*}{\pi a_L^3/6}-\alpha^3\frac{\partial(\xi+\gamma)}{\partial\phi_L^{sol}}\Pi(\tilde{\phi}_S^{sol})-\phi_L^{sol}\frac{\partial ln(v^*)}{\partial\phi_L^{sol}}.\end{aligned} \tag{3.21}$$

Here, the terms involving the derivatives of the free-volume coefficients account

[5]The last term in this equation was omitted when first published in Phys. Rev. E. All of the results in that paper, however, were calculated using the correct equation.

for the dependence on ϕ_L^{sol} of the volume accessible to the small spheres. The term containing $\partial\gamma/\partial\phi_L^{sol}$ represents the loss of free energy due to the excluded-volume overlap. This term "drives" the phase separation. The (-4) in the fluid-phase chemical potential comes from $\mu_{0,L}^{fl}$, defined above.

3.3 Results

We numerically solved these three equations for the volume fractions of coexisting phases at equilibrium. To obtain the solution, the numerical recipes routine amoeba.c was used to minimize the difference between the right- and left-hand sides of the equations by moving in the ϕ_S-ϕ_L plane [99]. Other techniques, such as the Newton-Raphson method fail to find solutions because some of the terms have very large derivatives. Solutions were verified graphically to make sure that they corresponded to minima in the free energy, not maxima. In figure 2.10 of the previous chapter, the calculated phase diagrams are presented along with the experimental data.

Our results for the monodisperse case (ϕ_S=0) agree closely with the results of computer simulations and experiments [31, 33, 39]. We predict the coexisting fluid and solid volume fractions to be 0.505 and 0.569, while the corresponding numbers from the computer simulations are 0.494 and 0.545. Considering that this theory is most reliable at low volume fractions, it is very reassuring (and perhaps simply lucky) that such good agreement is obtained.

A sample phase diagram is shown in Fig. 3.12(a) for $\alpha = 6.7$. At low total ϕ, the sample is a single binary fluid phase. At higher ϕ, some of the spheres form the solid phase, with fluid and solid volume fractions given by the end points of the tie lines. The present theory agrees well with the theory of Poon and Warren [75], despite the different approximations. The theoretical phase diagrams also agree reasonably well with our experimental results, especially for the higher values of α. When $\alpha < 10$, our measurements generally show that the solid phase is more difficult to form than predicted (*i.e.* it forms at higher ϕ_S than predicted). This trend may be due to the increased confinement of the small spheres as α is reduced. Although our model does account for the reduced volume available to the small spheres, we ignore the *shape* of this accessible volume, which becomes increasingly convoluted in the interstices of the solid phase as α decreases. We ignore the redistribution of the small spheres within these interstices (please refer to section 1.3.4, page 13). As will be discussed in the next chapter, the shape of a pore can influence the free energy even when ϕ is not changed.

Our assumption that the crystal contains no defects probably also underestimates the free energy, since the observed crystals had many such defects. Both of these assumptions could cause the present model to predict phase separation at volume fractions lower than those observed. The relatively large disagreement of theory and experiment for $\alpha = 6.7$ is at least partly due to the fact that the bulk-phase

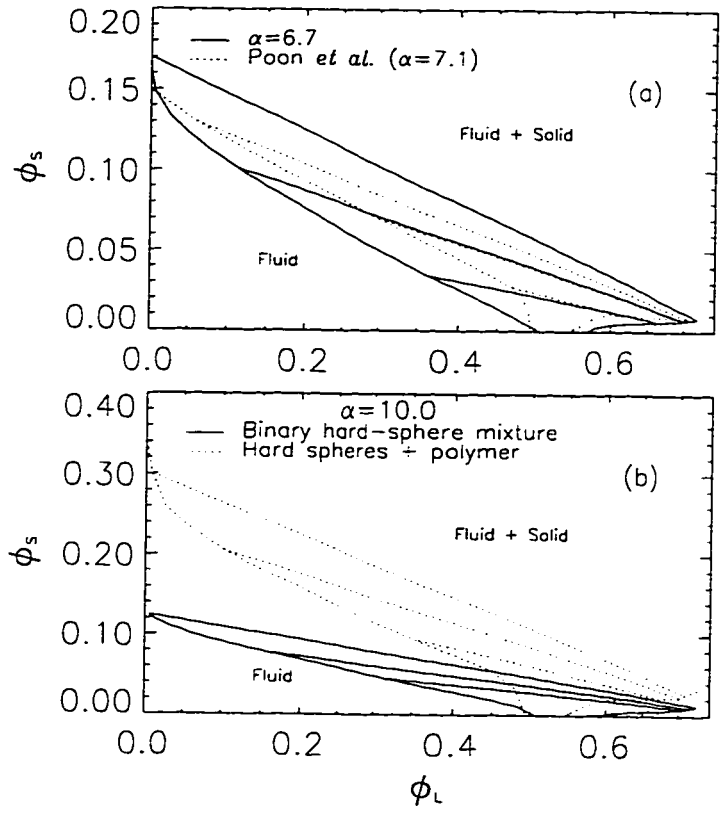

Figure 3.12: (a) A phase diagram calculated from the present theory (α =6.7, solid curves) is compared to that of Poon and Warren (α =7.1, dotted curves). In (a) and (b), the curved lines represent liquidus curves while the straight lines are tie lines whose end points correspond to the volume fractions of the coexisting solid and fluid phases at equilibrium. (b) A phase diagram calculated from the present theory (for binary hard-sphere mixtures) is compared to that of Lekkerkerker *et al.* (for mixtures of hard spheres and polymer). The hard-core repulsion of the small particles dramatically widens the region of instability of the fluid phase.

separation is pre-empted by the surface-phase separation. Our model predicts only the concentrations for which the bulk solid is stable with respect to the bulk fluid – we do not predict whether this bulk phase is metastable with respect to the surface solid. Possibly, in the region of "□" in figure 2(a), the surface solid phase forms and reduces ϕ_L in the bulk enough to make the bulk fluid phase stable. Finally, the slight non-ideality of the polystyrene spheres could explain the disagreement. The theory predicts that, in some samples, the 0.825 μm large spheres in the solid phase lie within 5 nm of one another. At such close range, the polystyrene spheres used in our experiments begin to repel one another due to the charges on the surfaces, thus competing with the depletion attraction. A correction for this effect could be incorporated into the model by including this interaction energy in the solid-phase free energy.

In Fig. 3.12 (b), the effect on the phase diagram due to the small particles' hard-core repulsion is revealed by a comparison of the results of the present approach to that of Lekkerkerker *et al.* [71], who consider mixtures of hard spheres with polymer. In the latter approach, the small particles are treated as an ideal gas, which has a pressure lower than that of a hard-sphere fluid of the same volume fraction (Fig. 3.5). As expected, the increased pressure exerted by the small spheres widens the fluid-solid coexistence region. In particular, with $\alpha = 10.0$, the hard-core repulsion of the small spheres lowers the values of ϕ_S along the liquidus curve by a factor of approximately

two.

3.4 Conclusions

I have presented a complete model of the fluid and solid phases of monodisperse and binary hard-sphere mixtures with size ratio, $\alpha, > 6.4$. Detailed comparison to scaled particle theory [98] and to computer simulations indicate that the present model is reasonably accurate for the range of volume fractions and particle sizes considered here. The results agree reasonably well with the measurements, suggesting that the basic physics is successfully captured in the model.

An advantage of this approach is that it can be extended to consider the stability of other phases, for example, binary crystal lattices or other structures that might arise in mixtures with $\alpha < 6$. The "cage volume" can be calculated for any lattice structure containing one or two species of particles. The theory can also be generalized to consider three-component mixtures such as the one shown in the photograph in the previous chapter (Fig. 2).

Chapter 4

Entropic Force Fields within Surface Microstructures

It is clear that the volume of a container can affect the thermodynamic state and the dynamics of a fixed number of particles within it. For example, decreasing the total volume of a colloid (by evaporating water) can cause colloidal crystals to form. In this chapter, the more subtle effects of the *shape* of a container will be investigated. All containers have surfaces; in small containers, the number of particles near the surface is comparable to the number in the bulk (Fig. 4.1). In such a case, many properties of the system as a whole – its freezing point, the distribution of particles within it, its viscosity, to name a few – are determined by the shape of the confining surfaces. The reader has already seen one example in this thesis: crystallization at the container's surface at volume fractions well below the bulk freezing point. Here we present the first demonstrations of a very fundamental and general mechanism at work among complex fluids in porous media and, we suspect, inside cells. Specifically, we have measured forces on the larger spheres that arise in binary hard-sphere mixtures in

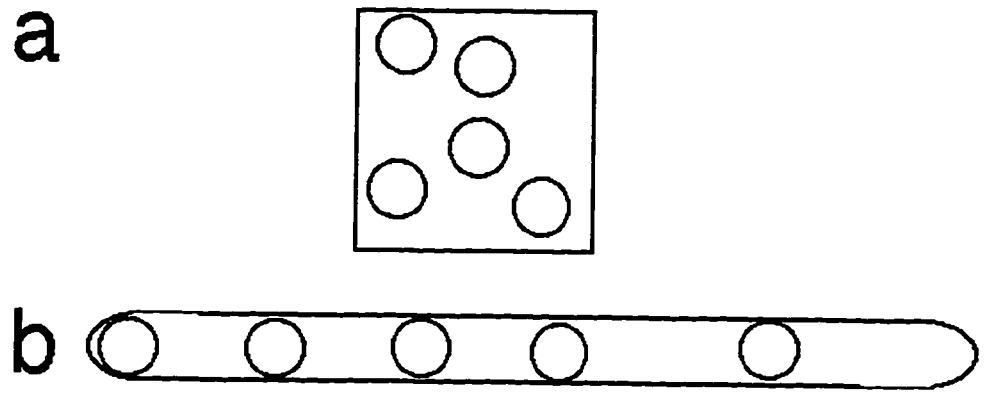

Figure 4.1: In sample containers with equal volumes but different shapes, the behavior of the particles can be very different. In (a), relatively few of the particles are within one sphere diameter of the surface. In (b), all of the particles are near the surface. In (b), excluded-volume (depletion) forces are likely to be important.

the presence of hard walls with various shapes ("microstructures"). There are no enthalpic interactions. The essential point is that these surface forces arise purely from excluded-volume effects when many particles are mixed together.

In addition to providing insight into the fundamental entropic effects of surfaces, these experiments suggest a novel application of depletion forces. In contrast to the previous work in bulk systems, we report the first use of the depletion mechanism to create *directional* entropic forces at *specific positions* in the sample. These "entropic force fields" can be used to trap or to impose directional flow on the macromolecules. Particles can be precisely positioned on a substrate in predetermined patterns or can be made to move in a deterministic way. Paradoxically, this control is accompanied by an *increase* of the total entropy[1].

[1] Although the larger spheres can be ordered or manipulated, there is no work done on the system

Control of submicron particles in suspension is of considerable technological importance. For example, improvements in our ability to manipulate particles are desirable to make devices requiring highly-ordered particle arrays, such as filters, efficient latex immunoassays [100], and photonic band-gap materials [101, 102, 103, 104, 105]. In addition, an understanding of the motions of small particles in the presence of complex geometries provides valuable insight into more complex systems, such as proteins inside cells [106, 107, 108].

The size of these particles and microstrucures is comparable to length scales accessible with modern silicon-processing techniques. Research along these lines promises a productive integration of techniques and materials from semiconductor and colloid technologies. The present work has benefited greatly from collaboration with experts in scanning-electron-microscope lithography techniques (see Chapters 6 and 7). A different technique that uses electron-beam lithography to make ordered particle arrays will also be presented in Chapter 6.

In this chapter, I describe experiments that demonstrate and measure entropic force fields that arise in the presence of three different microstructures. In the first case, the large sphere is repelled from the edge of a terrace by a free-energy barrier approximately $2k_BT$ in magnitude (section 4.1) [109]. In the second, it is confined to the inside of a corner (section 4.2) [110]. The third case, motion induced along a wall

and the second law of thermodynamics is not violated.

of continuously changing curvature, will be discussed in detail in the next chapter.

4.1 Repulsion from the Edge of a Terrace

In our first demonstration [109], we have studied the reflection of a submicron sphere from a step edge, as shown in Fig. 4.2. The smaller spheres push the larger spheres away from the edge of the cliff!

4.1.1 Measurement of a Free Energy Barrier

A transparent glass cell approximately 100 μm thick contained an aqueous suspension of nearly-hard-sphere polystyrene particles with diameters 0.46 μm and 0.083 μm and volume fractions (ϕ_L and ϕ_S) 10^{-5} and 0.30, respectively. Because ϕ_L was so small, the large spheres were an average of several microns apart and did not interact with one another. NaCl (0.01M) was added to screen out sphere-wall electrostatic interactions over a distance of approximately 5 nm [73, 20] to obtain nearly ideal hard-core interactions. The effects of gravity were negligible due to the small sizes of the particles. A glass cover slip with polished surfaces provided the smooth terrace and step edge inside the cell. As shown in chapter 2, the small spheres induce a depletion attraction between the large spheres and the wall. Thus, a large sphere placed on the terrace diffused on the surface for many seconds before escaping to the bulk. By following the two-dimensional trajectories of these large spheres, we

measured the forces acting on them near the step edge.

A laser trap [111, 112, 113, 114, 115] was used to grab a single large sphere and place it on the terrace at a fixed distance of 0.56 ± 0.06 μm from the step edge (Fig. 4.2(b)). The trapping power was provided by a Nd:YLF laser (1053 nm) in CW mode, with $\approx$ 5 mW of power into the objective. Further details of the optics are provided in Chapter 7. After the large sphere was positioned manually, the computer took control of the experiment. An macro written to run within NIH Image software controlled all of the electronics. The edge of the terrace was first determined to within $\approx$ 0.5 pixels by comparing the light intensity profile across the edge to the known intensity at the edge of an opaque screen. Very similar results were obtained by finding edge of a sphere that was pushed against the cliff edge with the laser trap. The macro then measured the position of a "fiducial mark" (a polystyrene sphere stuck irreversibly to the wall) in order to account for drift of the microscope stage. A region of interest (ROI) ($\approx$ 10 μm on an edge) was defined by computer, positioned so that the origin of the ROI was located a known distance from the edge. The laser trap was then blocked by a mechanical shutter and the motions of the diffusing sphere were followed. We used a 100x objective (Zeiss Plan-Neofluar, numerical aperture =1.3) with differential interference contrast (DIC) image enhancement and 1.6x "optovar" tube lens. Images were captured in real time using a charge-coupled-device (CCD) camera. At this magnification, one camera pixel corresponded to 0.080 μm. Only the

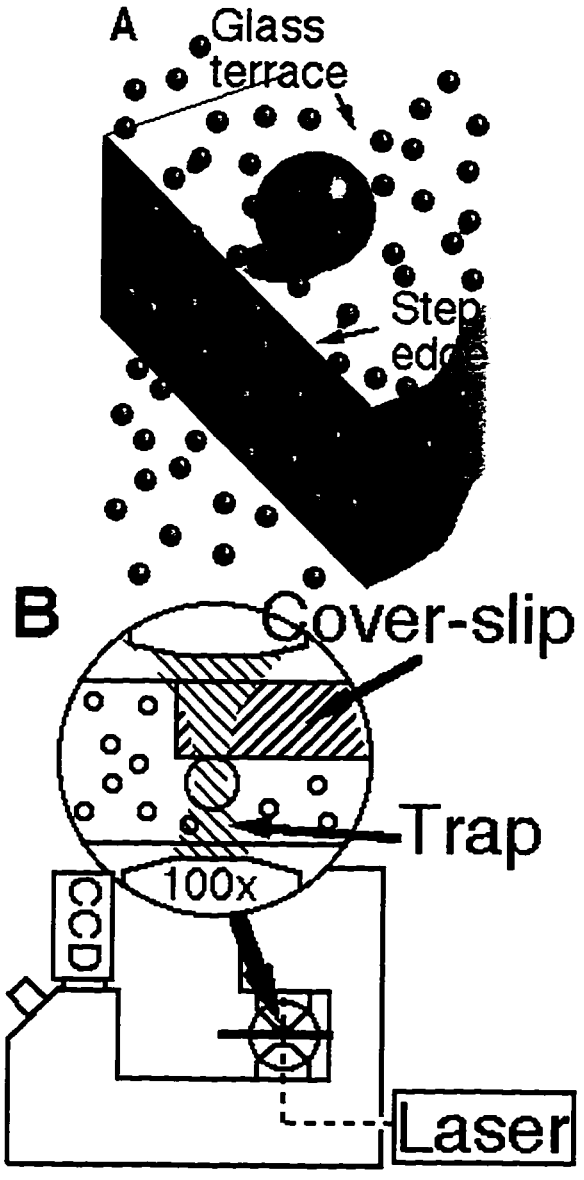

Figure 4.2: (a) Drawing of a single large sphere near the edge of a terrace, representing the geometry of our experiment. The surrounding small spheres cause the large sphere to move in two dimensions on the surface and to be repelled from the step edge. (b) Schematic diagram of the inverted optical microscope, laser trap, and sample cell used in the experiment.

image-sections within the ROI were saved on the computer.

To obtain the data shown here, we repeated the trap-release process approximately 1400 times. Images 0.1 s apart were processed and the the center-of-mass large-sphere positions were measured with a precision of approximately 0.04 μm (0.5 CCD pixels). The total number of particles in view was 1388 after 0.1 s but decreased by 33% over four seconds due to escape of the spheres vertically from the flat surface into the bulk. In the course of collecting the data shown here, we used several different 0.46-μm spheres and different sample cells and always obtained similar results.

We quantified the effect of the step edge by measuring directly the Helmholtz free energy, F, of the system as a function of the distance of the large sphere from the step edge (Fig. 4.3). From our measurements of the large-sphere trajectories, we proceeded according to a technique invented by Crocker and Grier [78]. We first measured the probabilities, $P_{ij}(\tau)$, that the large sphere jumped from the jth the ith spatial bin during a time interval of length τ (0.1, 0.2, or 0.3 s). The $P_{ij}(\tau)$ values are independent of the initial conditions, and thus depend only on the system itself. In particular, the ith component of the eigenvector of the matrix $P(\tau)$ with unit eigenvalue is proportional to e^{-F_i/k_BT}, where F_i is the Helmholtz free energy evaluated at the ith bin. (For details of this analysis technique, see Chapter 7.) The force on the large sphere points in the direction of decreasing F with magnitude given by the gradient of F. To show the effect of the step edge on particle motions, we

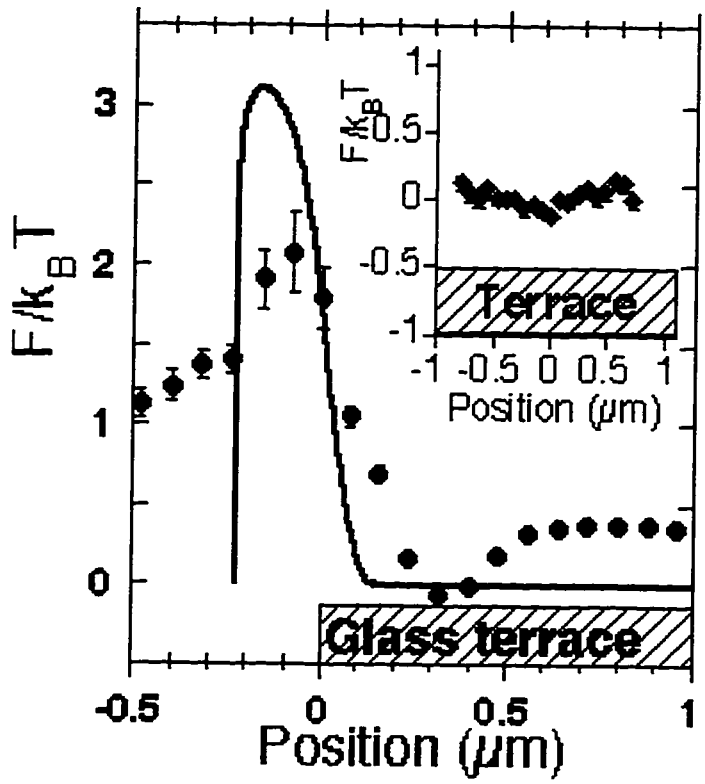

Figure 4.3: The measured free energy of the mixture in units of the thermal energy, F/k_BT, as a function of the distance of a large sphere from the step edge located at zero. The circles represent measurements and the solid curve was calculated using the ideal-gas depletion theory described in the text. (Inset) F/k_BT *vs.* large-sphere position in the direction parallel to the edge. There is no barrier.

also present histograms of the large-sphere positions at two times: 0.1 s after release and 4.1 s after release (Fig. 4.4). The height of each data point gives the number of events in which the sphere was observed inside a 0.12 μm bin centered at that point. These plots therefore represent the probability distribution of the large sphere along the surface.

Our results clearly indicate free diffusion along the direction parallel to the step

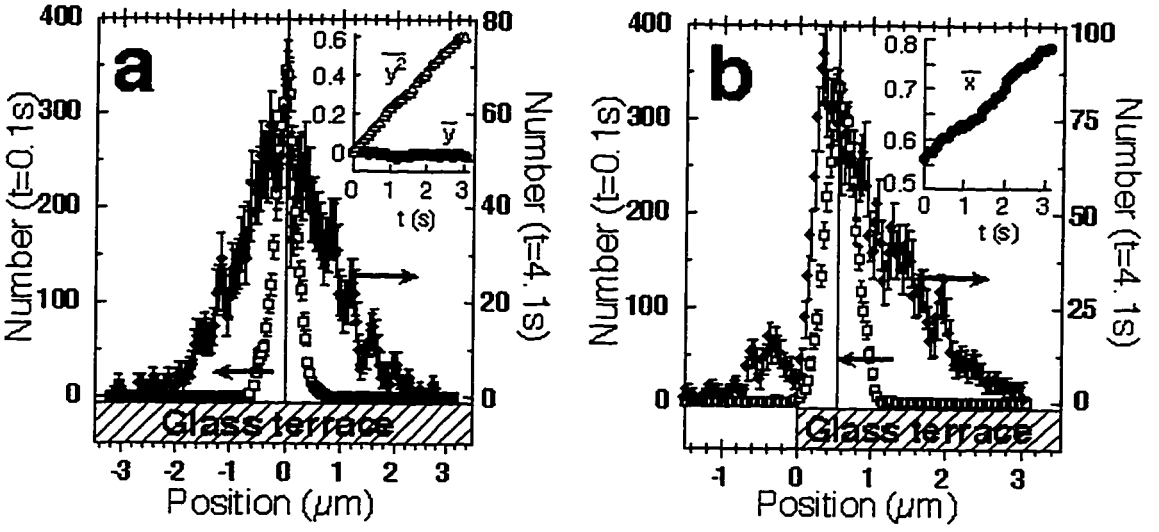

Figure 4.4: (a) Measured probability distributions of a single large sphere in the direction parallel to the step edge at two different times after release from position zero. Hollow squares (left axis): 0.1 s; filled diamonds (right axis): 4.1 s. (Inset) Upper curve: measured mean-square position, $\bar{y^2}$ (μm^2), *vs.* time, t (seconds), after release. Lower curve: mean position, $\bar{y}$(μm). Error bars are smaller than the plot symbols. (b) Measured probability distributions at the same times for motion perpendicular to the step edge. The vertical line indicates the starting position, 0.56 μm. (Inset) Plot of the mean position, $\bar{x}$(μm), vs. t. These results demonstrate reflection of the sphere from the edge of the terrace.

edge: the free energy was constant (inset of Fig. 4.3). Furthermore, the mean position, $\bar{y}$ (inset of Fig. 4.4), remained zero at all times and the probability distribution remained symmetric about the starting position (zero). The mean-square position, $\bar{y^2}$, was proportional to time, as is characteristic of diffusion in one dimension. From the slope of the plot of $\bar{y^2}$ *vs.* t, we found that the diffusion coefficient, D, was 0.10 $\mu m^2/s$. The diffusion is slower by a factor of approximately 5 compared to the bulk value, due to hydrodynamic friction when the sphere is very close to the wall. Thus, the presence of small spheres and surfaces drastically reduces the mobility of the larger spheres.

Perpendicular to the edge, however, there was a pronounced free-energy *barrier* approximately $2k_BT$ in magnitude, located at the step edge. Thus, as a particle moved toward the edge, the free energy of the system increased, resulting in a force of approximately 0.04×10^{-12} Newtons pushing the particle back away from the edge. The probability distributions illustrate the effect of this barrier on particle motion. First, the distribution was asymmetric after 4.1 s, decreasing dramatically to the left of the edge because few of the particles were able to "escape" laterally across the edge of the terrace. The observed non-zero escape probability is an expected result of thermal fluctuations (see [116] and the excellent article by S. Chandrasekhar in [8]). Second, the peak of the probability distribution shifted from the starting point toward the edge where the large spheres accumulated. If the barrier did not exist (i.e.

if the large spheres simply diffused freely across the edge and disappeared from view), the probability-distribution peak would have shifted to the *right*, instead of to the left as shown in Fig. 4.4(b). Third, the mean particle position, $\bar{x}$, increased (moved away from the edge) with time because the particles were repelled from positions less than zero. We point out that the small dip in the free energy and the small peak in the late-time probability distribution near -0.23 μm correspond to spheres that escaped across the barrier and adhered to the vertical surface of the step. Finally, the origin of the shallow free-energy minimum located 0.3 μm to the right of the edge is uncertain but may result from a non-uniformity in the small-sphere concentration induced by the step edge.

As a crude comparison to the histogram in Fig. 4.4 (b), one can calculate exactly the distribution of a particle diffusing near a perfectly reflecting wall (*i.e.* an infinite potential) located at $x = 0$ (Fig. 4.5). The solution is a Gaussian function centered at the starting point, x_0 *minus* a Gaussian centered at $-x_0$. This solution (not properly normalized) is plotted using the measured diffusion constant 0.1 and 4.1 s after release of the particle from $x = 0.56$ μm, as in the experiment. The distribution becomes asymmetric and the peak shifts *toward* the barrier, very similar to Fig. 4.4(b).

We stress that the lifetime of large spheres on the surface depends *only* on the concentration of small spheres. In a sample with small-sphere volume fraction reduced by a factor of 2 (to 0.15), the average lifetime of a large sphere on the surface

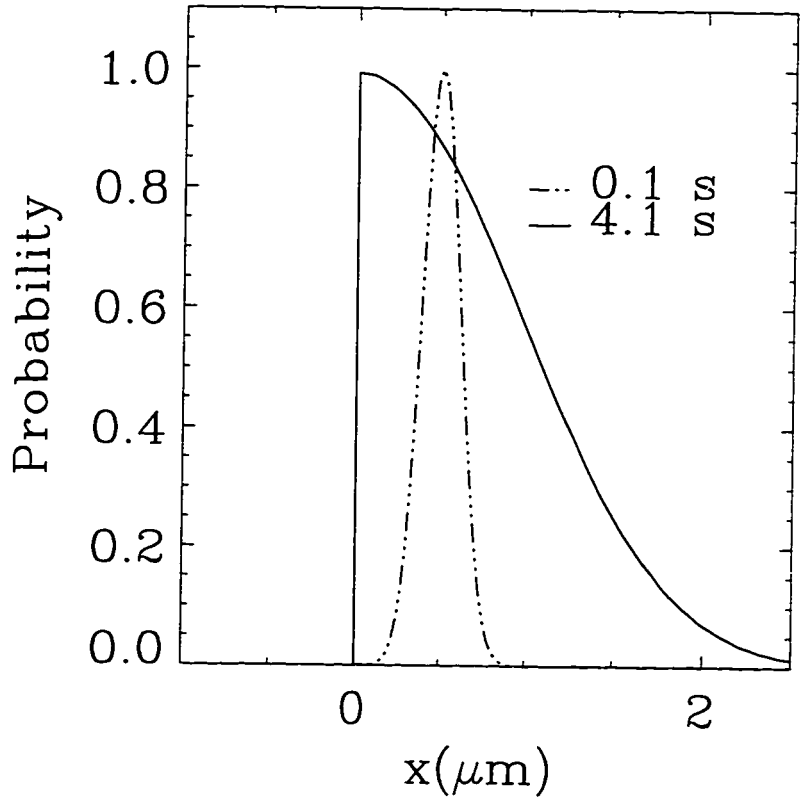

Figure 4.5: Exact calculation of the probability distributions of a particle diffusing near an infinitely-repulsive wall located at $x = 0$.

was reduced by a factor of 3. Since other interactions (e.g. electrostatic, van der Waals, or hydration forces) are not expected to depend strongly on the small-sphere concentration, we concluded that they are much too weak to account for the forces measured here. Further evidence of the nearly-ideal hard-core interactions in this experiment can be found in [73].

4.1.2 Comparison to Theory

We can explain the repulsive force field measured in the experiment using the depletion force theory described in the previous chapters. Recall that the centers of mass of the small spheres cannot approach within one radius of the walls or the large-sphere surfaces. When a large sphere is next to the flat wall, the exclusion zones overlap, thereby increasing the volume accessible to the small spheres (hence their entropy). The depletion force holds the large sphere against the surface, along which it diffuses in (approximately) two dimensions. When the large sphere protrudes past the edge, however, the excluded-volume overlap and entropy decrease – the free energy increases (Fig. 4.6). This free-energy gradient is equivalent to a *force* of approximately 10^{-12} Newtons pushing a large sphere along the wall, away from the edge. From another point of view, when the large sphere protrudes past the edge, a small piece of its surface area (ΔA) becomes exposed to collisions with the small spheres. In the ideal gas approximation, the resulting force is given by $P_S\ \Delta A$.

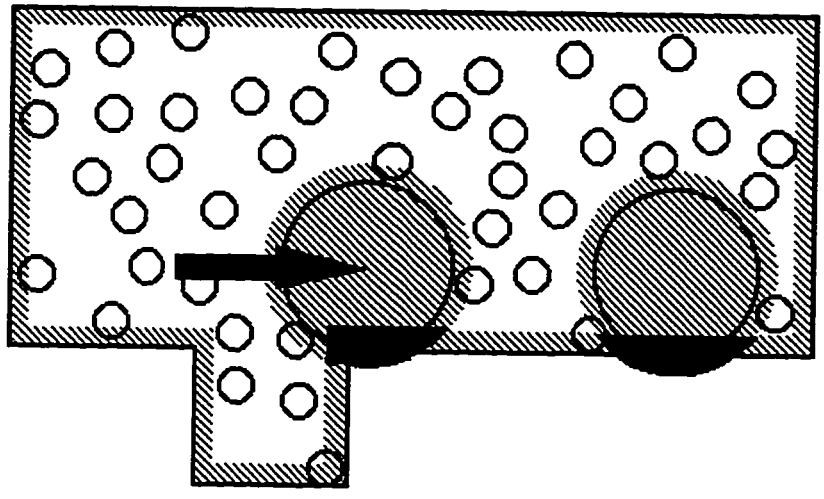

Figure 4.6: Illustration of the origin of the step-edge repulsion. As in Chapter 1, the centers of the small spheres are excluded from the hatched regions along the wall and along the large-sphere surfaces. When a large sphere is next to the flat section of the wall, the excluded-volume overlap (black region) and entropy are maximized. When the large sphere protrudes over a trench, the overlap *decreases*, so that the sphere is repelled from the edge as indicated by the arrow.

For comparison to our results, we have calculated the Helmholtz free energy, F, of the sample as a function of the distance of a single 0.46-μm sphere from the edge, considering only the entropic excluded-volume effect. The small spheres were treated as an ideal gas with volume fraction 0.3. The ideal gas approximation has been found to estimate accurately the contact value of the depletion energy [26].

There is a substantial free-energy barrier at the edge with a magnitude which depends on the trajectory one assumes for the large sphere. If one assumes that the sphere clings to the surface as it moves down *around the corner* of the step edge, the free energy increases to approximately $3k_BT$ at the edge, then returns to zero at -0.23 μm, where the sphere lies on the vertical surface (solid curve, Fig. 4.3. By contrast, if one assumes that the sphere moves at constant height, starting on the terrace far from the edge and moving horizontally past the edge, the free energy barrier exceeds $5k_BT$ (not shown). When the large sphere is slightly *above* the terrace, the magnitude of the barrier is reduced because the excluded-volume overlap is smaller. The fact that some of the particles in the experiment were slightly above the surface could explain why the measured barrier is less than $3k_BT$. The fact that the measured free energy does not return to zero to the left of the step at -0.23 μm simply reflects our observation that some of the particles escaped into the bulk (where $F \approx 5k_BT$) while others adhered to the vertical surface of the step (where $F \equiv 0$).

In Fig. 4.7, the magnitude of this step-edge barrier is plotted for all large-sphere

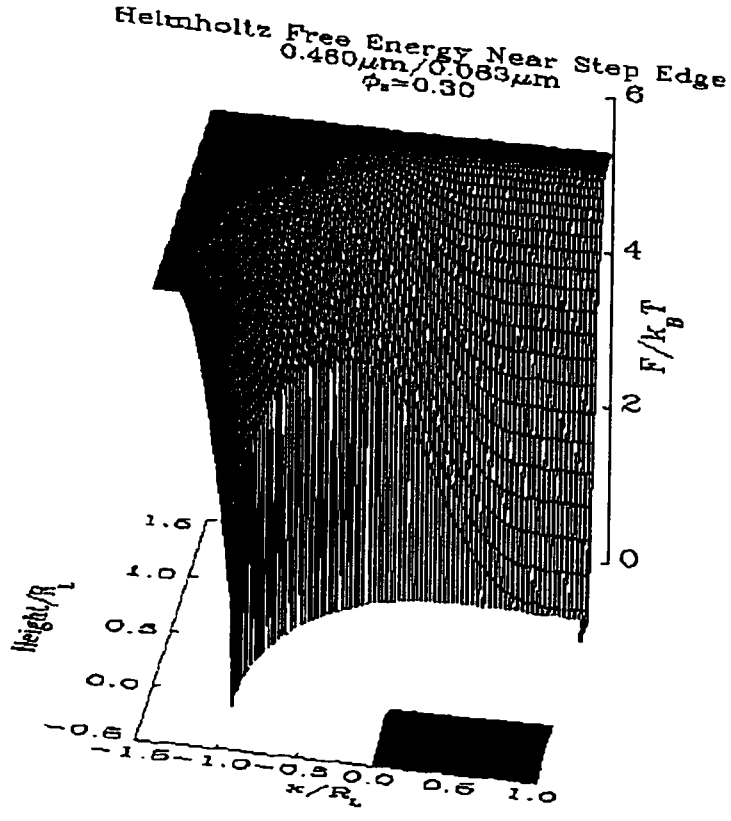

Figure 4.7: Surface plot of predicted free energy *vs.* position of the large sphere's center. The ideal gas approximation was used, with ϕ_S=0.30 and $a_L/\ a_S$= 5.7. R_L is the radius of the large sphere. The black region is the step edge and the particle cannot explore the white region which is within R_L of the wall.

positions. In the figure, the corner of the terrace is located at (0,0) (shown in black). The center of the large sphere is excluded from all points within one radius of the terrace (shown in white).

4.1.3 Conclusions

This experiment has provided the first measurement of the depletion potential *vs.* large-sphere position in a binary hard-sphere mixture. More important, perhaps, is the demonstration that these depletion effects can have dramatic, if unexpected, effects at edges.

4.2 Confinement to a Corner

One can also design surface microstructures that will *trap* particles instead of repelling them. The simplest example is a corner, where the exclusion zone around a large sphere will overlap with *two* walls. In order for the large sphere to diffuse away from the corner, it must lose its overlap with (at least) one wall. Just as the large spheres were loosely confined to a planar wall by the depletion force, they can be confined to diffuse along a one-dimensional *line* at a corner (Fig. 4.8).

The dynamics and thermodynamics of such a "quasi-" one-dimensional system can be quite different from a two- or three-dimensional system. Furthermore, since the equilibrium particle density is higher in the corner, one might expect that nu-

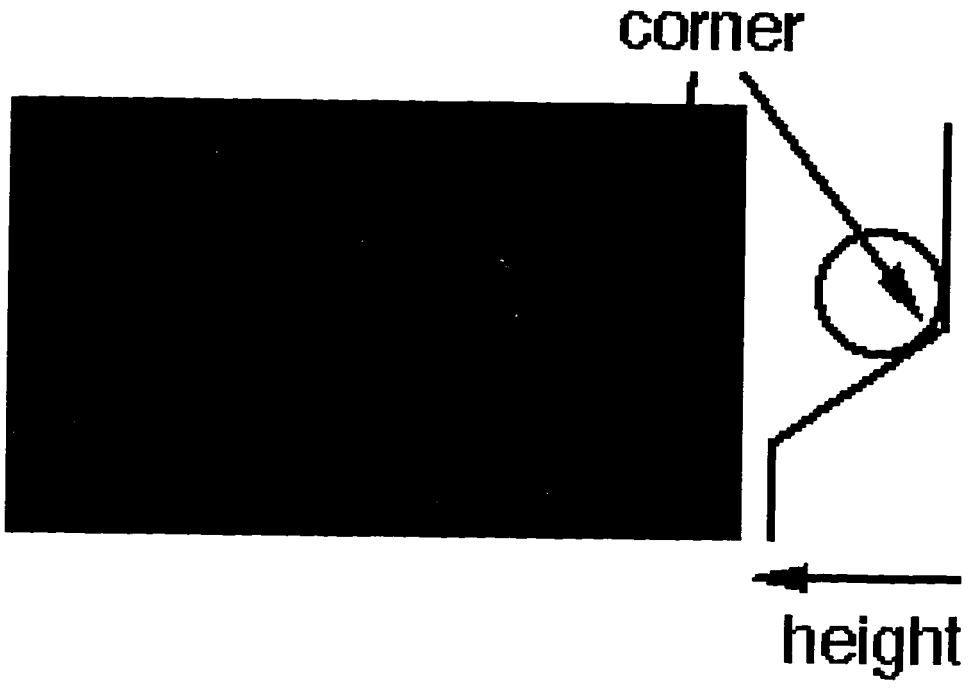

Figure 4.8: Optical micrograph of 0.474-μm spheres (ϕ_L=0.03) that are diffusing along the line of a corner. They are pinned there by the (invisible) small spheres (0.083 μm, ϕ_S=0.27). The nearly white horizontal streak is the line of the corner, illustrated in cross-section to the right of the figure.

cleation would occur there at lower ϕ_S, just nucleation along a wall occurs at lower ϕ_S than in the bulk (see Chapter 2, Section 2.4.2, page 61). The optical micrograph in Fig. 4.9 demonstrates this "prefreezing" in the corner. Here, we observed nucleation of crystallites in corners, but not at the flat surface or in the bulk. The geometric constraint of the wall could also force nucleation of crystallites that are more ordered than those growing on a plane. Finally, the corner aligns the crystals with respect to the axis normal to the plane, a potentially useful feature when making ordered particle arrays.

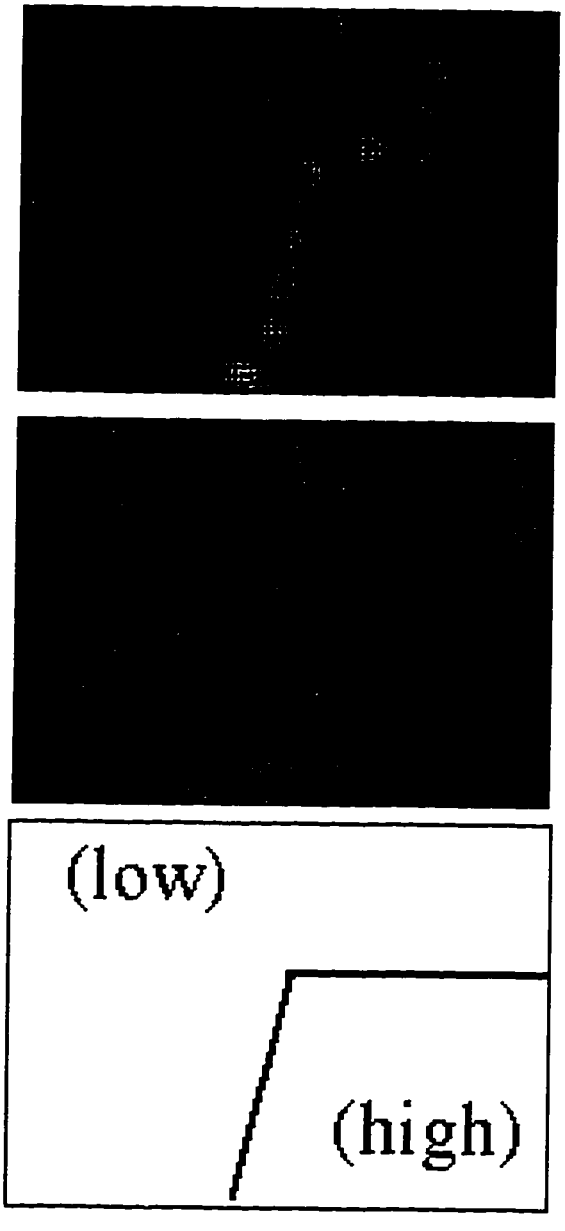

Figure 4.9: Optical micrograph of the 0.474-μm spheres (ϕ_L=0.03) in a mixture also containing smaller spheres (a_S=0.083 μm, ϕ_S=0.27). The spheres are on the surface of a silicon substrate, the contour of which is illustrated in the bottom panel. The first two panels are separated by 10 minutes. Nucleation of the larger spheres occurs along the corner, but not on the flat surface or in the bulk.

This section presents the first demonstration of depletion-confinement of large spheres in a corner [110]. We have also measured the ϕ_S-dependence of the depletion free energy. Here, the goal was to discover whether assuming that the small spheres are an ideal gas accurately describes the ϕ_S-dependence of the confinement potential. We found that the hard-sphere (rather than the ideal-gas) model is, in this case, more accurate. We have quantified the depletion energy in three samples which had different values of ϕ_S. I will first describe the procedure used to measure the average time a particle spends in the corner "trap" (section 4.2.1), then show how this gives us the depth of the depletion potential (section 4.2.2).

4.2.1 Measurements of Lifetimes

To quantify the strength of the corner attraction, we have measured the average lifetimes of the large spheres in a corner. We prepared three samples with a_L, a_S= 0.474, 0.083 μm, [NaCl] = 0.01 M, ϕ_L= 0.015 , and ϕ_S= 0.249, 0.260, and 0.285. We injected $\approx$ 0.30 mL of solution into a sample cell that included a piece of silicon substrate, glued to the slide with the bottom side exposed (Fig. 4.10(a)). The silicon substrate was simply a small (100 mm x 100 mm) piece of a wafer which had the (100) axis normal to the top (polished) surface. The bottoms of such wafers are covered with naturally-occurring truncated pyramids formed by the intersections of smooth Si crystal planes. These pyramids conveniently provided a large number of

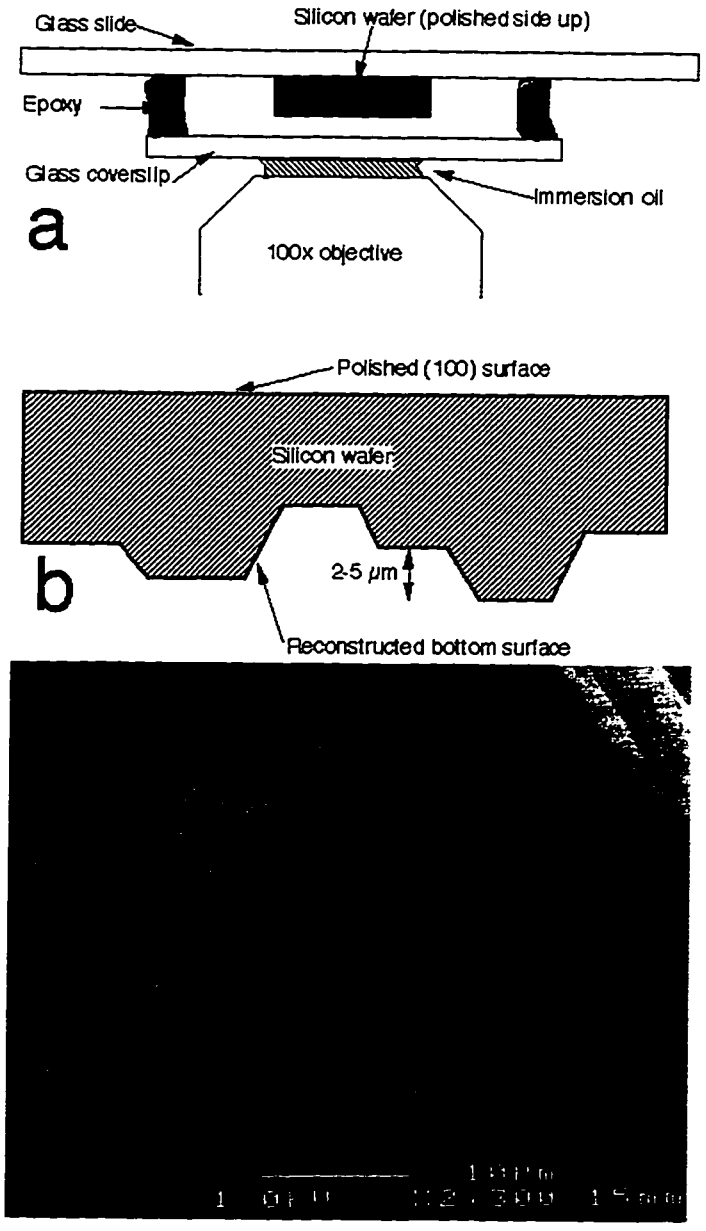

Figure 4.10: (a) Schematic diagram of sample cell and imaging geometry used to study the diffusion of polystyrene spheres near corners. Figure (b) shows a cartoon of the magnified cross-section of the silicon wafer, which is covered with microscopic truncated pyramids that provide sharp corners. The bottom figure is a scanning-electron micrograph of a (dirty) silicon surface.

corners with an open angle of $\approx 150°$ (Fig. 4.10(b)). In the experiment, a large sphere diffusing along the corner was chosen at random and a stopwatch was started. As soon as the sphere in question diffused away from the surface ("escaped"), the stopwatch was stopped and the time written down. The sphere was considered to have escaped when it had ventured a distance roughly equal to its radius from the corner *or* when its diffusivity suddenly increased. The latter criterion (used by Kaplan *et al.* [21] to distinguish particles at the surface from those in the bulk) relies on the dramatic decrease in hydrodynamic friction when the sphere moves away from the corner. Lifetimes were taken for 100-200 events in each of the four samples.

There is an attraction between the silicon surface and the large particles that is not due to depletion, but rather to electrostatic effects. We discovered this other force by measuring the diffusion coefficient, D, of an isolated large sphere in a binary mixture[2] (a_L, a_S = 0.460, 0.083 μm; ϕ_L, ϕ_S = 8.5x10^{-5}, 0.251) with four different concentrations of NaCl between 0.008 M and 0.08 M. On a *glass* substrate, the four values of D are the same within uncertainty (Fig. 4.11). On a silicon surface, however, D increases roughly linearly with [NaCl]. A likely explanation for this result is that there is an electrostatic attraction between the dipole cloud around the large sphere and the image of the cloud in the silicon (for a discussion of image charges, see Chapter 2 of [117]). As [NaCl] is increased, the magnitude of this attraction (which is assumed

[2]The small spheres served to keep the large spheres near the surface.

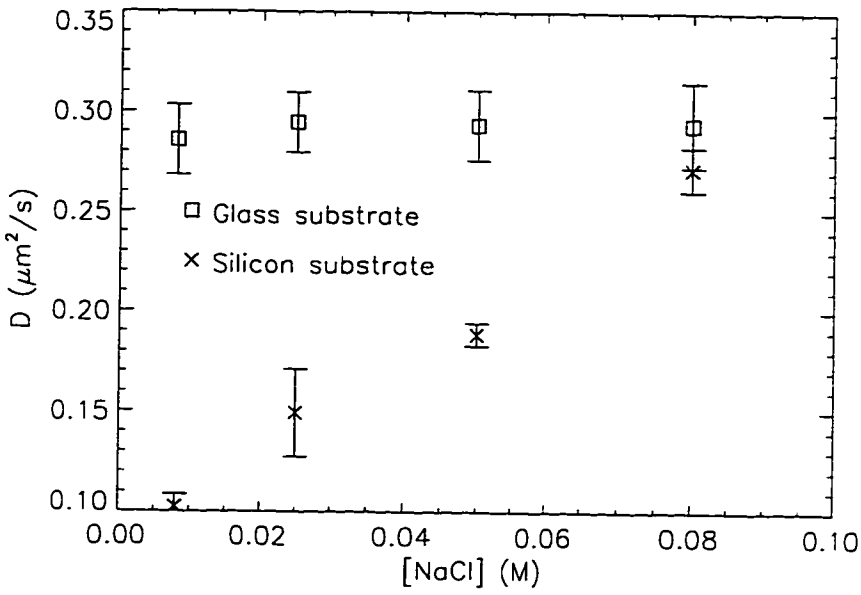

Figure 4.11: Measured diffusion coefficient (D) *vs.* salt concentration on glass and on silicon. The diffusion coefficient is independent of [NaCl] on glass, but not on silicon.

to follow the Debye-Huckel law) is decreased. Thus, at low [NaCl], the sphere was held close to the surface; at higher [NaCl], the sphere was farther from the surface. In the latter case, the hydrodynamic friction was reduced and D was increased. We expect that this electrostatic effect does not depend on ϕ_S. Therefore, as long as we are looking at the *functional dependence* of $F(\phi_S)$ and not at the magnitude of F, the electrostatic effect drops out of the analysis. For future experiments, however, it is useful to note that the diffusivities on glass and on silicon appear to converge at [NaCl] $\approx$ 0.09 M. Unfortunately, at such a high salt concentration, the particles may become unstable and flocculate.

4.2.2 Theory

We expect that increasing ϕ_S would increase the strength of the depletion potential and therefore increase the average corner lifetime. To convert the lifetime data to free-energies, it is necessary to understand the statistics of the escape process. Consider a particle that is trapped in the corner by a stationary depletion potential. The probability of escape in the short time interval dt is given by dt/τ, where τ contains the information of interest (see equation (4.3) below). Of course, the probability that the particle did *not* escape is $1 - dt/\tau$. The probability, $P(t)$ of escaping after time t is thus given by

$$P(t) = \frac{1}{\tau}(1 - dt/\tau)^{(t/dt)} = \frac{1}{\tau}e^{-t/\tau}. \tag{4.1}$$

The second equality comes from a series expansion of the exponential function as $dt \to 0$. The experimental data agree well with this exponential form.

The mean time that a particle spends in the corner is τ (computed by integrating $tP(t)$ from 0 to infinity and normalizing). There are, therefore, many ways to calculate τ from the data. Making a histogram of lifetimes and fitting to equation 4.1 provides one estimate of τ. Unfortunately, this procedure is quite sensitive to the time-intervals used in the histogram. On the other hand, computing the mean of the data is inaccurate because there are no reliable data for times less than ≈ 1 s. A more robust method is to plot the total number of lifetimes, $N(t_0; t)$, between t_0 and

t. From equation 4.1, we find

$$N(t_0;t) = N_{\text{total}} \int_{t_0}^{t} P(t')dt' = N_{\text{total}}(e^{-t_0/\tau} - e^{-t/\tau}). \tag{4.2}$$

From our data, we counted the number of lifetimes, $N(t_0;t)$ that were between $t_0(\approx 2$ s) and t. We used $\sqrt{N(t_0;t)}$ as an estimate of the statistical uncertainty. We then fit $N(t_0;t)$ to the function in equation (4.2) and determined τ for three different ϕ_S (Fig. 4.12(b)).

The mean corner occupation time is related to the depth of the free-energy well that holds the particle in the corner:

$$\tau = \tau_D e^{\Delta F/(k_B T)}, \tag{4.3}$$

where τ_D is an average time between attempts to hop across the barrier (the subscript D stands for diffusive) and ΔF is the magnitude of the free-energy barrier that inhibits escape from the corner. The above formula can be proved in a rigorous way when $\Delta F \gg k_B T$ (see [116] or the article by Chandrasekhar in [8]). There is, however, a simple physical interpretation. The probability that a particle has sufficient kinetic energy to escape is proportional to the Boltzmann factor, $e^{\Delta F/(k_B T)}$, while the amount of time needed for such a particle to move past the barrier is τ_D. An estimate of τ_D is given by L^2/D, where L is the width of the trap and D is the particle's diffusion coefficient. D depends (weakly) on ϕ_S because the small spheres increase the viscosity of the solution. We neglect this ϕ_S-dependence, simplifying the analysis while introducing errors that are much smaller than the uncertainties.

For $\Delta F(\phi_S)$, we use the trial function $\Delta F = P_S(\phi_S)\Delta V_{\text{overlap}}$. Thus, from equation (4.3), we have $\ln(\tau) = P_S(\phi_S)\ \Delta V_{\text{overlap}} + C_0$. The quantity C_0 is independent of ϕ_S. A plot of $\ln(\tau)$ *vs.* P_S should be a straight line with a slope that depends on V_{overlap}, which is known. Non-depletion forces (independent of ϕ_S) will contribute to C_0 but will *not affect the slope* of the plot.

To look for an accurate functional form for $P(\phi_S)$, we have plotted $\ln(\tau)$ as a function of (dimensionless) pressure using the ideal-gas model (Fig. 4.12 (top)) and using the hard-sphere model (Fig. 4.12 (bottom)). The reduced pressures $(6P/(\pi a^3 k_B T)$ are given, respectively, by ϕ_S and by $(\phi_S + \phi_S^2 + \phi_S^3 - \phi_S^4)/((1-\phi_S)^3)$. The latter is the Carnahan-Starling pressure for a hard-sphere fluid [94]. In both cases, an approximately straight line is obtained (which does not say too much, since there are only three data points).

We now compare the measurements to predictions based on the ideal-gas and hard-sphere pressure. The geometry of this experiment is shown in Fig. 4.13, and V_{overlap} is shown in black. The volume of the excluded-volume overlap, V_{overlap} was calculated. The dashed line in Fig. 4.12 represent the predicted results, with the arbitrary additive constant chosen so that the line lies on the plot. The hard-sphere pressure clearly captures the ϕ_S-dependence more accurately than the ideal-gas law (although it does slightly overestimate it).

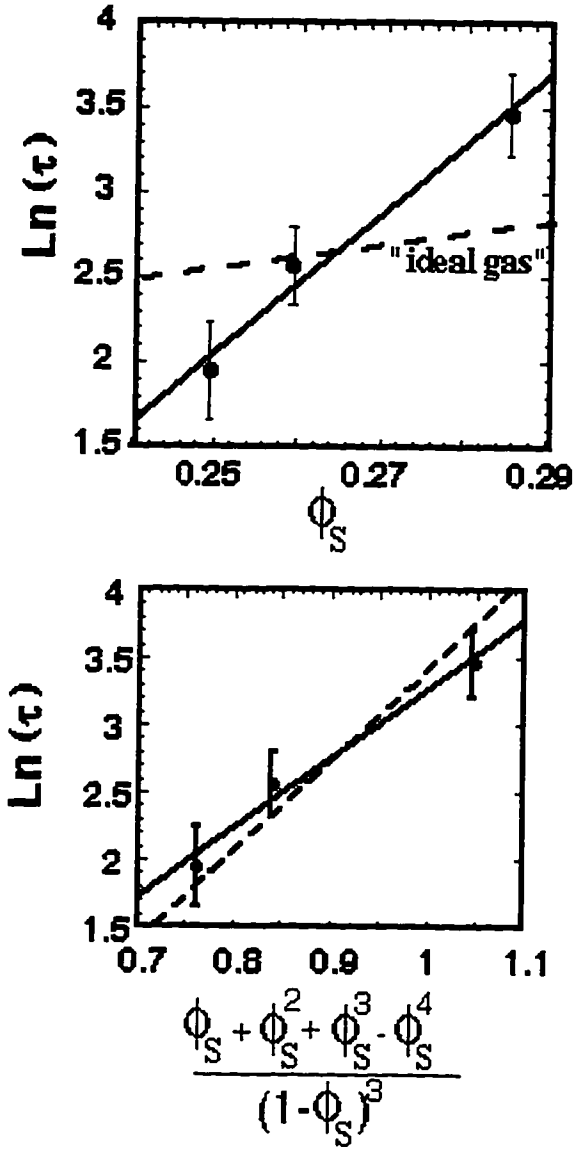

Figure 4.12: Plot of $ln(\tau)$ *vs.* ϕ_S (top) and *vs.* $(\phi_S + \phi_S^2 + \phi_S^3 - \phi_S^4)/(1 - \phi_S)^3$ (bottom). The solid lines are a straight-line fit to the data. The dashed lines represent the predictions of the ideal-gas model (top) and the Carnahan-Starling hard-sphere model (bottom). The slope of the measured data agrees better with the hard-sphere result.

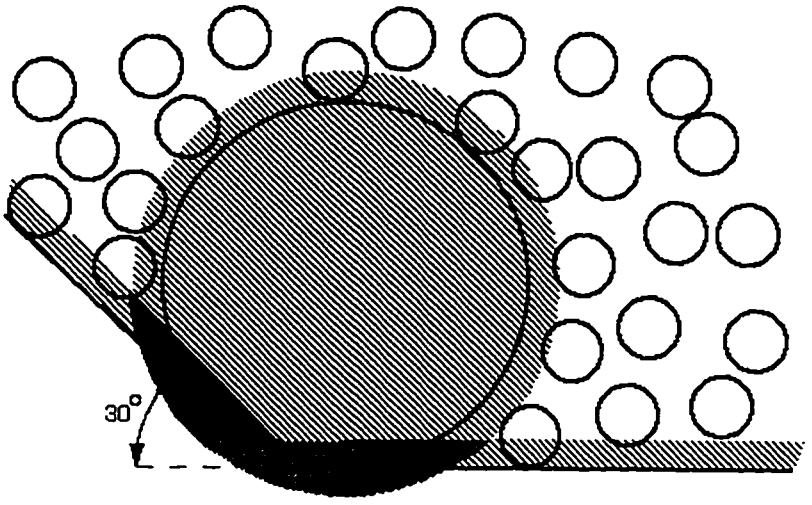

Figure 4.13: Cartoon showing the change in excluded-volume overlap when a large sphere "escapes" from a corner. If the large sphere moves to the right, along the wall, then the volume accessible to the small spheres is reduced by the volume of the black region.

4.2.3 Conclusions

The above results clearly show that the large spheres are confined in a corner by a potential that increases as ϕ_S is increased. In addition to measuring the ϕ_S-dependence of the confining potential, we have identified some interesting kinetic effects at such quasi-one-dimensional corners (Fig. 4.8 and 4.9).

Recent simulations and liquid-structure theory calculations (HNC closure) by Dickman *et al.* [26] have shown that the ideal-gas law accurately estimates the minimum ("contact") value of the depletion free energy, F_{min}, *i.e.* $F_{\text{min}} \propto \phi_S$. The *barrier* that confines the large sphere in the corner, however, exceeds F_{min} because of the repulsive bump (of magnitude F_{rep}) in the depletion potential that holds the large sphere to the wall (Fig. 4.14). Our experiment shows that $F_{\text{min}} + F_{\text{rep}}$ increases almost as steeply as $(\phi_S + \phi_S^2 + \phi_S^3 - \phi_S^4)/((1-\phi_S)^3))$, not like ϕ_S. Dickman *et al.* found that $F_{\text{min}} + F_{\text{rep}}$ increases only slightly faster than ϕ_S. A possible explanation of the the disagreement may be that the density of small spheres in the corner may be enhanced by geometric (entropic) effects or by the electrostatic forces with the silicon. Since F_{rep} is due to a layering of small spheres along the wall, enhancing this layering should enhance F_{rep} above the value expected at a flat wall. The disagreement begs for further investigation.

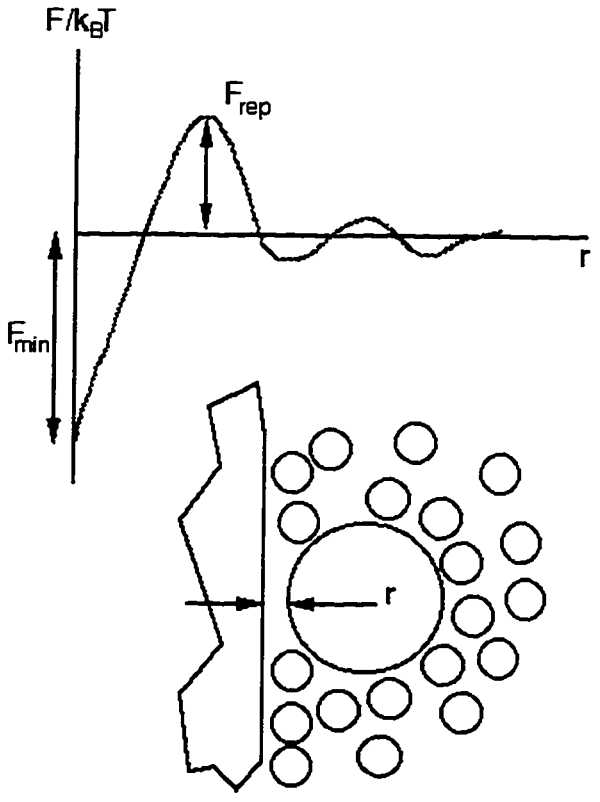

Figure 4.14: Schematic plot of the depletion free energy as a function of the distance, r, between the large sphere and the wall. There is a modest repulsion at $r = a_S/2$ due to the structure of the small spheres.

4.3 Other Microstructures and Applications

Building on the effects demonstrated in our experiments, one can devise structures of potentially greater use to trap the larger particles or to induce drift. For example, confinement could be useful in arranging microscopic spheres along a line (Fig. 4.15(a)). Using conducting particles (such as colloidal gold) in this way could lead to a new way to make conducting wires only a few nanometers in thickness. A microscopic circular terrace can be used to trap a single large sphere. The sphere would be attracted vertically to the flat surface and would be constrained laterally by the step-edge barrier that we have measured. An array of such islands could be used to make the large spheres self-assemble in a chosen pattern (Fig. 4.15(b)).

The next chapter will describe another application in which the large sphere is pushed a distance of several a_L along a wall of continuously changing curvature. The strength and range of these entropic force fields can be controlled by varying ϕ_S, a_L and a_S. In practical systems, the barriers can be as strong as several k_BT and tens or hundreds of nanometers in range.

These experiments provide some insight into the distribution and dynamics of particles in porous media. Foe example, we expect that if there are particles of different sizes, the larger ones will crowd together near the corners. The diffusion of these particles will be substantially less than the bulk (Einstein) diffusion due to hydrodynamic friction. Furthermore, aggregation of the larger particles into a solid

phase could occur in the smaller pores (in which more of the total volume is near the surfaces) but not in the larger pores. As discussed in the next chapter, similar effects may occur in cells, where pores are created by protein filaments [106, 107, 108].

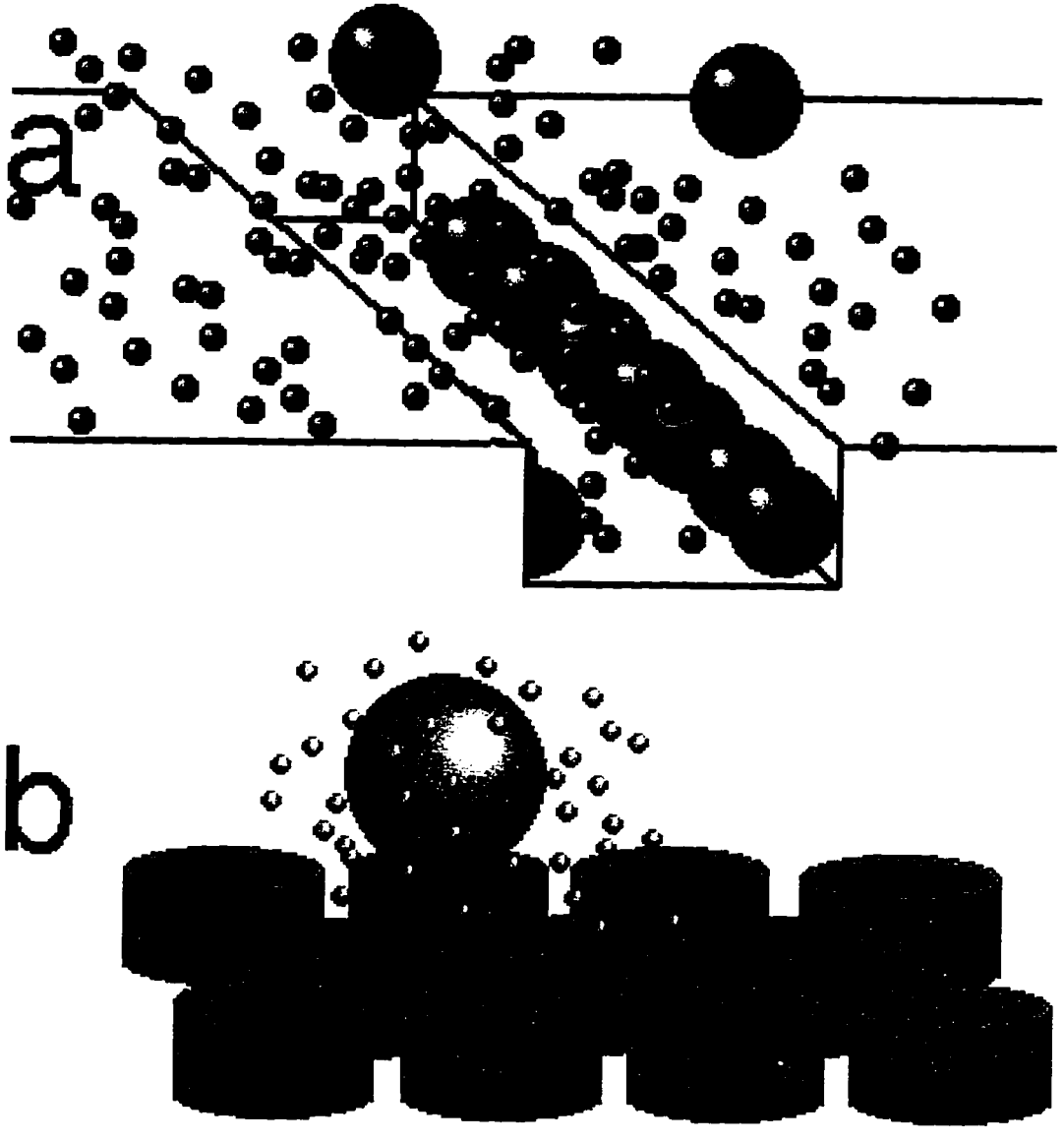

Figure 4.15: Cartoons of surface microstructures that could order the large sphere while increasing the total entropy. (a) The large spheres could form a single line (a "wire"). (b) The large spheres could order themselves in two dimensions, following the symmetry of the substrate.

Chapter 5

Hard Spheres inside Vesicles: Curvature and Excluded-Volume Effects

We continue to investigate the effects a container's shape on the properties of the particles within it. This chapter will focus on the interplay of wall curvature and particle motion. In mixtures of large and small spheres, we have found that the distribution of the large spheres can be dramatically enhanced at regions where the wall is highly curved [118]. We have trapped polystyrene spheres of two sizes inside rigid (multilamellar) phospholipid vesicles. Using optical microscopy, we measured the positions of the larger spheres and found that, when small spheres were present, the large spheres were pinned to the wall of the vesicle and were pushed *along the wall* in the direction of increasing curvature. Simply adding small spheres to the vesicle enhances the density of the larger spheres at the one point along the vesicle wall where the curvature is greatest – a novel example of self-ordering in a binary particle mixture. This experiment will be described in section 5.1.2.

Conversely, when the vesicle wall is flexible (*unilamellar*), the depletion force

could induce a change in shape of the vesicle. In section 5.2, a theoretical model will be presented, along with our conclusion that when the diameter ratio exceeds approximately 20, the vesicle can envelop a large sphere. The mechanism involves a competition between the depletion force (which "wants" the vesicle to wrap around the large sphere) and intra-membrane forces (which resist bending). As before, only the *ratio* of particle sizes matters, so that the ideas can be studied experimentally at micron-lengths, then applied to such smaller lengths (perhaps a few nanometers).

The interplay of curvature and excluded-volume (depletion) forces demonstrated here is not restricted to hard-sphere mixtures inside single-component vesicles. Indeed, the results may be relevant for a wide range of systems, especially the interior of biological cells. It is already well known that the highly-curved ends of cells are often the regions of greatest chemical activity and that the shape of a cell can determine whether cells live or die [119]. It is tempting to think that depletion forces could enhance the density of some macromolecules in these regions, and enhance the association of some molecules with the membrane. Does depletion, in fact, play a role? The key ingredients for depletion-curvature effects are: a wall with varying curvature, particles with short-ranged rupulsive interactions and of various sizes, and diffusion. The cellular interior certainly has the first two. The cell wall (also a phospholipid vesicle, but complicated by protein networks attached to it) can have a variety of shapes, including that of a cigar in the case of nerve cells. Furthermore, organelles

inside (eukaryotic) cells take on a tremendous variety of shapes. Some are highly convoluted combinations of concave and convex surfaces (the Golgi apparatus and endoplasmic reticulum, for example [108]). There are myriad proteins (2 to 20 nm), liposomes (up to 100 nm) and organelles (microns) at high total concentrations inside cells. For moving things over long distance, cells have highly-developed machinery called molecular "motors" (see, for example, [120]). Some liposome "shuttles" do, however, diffuse as a way of transporting proteins to specific, nearby sites [121]. It is tempting to consider that the entropic curvature effects demonstrated here might play some role in the remarkable specificity and efficiency of molecular interactions and transport, as well as endocytosis. We will have to wait for experiments to settle the issue.

Entropic forces might, moreover have played a role in the evolution of the rigid structure that holds the cell nucleus near the center of the cell [108]. Without such a structure, the nucleus could be strongly pinned to the cell wall by the proteins and liposomes in the cytoplasm [122].

Although this work is, to our knowledge, the first to demonstrate wall curvature effects, Minton has considered theoretically the biological implications of other pore shapes (cylinders, cubes, rod-arrays, and others) [106, 107]. His calculations show that confinement of macromolecules within pores can substantially alter their mobility, polymerization rate and shape. Real macromolecules, however, interact by a variety

of non-entropic forces (electrostatic, hydrophobic, van der Waals), which tend to complicate (as well as enrich) their behavior. Our goal is to understand these very general excluded-volume effects in their barest form – among hard spheres.

5.1 Rigid Walls

5.1.1 Calculation of Depletion Force along a Curved, Rigid Wall

The shape of the wall can lead to entropic forces in a specific direction *along the wall.* For example, the last chapter showed that the larger spheres are locally repelled from an edge cut into the wall [109] and attracted to a corner (*i.e.* where the "wall" meets the "floor") [110]. If the wall has constantly-changing radius of curvature, these forces were predicted to act everywhere along it [109]. As shown in Fig. 5.1, when the large sphere is near the wall, the overlap volume depends on the wall's curvature radius. When near a concave wall, the large sphere will therefore move in the direction of increasing curvature to minimize the small spheres' excluded volume. We can estimate the free energy ($F(R_C)$) as a function of the curvature of the wall (R_C) where the large sphere touches it. Within the ideal-gas depletion force model, $F(R_C) = -P_S V_{\text{overlap}}(R_C)$. P_S is the small-sphere osmotic pressure (from the ideal gas law) and $V_{\text{overlap}}(R_C)$ is the excluded-volume overlap, the black region in Fig. 5.1. In Fig. 5.2, the calculated $F(R_C)$ is plotted as a function of R_C. Here, the wall was assumed to be locally spherical with a radius of curvature $= R_C$ at the point of contact

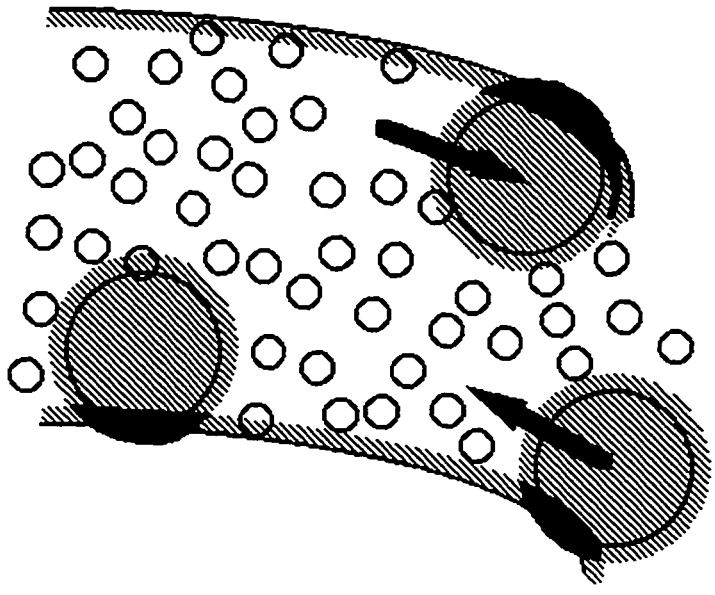

Figure 5.1: Cartoon illustrating the depletion force along a wall with varying curvature. Because of the changing wall curvature, the size of the excluded-volume overlap depends on sphere position. The large sphere will move along the wall to maximize the size of the overlap region, as indicated by the arrow.

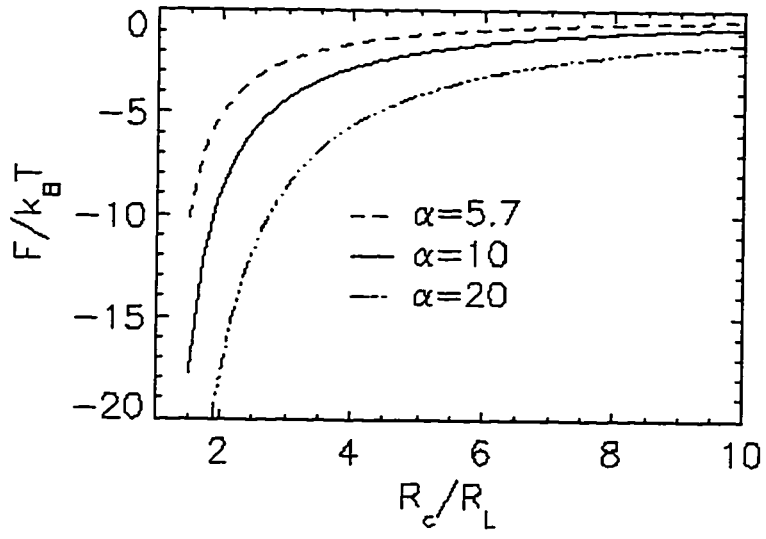

Figure 5.2: Plot of the free energy F of a binary mixture when the large sphere is against a concave wall with curvature radius R_C.

with the large sphere. We have chosen the ratio of radii, $R_L/R_S(\equiv \alpha) = 5.7, 10.0$ and 20.0 and ϕ_S= 0.30. We defined $F = 0$ on the flat wall. The gradient of F is a lateral force that pushes the large sphere along the wall. The force can be tens or hundreds of femtoNewtons (10^{-15} N) in magnitude.

5.1.2 Measurement of Depletion Force along a Curved, Rigid Wall

In this section, I will describe measurements of the depletion force along the wall as a function of wall curvature. We have experimentally quantified the magnitude of the depletion force that holds the large sphere against the wall and found reasonable agreement with the ideal-gas prediction.

To measure this surface entropic force, we studied the distribution and dynamics of

microscopic nearly-hard spheres trapped inside rigid, pear-shaped vesicles. A brief review of the experimental procedure is given here; the reader should refer to Chapter 7 for more details. The vesicles were prepared from a phospholipid (1-Stearoyl-2-Oleoyl-sn-Glycero-3-Phosphocholine (SOPC), Avanti Inc., U.S.A.), dissolved in chloroform (25 mg/mL). After evaporating the chloroform from 200 μL of SOPC solution, we added 100 μL of salt water with charge-stabilized polystyrene spheres (Seradyn, IN, USA) in suspension. The salt (0.01 M NaCl) served to screen out electrostatic forces over a distance of $\approx$ 5 nm, the Debye-Huckel screening length [20]. Thus, our sample closely resembled an ideal hard-sphere and hard-wall (HSHW) system. Rigid, multilamellar vesicles of diverse shapes and sizes immediately formed with colloidal spheres trapped inside. We injected the solution into a 10-μm thick glass container for viewing under an optical microscope (100x objective with 1.30 numerical aperture, in transmission mode). Most of the vesicles were part of large clusters, which were held nearly immobile between the glass plates. We always chose at least one object (another sphere, for example) that was rigidly attached to the vesicle in order to track center-of-mass motions of the vesicle. Images of a planar slice, 600 nm thick, through the center of vesicles were captured, then later digitized (Fig. 5.3). Images in which the large sphere was not in focus (*i.e.* within the 600 nm slice) were ignored.

We quantified the behavior of the mixture by measuring its free energy, $F(\mathbf{r})$, as a function of the position of a sphere of radius $R_L = 0.237\,\mu$m. First, using NIH

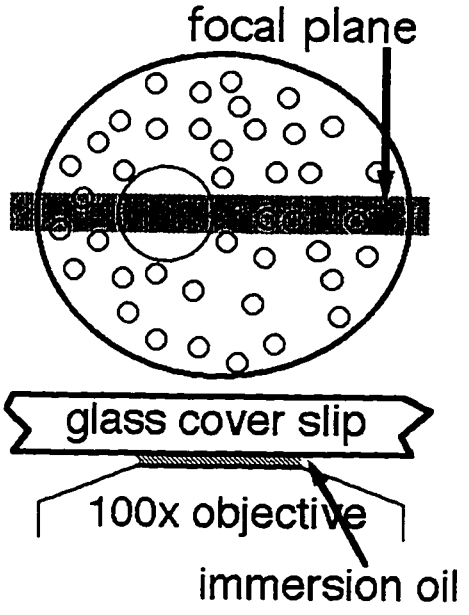

Figure 5.3: Cartoon of the 600-nm thick optical slice through an SOPC vesicle.

Image software, we determined the in-plane position of the sphere's center of mass, $\mathbf{r}$, ($\pm 0.08 \mu$m) when it appeared in the imaged slice. From these data, we used two techniques to extract $F(\mathbf{r})$. In the first, the number of times $N(\mathbf{r}_i)$ the sphere appeared at a given bin located at $\mathbf{r}_i$ defined the density distribution. Assuming that each measurement event was independent of the others, $N(\mathbf{r}_i)$ follows the Boltzmann distribution: $N(\mathbf{r}_i) \propto \exp(-F(\mathbf{r}_i)/k_\mathrm{B}T)$. Since a systematic error can arise if events are not completely independent (*i.e.* not separated by an infinite time), we waited a minimum of 0.6 s between measurements. During this time the mean square displacement was ≈ 0.3 μm, larger than the 0.07-0.13 μm bin sizes. We also collected data over a period of 30-80 minutes, enough time for the sphere to explore all of

the available space. We therefore used the logarithm of the sphere's distribution to extract the free energy.

The dynamics of the diffusing 0.237-μm sphere provided the second way to measure $F(\mathbf{r}_i)$, as described in [78, 15] and in Chapter 7. The region along the inner surface of the vesicle was divided into several equal-area bins. We considered only events in which the center of the large sphere was within 0.28 μm of contact with the surface in consecutive frames (separated by a time τ). From our videotape, we counted the number of times ($N_{ij}(\tau)$) the sphere was located in bin j at time t and in bin i at time $t+\tau$. The transition probability matrix, $P_{ij}(\tau)$, is given by $N_{ij}(\tau)/N(\mathbf{r}_j)$. The measured matrix P_{ij} contains information about the equilibrium state of the system. In particular, the eigenvector ($\hat{\mathbf{e}}$) of P_{ij} with unit eigenvalue is proportional to the Boltzmann factor: $\hat{\mathbf{e}}_i \propto \exp(-F(\mathbf{r}_i)/k_\mathrm{B}T)$. We obtained indistinguishable results with $\tau = 0.1$, 0.2 and 0.3 s and with various bin sizes. This technique avoids fit parameters and possible systematic errors arising from the density-distribution approach. It also avoids potential errors arising from a slow change in shape of the vesicle, which would affect the distribution averaged over a long time but would not affect the short-time particle dynamics.

We report here the results from two different samples. The first "control" sample contained a solitary 0.237-μm sphere (no small spheres) diffusing freely inside a vesicle. The measured density distribution is shown in Fig. 5.4(a). The sphere distri-

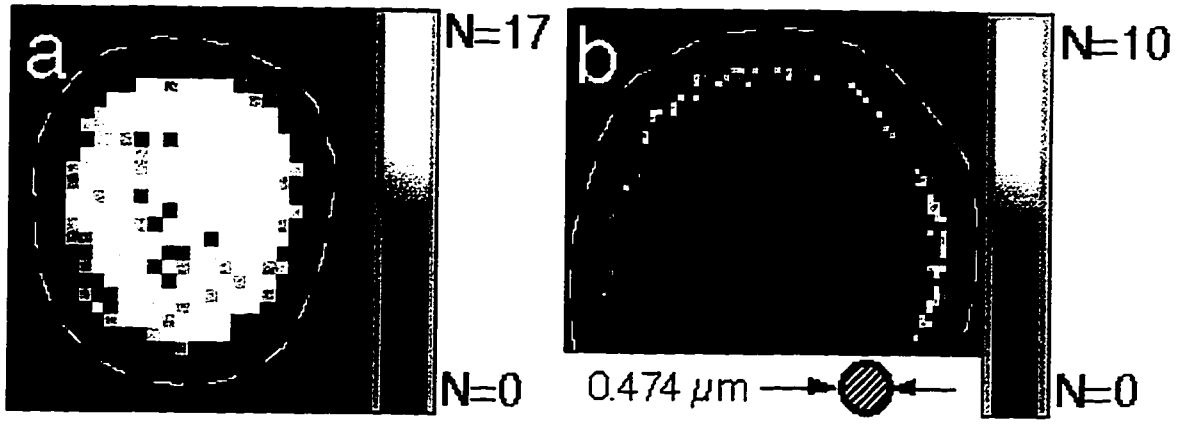

Figure 5.4: (a) Probability distribution of a single 0.237-μm-radius polystyrene sphere inside a vesicle (no small spheres). The white dashed line is the edge of the vesicle, and the colored points indicate the number of times, N, the center of the sphere was observed in a bin located at a given point. There were 2000 events and the bins were 130 nm x 130 nm. The sphere simply diffused freely throughout all of the available space. (b) Same as in (b), but with a vesicle that also contained small spheres ($\phi_S = 0.30, R_S = 0.042$ μm, $\alpha = 5.7$). There were 2300 events and the bin size was 65 nm. The large sphere was clearly attracted to the vesicle wall, especially where the vesicle was most curved.

bution is uniform: there is no significant interaction between the vesicle wall and the polystyrene sphere, as expected due to the very short Debye-Huckel screening length.

The behavior changed noticeably when small spheres were added to the interior of a vesicle. In Fig. 5.4(b), we show the distribution of a $R_L = 0.237$ μm sphere in a binary mixture with $\phi_S = 0.3, R_S = 0.042$ μm ($\alpha = 5.7$). The distribution is highly non-uniform, with a significantly higher probability of finding a large sphere within about 0.28 μm of the surface. The apparent width of this "surface" region exceeds $2R_S$ due to uncertainties in the particle positions and, possibly, due to a slight tilt of the vesicle wall away from vertical. In this sample, there were actually

two large spheres. Since we did not want to consider interctions among large spheres, we ignored all images in which the large spheres were within $\approx 2\ \mu$m of one another. We also disregarded the bottom section of the vesicle (the section that is not shown in Fig. 5.4) because there was a particle permanently stuck there.

We measured the average number of times the large sphere appeared in each bin within 0.28 μm of the surface and the average number per bin in the bulk. We defined the natural logarithm of the ratio of these numbers as $F_0/(k_BT)$, a measure of the average strength of the depletion attraction. We found $F_0 = (2.2 \pm 0.5)k_BT$.

Theoretically, $F_0 = \ln < e^{-F/k_BT} >= \ln \int_{R_L}^{R_L+0.28\ \mu\mathrm{m}} [\mathrm{d}r/0.28\ \mu\mathrm{m}]\, \mathrm{e}^{-V(r)/k_BT}$, where r is the distance from the large-sphere center to the wall and $V(r)$ is given by the depletion force model. Although the vesicle wall was curved, we can predict a lower bound of F_0 by assuming the wall was flat (see section 1.3.2):

$$V(r) = \frac{-k_BT\phi_S}{4R_S^3}(r - R_L - 2R_S)^2(r + 2R_L + R_S). \tag{5.1}$$

Putting in the numbers gives a theoretical prediction of $F_0 = 1.97k_BT$. Here we have neglected thermal fluctuations in the shape of the vesicle wall and residual electrostatic repulsion. Constraining the large sphere to lie 5 nm away from the wall, for example, reduces the predicted result to 1.45 k_BT. The 0.7-k_BT difference from our measured result is likely due to the curvature of the wall, which would enhance the observed F_0 as discussed in the following paragraph. These results are consistent with recent calculations showing that the ideal-gas approximation accurately predicts

the depletion well depth at contact (although it misses the relatively weak, long-range depletion repulsion) [26].

The distribution in Fig. 5.4(b) demonstrates a higher large-sphere occupation where the vesicle surface is more curved. From the sphere dynamics, we obtained the total free energy, F, as a function of sphere position when it was near the surface. The inset of Fig. 5.5 shows the measured F as a function of the position, s, along the vesicle's perimeter. The slope of this curve reveals a maximum force of $20\text{x}10^{-15}N$ pushing the large sphere along the wall. We also determined the curvature radius at points along the wall. To do this, we fit polynomial funtions to the edge of the large-sphere distribution, then extrapolated outward a distance R_L perpendicular to each point on the edge of the distribution. (The same technique was used to define the boundary between the "surface" region and the "bulk region, 0.28 μm inside the edge of the distribution.) In Fig. 5.5, we plot the measured free energy as a function of wall curvature radius, R_C. The free energy decreased by approximately $1.5k_BT$ when the curvature radius decreased from 20 μm to 2 μm.

For comparison to our results, we used the depletion-force model described in section 5.1.1 to calculate the free energy as a function of wall curvature: $F(R_C) = -P_S V_{\text{overlap}}(R_C)$. Here, P_S is the small-particle osmotic pressure (from the ideal-gas law) and $V_{\text{overlap}}(R_C)$ is the size of the excluded-volume overlap. The solid line in Fig. 5.5 represents the theory. We assumed that the vesicle wall was locally spherical

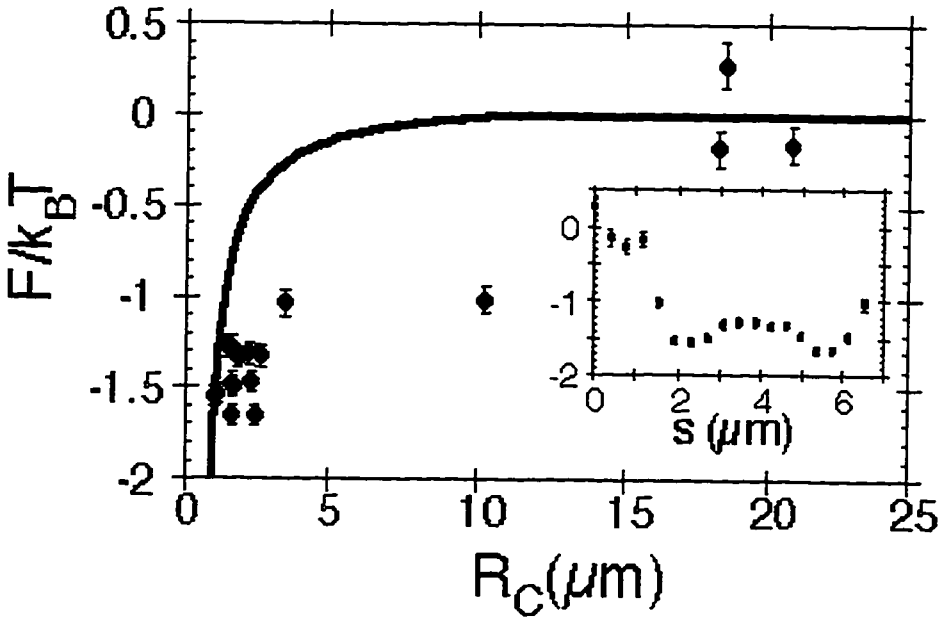

Figure 5.5: The measured total free energy of the binary mixture, F, when the large (0.237-μm-radius) sphere was at the vesicle wall. F is plotted in units of $k_{\mathrm{B}}T$ as a function of the wall curvature radius, R_C. The symbols represent measurements and the line represents the results of the calculation described in the text. (Inset) F/k_BT *vs.* position, s, along the perimeter of the vesicle. The origin (s=0) is located at the lower left of the vesicle shown inthe previous figure

at each point along its surface. Since we could only measure R_C in the image plane, we assumed that this also determined the out-of-plane curvature. This approximation probably explains the scatter in our data points. The large sphere was assumed to touch the vesicle wall. In both theory and experiment, the free energy was set to zero in the limit of large curvature radius (flat wall). The measured 1.5-k_BT free-energy change is consistent with the theoretical results.

5.1.3 Conclusions

We have demonstrated that variation in the curvature of a wall can noticeably change the distribution of particles in the presence of much smaller particles. Our measurements of the free energies and forces agree quite well with the predictions of the depletion model when the small spheres are assumed to be an ideal gas. In the next section, we use these results to consider what can happen when the wall is allowed to bend.

5.2 Flexible Vesicle Walls

So far we have shown that curvature of a *rigid* wall induces forces on the large spheres in binary particle mixtures. To conclude this chapter, we consider theoretically a binary hard-sphere mixture in the presence of *flexible* walls. This extra degree of freedom introduces a competition between depletion and curvature energy that can

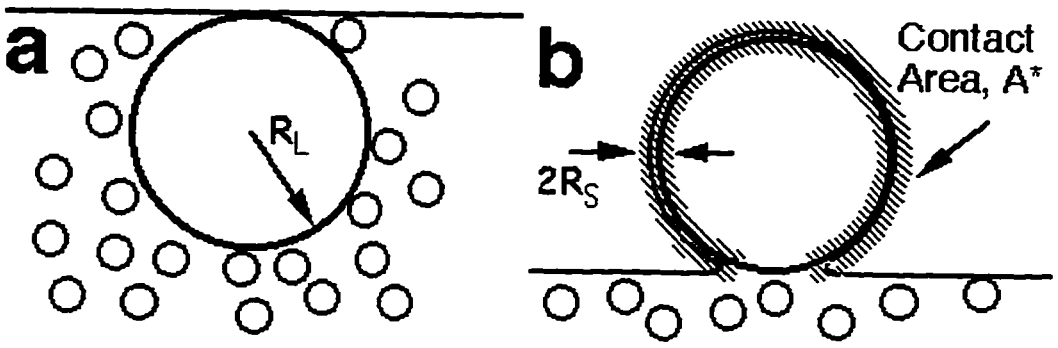

Figure 5.6: Cartoon demonstrating how hard spheres can induce a change in shape of a vesicle. (a) When the membrane is flat, the excluded-volume overlap is minimized and the curvature energy is zero. (b) When the vesicle envelops the large sphere, the curvature energy increases, but so does the excluded-volume overlap (hatched region).

produce a variety of new phenomena. For example, we expect that under some circumstances, the membrane will spontaneously bend around the large sphere (Fig. 5.6). We anticipate that these effects will be observable and that understanding this mechanism will be essential to predict the behavior of unilamellar phospholipid vesicles containing particles of different sizes.

The membrane will spontaneously envelop the large sphere only if the resulting total free energy change, ΔF, is negative. Our experiment indicates that the membrane-particle interactions are very short-ranged, so we use the hard-sphere and hard-wall approximations. We therefore divide the full free energy into two terms, one representing the net adhesion induced by the colloidal spheres, the other the vesicle's bending energy: $F = F_{\text{adh}} + F_{\text{ves}}$.

The experiment described in section 5.1.2 shows that, for rigid membranes, F_{adh}

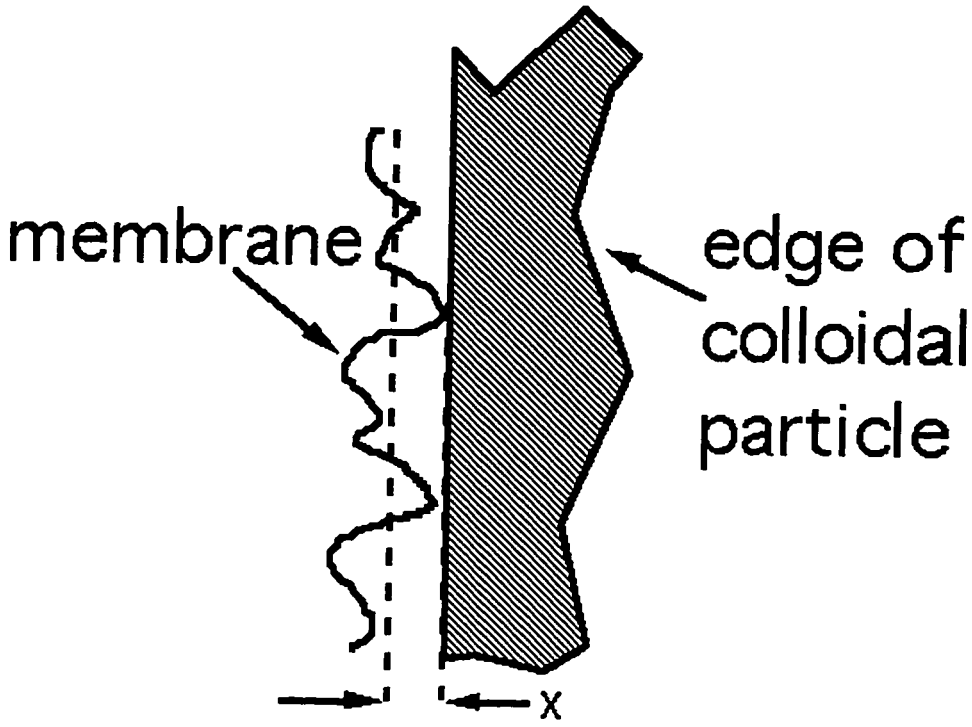

Figure 5.7: Illustration of the entropic repulsion between a hard object and a fluctuating membrane.

can be well described by the depletion-force model. For flexible membranes, we must add a new contribution to F_{adh} to account for the "steric repulsion" effect [123, 124, 125] (Fig. 5.7). For $R_S \ll R_L$ we may approximate the latter by the interaction between a flat hard wall and a fluctuating membrane at constant mean separation x. This free energy is given by [126, 127]

$$F = A^* \frac{0.06(k_{\text{B}}T)^2}{\kappa x^2}, \tag{5.2}$$

where A^* is the area of contact between the membrane and the sphere (Fig. 5.6(b)). For unilamellar phospholipid membranes, the bending stiffness, $\kappa \approx 15 k_{\text{B}}T$ (see [128]

and the article by R. Lipowski in [129]).

For the depletion-force contribution to F_{adh}, we assumed that the vesicle shape conforms with the sphere. In this case, the change of excluded volume upon adhesion is $A^*(2R_S - x)$. We used the ideal-gas approximation and chose the small-sphere volume fraction to be $\phi_S = 0.3$. Thus, we find

$$F_{\text{adh}} = A^*[\frac{0.06(k_{\text{B}}T)^2}{\kappa x^2} - \frac{3\phi_S k_B T}{4\pi R_S^2}(2 - \frac{x}{R_S})]. \tag{5.3}$$

We minimized the total adhesive energy (depletion attraction plus steric repulsion) by setting $\partial F_{\text{adh}}/\partial x$ to zero and found

$$x^{\text{min}} = R_S(\frac{8(0.06)\pi k_B T}{3\kappa\phi_S})^{1/3}, \tag{5.4}$$

and

$$F_{\text{adh}}^{\text{min}} = \frac{3\phi_S k_B T}{2\pi R_S^2}[\frac{3}{2}(\frac{0.06\pi T}{3\kappa\phi_S})^{3/2} - 1], \tag{5.5}$$

where x^{min} is the position where F_{adh} reaches its minimum value, $F_{\text{adh}}^{\text{min}}$. Plugging in $\kappa = 15k_BT$ and ϕ_S= 0.30, we find that $x^{\text{min}} \sim 0.5R_S$ and $F_{\text{adh}} = -0.091k_{\text{B}}T \cdot A^*/{R_S}^2$. For extremely flexible membranes with $\kappa \sim k_{\text{B}}T$ the adhesion is lost completely because $F_{\text{adh}}^{\text{min}}$ is always positive (see equation (5.3)) [130].

The vesicle's elastic energy, F_{ves}, depends only on the membrane curvature. We neglected the constant-volume and constant-area constraints of a vesicle and instead considered an infinite membrane. The free energy cost of bending can be written in

the following form:

$$F_{\text{ves}} = \frac{\kappa}{2}\int dA\,(\frac{1}{R_C^{(1)}} + \frac{1}{R_C^{(2)}})^2, \tag{5.6}$$

where $R_C^{(1,2)}$ are the two principal curvature radii and the integral extends over the entire membrane surface [131, 132]. In this case, $R_C^{(1,2)} = R_L$. Thus the local curvature energy change upon adhesion is just $F_{\text{ves}} = 2\kappa A^*/{R_L}^2$. Combining $F_{\text{adh}} + F_{\text{ves}}$, we see that adhesion and engulfment are favored when

$$\Delta F = A^*(\frac{-.091k_BT}{R_S^2} + \frac{2\kappa}{R_L^2}) < 0. \tag{5.7}$$

When the factor in parentheses is negative, the system will want to maximize A^*: the vesicle will want to completely engulf the sphere. Engulfment can occur when $\alpha > \alpha_{\text{crit}} \equiv \sqrt{2\kappa/0.091k_{\text{B}}T} = 18$ (when $\kappa = 15k_BT$). A more detailed analysis of the deformation of vesicles at a generically sticky surface, specialized to the case of interest here, gives a similar result [133]. The required regime for α is easily accessible, using either polymers or spheres as the small particles. The search for vesicle shape changes induced by hard spheres is currently under way with Derek T. Wong, Dennis E. Discher, Keng Hui Lin, and Arjun G. Yodh.

Even if engulfment is energetically allowed, however, there may still be a large free energy barrier inhibiting it. One can characterize the amount of bending by the half angle, θ, of the region of contact (see Fig. 5.8). Initially, at $\theta = 0$, there is no bending. At intermediate stages ($\theta \approx 90°$), the membrane must bend back to meet the flat, unperturbed section (see the arrow in Fig. 5.8(b)). The curvature cost of this extra

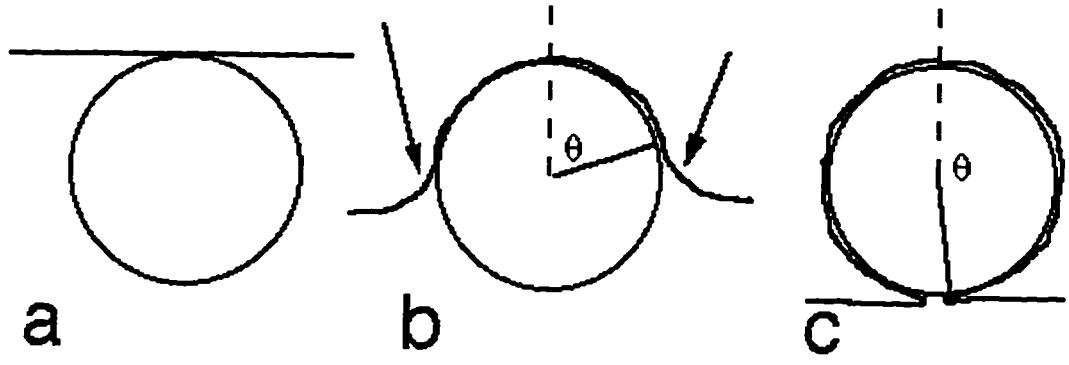

Figure 5.8: Illustration of the free energy barrier against complete envelopment of a large sphere. The arrow in (b) points to a region where there is curvature that is not included in the above calculations.

piece is not included in the above calculations and could present a substantial barrier against spontaneous envelopment. At complete envelopment (Fig. 5.8 (c)), the area of the highly-curved "neck" of the membrane vanishes, so that the total extra energy cost at the neck could be quite small. In this last case, the above equations account for all of the membrane curvature. At sufficiently high α, the barrier when $\theta \approx 90°$ may disappear (a case similar to a spinodal point in phase transitions). We emphasize that there is no inherent size scale in this model, so that these effects should also occur at the 100-nm length scale of typical liposomes.

5.3 Conclusions

We have measured for the first time a curvature-induced entropic force in a system of hard spheres trapped in a rigid vesicle. The results show that the distribution of

particles within the vesicle is strongly affected by the local shape of the vesicle wall. Furthermore, a simple estimate predicts shape transitions of unilamellar phospholipid vesicles induced by particles inside the vesicle. The ideas presented here suggest a way to understand several phenomena in cellular interiors and complex fluids inside porous media. For example, in a vesicle whose membrane contains multiple species of lipids, the lipids can segregate into regions with different curvatures [134, 135, 136]. In such a sample, the particle distribution, which depends on curvature, would correlate with the local *composition* of the membrane (see Fig. 5.9). This mechanism may provide considerable size-specificity in associations between macromolecules and lipids. Finally, when the size ratio is more extreme or the vesicle wall is less rigid, the spheres may be able to induce fission [136] of the vesicle since the large sphere and its surrounding membrane may break away from the rest of the vesicle.

If there are many large spheres inside the vesicle, there are likely to be membrane-mediated interactions among those spheres that are against the deformed wall. Possibly, the large spheres will mutually repel one another and form a lattice along the vesicle's surface. In the example of Fig. 5.10, moving the larger spheres closer together would require bending the membrane more, which costs energy.

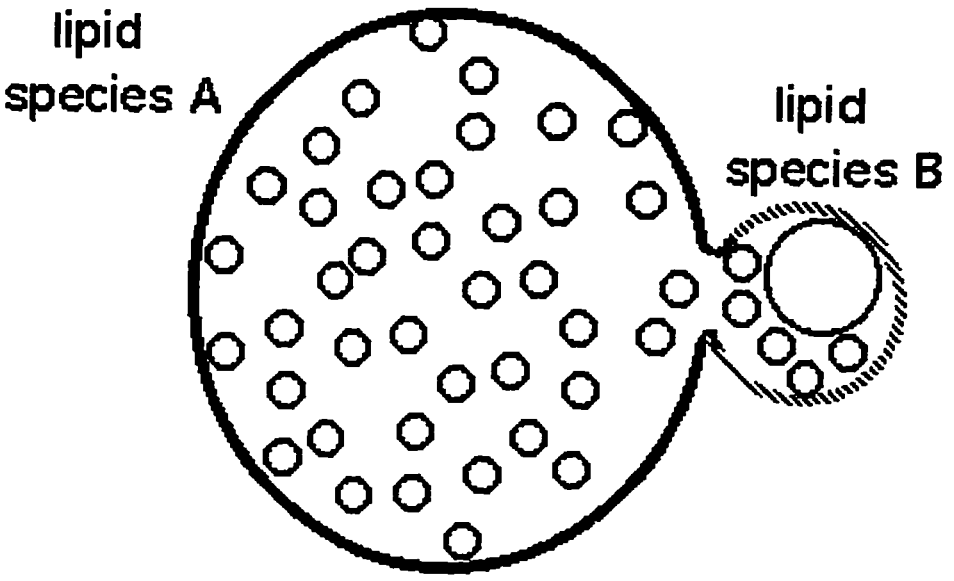

Figure 5.9: Cartoon showing how the distribution of particles in a vesicle can correlate with the composition of the two-component membrane. Regions of the membrane that have different compositions (A or B) can have different curvatures. The larger sphere(s) will tend to occupy the more higly-curved section.

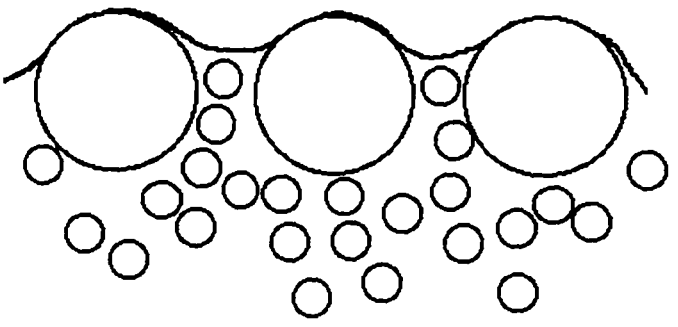

Figure 5.10: Illustration of membrane-induced interactions that could arise among large spheres that are stuck to the membrane by the depletion force.

Chapter 6

Colloidal Assembly

In this chapter, I will describe our development of new techniques to fabricate ordered two- and three-dimensional arrays of submicron colloidal particles. The first technique combines electron-beam lithography and chemistry to make an array of "glue spots" on a substrate, which irreversibly bond to anionic particles (section 6.2). The second technique, called "convective assembly", involves controlling the rate of evaporation of the solvent from the particle suspension. We have extended an existing technique for making ordered *two*-dimensional triangular arrays, allowing us to make *three*-dimensional arrays that are a few layers in thickness (section 6.3). The goal will be to combine these two techniques to allow three-dimensional fabrication of a wide range of structures (section 6.4.1). In contrast to the techniques introduced in Chapters 4 and 5, these techniques both involve irreversible bonding of particles to substrates and to other particles.

There are at least two types of fundamental experiments that may become possible

using the techniques discussed in this chapter. In the first case, we will make particle arrays of various structures and study their optical (or photonic) properties. Areas of experimental focus will include the effects of packing defects and of binary lattices (of two different particle sizes or refractive indices). A brief review of photonic band structure and of some of its practical applications is given in section 6.1.1.

In the second set of fundamental experiments, "seed" crystals of various symmetries will be fabricated to study fundamental aspects of nucleation in colloids. For example, the rates of growth of a face-centered cubic lattice from its (100), (110), and (111) planes [1] will, in general be different. We will be able to measure the differences among these directions by exposing previously-assembled (100), (110), and (111) planes of spheres to a suspension of hard spheres. We would like to know which plane will grow into the bulk the fastest and which will form the most ordered lattice. Seed crystals that have a lattice parameter that differ slightly from the most stable value will allow us to determine the effects of strain on the growth kinetics and structure [138]. The effects of entropy on growth kinetics may be relevant for understanding a wide variety of non-equilibrium problems. Finally, fabrication of quasicrystalline patterns will allow investigation of the thermodynamic stability of this state of matter [139].

Other applications of submicron-scale templates include more efficient latex im-

[1] For definitions of the standard crystallographic notation used here, see Ch. 4 of [137].

munoassays [100]. Compared to disordered ones, ordered particle arrays would have pores that are all the same size, potentially allowing finer control of particles that will pass through or be trapped by a filter. Ordered films also have higher densities, which might improve sintering processes [140]. Single-layer films can also be used as masks (see [141] and references therein). A metallic or semiconducting material could be deposited onto a particle array using a directional method (such as thermal evaporation). After the particles are removed, the substrate would only be covered with the deposited material where there were interstices between particles. Varying the angle of deposition offers some control of the sizes and shapes of the resulting spots. Finally, arrays of cells, which could be attached using the technique described in section 6.2, are potentially useful as biosensors [142].

6.1 Background

6.1.1 Photonic Band Gap Materials

In the last decade, some very remarkable optical properties have been discovered in ordered lattices of particles whose diameter (a) is comparable to the wavelength (λ) of light. Much has been written on the subject and a brief review is included here. In the most outstanding case – a "photonic band gap material" – light of a certain range of frequencies cannot propagate *in any direction* inside the lattice (see [101, 104, 105, 143] and the article by Yablonovitch in [102]). The resulting

physical situation is analogous to the band gap of electrons in a semiconductor. The *electronic* band gap is a range of energies with no electron states. Electrons are waves, like photons, and feel a periodic potential, analogous to a periodic refractive index. Similarly, there are no (propagating) photon states in a *photonic* band gap. These photonic band gaps are a purely classical effect that can be demonstrated by solving Maxwell's equations. Since this task is rather onerous, two greatly simplified models help to guide us. From one simplified point of view, the photonic band gap arises from strongly enhanced Bragg scattering. Every colloidal crystal Bragg scatters light of specific frequencies incident along specific directions; photonic band-gap materials "Bragg scatter" light in all directions. The Bragg model assumes that the amplitude of incident radiation that is scattered from each particle is the same [137]. In these highly-scattering systems, however, the intensity of the incident radiation is strongly attenuated as it enters the sample and the Bragg model fails.

Perhaps a more useful point of view is to think of coupling among the particles. Among atoms, stronger electronic coupling broadens the electronic bands and thus diminishes the band gaps. Similarly, strong optical coupling (corresponding to a transparent sample) eliminates photonic band gaps. To obtain a band gap, one needs to excite a Mie resonance[2] within each particle. For particles of size comparable to the wavelength of light, there are rather sharp peaks in the scattering cross section –

[2]The scattering of light by particles whose diameter is comparable to the light's wavelength is the subject of Mie theory [144].

resonances – at some wavelengths and scattering angles. In such cases (such as when $\lambda/n = 2a$, where n is the particle's refractive index), the light wave resonates within the particle, "decoupled" from the other particles. The occurrence of a dramatic Mie resonance does seem to coincide with the occurrence of a photonic band gap [102].

Spontaneous emission of light inside the photonic band gap is prohibited [101, 104, 105, 143, 145]! The laws of quantum mechanics (*e.g.* Fermi's Golden Rule) state that in order for a photon to be emitted, there must exist a state for it to occupy [146]. If there is no such state, then no photon is emitted. These materials therefore present an opportunity to inhibit altogether the spontaneous emission of visible light in a range of frequencies. Even more possibilities arise near defects in the crystalline lattice, which could be designed to allow a single mode within the (bulk) gap to propagate. A defect in a photonic band-gap material will act as a waveguide, allowing control of the direction and polarization of the emitted photons. Such materials could be used as light-pipes (which can curve at the micron length scale!)[143, 101] and as laser cavities. In many devices that convert electrons to light (or *vise versa*), spontaneous emission represents a loss of energy. In lasers, for example, spontaneous emission reduces the population of excited atoms but does not contribute to the in-phase oscillation within the cavity. A "threshold current" must be overcome so that stimulated emission overcomes spontaneous emission [147]. Eliminating spontaneous emission except along a (single-mode) cavity would force *all*

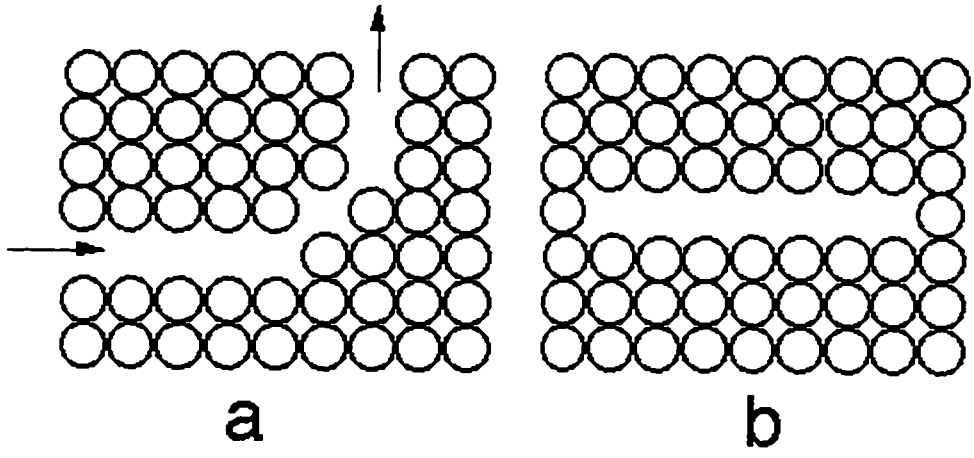

Figure 6.1: Illustration of the use of defects in photonc band-gap materials as (a) waveguides and (b) cavities. The defects could be designed so that there exist(s) state(s) within the bulk photonc band gap. Photons in these states would be confined within the defect.

of the emitted light into the cavity, allowing threshold-free and highly efficient lasers, single-mode light-emitting diodes (LEDs), and more efficient solar cells.

Useful properties are also found in the absence of a full photonic band gap. Even though light in an (incomplete) gap can propagate in some directions, the photon density of states can be suppressed at some wavelengths [148] and enhanced at others [149], allowing control of electronic transition rates. Furthermore, light propagation is restricted to a small range of angles, potentially allowing directional emissive displays and waveguides.

The challenges of sub-micron-scale fabrication have so far frustrated all attempts to make photonic band-gap materials. There are three requirements: (1) the ratio of refractive indices (particles to background or *vise versa*) must exceed approximately

two, (2) the optimal crystal structure must be chosen, and (3) it must be built at the sub-micron length scale. Semiconductor compounds can have high refractive indices and low absorption (*e.g.* GaAs, $n \approx 3.5$). Some early attempts therefore used semiconductor lithography techniques to make full-band-gap structures in one dimension [149] and in two [150]. Extending this technique to three dimensions is difficult because only the surface is accessible by the etchants.

Three-dimensional assembly of colloidal particles, therefore, provides a vary attractive alternative to lithography. Some advances in sol-gel chemistry, however, may be required to get a sufficiently large refractive-index contrast. Microspheres of high-refractive-index materials do exist but with polydispersity greatly in excess of the maximum of $\approx 10\%$ necessary for formation of highly-ordered crystallites [151, 152, 153]. There also exists the possibility of making a composite, core-shell particle. A thin shell of high-refractive-index material could substantially enhance the Mie resonances within the particle and improve the chances of making a full band gap. Furthermore, since most of the material would be of relatively low refractive index, a Mie resonance at a given wavelength is likely to occur in a core-shell particle that is larger than the equivalent solid, high-n particle. This larger size might make the assembly process easier to control by reducing the spatial precision required to have a sufficiently ordered lattice.

The design of structures so far has been guided by finding solutions of Maxwell's

equations in various periodic lattices. There are, however, some general guiding principles. The Bragg point of view tells us what type of structure is needed: a nearly spherical Brillouin zone maximizes the chance that stop bands at a given λ will overlap in all directions. The coupled-particle point of view indicates that a large refractive-index contrast is needed and that the wavelength must be chosen to maximize the Mie resonance. More careful calculations also indicate that the optimal particle volume fraction (ϕ) is approximately 0.2-0.3 and that the crystal should be close-packed. A structure that combines all of these properties is a diamond comprised of close-packed spherical particles (ϕ=0.34) whose refractive index is twice that of the surrounding medium [154]. A face-centered-cubic (FCC) lattice of spheres (of high or low n) is now understood not to exhibit a full gap [155, 156]. Breaking the FCC symmetry by using non-spherical particles [157] or by adding a basis to the lattice [158] can, however, open up a full band gap.

Even with the relatively low-n materials currently available (for polystyrene, $n =$ 1.59 in the visible), we can improve our understanding of photonic structure. The photonic band structure of low-refractive-index-contrast colloidal crystals of face-centered cubic structure (FCC) [159, 160] (including bulk point defects [161]) and body-centered-cubic structure (BCC) [67] have recently been measured and compared to theoretical predictions.

6.1.2 Other Assembly Techniques

Van Blaaderen, Ruel, and Wiltzius recently demonstrated a new technique for "colloidal epitaxy" [138]. Using optical lithography, they made samples with an ordered planar array of submicron holes in a 0.5-μm-thick layer of poly(methylmethacrylate) (PMMA). A suspension of silica spheres in water and glycerol was then admitted into the sample. Because the particles were heavy (density > 2 g/cc), a gravitational potential of $\approx 0.5k_BT$ guided them into the holes. A second layer occupied the interstitial sites above the first layer, etc.. Highly-ordered face-centered cubic crystals several mm in thickness were made.

Applying a voltage across a sample can also induce forces on particles, causing them to order themselves [162, 163, 164, 165]. Electrohydrodynamic forces arise from the flow of water around the particles, pulling them together. The technique works with charged or neutral particles with diameters ranging from 16 nm to one μm. Some degree of spatial control can be obtained by patterning electrodes on a surface [165]. In all of the reported experiments, however, only patterns with triangular order were made. This technique does not offer the ability to make different symmetries, defects, or non-periodic patterns.

Another technique involves deposition of alternating layers of positively- and negatively-charged species. The electrostatic attraction between the particles causes them to form stacked monolayers that are usually disordered within the plane [166,

167].

6.2 Making Colloidal Templates with Electron-Beam Lithography

We have developed a technique that allows anionic particles in suspension to be arranged on a glass surface in any two-dimensional pattern [168]. Unlike another approach that relies on optical lithography [169], the present method allows precise positioning of particles arranged in close-packed or spread-out arrays. It also allows formation of binary lattices (section 6.3). We demonstrate the technique by arranging plain polystyrene sulfate spheres and carboxylate-modified polystyrene spheres in square and triangular patterns on a glass coverslip. The following section contains a brief summary of the technique. The details of the experimental procedure are given in Chapter 7.

6.2.1 Experimental Procedure

An outline of the technique is shown in Fig. 6.2. Steps (a) and (b) are standard electron-beam lithography procedures. A plain cover glass is cleaned in an acid wash, then covered with a 150-nm layer of poly(methylmethacrylate) (PMMA) and a 40-nm layer of Al (not shown). Inside a scanning-electron microscope (SEM), the chosen pattern of tiny 50-nm squares is written. The Al layer is then removed with strong NaOH, and the PMMA is washed away where it was exposed to the electron beam

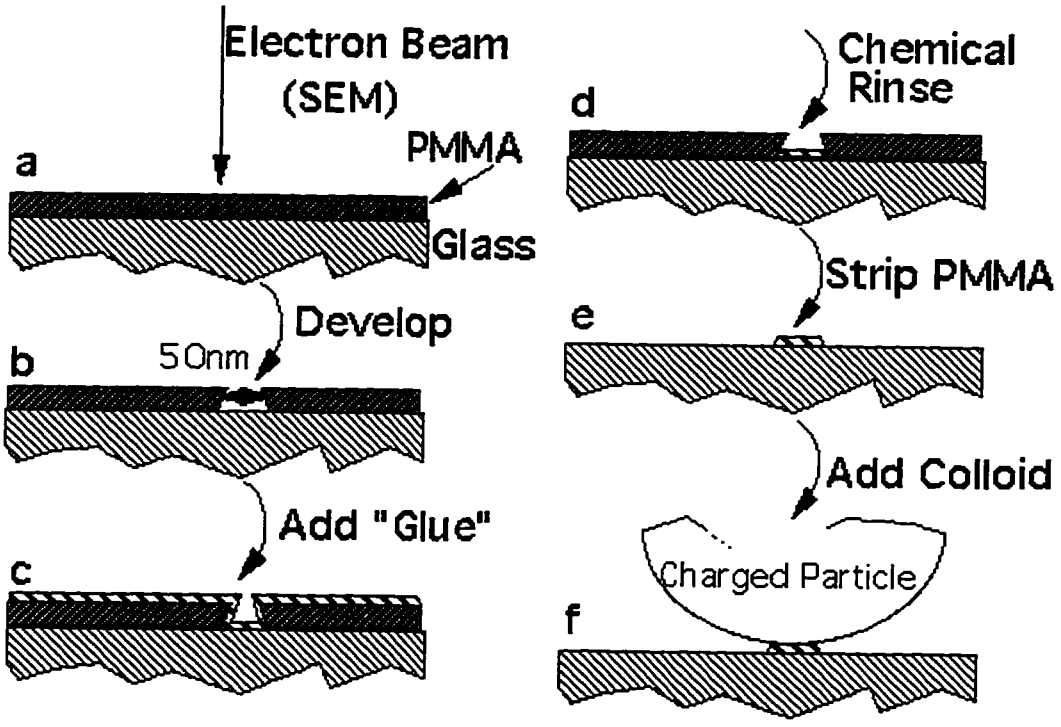

Figure 6.2: Schematic of the lithographic procedure for making two-dimensional particle arrays. The steps are briefly described in the text, with more deatils provided in Chapter 7.

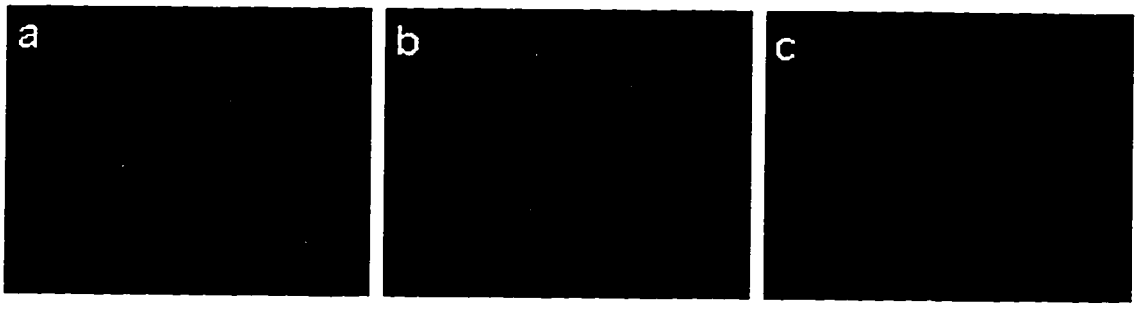

Figure 6.3: Optical micrograph of 11x11 patterns of holes in PMMA. (a) A close-packed sqare lattice designed for 460-nm spheres. (b) A BCC lattice designed from 460-nm spheres. (c) A triangular lattice, the first layer of a close-packed diamond structure of 460-nm spheres. Since these holes are so easily visible, they are probably overexposed. (Micrographs by Jonah Paransky.)

(using a standard developer). In step (c), the sample is exposed to "glue" molecules (discussed below) that stick to the glass where it is exposed. In (d), the excess glue is removed, followed by the remaining PMMA in step (e). Finally, in (f) the substrate is exposed to an aqueous colloid (pH 7, $\approx$0.01 M NaCl) for four hours to allow the particles to diffuse onto the glue sites and stick there. The sample is then rinsed with clean water, leaving only the particles that are stuck to the glue spots (along with a very low density of randomly-stuck particles).

Optical micrographs of the substrate at various stages help to illustrate the procedure. Fig. 6.3 shows an optical micrograph (100x) of a substrate just after the PMMA has been developed (see (b) of Fig. 6.2). The "50-nm" holes are clearly visible. On closer inspection, however, it appears that samples that look like this are, in fact, overexposed to the electron beam. The PMMA, when overexposed, becomes strongly *resistant* to removal by the developer, leaving a small mound in the center of the

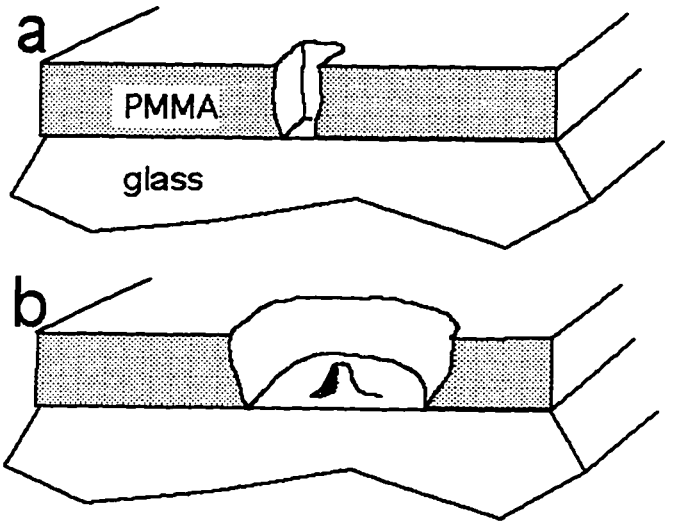

Figure 6.4: Cartoon of (a) a good exposure and developing of PMMA layer and of (b) an overexposure. The small mound in (b) is a result of drastic overexposure to the PMMA (adapted from SEM micrographs by George H. Watson).

hole. In addition, the developed hole gets wider due to electron scattering. Fig. 6.4 illustrates the appearance of a well-exposed 50-nm hole (a) and an overexposed "50-nm" hole (b). The sample shown in Fig. 6.3 is similar to Fig. 6.4 (b). The optimal exposure time depends on the hole size and the array size and spacing (see Chapter 7). During exposure calibration, the holes should be checked after developing by sputtering a thin layer of Au, looking at the sample in the SEM, and comparing it to Fig. 6.4.

We have used two different "glue" molecules. 3-aminopropyltriethoxysilane (from Polysciences), hereafter called AS, was abandoned after a few months due to contamination of our stock solution. After buying new stock solutions from two companies and finding them both to be contaminated, it became clear that AS was not the most

convenient choice. The AS works – in principal – by covalent bonding of the reactive silane to the silicon in the glass [170]. Our approach, which worked for several months before suddenly failing, was to expose the sample to full-strength AS for 20 s, then rinse with ethanol, methanol, and iso-propyl alcohol (IPA). This procedure relies on a thin adsorbed layer of water on the glass surface to hydrolyze the silane and make it reactive. The amount of adsorbed water depends strongly on atmospheric conditions. In addition, the orientation of the AS molecules appears to be very dependent on the pH of the solution. For these reasons, as well as the apparent contamination of the stock solution, we could not repeatably make a complete monolayer of AS on the glass.

The other glue, poly-L-lysine, is a polycationic molecule (at pH near 7) that forms ionic bonds with the negatively-charged glass surface. It is often used to attach biological cells to glass substrates [171]. When the particle suspension or cells are introduced to the glass substrate, the poly-L-lysine holds the particles to the glass by ionic bonds. The bonds are strong enough to prevent the particles from diffusing away or from being washed away when the sample is washed under a gentle jet of water. They cannot withstand an ultrasound bath or evaporation of the water, as will be discussed is section 6.4.1. We used the poly-L-lysine solution as received from Sigma Diagnostics (St. Louis, MO, cat. no. P8920, 0.1% w/v in water). As a simple test of the ability of poly-L-lysine to hold the particles, we placed a drop of the poly-L-lysine

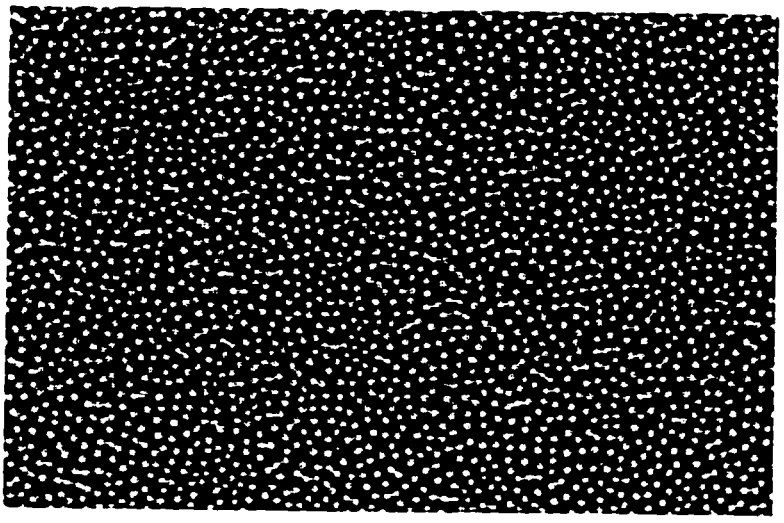

Figure 6.5: Optical micrograph of 0.460-μm-diameter spheres stuck to glass by poly-L-lysine. A slide not exposed to the poly-L-lysine would typically have $\sim$ 10 particles in the field of view.

solution on a glass coverslip for between 30 s and 15 min., rinsed it with de-ionized and filtered water, and exposed it to polystyrene spheres in solution at pH $\approx$ 7 and [NaCl] $\approx$ 0.01 M. It is believed that a single monolayer of the poly-L-lysine covers the glass, effectively making the surface cationic (+). A typical result is shown in Fig. 6.5: the substrate is fully packed with 0.46-μm spheres.

6.2.2 Results

Fig. 6.6 shows optical micrographs of 0.46-μm-diameter polystyrene spheres that are stuck to patterns written with the electron-beam lithography procedure. The glue molecules used in (a) and (b) were, respectively, AS and poly-L-lysine. In (a), there is low "background coverage" and reasonably high occupation of the glue sites ($\approx$ 70%).

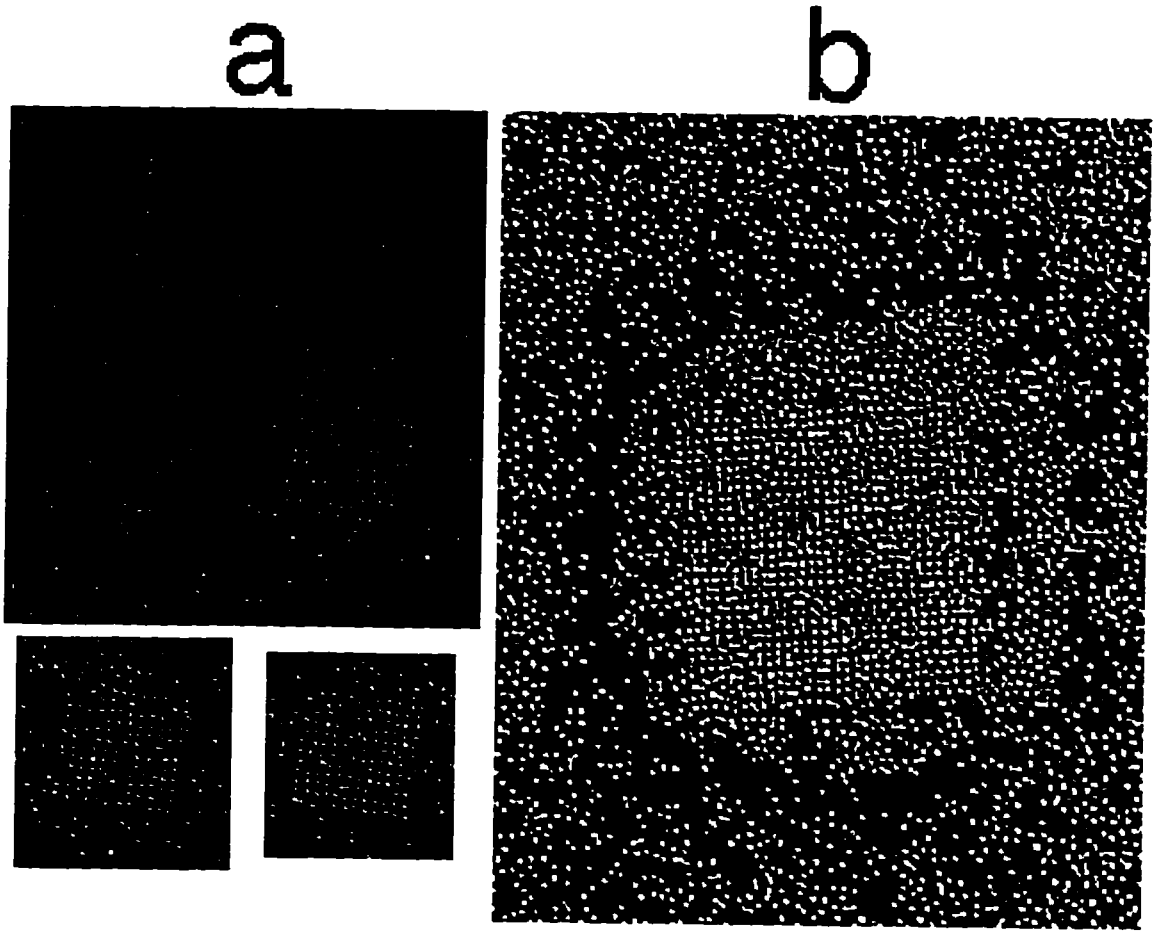

Figure 6.6: Optical micrographs of 0.46-μm polystyrene spheres stuck to two-dimensional patterns made by electron-beam lithography. (a) 12x12 arrays of various symmetries are shown (AS glue) (Micrograph by Jonah Paransky). (b) 30x30 square array of particles (acid wash; Poly-L-lysine glue) (Sample and micrograph by George H. Watson, Derek Rethwisch and Joe Matteo).

This was among the better of the samples made with AS. In (b), the glass was carefully acid-washed first, then processed as above, but with poly-L-lysine glue. The coverage of the glue spots is much higher – very near 100%, but the background coverage is also very high, probably due to contamination during the rinsing procedure. The improved coverage of the lattice sites may be due to the preliminary acid wash which is thought to increase the number of $(OH)^-$ on the glass surface by a factor of nearly 2. Some further work is needed to isolate and remove the source of the background coverage.

This technique will allow fabrication of a wide variety of patterns using a wide variety of particles. Defects can be intentionally made by omitting some sites, adding extra sites, etc. The array can be as large as 86 μm x 86 μm without further alteration of the procedure. The minimum size of the glue spots appears to be approximately 50 nm (estimated by the deviation of particles from the spot position). Finally, since the glue works by an ionic interaction, this technique should work for any negatively-charged bodies, such as biological cells and TiO_2 particles.

6.3 Convective Assembly of Three-Dimensional Colloidal Crystals

Convective assembly allows simple and rapid fabrication of macroscopic, highly-ordered, monolayer particle arrays [172, 173, 174, 175, 176]. We have adapted the technique to allow deposition of *multiple layers* of particles, with each layer organized

according to the layer of particles below it [177]. In this section, I will first describe the physical principles of the technique (section 6.3.1), then describe our experimental procedure (section 6.3.2), and finally present optical micrographs of some samples, including AB_2 colloidal crystals (section 6.3.3).

Compared to the lithographic technique of section 6.2 and of [138], the convective assembly discussed here offers the potential of multiple layers of different species, large coverage area and ease of use. While it does not allow monolayers to be arranged with arbitrary patterns, we do find that particles deposited onto an *existing* particle array will follow the pattern of the existing array. Another important advantage of convective assembly is that it drives off the solvent, thereby increasing the refractive-index ratio (particle:background medium) from 1.2 to 1.6 in the case of polystyrene spheres and water. Our goal will therefore be to use the lithographic technique for the first layer, then use convective assembly for subsequent layers (section 6.4.1).

6.3.1 Theory

Nagayama and coworkers have developed the technique of convective assembly of a monolayer. They found that pulling a glass substrate out of a colloidal suspension at a controlled rate led to formation of a macroscopic, triangular, close-packed macroscopic monolayer of particles (see Fig. 6.13). The following brief discussion of the mechanism is adapted from their papers [172, 173, 174, 175, 176].

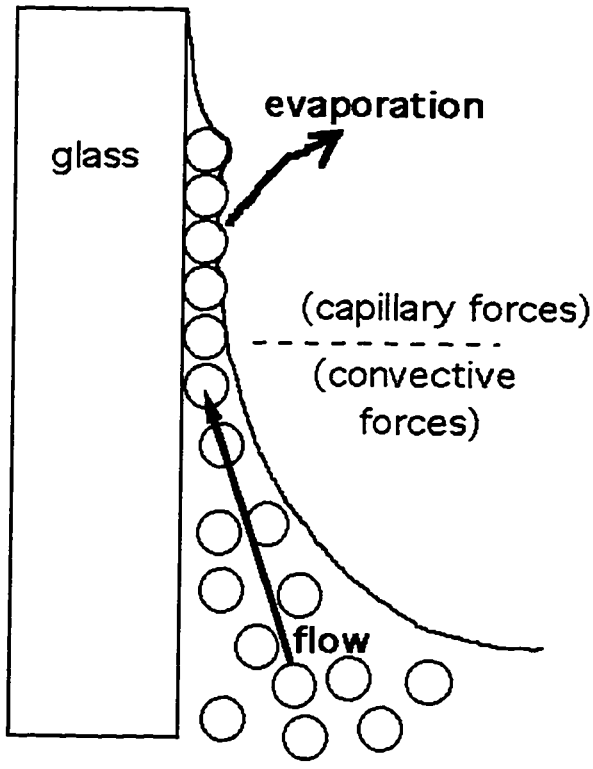

Figure 6.7: Illustration of the forces at work in convective assembly. Evaporation of the water from the thin film causes an influx of water and particles. The particles are pinned where the film is thinner than their diameter (next to the dashed line). Above this pinning point, the particles are pulled toward one another by capillary forces.

The cartoon in Fig. 6.7 illustrates the two types of forces involved: convective (flow) and capillary forces. To understand the convective forces, we consider the shape of the water-air interface in the absence of particles (Fig. 6.8). The key to the technique is to use a hydrophilic substrate such as clean glass so that the water forms a thin film. Water is lost by evaporation from the air-water interface. Therefore, there is a large net flow of water through area A in Fig. 6.8 to compensate for the evaporation from the large area of the thin film. If there are particles in suspension,

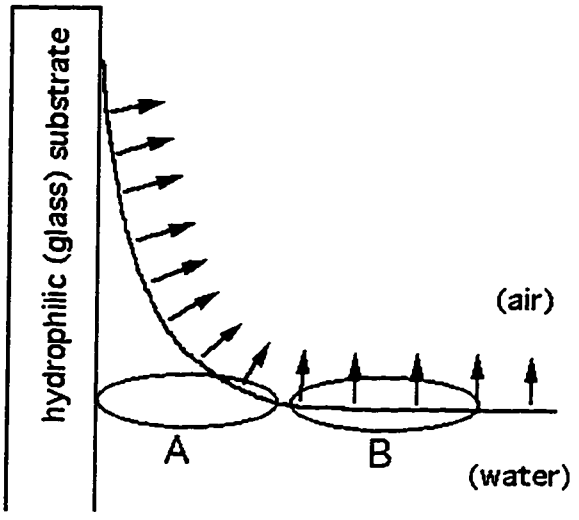

Figure 6.8: Cartoon of the thin film formed by water at a hydrophilic glass surface. The arrows represent water evaporation. The vertical water flow through area A is much larger than through area B to compensate for the evaporation.

they are carried by the flowing water. By mounting an unsealed sample on an optical microscope, we have observed submicron particles rushing toward the drying front at a rate of several μm/s. The particles become trapped at the line (normal to the page in Fig. 6.7) where the film becomes comparable to their diameter. The rate of pulling the substrate from the suspension must be controlled so that the pinning point recedes at the same rate that new particles flow in from the bulk. Pulling too slowly results in accumulation of particles in more than one layer; pulling too fast results in sparse coverage.

Above the pinning point, the particles are still wet by the water. The top part of Fig. 6.7 shows the curved meniscus that forms between neighboring particles. In-

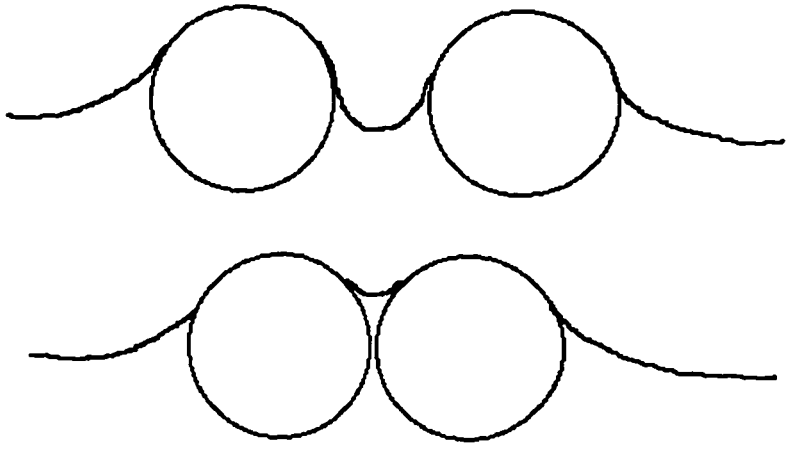

Figure 6.9: Illustration of the capillary force that pulls immersed particles toward one another. As the particles move together (from (a) to (b)), the surface area of the water decreases.

tramolecular forces among the water molecules attempt to minimize the area of the meniscus, resulting in a "capillary" force that pulls the particles into contact with one another (see Fig. 6.9 and [178]). This process orders the particles into a planar close-packed, triangular crystal (the structure having the highest possible density).

In addition to pulling the particles together, the capillary force pulls particles *toward the substrate.* This component of the force enables convective assembly of non-triangular structures on a second layer. An example is illustrated in Fig. 6.10. Here, the relatively small particles in suspension are deposited atop the interstices of the underneath layer. The component of the capillary force that pulls toward the substrate overwhelms the force pulling particles toward one another. Thus, the *size* of the particles in the first layer determines the *spacing* of particles in the second layer. The essential requirement of convective assembly of a second layer is that the

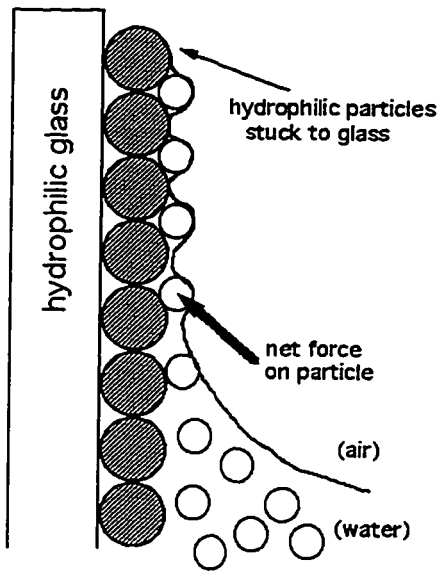

Figure 6.10: Illustration of the ordering of particles in a second layer atop the first layer. The capillary force (large arrow) pushes the small spheres toward the substrate and into the interstitial gaps of the large spheres.

particles in the underneath layer must be as hydrophilic as possible so that a thin film of water forms.

With multiple-layer deposition, we can make binary crystals [177]. For example, a simple geometric calculation shows that when the ratio of sphere sizes, $\alpha > 1.733$, the smaller spheres can cover all of the interstices in the layer of larger spheres, making a honeycomb plane (see the stacking of marbles shown in Fig. 6.11). When α <1.896, a subsequent layer of large spheres will fit in uniquely-defined holes. There is therefore a range of "magic sphere sizes", $1.733 < \alpha < 1.896$, for which large- and small-sphere planes can be alternated, thus forming an AB_2-type crystal lattice. Using spheres of diameters 0.832 and 0.460 μm($\alpha = 1.81$), we have stacked as many as five layers of spheres (large, small, large, small, large). Optical micrographs that show the layers of large and small spheres are shown in section 6.3.3.

Altering the refractive indices of the spheres in different layers could improve the photonic structure by changing the magnitudes of the wave vectors in some directions (by a factor of n_A/n_B, the ratio of the refractive indices of spheres in the different layers), effectively making the Brilloun zone more spherical. Another possibility includes high-refractive index small spheres and transparent large spheres. The resulting structure – parallel honeycomb planes – is an attractive system for studying two-dimensional photonic structures, since the honeycomb structure is predicted to have a wide band gap [101].

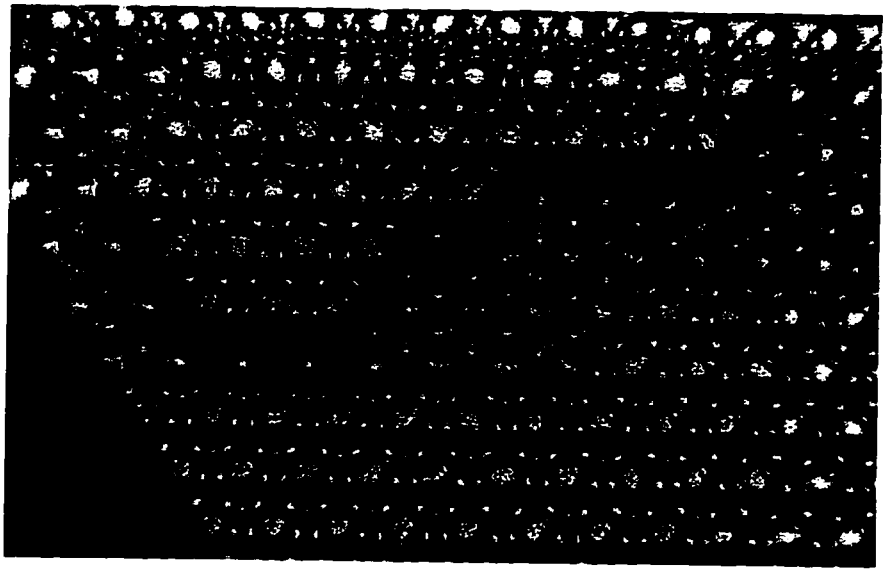

Figure 6.11: Photograph of marbles in the AB_2 binary crystal structure. The size ratio is 1.8.

6.3.2 Experimental Procedure

Fig. 6.12 shows our apparatus for convective assembly. It is similar to the apparati described in [175, 174]. (Other techniques are reported in [173, 172].) A stepper motor was attached to a rigid support that was bolted to a table to avoid vibrations. A threaded rod was epoxied to the motor's drive shaft and threaded through a nut (the black rectangle in the figure). The nut was epoxied to an iron bar which slid on a bed of vacuum grease along a fixed aluminum bar. Thus, as the motor turned, the iron bar moved up or down. A small piece of glass coverslip (≈25mm x 8mm) was attached upright to the iron bar by a magnet. An integrated circuit (IC) chip was used to control the stepper motor (UCN-5804B BiMOS II Translator/Driver, part no.

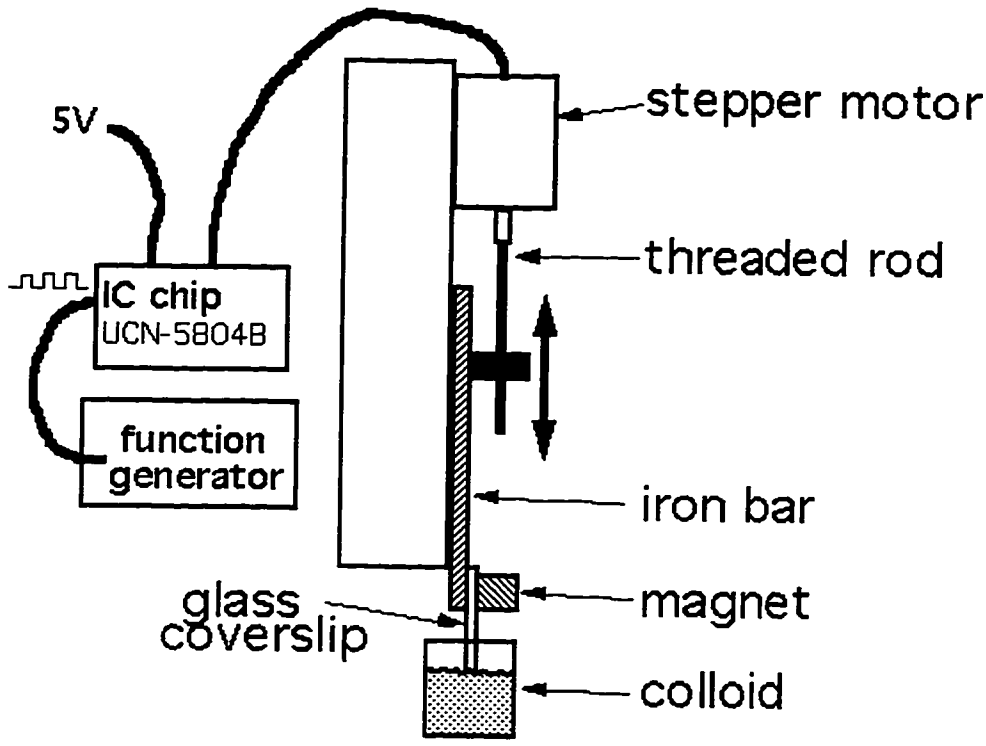

Figure 6.12: Apparatus used for convective assembly. The motor turns a threaded rod which slides the iron bar upward, pulling the glass coverslip out of the colloid. A function generator controls the turning rate of the motor.

Q5029 from Herbach and Rademan Co., NJ, 800-848-8001). The five volts required to power the IC chip's logic also drives the motor with sufficient torque. The controller chip requires a square-wave (TTL) signal from a function generator to control the motor's turning rate. With the thread pitch and motor-drive mode that I selected, the glass substrate moved at a rate given by $1.9f$ μm/s, where f is the frequency (in Hz) of the square-wave generator. Typical drive speeds are between 8 μm/s (for .83 μm spheres) and 20 μm/s (for .46 μm spheres). The entire assembly was surrounded by a plexiglass box to reduce the irreproducible effects of wind currents. The glass sample was placed on the iron bar, lowered into solution as far as possible ($\approx$ one cm), then raised at the desired rate. For inspection under the microscope, the sample was placed face down on a small piece of parafilm on a glass slide. Gently heating the parafilm over low heat and then squeezing it between the coverslip and slide holds everything together. The coverslip can later be easily removed for application of another layer of particles.

To deposit multiple layers, the samples were simply redipped. Samples must first be thoroughly dried, however, by placing them in an oven at $\approx 90°$ C for a few hours. If the samples are not sufficiently dried, the particles are removed by the water upon redipping into solution. We have found that the more hydrophilic the glass is, the greater the risk of the particles being removed. On the other hand, if the particles are overheated, they deform visibly [179]. For example, 0.793-μm spheres heated at

105° for 4 h, 20 min were visibly deformed under the optical microscope; heating at lower temperatures or for 2 h did not modify the particles in any visible way.

To apply multiple layers (and for optimal single layers) it is essential to use highly-hydrophilic particles. We used carboxylate-modified polystyrene spheres. These particles are available from many distributors (including Seradyn, Inc. (317-266-2000) and Bangs Laboratories (317-570-7020)). The average surface area per charge is approx. 20 (Angstrom)^2 per charge, approximately 20 times smaller than than plain polystyrene sulfate spheres.

6.3.3 Experimental Results

An example of a well-ordered monolayer of carboxylate-modified 0.832-μm-diameter spheres is shown in Fig. 6.13. This figure shows another very general feature of convectively-assembled patterns: there are alternating monolayer and multi-layer regions that form stripes perpendicular to the pull direction [176]. These stripes are visible to the eye. The particles on the left side of Fig. 6.13 form a triangular monolayer. We have found that washing the coverslips in an acid solution (see Chapter 7) greatly increases the size of the well-ordered monolayer regions. Those on the right side of Fig. 6.13 have formed a triangular bilayer (which is not so well-ordered in all samples). The narrow transition region, which appears dark in the photograph, almost always contains crystallites of *square* symmetry. The transition from

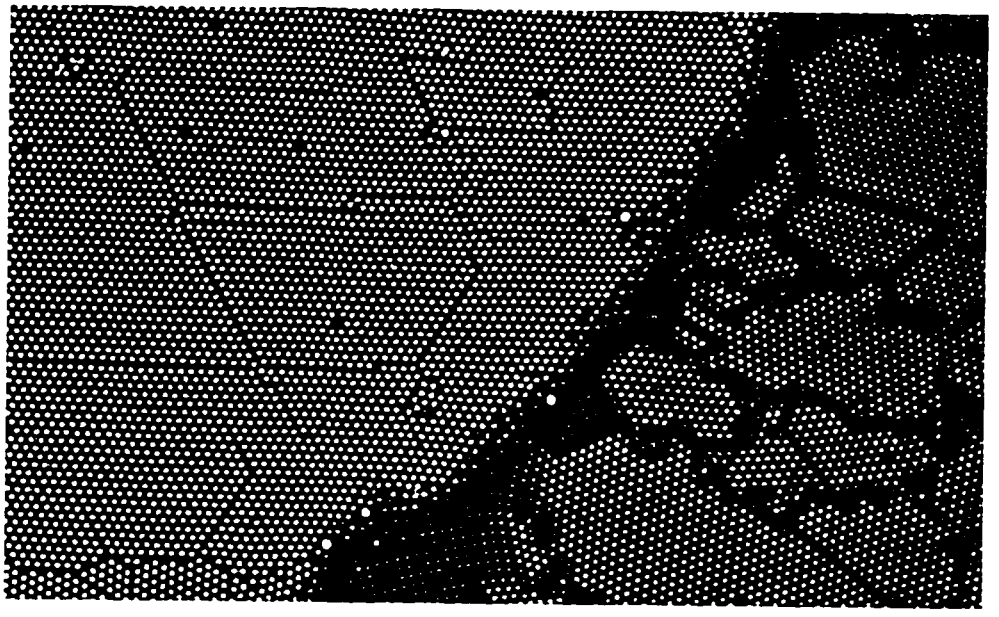

Figure 6.13: Optical micrograph of a sample after one round of convective assembly. Monolayer triangles, bilayer squares, and bilayer triangles are visible from left to right. The spheres are 0.832-μm in diameter. The sample was pulled from solution toward the left.

single-layer triangular to two-layer square, then two-layer triangular is very similar to structures found in equilibriated samples of polystyrene spheres confined between two plates in a wedge geometry [180]. In those experiments, gradually increasing the plate spacing caused the structure to pass through the same sequence of structures. The explanation of the stripe patterns is that the water interface moves across the glass substrate with a periodic stick-slip motion [176]. While the water "sticks", the interface moves relatively slowly, so that multiple layers of particles accumulate there. While the water "slips", a monolayer is formed. At some time between sticking and slipping, perhaps the particle accumulate in a double layer and have time to form the equilibium structure corresponding to the double-layer square symmetry found in [180]. Attempts to further increase the size of the monolayer regions by changing the angle between the pull rate and the force due to gravity are currently under way.

Figs. 6.14 and 6.15 show optical micrographs of *multilayer* AB_2 structures of 0.832-μm and 0.460-μm carboxylate-modified spheres. The point of view is the same as that of Fig. 6.11 (which is a photograph of cm-sized marbles). These micrographs do not represent the thickest or largest crystallites that we have made, but they show the layering most clearly. Visualizing more than two layers of particles is difficult, but is made much easier by a computer-controlled microscope focus control and image acquisition (see Chapter 7). Sputtering a few nanometers of gold on the sample and viewing it under the scanning electron microscope could also help. We have attained

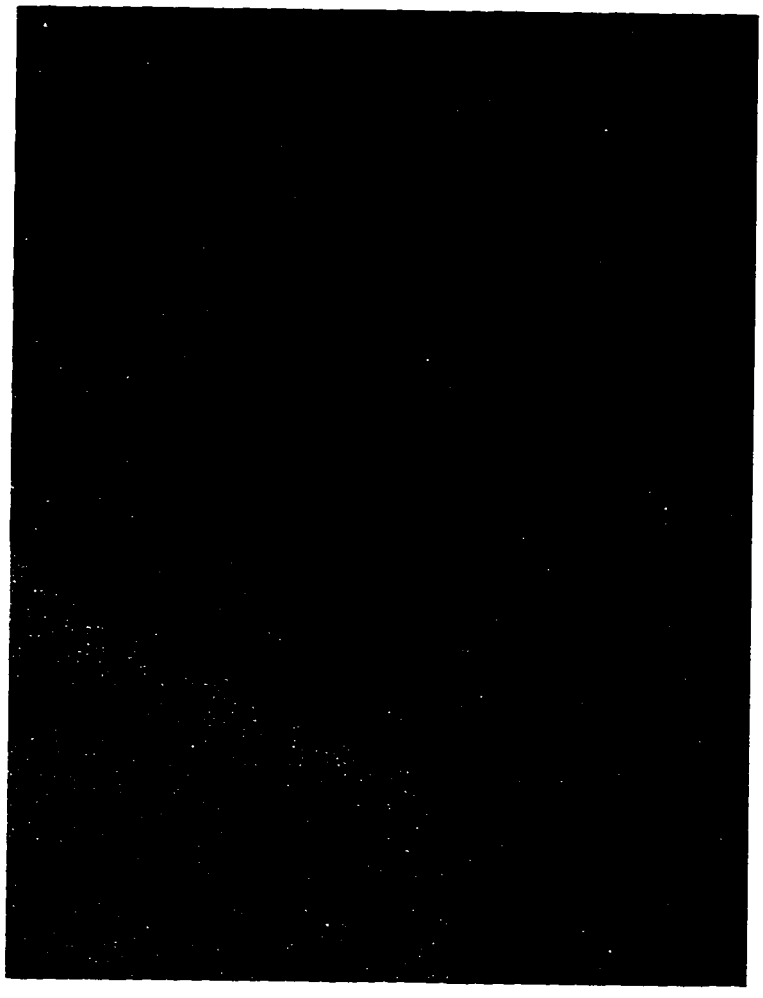

Figure 6.14: Optical micrograph of three layers of a binary AB_2 crystal made by convective assembly. The sphere diameters are 0.832 and 0.460 μm($\alpha = 1.81$). Moving outward from the lower-left corner, we see clean glass, a close-packed monolayer of large spheres, a two-layer region, and a three-layer region. In the one-layer region, the large spheres appear as gray circles which appear to be well separated but which are, in fact, close-packed. In the two-layer region, the small spheres are visible as small black dots in a honeycomb pattern. In the three-layer region, the white large spheres lie directly above the large spheres on the bottom layer.

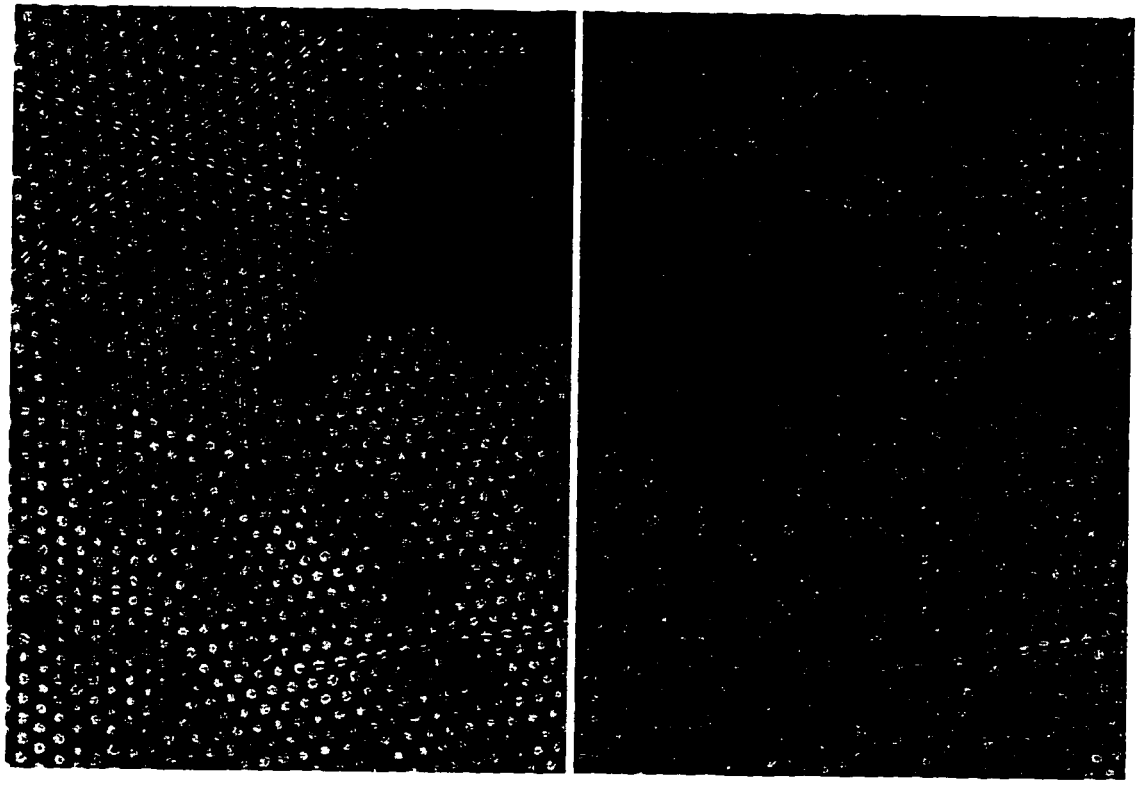

Figure 6.15: Optical micrographs of two different planes in the same area of an AB_2 crystal made by convective assembly. The sphere diameters are 0.832- and 0.460-μm. The micrograph on the left shows the close-packed layer of large spheres at the wall. The one on the right shows the plane ≈ 1 μm above the first layer. The black lines show that the large spheres in the first and third planes are atop one another. The small black spots on the bottom half of the photograph on the right are the small spheres, which are arranged in hexagons centered on the large spheres.

a maximum of five layers (by dipping five times). More layers will be possible when the area of the ordered domains in the first layer is increased.

6.4 Conclusion

6.4.1 Combining Lithography and Convective Assembly

The fact that the smaller sphere in the AB_2 structures reported in section 6.3.3 were pulled by capillary forces into alignment with the substrate layer suggests that we can build atop a variety of substrates. For example, a square substrate assembled using the lithographic technique could be used as a substrate for convective assembly, allowing truly three-dimensional crystals to be made. Two-dimensional rectangular or other crystalline (and perhaps even quasi-crystalline) symmetries might, in this way, be propagated into three dimensions. A potential difficulty is that the particles that are held in place by the (poly-L-lysine) glue might be torn away by the capillary forces that occur during convective assembly. Simply allowing the lithographically-assembled patterns to dry always results in particles being pulled toward one another to the point of contact. Non-close-packed arrays might therefore be destroyed. Solutions to this potential problem might include first replacing the water with a solvent of low surface tension and then drying the monolayer pattern. Other possibilities include adding surfactant to reduce surface tension, or drying off the solvent near its critical point or boiling point.

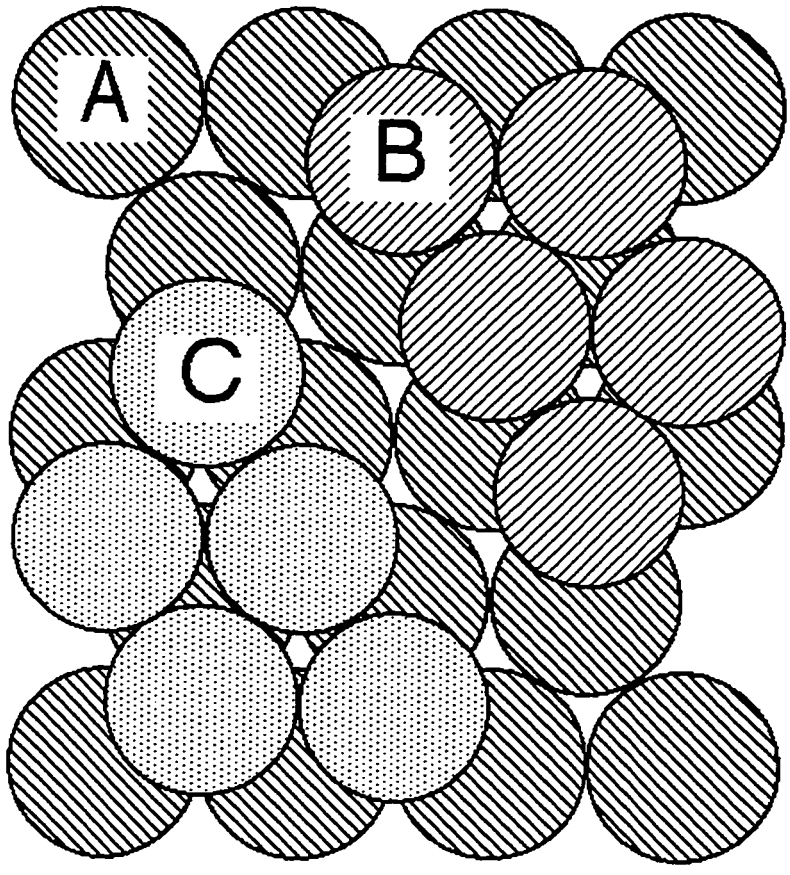

Figure 6.16: Illustration of the stacking faults that arise when stacking spheres randomly atop a layer with triangular order. There are two ways (B and C) to stack spheres in the second plane. A defect occurs where B and C meet.

An ordered layer of anionic particles might from a similarly ordered array of cationic particles due to the electrostatic attractions. Since cationic particles are available commercially, it is probably worth trying this rather simple experiment.

A first layer of triangular symmetry does not uniquely determine a three dimensional crystal structure. The problem, illustrated in Fig. 6.16, is that there are two ways to stack on top of the first layer (which I will call A). The two possible second

layers, B and C, are shifted with respect to one another. Thus, if the second layer is allowed to grow by a random diffusive process, there will always be defects in the plane where regions of type B meet regions of type C. Furthermore, there is no long-range order normal to the plane, so that face-centered cubic ($ABCABCAB...$) and hexagonal close-packed ($ABABAB...$) will not form. It is possible that since convective assembly applies the second layer along the direction of the pull, there will not be in-plane defects. There is, however, no reason to expect any long-range order normal to the plane. (Of course, using spheres of alternating sizes can solve this problem, as in the example of AB_2). The FCC structure can, however, be made starting from a close-packed square lattice (the (100) plane). Stacking spheres on top of a planar array with square or rectangular symmetry can lead to a unique crystal.

The only arrangement of high-refractive index spheres that is currently known to exhibit a full photonic band gap is a diamond structure [154]. Alas, the only way (that I could find) to stack marbles in a diamond lattice is to start from the (111) plane, which has triangular symmetry. Despite the problems pointed out in the previous paragraph, it is probably worth while to attempt this structure. It is possible that the random stacking sequence (ABC, etc.) will not destroy the photonic properties. A diamond-*like* structure (that has a random sequence of ABC) may be attainable with convective assembly by starting with a close-packed triangular plane of spheres of diameter a, and building on top of them with spheres of size $(a\sqrt{6}/4)$.

Diamond is known to be unstable when there exist only centro-symmetric forces between particles. In convective assembly, however, there is a non-centro-symmetric component that points toward the substrate.

6.4.2 Light Scattering Experiments

Once the samples are made, the propagation of light through them can be studied by performing scattering experiments in an optical microscope (see Chapter 7 for more details). The microscope allows simultaneous imaging and scattering and allows experiments on small samples. To study two-dimensional arrays, the incident light can be sent through the glass substrate at an angle close to the interface, so that it is critically reflected (see section 7.3.5, page 209). In thas case, there will be an evanescent wave that propagates along the glass surface on the side where the particles are arranged. The experiments can be done using a high-numerical-aperture objective. The intensity of light reflected and transmitted can be measured as functions of λ and incident direction. Furthermore, using a near-field optical microscope, the spatial distribution of light intensity can be measured with high precision ($\approx$ 20 nm) near defects. Such experiments would provide valuable information about the nature and spatial extent of modes that can propagate along defects. The emission spectra of dye molecules inside a colloidal crystals (and near defects) could also be measured to see how the modes affect emission [181]. Similarly, transmission through and

reflection from three-dimensional samples can be measured for various λ, directions, and structures.

Chapter 7

Experimental Methods

7.1 Introduction

This chapter contains more detailed discussions of the experimental procedures that I used in obtaining the results in Chapters 2-6. The reader should keep in mind is that this is what *was* done and that there may well be better ways to do some things. Some of the procedures, such as in section 7.5.4 are still under development.

There are four experimental topics covered in this chapter. In section 7.2, I will describe the details of mixing colloid samples, sample cells, and vesicles. Section 7.3 contains some details about the care and use of the microscope and associated equipment for imaging, for laser tweezers, and for light scattering. Section 7.4 describes use of a Macintosh computer to control a shutter and focus-drive and to acquire images, and some details on image analysis. Finally, in section 7.5, I will describe some details of the electron-beam lithography and wet chemistry techniques that were developed for making arrays of microscopic particles and for etching microscopic holes in silicon.

7.2 Sample Preparation

7.2.1 Colloids

All of the samples used in this thesis were aqueous suspensions of polystyrene sulfate spheres (with the exception of the carboxylate-modified particles that were used for convective assembly; page 183). All of the samples were bought from Seradyn, Inc. ((317) 266-2000) (with one exception). Other distributors include Bangs Labs ((317) 570-7020), Interfacial Dynamics, Duke Scientific, and Molecular Probes ((541) 465-8300). Typically, the particles are monodisperse to within about 2%, or a little bit more if the particles are less than 100 nm in diameter. Some of these companies make their own particles and some buy them from distributors, but none will tell you exactly what is inside them. Each has a proprietary anionic surfactant which is thought to stick to the particles and enhance their surface charge density, thus making them more stable against flocculation. For example, at least some particles from Bangs Labs have much more surfactant that those from Seradyn, which adversely affected the results of convective assembly. I suggest using one supplier for all particles in any particular experiment. The Seradyn spheres were found to resemble hard spheres by checking that freezing occurs in a monodisperse mixture only when the volume fraction (ϕ) is near 0.494 [60, 20]. We therefore used these samples as delivered. When diluting them, we used filtered, de-ionized water that had 0.01 M NaCl added to it. In my experience, the Seradyn particles are stable when the salt concentration

is less than ≈ 0.09 M. Above that point (which varies somewhat), they flocculate.

Stock colloids should be kept in the refrigerator to reduce the chance of biological contamination. In addition, stock solutions (especially those with $\phi > 0.1$) should be "cleansed" every few months (or before each set of experiments) to remove flocculates. The simplest way to do this is to centrifuge the solution at a rate chosen so that the *individual* particles do not sediment, but the clusters do. For example, for 83 nm spheres, a centrifuging speed of approximately 4000 turns per minute for 1 to 10 minutes works well. Since colloidal particles sediment at a rate proportional to the diameter squared (not cubed – see [7, 12]), large particles should be spun at a slower speed. The supernatant is then removed and stored in a cleaned bottle. For a survey of centrifuge techniques, see [108].

The volume fractions of new or newly-cleansed stock solutions should be checked by weighing a small glass vial, adding ≈ 0.2 mL of solution, and weighing again. After being stored in an oven (near 50 ° C) for two days, the sample is weighed again.

Pipettes are an extremely convenient method for measuring small quantities (10-1000 μL) of an aqueous solution. The pipettes should be treated well (never set on their sides, never stored with solution in the tip), and should be calibrated every few months using a mass balance. Pipette tips should always be used only once, never re-injected into the stock bottle. Even when pipettes are used, the quantities should always be checked on a mass balance. The Mettler balance in room 314 of the LRSM

is precise to within ≈ 0.1 mg.

7.2.2 Vesicles

To make vesicles, we used 2-Oleoyl-sn-Glycero-3-Phosphocholine (SOPC) purchased from Avanti Polar-Lipids, Inc. (Alabaster, AL (800) 227-0651). They ship it dissolved in chloroform with a concentration of 25 mg SOPC per mL of solution. We used it as received and stored it in a freezer. Ideally, we would only open the stock bottles in a glove box to avoid letting air into the bottles.

The procedure for making the multilamellar vesicles of Chapter 5 was simply to inject 200 μL of SOPC solution in a 12x75 mm test tube, evaporate the chloroform with a jet of nitrogen under a hood, add 100 μL of aqueous solution, and put in the ultrasonic bath for ≈ 2 min. The result was vesicles of diverse shapes and sizes, but almost all appeared to be multilamellar. Unilamellar (or, at least, few-lamellar) vesicle can be distinguished by their low optical contrast and by their shape fluctuations. The multilamellar vesicles were visibly thick and very rigid. If the added aqueous solution contained polystyrene spheres, some of these appeared on the inside of the vesicles.

To make unilamellar vesicles, we have adopted the following procedure (developed with John Crocker, Derek Wong, and adapted from the procedure of Prof. Dennis E. Discher and coworkers). A 12x75-mm test tube containing a freshly-blown-dry SOPC

sample is placed into a larger test tube and sealed except for a glass tube that carries nitrogen gas in and a hose that carries the gas out (see Fig. 7.1 (a)). The assembly is heated in an oven at 35° C while the dry nitrogen gas gently flows through. After several hours, the flow of dry nitrogen gas is replaced by a flow of water-saturated nitrogen gas that is saturated by water by bubbling it through a test tube of water (see Fig. 7.1 (b)). After 20 min. or more, the aqueous solution is added to the test tube and shaken for a couple of minutes. The ultrasound bath is not used for fear of breaking the large, visible vesicles into small invisible ones.

The solution of vesicles should only be diluted with water that has exactly the same ionic concentration as the colloid solution that was added to the SOPC. Otherwise, the vesicles can swell or shrink due to the osmotically-induced flow of water into or out of the vesicles. Possibly the best way to equalize the ionic strength of the water ad the colloid solutions is with dialysis.

7.2.3 Treatment of Glass: Hydrophilic and Hydrophobic Surfaces

A few colloidal spheres (roughly 1/100 μm^{-2}) seem to stick to a glass surface no matter whether it is cleaned by wiping with a Kimwipe and methanol, boiled in detergent solution or acetone or acid-washed. For viewing samples under the optical microscope, therefore, I simply wipe with methanol three times (or until visibly clean). Before reusing glass sample cells (such as the optical cells), they should be washed to remove

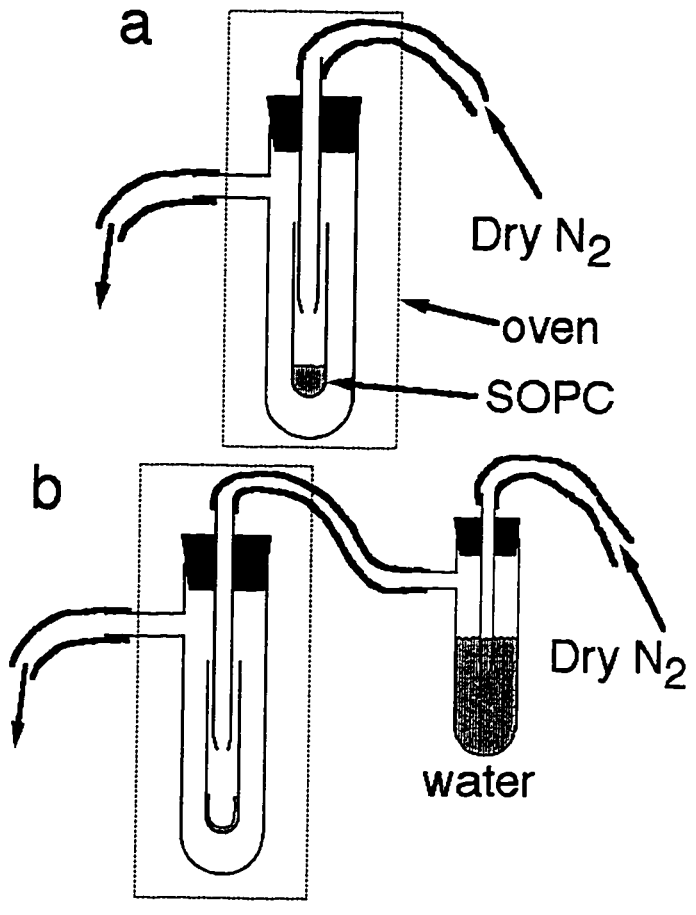

Figure 7.1: Schematic diagram of procedure for making vesicles. A small amount of the SOPC solution is in the small test tube. The outer, larger, test tube is sealed to maintain a (nearly) oxygen-free environment. In (a), the chloroform is driven off by a flow fo dry nitrogen. In (b), the SOPC is "preswelled" by nitrogen gas that is saturated with water vapor. The oven temperature is $\approx 35°$ C.

the residue of the previous experiment. Plentiful rinsing and *minimal* ultrasonicating (which can break cells apart) can be used to remove most of the residue, followed by boiling in de-ionized and ultra-filtered (DIUF) water with detergent, then rinsing with DIUF water, then boiling in DIUF water, then rinsing again in DIUF water and, finally, acetone or methanol (HPLC grade).

For applications that are sensitive to the chemical state of the glass (such as convective assembly and, perhaps, bonding of poly-L-lysine), an acid wash should be used to remove organic and metallic impurities. We have followed a recipe given to us by Denis Pilloud (Univ. of Penn, Biophyics Dept.). Whereas unwashed glass is said to have $\approx$ 60% coverage with $(OH)^-$, acid-washed glass is said to have $\approx$ 100% coverage and is therefore very hydrophilic. The full procedure is to wash in detergent, then store in NaOH (sodium hydroxide; 5 M) for one h, then in "No Chromix" solution (concentrated H_2SO_4 (sulfuric acid) and 50 mM $(NH_4)_2S_2O_8$ (ammonium persulfate)) for one h, then wash with DIUF water. The glass can then be stored in isopropyl alcohol until needed. *Safety precautions must be followed*, since the sodium hydroxide and sulfuric acid solutions are hazardous. Other glass-cleaning procedures and a much broader description of the properties of glass are given in [182].

Glass surfaces can also be made hydrophobic by means of a simple technique. Such slides are useful for oily samples, such as liquid crystals or inverse emulsions. Our procedure was to place a drop of 100% dichlorodimethylsilane (Alfa Aesar, stock no.

14075 (800) 343-0660) on the glass substrate, wait a few seconds, then immediately rinse in a bath of ethanol. The silane bonds to the glass, forming a monolayer with the hydrophobic methyl groups facing outward. After drying the samples, they should appear perfectly clean to the eye and should repel water. "Silanated" hydrophobic glass coverslips can also be purchased.

7.2.4 Making Glass Sample Cells

For viewing samples under the microscope, I made cells from glass slides, coverslips, and 5-minute epoxy. The coverslips were first glued to the slide along two edges only. After the glue dried (at least one h), the sample was injected from one open edge while the air flowed out the other open edge, thus avoiding air bubbles. The open edges were then sealed with a fresh batch of epoxy. As an alternative, Norland optical adhesive (New Brunswick, NJ) has the advantages of (1) a very low rate of leaching salt [15], (2) curing rapidly when exposed to ultraviolet light and (3) being available in a range of viscosities. Cells that could be disassembled without damage were made using parafilm in place of epoxy. Slightly heating the parafilm on a hot plate at its lowest setting makes a sufficiently strong bond that can also be taken apart. Epoxy cells, when made carefully, could last many days before leaking. Since I did not know the leaching characteristics of parafilm, I did not use it for aqueous samples.

7.3 Using the Microscope

7.3.1 Cleaning Optics

For any optics experiments, all components must be covered when not in use and should periodically be checked for dust. The best way to clean mirrors and lenses is the "drop and drag" technique, using a drop of methanol (HPLC grade) and a clean piece of lens paper. Hard-to-reach optics should be cleaned using plastic tweezers and a piece of lens paper. One should avoid touching the lens paper except at the edges, and not use Kimwipes, which are abrasive. Acetone, which removes some coatings, should never be used without the advice of the company that made the optic.

7.3.2 Care of the Optical Microscope

Microscope objectives should *never* be cleaned using a solvent of any kind (except with the advice of a Zeiss technician). The adhesives and anti-fungus compounds can be destroyed by solvents. The oil-immersion objectives should always be wiped off with a clean piece of lens paper after use. If the oil stays on the objective, it can seep in and do damage.

The lenses in the condenser tower should periodically be checked for dust and either blown clean with clean, dry gas or cleaned with lens paper and methanol. Unfortunately, some of the lenses and mirrors are truly inaccessible. To avoid getting dust in the hole underneath the sliding beam splitter holder, I suggest that the sliding

analyzer *always* be kept in its fully inserted position when the microscope is not in use.

7.3.3 Imaging: the Zeiss Axiovert 135

In the Zeiss microscope, samples can be illuminated from above (in "transmission mode") or from below ("reflection" mode). A simplified schematic diagram is in Fig. 7.2; a more complete diagram can be found on a poster made by the Zeiss Company (Thornwood, NY (914) 747-1800). A helpful detailed discussion of microscope optics is found in [183] and some specialized techniques are described in [184]. The microscope is an extraordinarily flexible and powerful platform for a wide range of experiments: imaging, scattering (section 7.3.5), spectroscopy, and manipulation with laser tweezers (section 7.3.4) and micropipettes. All of the above can be done simultaneously.

For looking at all but the most opaque colloids, transmission mode generally has better contrast. For looking at opaque samples (very dense colloids or silicon wafers), reflection mode is necessary. In transmission mode, it is essential to choose the right condenser and to focus it as well as the objective. In general, the numerical aperture (NA) of the condenser should be matched to that of the objective used. We used NA = 1.4 and 0.32 condenser lenses with oil-immersion objectives and with non-immersion objectives, repsectively. Objectives and condenser lenses with NA greater

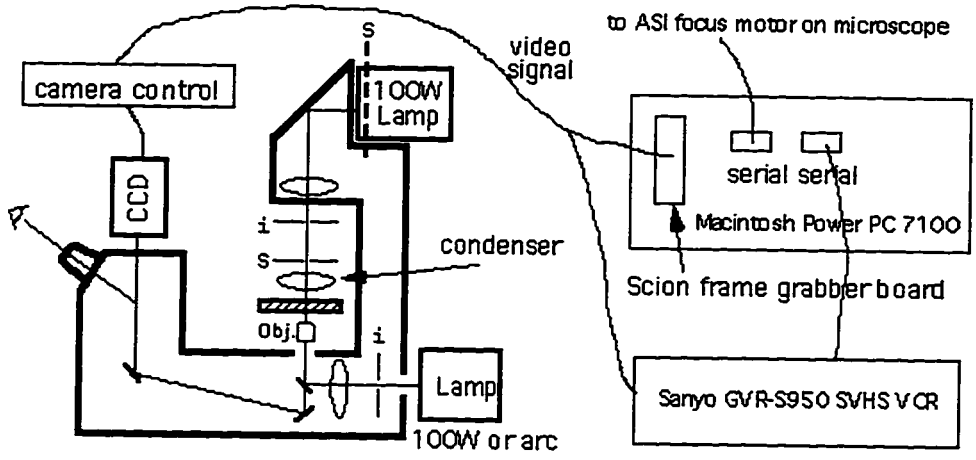

Figure 7.2: Schematic diagram of the Zeiss Axiovert 135 optical microscope. The labels "i" and "s" represent image and scattering planes, respectively.

than 1 require immersion oil for best results. To focus the objective, first check that the "optovar" lens (on the rotating mount below the objective) is set to "1x", then place the smallest possible drop of oil on the objective and raise it until the oil touches the sample. Then, looking into the eyepiece, turn the fine focus control to raise the objective until something is seen. Gently moving the stage back and forth or looking at the edge of the sample helps. If nothing can be seen, remove the sample, wipe the oil from the objective and sample and start again. After the objective has been focussed, the condenser should be focussed by completely closing the upper iris on the condenser (labelled "i" in Fig. 7.2) and moving the condenser up or down until the iris is clearly in focus. Two knobs on the condenser should be used to center the iris in the field of view. The iris can now be opened as desired and the condenser is properly focussed for "Koehler" illumination (equal intensity at all positions positions

in the sample and at all angles).

In Fig. 7.2, there are three irises. Two are placed in the image plane and are labelled "i". The other is in the scattering plane and is labelled "s". The image and scattering planes are related by Fourier transform. For example, closing the image-plane irises will reduce the size of the illuminated sample in the field of view. Closing the scattering-plane iris will reduce the range of angles of illumination, effectively reducing the NA of the imaging system. The axial and in-plane resolution of the microscope improves and the contrast decreases as the NA is increased.

There are many methods for increasing the contrast of images. Most of the images printed in this thesis were obtained without any image-enhancing optics. Some were taken with differential interference contrast (DIC), a technique that can greatly enhance the contrast of colloidal spheres and of variations in the sample height as small as a few nanometers. DIC was essential for visualizing particles on reflective silicon surfaces. To use DIC in transmission mode, two linear polarizers and two Wollaston prisms [185] must be placed on either side of the sample. Starting from the lamp, the light goes through one linear polarizer, a Wollaston, the condenser, the sample, the second Wollaston, a second polarizer (orthogonal to the first), then the eyepice. The Wollaston prism (also called a "DIC slider") is a biaxial material that converts an incoming, linear-polarized, beam into two slightly divergent beams with orthogonal linear polarizations. If there is nothing in the sample plane, the second Wollaston

simply undoes what the first did, resulting in a linear-polarized beam which is blocked by the second polarizer. If there is a sample with an edge (which scatters light in a highly-polarization-dependent way), one polarization component is attenuated and the polarization after the second Wollaston is *rotated.* This spot will appear bright in the image. In transmission, DIC works best with the scattering-plane iris fully open and the position of the second "DIC" slider adjusted to optimize contrast. DIC does not work well with opaque samples because the incident light loses its polarization. In reflection, only one Wollaston is needed. The Zeiss Plan-Neofluar 100x (1.3 NA) objective is optimized for DIC and works well.

The optovar rotating lens mount on the Zeiss allows the objective magnification to be multiplied by 1x, by 1.6x, or by 2.5x. There is also a 4x tube lens that goes between the CCD camera mount and the microscope. Most of the images that were analyzed were taken with the optovar set to 1.6x, which seemed the best compromise between making the particle cover as many pixels as possible (≈ 25) and distorting the image too much.

A floating stage is essential for work in the LRSM laboratory. We used a small one, roughly 3'x4' (Kinetic Systems, "Vibraplane 2212" (617) 522-8700), which reduced the vibrations to a magnitude of less than 1.5 nm (measured using a technique described briefly in section 7.4.1.

7.3.4 Laser Tweezers

The same optics that are used for high-resolution imaging are, fortunately, also useful for laser tweezers [111, 112, 113, 114, 186, 187, 115]. A brief review of the literature seems to indicate that an objective with NA greater than 1.2 is needed. We have used both the Zeiss Plan-Neofluar (100x, NA = 1.3) and the Zeiss Plan-Apochromat (100x, NA = 1.4) with good results. All that is needed is to overfill the back aperture of the objective with a collimated, Gaussian beam (so that the incident beam resembles a plane wave). Our experimental arrangement is shown in Fig. 7.3. A solid-state Nd:YLF (1053 nm, up to 20W CW) laser was used as the trapping beam (infrared traps have the advantages of less heating of the sample and greater axial trap stability than visible-light ones). A power of $\approx$ 10 mW into the objective was sufficient to grab polystyrene particles between 0.5 and 1.0 μm in diameter. For convenience during alignment and for finding the trap position on the monitor, a colinear helium-neon (HeNe; 633 nm, $<$ 1 mW) laser beam was used.

We used a Nd:YLF solid-state laser (Quantronix) as a continuous-wave (CW) source of infrared laser light (1053 nm wavelength). Only the spherical lens, the mode selector and the polarizer-shutter were in the laser cavity; other pieces (which are necessary for mode locking) were bolted to the table outside the beam path. Periodic maintenance includes replacement of the de-ionizer filter for the internal, closed-loop water supply and refilling of the internal water supply using water from

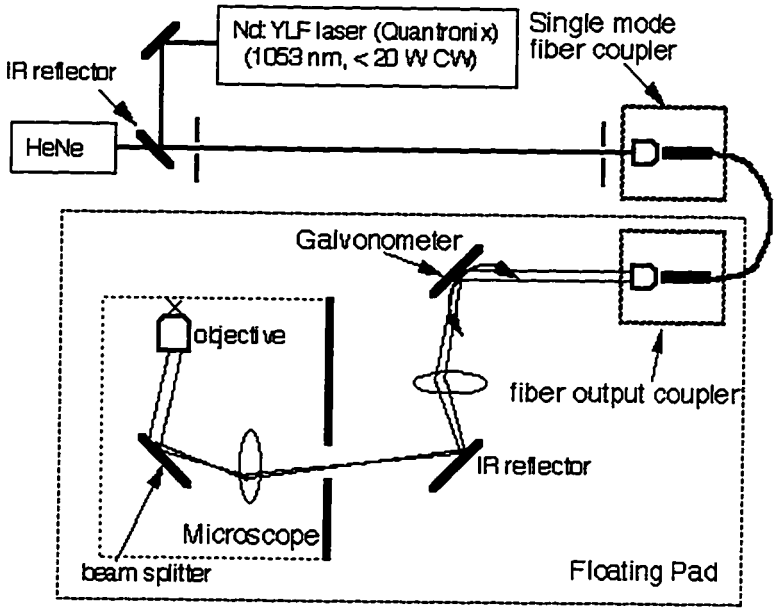

Figure 7.3: Schematic diagram of the optics for control of the laser tweezers.

the tap in the hallway outside room 314.

A single-mode fiber served as a spatial filter (selecting only the lowest Gaussian transverse mode [147]) and as a mechanical isolator. Single-mode fibers are easily cleaved (with practice, it takes less than an hour) and can be aligned (in about an hour) to allow better than 50% transmission up to ≈ 2 W. When setting up the fiber, it is very convenient to have (as always) at least two mirrors between the laser and the coupler, and to have two irises between the last mirror and coupler (Fig. 7.3). This arrangement makes realignment of the beam very simple: the first mirror (near the laser) is aligned so that the beam goes through to first iris, then the second mirror is aligned so that the beam goes through the second iris (some more small adjustments

of the mirror positions may be required). At this point, there should be a detectable amount of power through the fiber. The 5 degrees of freedom (3 translational, 2 rotational) of the single-mode fiber coupler can then be systematically tweaked to maximize the power coming out of the other end of the fiber. In these experiments, the output end of the fiber and the microscope were both bolted to the floating stage.

To scan the laser tweezers in three dimensions, some lenses and mirrors were mounted external to the microscope (Fig. 7.3). The key is to set up a telescope between a rotating mirror and the microscope objective [115] (note that one lens of the telescope is already mounted inside the microscope). The telescope simultaneously expands the beam as necessary and images the rotation point of the mirror onto the back aperture of the objective. Thus, any beam the hits the center of the rotating mirror will enter the objective. Rotating the mirror changes the angle at which the beam enters the objective. Since the back aperture of the objective defines the scattering plane, changing the *angle* there corresponds to changing the *lateral position* in the image plane. We used a pair of galvonometers to rotate the mirrors in two dimensions (Cambridge Technologies model no. 6350 (617) 923-1181). These galvonometers can be controlled with analog (from a function agenerator) or with digital signal. The $\pm$ 20 $^\circ$ of rotation are divided into 2^{16} angular positions. When a 16-bit digital "word" is sent to the galvo, it races to the corresponding position as fast as it can. The galvonometers were mounted separately and therefore rotated about

axes located at different points. Choosing lenses with long focal lengths minimizes the resulting beam distortions if the galvonometers are placed as close together as possible. The lenses used here had focal lengths of roughly 10 to 20 cm. John Crocker found that spherical abberation of the laser beam could be minimized by switching the lens installed in the microscope by Zeiss with one that had a focal length that was longer by a few cm.

Alignment of the tweezers is aided by turning on the 100W Halogen lamp mounted on the top of the microscope and inserting the beam splitter so that the white-light beam exits through the back port. When the iris near the back port is nearly closed, the laser beam coming into the microscope should be aligned so that it is colinear with the white-light beam coming out from the microscope.

7.3.5 Light Scattering in the Optical Microscope

By placing point detectors (optical fibers) or a camera in the scattering plane, one can do scattering experiments in the microscope [184, 188]. The Zeiss Axiovert 135 has an optovar rotating lens assembly under the objective that allows the scattering plane to be imaged at the eyepiece or camera mount (the lens labelled "ph"). A very simple scattering experiment can be performed, for example, with a fiber output coupler. When the lamp (in the top position) is replaced by the fiber coupler, the fiber tip will be near the scattering plane (dashed line in Fig. 7.2), as can be verified

by looking through the "ph" lens) . The fiber will illuminate the sample with a plane wave. Translating the fiber changes the incident angle. The scattered light can be imaged in the scattering plane, revealing the structure factor of the sample. The maximum angle of incidence is limited by the NA of the objective. For an oil-coupled objective with NA = 1.4, light can be sent in and collected up to 70 ° from vertical. A similar experiment can be done for backscattering. Scattering from an ordered layer of spheres of known sizes (made with convective assembly – see Chapter 6) will calibrate the position of the fiber in terms of the scattered wave vector. Evanescent-wave scattering from aqueous samples will also be possible using an objective with NA > 1.33, the refractive index of water. With these techniques, scattering experiments can be performed on the small crystallites discussed in Chapter 6.

7.4 Computer Control, Acquisition, and Image Analysis

We used a charge-coupled-device (CCD) camera (Hamamatsu model 2400-77E) on the microscope to capture images. A Macintosh Power PC 7100 with a Scion frame grabber card (Scion Co. model LG-3 (301) 695-7870) were used for control and image acquisition (Fig. 7.2). The Scion board has on-board RAM chips for storing a maximum of 32 frames (this was before the days of PCI busses in computers; new frame grabber boards can write frames directly to the computer's RAM). To store images on videotape, we used a super-VHS format VCR (Sanyo GVR-S950, from

Peirce-Phelps, (800) 248-4440). This VCR has the truly useful feature of labelling each frame using the audio track so that when the tape is played back, the precise timing is known. It can also go to specific frames on command from a computer via RS-232 control (see Appendix A).

All of the images were captured using a software package called NIH Image running on a Macintosh Power PC 7100. NIH Image is available free (along with extensive help files) from the FTP site "zippy.nimh.nih.gov". Macros in the Pascal language make it a very flexible and powerful system for hardware control, image acquisition, and image processing. Scion provided software tools to allow frame capture and analog output from the board using NIH Image. This analog output was connected to an electronic relay, which was used to switch a mechanical shutter in the step-edge repulsion experiment of Chapter 4. Because of the critical timing in that experiment, the frames were grabbed and stored on the frame grabber in real time. For experiments that were not synchronized with some external event, videotape was used to record the data. NIH Image software can also send output through the computer's serial port, allowing control of the VCR and of the focus-drive motor mounted to the microscope (ASI, model MFC-1 (800) 706-2284). For three-dimensional images (as in Chapter 6, section 6.3.3, page 187), a macro can be written to move the focus to a specific point, grab a frame, go to a new focus point, grab another frame, etc. (see Appendix). Using NIH Image, the resulting stack of images can then be sliced in the

vertical direction.

7.4.1 Image Processing and Analysis

A remarkable feature of video microscopy is that displacements of particles can be measured with nm-precision, even though the *shape* of particles cannot be resolved below $\approx$ 200 nm. The image processing for this thesis was done with NIH Image, which has built in to it several algorithms for enhancement and measurement. For all images that were analyzed, the particles were clearly distinguishable by eye. The enhancement was done, therefore, only to make the computer more likely to look at the correct object and to find its center more accurately. The built-in routines called "shadow" (for DIC images), "erode", "dilate" and the arithmetic commands (for background subtraction) were used most often. The algorithms of choice will depend strongly on the optical arrangement used. The measurement uncertainty was estimated by repeated measurements of the position of a particle that is fixed to a substrate. Deviations of the apparent position are due to electronic noise and fluctuations of the light intensity due to noise in the lamp or due to particles moving outside the focussed region. In all images, the particle of interest was selected manually using the "wand" tool, an extremely tedious process that does, at least, give confidence that the processing algorithms are not giving erroneous results. The resolution required for these experiments (50-100 nm) was easily obtained using the "density slice" tool,

in which all pixels with a user-specified range of intensity values are selected. The perimenter of each isolated blob is fit to an ellipse, the central position of which is written to a data file. A more precise method is to take the brightness-weighted centroid [15, 189]. The most precise method of all (as far as I am aware) is to fit the intensity pattern of the object with a reference pattern and calculate the position of the reference pattern that best fits the object [190]. We have been able to resolve the position of half-micron spheres to within 1.5 nm using this technique with DIC imaging.

The vertical position of a particle can also be obtained by looking at its apparent brightness and size [191]. The focus motor provides a simple way to calibrate by taking images of a fixed particle as the focus depth is changed. With the simple algorithms described above, a resolution of approximately 100 nm is possible.

7.5 Electron-Beam Lithography and Microassembly

In this section, I will describe our latest procedure for making microscopic patterns of polystyrene spheres on a glass substrate (see Chapter 6, section 6.2 [168]). The procedure has undergone considerable changes and can probably be improved further. The necessary equipment is found in the basement lab of the David Rittenhouse Laboratory (DRL) or in the Microfabrication Facility of the Electrical Engineering Dept. in the Moore Building. Since the humidity control in both of these labs is

inconsistent, it is a good idea to write down the humidity every time the procedure is followed. Ideally, the entire procedure should be done, from start to finish, in one day. While this is physically possible, it is difficult and inconvenient. Probably the best times to stop for the night would be when the sample is in the vacuum chamber of the thermal evaporator or of the SEM. For proper training in the use of these pieces of equipment, the reader should refer to the experts in Charlie Johnsons's research group.

7.5.1 Coverslip Preparation

We start with two ordinary glass coverslips, 18x18mm. Number $1\frac{1}{2}$ are better than number 1 coverslips because the added thickness reduces the chance of breakage. Larger coverslips will not fit easily into the scanning-electron microscope. To distinguish top from bottom, it is essential to make some asymmetric mark on the glass. I chose to cut a small triangle from the upper right corner, with the longer edge of the triangle along the top edge of the glass. Viewed upside down and rotated so that the cut is at the upper right corner, the longer edge of the triangle will be along the side (Fig. 7.4).

Experimental evidence suggests that it is best to use the acid wash procedure described in section 7.2.3. Good results were sometimes be obtained by carefully cleaning 3 times with Kimwipes and methanol. Although easier, this technique might

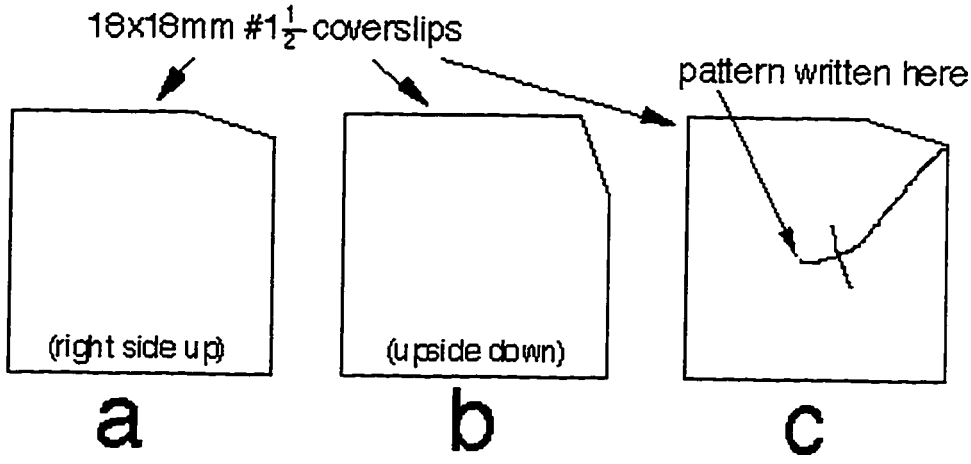

Figure 7.4: Marking and scratching coverslips. The asymmetric triangle that is cut off the corner allows (a) and (b) to be distinguished. In (c) a sample scratch is shown. leading from the corner to the middle, where the pattern is written.

be more susceptible to failure due to a dirty substrate. Cleaning should be done after clipping the corner. A 150-nm thick layer of poly(methylmethacrylate) is then applied using a spinner. The sample is placed on the spinner holder and $\sim$ 3 drops of PMMA solution (2% PMMA in chlorobenzene) is placed on it (enough to cover roughly half of the glass). The sample is then spun at 4800-5000 revolutions/min for 45 s, then placed on a hot plate set at 190 ° C for 30 min. A layer of aluminum (Al) should then be applied with minimal delay. In a thermal evaporator, 45-60 nm of Al [1] is deposited onto two substrates at a rate of $\approx$ 0.2 nm/s.

[1] According to the gauge on the thermal evaporator in DRL, these thicknesses correspond to 30-40 nm.

7.5.2 Electron-Beam Lithography

The next step is to write the pattern using the scanning-electron microscope (SEM) in the basement of DRL. Before mounting the sample, however, each sample should be scratched with a sharp needle to make an easily-visible trace that will make it easier to find the pattern(Fig. 7.4). The two samples are mounted using two *small* pieces of carbon tape on each, and a small droplet of silver paint for better electrical grounding. The following specifications were used to write the sample: accelerating voltage: 40keV; beam current (in the hole, at 1000x): -26.5 pA; z-setting of the stage: 15; magnification when writing: 1000x; mechanical aperture: 3. The computer files used to control the electon beam ("lit" files for "Elphy 3.3" software by Raith, GmbH) are stored on the accompanying computer in the directory "johnson\current\tony". The procedure used when writing is to focus the microscope near the edge of the sample, then move to the center (near the scratch), then focus again. Four fields of view are written around the focus point, each 200 μm from the focus dot. The stage is then moved 600 μm, refocussed, and four more samples are written, etc. The first pattern written on each substrate is always the "F-mark" (file = F2.lit; 13-bit resolution; dwell time = 0.033 ms). This writes an 86-μm "F" that is relatively easy to find and that orients the sample.

The optimal exposure time (dwell time) seems to be around 100 μs for arrays of 50-nm squares. We always used a settling time of 0.1 ms. We have not made a

systematic search for the best dot size.

7.5.3 Glue Processing

All of the following steps are done under a fume hood, wearing gloves and goggles. The sample must never be allowed to dry between rinsing steps (except when spun dry). Each step has a dedicated Petri dish, which should be rinsed after every use.

The aluminum is first removed by dunking the sample into a strong NaOH solution for 3 min. (a Petri dish half-filled with de-ionized, ultra-filtered (DIUF) water and 2 or 3 slugs of NaOH; wait a few minutes for the NaOH to dissolve completely), then placed in DIUF water for at least one minute. The samples are developed in a 1:3 solution of methyl isobutyl ketone (MIBK) in isopropyl alcohol (IPA) for 50 s, then placed in IPA for 2 minutes. The sample should then be spun dry and inspected under the optical microscope in the DRL lab (10x objective, DIC). The scratch and F-mark should be visible, as well as focus dots and (perhaps) arrays of dots.

The glue is then applied. If using poly-L-lysine, the procedure is to place a few drops of stock solution (see page 170) over the center of the substrate for 5 to 10 minutes. A longer exposure *could* damage the adhesion of the PMMA to the glass (not known for sure). It seemed that a shorter exposure did not allow the poly-L-lysine enough time to coat the substrate fully. The poly-L-lysine is then rinsed away with a jet of water, and the sample either rinsed in a Petri dish of water or squirted

while being spun dry. The PMMA is then stripped away by the following steps (5 min. each): acetone (placed on hot plate at 100°); glacial acetic acid; acetone (heated as before); glacial acetic acid; acetone. Finally, the sample is *quickly* placed on the spinner and spun dry (45 s, 5000 rpm). The sample should look perfectly clean to the eye.

7.5.4 Adding the Colloidal Particles

When adding the particles, I found it most convenient to make a sample cell that could be easily made and taken apart if desired. A double-layer of parafilm, arranged in three small pieces and heated on a hot plate at lowest setting, is sticky enough to hold the coverslip (face-down) against a glass microscope slide. A double layer should be used, since a single layer can lead to irreparable air bubbles. The colloid is then added (volume fraction = 0.003, [NaCl] =0.01M; a higher volume fraction seems to increase the amount of coverage of the background). The entire sample (slide and coverslip) is carefully wrapped in parafilm to prevent drying. Four hours later, the parafilm wrapper is removed and the sample is gently flushed with DIUF water and inspected under the optical microscope. The F-mark, scratch, and dot arrays should be covered with a high density of particles, with negligible density elsewhere. As many images as possible should be taken and saved to correlate the particle coverage with the electron-beam parameters and spot size.

7.5.5 Etching Microscopic Holes in Silicon

There are many experimental possibilities that arise from the entropic force-field ideas of Chapter 4. With electron-beam lithography, one has the hope of making microscopic structures with interesting, even useful features (including, potentially, an entropic ratchet). In an effort to demonstrate the entropic effects at a rigid wall of changing curvature radius, we made microscopic holes in silicon. We chose two shapes: a "grand piano" and a series of grooves, to demonstrate the curvature effects and step-edge repulsion and barrier-hopping. Zhiming Yu and Prof. A. T. (Charlie) Johnson contributed great amounts of time and expertise to this project. Unfortunately, we were ultimately foiled by surface roughness.

Silicon (100) wafers were first coated with 70 nm of chrome and 150 nm of PMMA, then the patterns were written with the SEM. After developing, a standard chrome etch was used, and the PMMA stripped, leaving a substrate covered with chrome except where the SEM had written. The sample was then etched in a plasma chamber with either SF_6 + $CCl_2{\cdot}F_2$ or CF_4 + H_2 (70-90% + 30-10%). The former mixture left vertical walls (which were good) as well as a lot of astonishingly tough polymer residue (which was bad). The second gas mixture left curved walls and no residue. Electron micrographs of our best samples are shown in Figs. 7.5, 7.6, and 7.7. Although the vertical profiles of both plama etchants were good, the outline of the pattern (presumably limited by the chrome etch) were somewhat rough ($\approx$ 100 nm). In

Figure 7.5: Scanning electron micrograph of a 300-nm deep piano-shaped structure etched in silicon. The scale bar represents one micron in length.

addition, colloid experiments on silicon were compromised by the non-hard-sphere attraction between silicon and polystyrene spheres. Due to some combination of these two effects, we were unable to see evidence of depletion-induced forces in these samples.

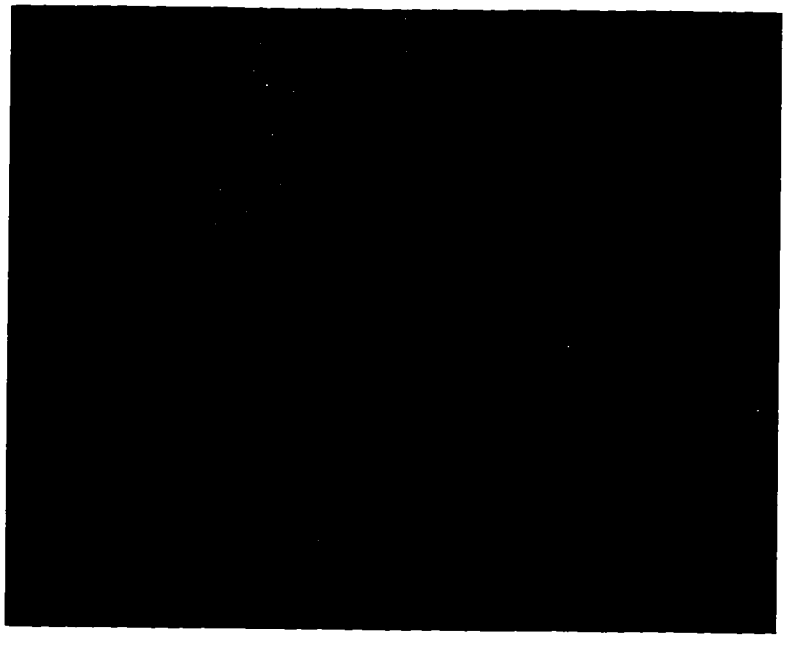

Figure 7.6: Scanning electron micrograph of a 100-nm-wide groove etched in silicon. The depth is $\approx$ 350 nm and the vertical edge profile is visible. The sample was made using a SF_6 + $CCl_2{\cdot}F_2$ plasma etch.

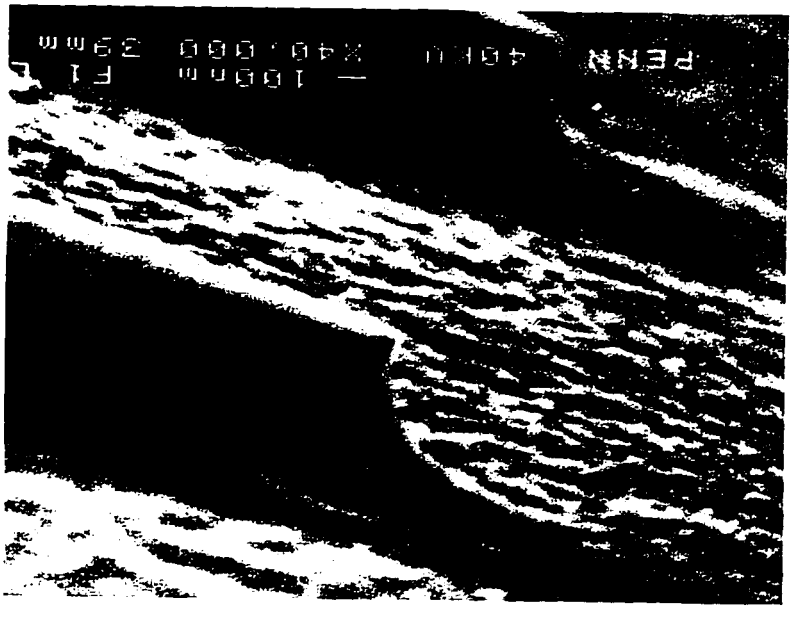

Figure 7.7: Scanning electron micrograph of the profile resulting from the $CF_4 + H_2$ plasma etch (30% H_2). The micrograph is oriented so that the unetched surfaces are on top and the rough etched surface is on the bottom.

Appendix A

NIH Image Macros

The appendix contains sample NIH Image macros for controlling the ASI microscope focus-control motor and the Sanyo GVR-S950 VCR. The NIH Image software and help files are available via ftp from zippy.nimh.nih.gov. These specialized applications are not covered in the help file that comes with the NIH Image.

The first macro simply moves the focus 0.1 microns up in the axial direction. Other control characters are listed in the ASI manual. Note that to use the ASI box manually after computer control, it may be necessary to flip the power on and off. Note that all commands for the ASI controller must be preceded by ctrl-f ($\hat{F}$) and ended by ctrl-g ($\hat{G}$). These key combinations must be included in the commands listed below, but might not appear in the text window within NIH Image!

```
{Macro Get-Z-Series, 3/97, T.D.}
Macro 'Z-scan /Z'
var i,num,snum:integer;
```

```
begin
RequiresVersion(1.48);
OpenSerial('9600 baud,no parity,eight data,one stop');
PutSerial('F̂ZĜ'); {zeros the position readout on the ASI box}
PutSerial('F̂I1Ĝ'); {sets the step-increment; in units of 0.1micron}
{ for example, I1 moves 0.1 microns}
{ minus sign moves down ( -10 = -1 micron)}
PutSerial('F̂GĜ');{moves the focus by the increment value}
Capture;
CloseSerial;
end;
```

The following macro gives an example of how to control the Sanyo GVR-S950 VCR. Upon running the macro, a window will appear and wait for a four-letter command (all in capital letters). The possible responses include PLAY, PAUS, and STOP and other possibilities that are listed in the Sanyo manual. Macros written with these lines of code are very useful for automatically grabbing frames from videotape. John Crocker has written a vastly more extensive and flexible file.

```
MACRO 'GVRS950 Control A/A';
var character,inchar,response:string;
```

```
TimeOutTicks,ModelNumber:  integer;

TimeOut:boolean;

Prefix,Suffix:integer;

begin

Suffix:=13;

{Cmd1:=65;}

inchar := GetString('input the string','COMMAND?');

OpenSerial('9600 baud,no parity,eight data,one stop');

PutSerial(Concat(inchar,Chr(13)));

end;
```

Appendix B

Determining Free Energy from Particle Dynamics

To extract information about the *equilibrium* state of a system by watching it while it is far from equilibrium (as in Chapter 4), we have implemented the technique of John Crocker and David Grier [78, 15], which they call the "Markovian Dynamics Extrapolation" (MDE). A "derivation" of the procedure is provided here as a complement to the one in [15] since, as is so often true in physics, there is more than one way to understand the problem.

We begin by writing down a "master equation" for the way in which the density (ρ_i) of particles at position i evolves with time, t:

$$\rho_i(t+\tau) = \sum_j P_{ij}(t+\tau|t)\rho_j(t). \tag{B.1}$$

The quantity $P_{ij}(t+\tau|t)$ is simply the probability that a particle located at position j at time t appeared at i at time $t+\tau$. In words, the equation simply updates the density at i by adding all of the probabilities that particles flowed into or out of i during the time interval τ. We now require one very important property: the "transition-

probability matrix" P must be independent of time t (although it does depend on the time *interval* τ). If P satisfies this constraint, it is said to be "Markovian". In general, this will be true if the potential acting on the particle is constant in time ("stationary").

We now write the same equation in matrix form:

$$\rho(t+\tau) = \underline{P}(\tau)\rho(\tau). \tag{B.2}$$

After an infinite time has passed, the system must have reached equilibrium, so that

$$\begin{aligned} \rho(t=\infty) &= \underline{P}(\tau)\rho(t=\infty) \\ &\propto e^{-F/k_BT}, \end{aligned} \tag{B.3}$$

where, of course, $\infty + \tau = \infty$. In our experiments, we measure P_{ij} and would like to know F_i or $\rho_i(\infty)$. From the form of the above equation, it is evident that $\rho(\infty)$ is simply the eigenvector of the matrix $P(\tau)$ that has unit eigenvalue. F_i/k_BT is the natural logarithm of the ith component of this eigenvector.

Appendix C

Glossary of Symbols and Acronyms

$a_{L(S)}$ is the diameter of a large (small) sphere.

α is the ratio of sphere diameters, large to small (a_L/a_S).

F is the Helmholtz free energy.

k_B is Boltzmann's constant.

Λ is the thermal wavelength.

μ is the chemical potential ($\partial F/\partial N$ at constant V).

μm is a micron, 10^{-6}m.

n is the refractive index.

nm is a nanometer, 10^{-9}m.

ϕ is the volume fraction of spheres (number density times the volume of one sphere).

$\tilde{\phi}$ is the effective volume fraction (Ch. 3).

$P_{ij}(\tau)$ is the probability that a sphere went from j to i during time interval τ.

P_S is the osmotic pressure of small colloidal spheres.

T is the temperature in Kelvins.

v^* is the volume accessible to spheres in a crystal lattice (Ch. 3).

AS = 3-aminopropyltriethoxysilane (page 169).

BCC = body-centered cubic structure.

CCD = charge coupled device (camera).

CW= continuous wave (referring to a laser).

DFT = density functional theory (Ch. 3).

DIC = differential interference contrast (Ch. 7).

DIUF=de-ionized and ultra-filtered (referring to water).

DRL = David Rittenhouse Lab, Univ. of Pennsylvania.

DYP = Dinsmore, Yodh, Pine (the theory described in Chapter 3).

FCC = face-centered cubic structure.

HCP = hexagonal close-packed structure.

IPA = isopropyl alcohol (2-propanol).

MIBK = methyl isobutyl ketone.

NA = numerical aperture (the sine of the half-angle of a light cone, times the refractive index).

PL = poly-L-lysine (page 170).

PY = Percus-Yevick approximation/closure (Ch. 3).

PMMA = poly(methylmethacrylate).

RHCP = random hexagonal close-packed structure.

RY = Rogers-Young approximation/closure (Ch. 3).

SEM = scanning electron microscope.

SPT = Scaled particle theory (see page 91).

TEM=transmission electron microscope.

Bibliography

[1] A. P. Gast, C. K. Hall, and W. B. Russel, *Polymer-Induced Phase Separations in Nonaqueous Colloidal Suspensions*, J. Coll. Int. Sci. **96**, 251 (1983).

[2] O. Mondain-Monval, F. Leal-Calderon, J. Philip, and J. Bibette, *Coupling between Electrostatic Double Layer Repulsion and Depletion Forces*, Phys. Rev. Lett. **75**, 3364 (1995).

[3] D. L. Sober and J. Y. Walz, *Measurement of Long Range Depletion Energies between a Colloidal Particle and a Flat Surface in Micellar Solutions*, Langmuir **11**, 2352 (1995).

[4] A. Milling and S. Biggs, *Direct Measurement of the Depletion Force Using an Atomic Force Microscope*, J. Colloid Interface Sci. **170**, 604 (1995).

[5] H. J. Guttman, C. F. Anderson, and J. M. T. Record, *Analyses of Thermodynamic Data for Concentrated Hemoglobin Solutions Using Scaled Particle Theory: Implications for a Simple Two-State Model of Water in Thermodynamic Analyses of Crowding in Vitro and in Vivo*, Biophys. J. **68**, 835 (1995).

[6] P. R. Wills, Y. Georgalis, J. Dijk, and D. J. Winzor, *Measurement of Thermodynamic Nonideality Arising from Volume-Exclusion Interactions between Proteins and Polymers*, Biophys. Chem. **57**, 37 (1995).

[7] H. C. Berg, *Random Walks in Biology* (Princeton Univ. Press, Princeton, NJ, 1993).

[8] *Selected Papers on Noise and Stochastic Processes*, edited by N. Wax (Dover, New York, 1954).

[9] M. Nichelatti, *Topics on Diffusion in Emulsions* (World Scientific, Singapore, 1994).

[10] A. Einstein, *Investigations on the Theory of the Brownian Movement* (Dover, New York, 1956).

[11] A. Vrij, *Polymers at Interfaces and the Interactions in Colloidal Dispersions*, Pure and Applied Chem. **48**, 471 (1976).

[12] W. B. Russel, D. A. Saville, and W. R. Schowalter, *Colloidal Dispersions* (Cambridge, New York, 1989).

[13] J. N. Israelachvili, *Intermolecular and Surface Forces* (Academic Press, London, 1991).

[14] J. L. Barrat, M. Baus, and J. P. Hansen, *Density-Functional Theory of Freezing of Hard-Sphere Mixtures into Substitutional Solid Solutions*, Phys. Rev. Lett. **56**, 1063 (1986).

[15] J. C. Crocker, *Probing Colloidal Interactions with Digital Video Microscopy and Blinking Optical Tweezers*, Ph.D. thesis, University of Chicago, 1996.

[16] J. Gregory, *The Role of Colloid Interactions in Solid-Liquid Separation*, Water Sci. Tech. **27**, 1 (1993).

[17] S. Asakura and F. Oosawa, *Interaction between Particles Suspended in Solutions of Macromolecules*, J. Polymer Sci. **33**, 183 (1958).

[18] S. Asakura and F. Oosawa, *On Interaction Between Two Bodies Immersed in a Solution of Macromolecules*, J. Chem. Phys. **22**, 1255 (1954).

[19] R. K. Pathria, *Statistical Mechanics* (Elsevier, Tarrytown, New York, 1972).

[20] P. D. Kaplan, J. L. Rouke, A. G. Yodh, and D. J. Pine, *Entropically-Driven Surface Phase Separation in Binary Colloidal Mixtures*, Phys. Rev. Lett. **72**, 582 (1994).

[21] P. D. Kaplan, L. P. Faucheux, and A. J. Libchaber, *Direct Observation of the Entropic Potential in a Binary Suspension*, Phys. Rev. Lett. **73**, 2793 (1994).

[22] Y. N. Ohshima, H. Sakagami, K. Okumoto, A. T. da, T. Igarashi, K. B. Shintaku, S. Toride, H. Sekino, K. Kabuto, and I. Nishio, *Direct Measurement of Infinitesimal Depletion Force in a Colloid-Polymer Mixture by Laser Radiation Pressure*, Phys. Rev. Lett. **78**, 3963 (1997).

[23] J. L. Parker, P. Richetti, P. Kekicheff, and S. Sarman, *Direct Measurement of Structural Forces in a Supermolecular Fluid*, Phys. Rev. Lett. **68**, 1955 (1992).

[24] S.-C. Kim, M. Calleja, and G. Rickayzen, *Density Profiles of Hard-Sphere Fluids Restricted by Hard and Permeable Walls*, J. Phys: Condens. Matter **7**, 8053 (1995).

[25] B. Gotzelmann, A. Haase, and S. Dietrich, *Structure Factor of Hard Spheres near a Wall*, Phys. Rev. E **53**, 3456 (1996).

[26] R. Dickman, P. Attard, and V. Simonian, *Entropic Forces in Binary Hard Sphere Mixtures: Theory and Simulation*, to be published in J. Chem. Phys. (July 1, 1997).

[27] X. L. Chu, A. D. Nikolov, and D. T. Wasan, *Effects of Particle Size and Polydispersity on the Depletion and Structural Forces in Colloidal Dispersions*, Langmuir **12**, 5004 (1996).

[28] T. Biben, P. Bladon, and D. Frenkel, *Depletion Effects in Binary Hard-Sphere Fluids*, J. Phys.: Condens. Matter **8**, 10799 (1996).

[29] J. C. Crocker, A. D. Dinsmore, D. A. Weitz, and A. G. Yodh, , (to be submitted) (1997).

[30] A. D. Dinsmore, A. G. Yodh, and D. J. Pine, *Phase Diagrams of Nearly Hard-Sphere Binary Colloids*, Phys. Rev. E **52**, 4045 (1995).

[31] P. N. Pusey and W. van Megen, *Phase Behavior of Concentrated Suspensions of Nearly Hard Colloidal Spheres*, Nature **320**, 340 (1986).

[32] P. N. Pusey, W. van Megen, P. Bartlett, B. J. Ackerson, J. G. Rarity, and S. M. Underwood, *Structure of Crystals of Hard Colloidal Spheres*, Phys. Rev. Lett. **63**, 2753 (1989).

[33] S. E. Paulin and B. J. Ackerson, *Observation of a Phase Transition in the Sedimentation Velocity of Hard Spheres*, Phys. Rev. Lett. **64**, 2663 (1990).

[34] S.-E. Phan, W. B. Russel, Z. Cheng, J. Zhu, P. M. Chaikin, J. H. Dunsmuir, and R. H. Ottewill, *Phase Transitionm, Equation of State and Limiting Shear Viscosities of Hard Sphere Dispersions*, Phys. Rev. E **54**, 6633 (1996).

[35] W. G. Hoover and F. H. Ree, *Melting Transition and Communal Entropy for Hard Spheres*, J. Chem. Phys. **49**, 3609 (1968).

[36] W. G. Hoover and F. H. Ree, *Use of Computer Experiments to Locate the*

Melting Transition and Calculate the Entropy in the Solid Phase, J. Chem. Phys. **47**, 4873 (1968).

[37] M. D. Rintoul and S. Torquato, *Metastability and Crystallization in Hard-Sphere Systems*, Phys. Rev. Lett. **77**, 4198 (1996).

[38] W. van Megen and S. M. Underwood, *Glass Transition in Colloidal Hard Spheres: Measurement and Mode-Coupling-Theory Analysis of the Coherent Intermediate Scattering Function*, Phys. Rev. E **49**, 4206 (1994).

[39] A. van Blaaderen and P. Wiltzius, *Real-Space Structure of Colloidal Hard-Sphere Glasses*, Science **270**, 1177 (1995).

[40] J. Zhu, M. Li, R. Rogers, W. Meyer, R. H. Ottewill, W. B. Russell, and P. M. Chaikin, *Crystallization of Hard-Sphere Colloids in Microgravity*, Nature **387**, 883 (1997).

[41] D. J. Courtemanche, T. A. Pasmore, and F. Van, Swol, *A Molecular Dynamics Study of Prefreezing Hard Spheres at a Smooth Wall*, Molecular Physics **80**, 861 (1993).

[42] D. A. Courtemanche and F. Van, Swol, *Wetting State of a Crystal-Fluid System of Hard Spheres*, Physical Review Letters **69**, 2078 (1992).

[43] P. Bartlett, R. H. Ottewill, and P. N. Pusey, *Freezing of Binary Mixtures of Colloidal Hard Spheres*, J. Chem. Phys. **93**, 1299 (1990).

[44] P. Bartlett, R. H. Ottewill, and P. N. Pusey, *Superlattice Formation in Binary Mixtures of Hard-Sphere Colloids*, Phys. Rev. Lett. **68**, 3801 (1992).

[45] J. V. Sanders, *Close-Packed Structures of Spheres of Different Sizes I:Observations on Natural Opal*, Philos. Mag. A **42**, 705 (1980).

[46] P. N. Pusey, W. C. K. Poon, S. M. Ilett, and P. Bartlett, *Phase Behavior and Structure of Colloidal Suspensions*, Proc. 2nd Liquid Matter Conf. Florence (September 1993).

[47] P. Bartlett and R. H. Ottewill, *Geometric Interactions in Binary Colloidal Dispersions*, Langmuir **8**, 1919 (1992).

[48] J. S. van Duijneveldt, A. W. Heinen, and H. N. W. Lekkerkerker, *Phase Separation in Bimodal Dispersions od Sterically Stabilized Silica Particles*, Europhys. Lett. **21**, 369 (1993).

[49] S. Sanyal, N. Easwar, S. Ramaswamy, and A. K. Sood, *Phase Separation in Binary Nearly-Hard-Sphere Colloids:Evidence for the Depletion Force*, Europhys. Lett **18**, 107 (1992).

[50] A. Imhof and J. K. G. Dhont, *Experimental Phase Diagram of a Binary Col-*

loidal Hard-Sphere Mixture with a Large Size Ratio, Phys. Rev. Lett. **75**, 1662 (1995).

[51] F. L. Calderon, J. Bibette, and J. Biais, *Experimental Phase Diagrams of Polymer and Colloid Mixtures*, Europhys. Lett. **23**, 653 (1993).

[52] H. De Hek and A. Vrij, *Interactions in Mixtures of Colloidal Silica Spheres and Polystyrene Molecules in Cyclohexane*, J. Colloid Interface Sci. **84**, 409 (1981).

[53] S. M. Ilett, A. Orrock, W. C. K. Poon, and P. N. Pusey, *Phase Behavior of a Model Colloid-Polymer Mixture*, Phys. Rev. E **51**, 1344 (1995).

[54] W. C. K. Poon, J. S. Selfe, M. B. Robertson, S. M. Ilett, A. D. Pirie, and P. Pusey, *An Experimental Study of a Model Colloid-Polymer Mixture*, J. Phys France **3**, 1075 (1993).

[55] J. Bibette, D. Roux, and B. Pouligny, *Creaming of Emulsions: the Role of Depletion Forces Induced by Surfactant*, J. Phys. II France **2**, 401 (1992).

[56] J. Bibette, D. Roux, and F. Nallet, *Depletion Interactions and Fluid-Solid Equilibrium in Emulsions*, Phys. Rev. Lett. **65**, 2470 .

[57] U. Steiner, A. Meller, and J. Stavans, *Entropic Phase Separation in Binary Emulsions*, Phys. Rev. Lett. **74**, 4750 (1995).

[58] M. Yasrebi, W. Y. Shih, and I. A. Aksay, *Clustering of Binary Colloidal Suspensions: Experiment*, J. Colloid Interface Sci. **142**, 357 (1991).

[59] T. Biben and J. P. Hansen, *Osmotic Depletion Non-Additivity and Phase Separation*, Physica A **235**, 142 (1997).

[60] P. D. Kaplan, *Optical Studies of the Structure and Dynamics of Opaque Colloids*, Ph.D. thesis, Univ. of Pennsylvania, 1993.

[61] D. J. Pine, D. A. Weitz, J. X. Zhu, and E. Herbolzheimer, *Diffusing-Wave Spectroscopy: Dynamic Light Scattering in the Multiple Scattering Limit*, J. Phys. France **51**, 2101 (1990).

[62] A. G. Yodh, D. J. Pine, P. D. Kaplan, M. H. Kao, and N. Georgiades, *Speckle Fluctuations and their Use as Probes of Dense Random Media*, Mol. Cryst. Liq. Cryst. Sci. Technol - Sec B **3**, 149 (1992).

[63] D. J. Pine, D. A. Weitz, P. M. Chaikin, and E. Herbolzheimer, *Diffusing-Wave Spectroscopy*, Phys. Rev. Lett. **60**, 1134 (1988).

[64] S. Fraden and G. Maret, *Multiple Light Scattering from Concentrated Interacting Suspensions*, Phys Rev. Lett. **65**, 512 (1990).

[65] P. D. Kaplan, A. G. Yodh, and D. F. Townsend, *Noninvasive Study of Gel*

Formation in Polymer-Stabilized Dense Colloids Using Multiply Scattered Light, J. Coll. Int. Sci. **155**, 319 (1993).

[66] P. Pieranski, E. Dubois-Violette, F. Rothen, and L. Strzelecki, *Geometry of Kossel Lines in Colloidal Crystals*, J. Physique **42**, 53 (1981).

[67] R. D. Pradhan, J. A. Bloodgood, and G. H. Watson, *Photonic Band Structure of BCC Colloidal Crystals*, Phys. Rev. B **55**, 9503 (1997).

[68] P. N. Pusey, A. D. Pirie, and W. C. K. Poon, *Dynamics of Colloid-Polymer Mixtures*, Physica A **201**, 322 (1993).

[69] W. C. K. Poon, A. D. Pirie, and P. N. Pusey, *Gelation in Colloid-Polymer Mixtures*, Faraday Discussions **101**, Gels ((1995)).

[70] L. D. Landau and E. M. Lifshitz, *Statistical Physics* (Pergamon Press, Oxford, 1980).

[71] H. N. W. Lekkerkerker, W. C. K. Poon, P. N. Pusey, A. Stroobants, and P. B. Warren, *Phase Behaviour of Colloid + Polymer Mixtures*, Europhysics Letters **20**, 559 (1992).

[72] C. F. Tejero, A. Daanoun, H. N. W. Lekkerkerker, and M. Baus, *Phase Diagrams of "Simple" Fluids with Extreme Pair Potentials*, Phys. Rev. Lett. **73**, 752 (1994).

[73] D. C. Prieve and N. A. Frej, *Total Internal Reflection Microscopy: A Quantitative Tool for the Measurement of Colloidal Forces*, Langmuir **6**, 396 (1990).

[74] A. D. Dinsmore, A. G. Yodh, P. B. Warren, and W. C. K. Poon, *Fluid-Solid Transitions on Walls in Binary Hard-Sphere Mixtures*, (submitted to Europhys. Lett.) (1997).

[75] W. C. K. Poon and P. B. Warren, *Phase Behavior of Hard-Sphere Mixtures.* Europhysics Lett. **28**, 513 (1994).

[76] A. van Blaaderen, A. Imhof, W. Hage, and A. Vrij, *Three-Dimensional Imaging of Submicrometer Colloidal Particles in Concentrated Suspensions Using Confocal Scanning Laser Microscopy*, Langmuir **8**, 1514 (1992).

[77] R. Evans and O. Parry, , J. Phys. Cond. Matt. **3(SA):1**, (1990).

[78] J. C. Crocker and D. G. Grier, *Microscopic Measurement of the Pair Interaction Potential of Charge-Stabilized Colloid*, Phys. Rev. Lett. **73**, 352 (1994).

[79] R. J. Buehler, J. R. H. Wentorf, J. O. Hirschfelder, and C. Curtiss, *The Free Volume for Rigid Sphere Molecules*, J. Chem. Phys. **19**, 61 (1951).

[80] H. N. W. Lekkerkerker and A. Stroobants, *On the Spinodal Instability of Highly Assymetric Hard-Sphere Suspensions*, Physica A **195**, 387 (1993).

[81] J. L. Lebowitz and J. S. Rowlinson, *Thermodynamic Properties of Mixtures of Hard Spheres*, J. Chem. Phys. **41**, 133 (1964).

[82] J. P. Hansen and I. R. McDonald, *Theory of Simple Liquids* (Academic Press, London, 1986).

[83] T. Biben and J. P. Hansen, *Phase Separation of Asymmetric Hard-Sphere Fluids*, Phys. Rev. Lett. **66**, 2215 (1991).

[84] Y. Rosenfeld, *Phase Separation of Asymmetric Binary Hard-Sphere Fluids: Self-Consistent Density Functional Theory*, Phys. Rev. Lett. **72**, 3831 (1994).

[85] Y. Rosenfeld, M. Schmidt, H. Lowen, and P. Tarazona, *Fundamental-Measure Free-Energy Density Functional for Hard Spheres: Dimensional Crossover and Freezing*, Phys. Rev. E **55**, 4245 (1997).

[86] B. Gotzelmann and S. Dietrich, *Density and Pair Correlation Functions of Hard Spheres in Narrow Slits*, Phys. Rev. E **55**, 2993 (1997).

[87] P. Bartlett, *A Model for the Freezing of Binary Colloidal Hard Spheres*, J. Phys. Cond. Matter **2**, 4979 (1990).

[88] A. R. Denton and N. W. Ashcroft, *Weighted Density-Functional Theory of Nonuniform Fluid Mixtures: Application to Freezing of Binary Hard-Sphere Mixtures*, Phys. Rev. A **42**, 7312 (1990).

[89] J. L. Barrat, M. Baus, and J. P. Hansen, *Density-Functional Theory of Freezing of Hard-Sphere Mixtures into Substitutional Solid Solutions*, Phys. Rev. Lett. **56**, 1063 (1986).

[90] S. J. Smithline and A. D. J. Haymet, *Density Functional Theory for the Freezing of 1:1 Hard Sphere Mixtures*, J. Chem. Phys. **86**, 6486 (1987).

[91] B. Vincent, J. Edwards, S. Emmett, and R. Croot, *Phase Separation in Dispersions of Weakly-Interacting Particles in Solutions of Non-Adsorbing Polymer*, Colloids and Surfaces **31**, 267 (1988).

[92] M. Dijkstra and D. Frenkel, *Evidence for Entropy-Driven Demixing in Hard-Core Fluids*, Phys. Rev. Lett. **72**, 298 (1994).

[93] J. S. van Duijneveldt and H. N. W. Lekkerkerker, *Three-Phase Equilibrium in a Binary Hard-Core Lattice Model*, Phys. Rev. Lett. **71**, 4264 (1993).

[94] N. F. Carnahan and K. E. Starling, *Equation of State for Nonattracting Rigid Spheres*, J. Chem. Phys. **51**, 635 (1969).

[95] K. Huang, *Statistical Mechanics* (John Wiley and Sons, New York, 1987).

[96] P. M. Chaikin and T. C. Lubensky, *Principles of Condensed Matter Physics* (Cambridge Univ. Press, New York, 1995).

[97] K. R. Hall, *Another Hard-Sphere Equation of State*, J. Chem. Phys. **2252**, (1972).

[98] J. L. Lebowitz, H. E., and E. Praestgaard, *Scaled Particle Theory of Fluid Mixtures*, J. Chem. Phys. **43**, 774 (1965).

[99] W. H. Press, S. A. Teukolsky, W. T. Vettering, and B. P. Flannery, *Numerical Recipes in C* (Cambridge Univ. Press, New York, 1992).

[100] L. B. Bangs, *Latex Immunoassays*, J. Clinical Immunoassay **13**, 127 (1990).

[101] J. D. Joannopoulos, R. D. Meade, and J. N. Winn, *Photonic Crystals: Molding the Flow of Light* (Princeton Univ. Press, New Jersey, 1995).

[102] *Photonic Band Gap Materials*, edited by C. M. Soukoulis (Kluwer Academic Publishers, Norwell, MA, 1996).

[103] *Photonic Band Gaps and Localization*, edited by C. M. Soukoulis (Plenum Press, New York, 1993).

[104] E. Yablonovitch, *Photonic Band-Gap Structures*, J. Opt. Sci. Am. **10**, 283 (1993).

[105] E. Yablonovitch, *Inhibited Emission in Solid-State Physics and Electronics*, Phys. Rev. Lett. **58**, 2059 (1987).

[106] A. P. Minton, *Confinement as a Determinant of Macromolecular Structure and Reactivity*, Biophys. J. **63**, 1090 (1992).

[107] A. P. Minton, *Confinement as a Determinant of Maromolecular Structure and Reactivity II: Effects of Weakly Attractive Interactions between Confined Macrosolutes and Confining Structures*, Biophys. J. **68**, 1311 (1995).

[108] B. Alberts, D. Bray, J. Lewis, M. Raff, K. Roberts, and J. D. Watson, *Molecular Biology of the Cell* (Garland Publishing, New York, 1994).

[109] A. D. Dinsmore, A. G. Yodh, and D. J. Pine, *Entropic Control of Particle Motion Using Passive Surface Microstructures*, Nature **383**, 239 (1996).

[110] A. D. Dinsmore and A. G. Yodh, , (unpublished) (1997).

[111] A. Ashkin, J. M. Dziedzic, J. E. Bjorkholm, and S. Chu, *Observation of Single-Beam Gradient Force Optical Trap for Dielectric Particles*, Optics Lett. **11**, 288 (1986).

[112] A. Ashkin, *Forces of a Single-Beam Gradient Laser Trap on a Dielectric Sphere in the Ray Optics Regime*, Biophys. J. **61**, 569 (1992).

[113] S. Chu, *Laser Trapping of Neutral Particles*, Scientific American **Feb. 1992**, 71 (1992).

[114] K. Svoboda and S. M. Block, *Biological Applications of Optical Forces*, Annu. Rev. Biomol. Struct. **23**, 247 (1994).

[115] R. S. Afzal and E. B. Treacy, *Optical Tweezers Using a Diode Laser*, Rev. Sci. Instrum. **63**, 2157 (1992).

[116] H. A. Kramers, *Brownian Motion in a Field of Force and the Diffusion Model of Chemical Reactions*, Physica **7**, 284 (1940).

[117] J. D. Jackson, *Classical Electrodynamics* (John Wiley and Sons, New York, 1975).

[118] A. D. Dinsmore, D. T. Wong, P. Nelson, and A. G. Yodh, *Hard Spheres inside Vesicles: Curvature-Induced Forces and Particle-Induced Curvature*, (submitted to Phys. Rev. Lett.) (1997).

[119] C. S. Chen, M. Mrksich, S. Huang, G. M. Whitesides, and D. E. Ingber, *Geometric Control of Cell Life and Death*, Science **276**, 1425 (1997).

[120] K. Svoboda, C. F. Schmidt, B. J. Schnapp, and S. M. Block, *Direct Observation of Kinesin Stepping by Optical Trapping Interferometry*, Nature **365**, 721 (1993).

[121] J. E. Rothman and F. T. Wieland, *Protein Sorting by Transport Vesicles*, Science **272**, 227 (1996).

[122] E. Sackmann, A. D. Dinsmore, and A. G. Yodh, , (private conversation) (1997).

[123] W. Helfrich and R.-M. Servuss, *Undulations, Steric Interactions and Cohesion of Fluid Membranes*, Il Nuovo Cimento **3D**, 137 (1984).

[124] C. R. Safinya, *Rigid and Fluctuating Surfaces: A Series of Synchotron X-Ray Scattering Studies of Interacting Stacked Membranes*, Phase transitions in Soft Condensed Matter 249 (1989).

[125] C. Safinya, D. Roux, G. Smith, S. Sinha, P. Dimon, N. Clark, and A. Bellocq, *Steric Interactions in a Model Multimembrane System: A Synchotron X-Ray Study*, Phys. Rev. Lett. **57**, 2718 (1986).

[126] R. Lipowsky and B. Zielinska, *Binding and Unbinding of Lipid Membranes: A Monte Carlo Study*, Phys. Rev. Lett. **62**, 1572 (1989).

[127] U. Seifert, *Configurations of Fluid Membranes and Vesicles*, Advances in Phys. **46**, 13 (1997).

[128] E. Evans and D. Needham, *Physical Properties of Surfactant Bilayer Membranes: Thermal Transitions, Elasticity, Rigidity, Cohesion, and Colloid Interactions*, J. Phys. Chem. **91**, 4219 (1987).

[129] *The Structure and Dynamics of Membranes*, edited by R. Lipowsky and E. Sackmann (Elsevier, Amsterdam, 1995), Vol. 1B.

[130] P. Nelson, A. D. Dinsmore, and A. G. Yodh, , (to be submitted) (1997).

[131] P. B. Canham, , J. Theor. Biol. **26**, 61 (1970).

[132] W. Helfrich, *Elastic Properties of Lipid Bilayers: Theory and Possible Experiments*, Z. Naturforsch **28c**, 693 (1973).

[133] U. Seifert and R. Lipowsky, *Adhesion of Vesicles*, Phys. Rev. A **42**, 4768 (1990).

[134] K. Berndl, J. Kas, R. Lipowsky, E. Sackmann, and U. Seifert, *Shape Transformations of Giant Vesicles: Extreme Sensitivity to Bilayer Asymmetry*, Europhys. Lett. **13**, 659 (1990).

[135] R. Lipowsky, *Budding of Membranes Induced by Intramembrane Domains*, J. Phys. II Fr. **2**, 1825 (1992).

[136] E. Sackmann, J. Kas, and J. Radler, *On Shape Transformations and Shape Fluctuations of Cellular Compartments and Vesicles*, Physica Scripta **T49**, 111 (1993).

[137] N. W. Ashcroft and N. D. Mermin, *Solid State Physics* (W. B. Saunders Co., Philadelphia, 1976).

[138] A. van Blaaderen, R. Ruel, and P. Wiltzius, *Template-Directed Colloidal Crystallization*, Nature **385**, 321 (1997).

[139] D. Levine and P. J. Steinhardt, *Quasicrystals. I. Definition and Structure*, Phys. Rev. B **34**, 596 (1986).

[140] M. N. Rahaman, *Ceramic Processes and Sintering* (Marcel Dekker, New York, 1995).

[141] C. Murray and D. Grier, *Colloidal Crystals*, American Scientist **83**, 238 (1995).

[142] P. Clark, *Cell Behavior on Micropatterned Surfaces*, Biosensors and Bioelectronics **9**, 657 (1994).

[143] J. Joannopoulos, P. Villeneuve, and S. Fan, *Photonic Crystals: Putting a New Twist on Light*, Nature **386**, 143 (1997).

[144] H. C. van de Hulst, *Light Scattering by Small Particles* (Dover, New York, 1981).

[145] R. Sprik, B. A. van Tiggelen, and A. Lagendijk, *Optical Emission in Periodic Dielectrics*, Europhys. Lett. **35**, 265 (1996).

[146] J. J. Sakurai, *Modern Quantum Mechanics* (Addison-Wesley, Reading, MA, 1985).

[147] P. W. Milonni and J. H. Eberly, *Lasers* (John Wiley and Sons, New York, 1988).

[148] J. Martorell and N. Lawandy, *Observation of Inhibited Spontaneous Emission in a Periodic Dielectric Structure*, Phys. Rev. Lett. **65**, 1877 (1990).

[149] M. Tocci and M. Scalora, *Measurement of Spontaneous-Emission Enhancement near the One-Dimensional Photonic Band Edge of Semiconductor Heterostructures*, Phys. Rev. A **53**, 2799 (1996).

[150] S. Kitson, W. Barnes, and J. Sambles, *Full Photonic Band Gap for Surface Modes in the Visible*, Phys. Rev. Lett. **77**, 2670 (1996).

[151] D. Wilhelmy and E. Matijevic, *Preparation and Properties of Monodispersed Spherical-Colloidal Particles of Zinc Sulphide*, J. Chem. Soc. Faraday Trans. 1 **80**, 563 (1984).

[152] G. Chiu, *The Preparation of Monodisperse Zinc Sulfide Sols*, J. Coll. Int. Sci. **83**, 309 (1981).

[153] T. Sugimoto, G. Dirige, and A. Muramatsu, *Formation Mechanism of Monodisperse CdS Particles from Concentrated Solutions of Cd-EDTA Complexes*, J. Coll. Int. Sci. **182**, 444 (1996).

[154] K. Ho, C. Chan, and C. Soukoulis, *Existence of a Photonic Band Gap in Periodic Dielectric Structures*, Phys. Rev. Lett. **65**, 3152 (1990).

[155] Z. Zhang and S. Satpathy, *Electromagnetic Wave Propagation in Periodic Structures: Bloch Wave Solution of Maxwell's Equations*, Phys. Rev. Lett. **65**, 2650 (1990).

[156] K. M. Leung and Y. F. Liu, *Full Vector Wave Calculation of Photonic Band Structures in Face-Centered Cubic Dielectric Media*, Phys. Rev. Lett. **65**, 2646 (1990).

[157] E. Yablonovitch and T. J. Gmitter, *Photonic Band Structure: The Face-Centered Cubic Case*, Phys. Rev. Lett. **63**, 1950 (1989).

[158] C. Anderson and K.P.Giapis, *Larger Two-Dimensional Photonic Band Gaps*, Phys. Rev. Lett. **77**, 2949 (1996).

[159] I. Tarhan and G. H. Watson, *Photonic Band Structure of fcc Colloidal Crystals*, Phys. Rev. Lett. **76**, 315 (1996).

[160] I. I. Tarhan, M. P. Zinkin, and G. H. Watson, *An Interferometric Technique for Measurement of Photonic Band Structure of Colloidal Crystals*, Optics Lett. **20**, 1571 (1995).

[161] R. D. Pradhan, I. I. Tarhan, and G. H. Watson, *Impurity Modes in the Optical Stop Bands of Doped Colloidal Crystals*, Phys. Rev. B **54**, 1 (1996).

[162] M. Trau, D. Saville, and I. Aksay, *Field-Induced Layering of Colloidal Crystals*, Science **272**, 706 (1996).

[163] M. Trau, S. Sankaran, D. Saville, and I. Aksay, *Electric-Field-Induced Pattern Formation in Colloidal Dispersions*, Nature **374**, 437 (1995).

[164] M. Trau, S. Sankaran, D. Saville, and I. Aksay, *Pattern Formation in Nonaqueous Colloidal Dispersions via Electrohydrodynamic Flow*, Langmuir **11**, 4665 (1995).

[165] S.-R. Yeh, M. Seul, and B. Shraiman, *Assembly of Ordered Colloidal Aggregates by Electric-Field-Induced Flow*, Nature **386**, 7 (1997).

[166] J. Schmitt, G. Decher, W. Dressick, S. Brandow, R. Geer, R. Shashidhar, and J. Calvert, *Metal Nanoparticle/Polymer Superlattice Films: Fabrication and Control of Layer Structure*, Advanced Materials **9**, 61 (1997).

[167] N. Kotov, I. Dekany, and J. H. Fendler, *Layer-by-Layer Self-Assembly of Polyelectrolyte-Semiconductor Nanoparticle Composite Films*, J. Phys. Chem. **99**, 13065 (1995).

[168] A. D. Dinsmore, G. H. Watson, Z.-M. Yu, J. Paransky, M. Aggarwal, A. T. Johnson, and A. G. Yodh, , (to be submitted) (1997).

[169] T. Sato, D. Hasko, and H. Ahmed, *Nanoscale Colloidal Particles: Monolayer Organization and Patterning*, J. Vac. Sci. Tech. B **15**, 45 (1997).

[170] E. P. Plueddemann, *Silane Coupling Agents* (Plenum, New York, 1991).

[171] D. Mazia, G. Schatten, and W. Sale, *Adhesion of Cells to Surfaces Coated with Polylysine*, J. Cell Biology **66**, 198 (1975).

[172] R. Micheletto, H. Fukuda, and M. Ohtsu, *A Simple Method for the Production of a Two-Dimensional Ordered Array of Small Latex Particles*, Langmuir **11**, 3333 (1995).

[173] N. D. Denkov, O. D. Velev, P. A. Kralchevsky, I. B. Ivanov, H. Yoshimura, and K. Nagayama, *Two-Dimensional Crystallization*, Nature **361**, 26 (1993).

[174] I. Peterson, *Butterfly Blue: Packaging a Butterfly's Iridescent Sheen*, Science News **148**, 296 (1995).

[175] A. Dimitrov and K. Nagayama, *Steady-State Unidirectional Convective Assembling of Fine Particles into Two-dimensional Arrays*, Chem. Phys. lett. **243**, 462 (1995).

[176] E. Adachi, A. Dimitrov, and K. Nagayama, *Stripe Patterns Formed on Glass Surface during Droplet Evaporation*, Langmuir **11**, 1057 (1995).

[177] A. D. Dinsmore, J. A. Matteo, D. Rethwisch, and A. G. Yodh, , (to be submitted) (1997).

[178] P. Kralchevsky and K. Nagayama, *Capillary Forces between Colloidal Particles*, Langmuir **1**, 23 (1994).

[179] A. Goudy, M. Gee, S. Biggs, and S. Underwood, *Atomic Force Microscopy*

Study of Polystyrene Latex Film Morphology: Effects of Aging and Annealing, Langmuir **11**, 4454 (1995).

[180] J. Weiss, D. Oxtoby, D. Grier, and C. Murray, *Martensitic Transition in a Confined Colloidal Suspension*, J. Chem. Phys. **103**, 1 (1995).

[181] J. K. Trautman, J. J. Macklin, L. E. Brus, and E. Betzig, *Near-Field Spectroscopy of Single Molecules at Room Temperature*, Nature **369**, 40 (1994).

[182] L. Holland, *The Properties of Glass Surfaces* (John Wiley and Sons, New York, 1964).

[183] S. Inoue, *Video Microscopy* (Plenum Press, New York, 1986).

[184] *New Techniques of Optical Microscopy and Microspectroscopy*, edited by R. J. Cherry (CRC Press, Boca Raton, FL, 1991).

[185] *Photonics*, edited by M. Balkanski and P. Lallemand (Gauthier-Villars, Paris, 1973).

[186] C. D'Helon, E. W. Dearden, H. Rubinsztein-Dunlop, and N. R. Heckenberg, *Measurement of the Optical Force and Trapping Range of a Single-Beam Gradient Optical Trap for Micron-Sized Latex Spheres*, J. Modern Optics **41**, 595 (1994).

[187] J. Y. Walz and D. C. Prieve, *Prediction and Measurement of the Optical Trapping Forces on a Microscopic Dielectric Sphere*, Langmuir **8**, 3073 (1992).

[188] R. Bar-Ziv, A. Meller, T. Tlusty, E. Moses, J. S. avans, and S. A. Safran, *Localized Dynamic Light Scattering: Probing Single Particle Dynamics at the Nanoscale*, Phys. Rev. Lett. **78**, 154 (1997).

[189] J. Crocker and D. Grier, *Methods of Digital Video Microscopy for Colloidal Studies*, J. Coll. Int. Sci. **179**, 298 (1996).

[190] J. Gelles, B. J. Schnapp, and M. P. Sheetz, *Tracking Kinesin-Driven Movements with Nanometre-Scale Precision*, Nature **331**, 450 (1988).

[191] G. Kepler and S. Fraden, *Video Microscopy Study of the Potential Energy of a Colloidal Particle Confined between Two Plates*, Langmuir **10**, 2501 (1994).